University of Strathclyde

Department of Pure and Applied Chemistry

Investigation of a drying process of needle-shaped particles using particle size analysis techniques and non-invasive Raman spectrometry

Peter Hamilton

A thesis submitted to the Department of Pure and Applied Chemistry, University of Strathclyde, Glasgow, in fulfilment of the requirements for the degree of Doctor of Philosophy.

2011

This thesis is the result of the author's original research. It has been composed by the author and has not been previously submitted for examination which has led to the award of a degree.

Signed: Date

To my family, *quis puttase, vultus et cerebro…*

Acknowledgements

Firstly, I would like to thank my primary supervisor Professor David Littlejohn for all of his expert advice, guidance and occasional direction throughout the duration of this work. This also extends to Dr. Alison Nordon and Dr. Jan Sefcik. Alison, for the countless interesting discussions and suggestions, both during meetings and the times I appeared at your door, not forgetting all your help in the lab and with MATLAB. Jan, for all the interesting discussions and important questions raised relating to the particle size aspects of this research. To all of you, I will always be extremely grateful.

As well as the mentioned academic support, I would like to thank Dr. John Andrews and Dr. Paul Dallin from Clairet Scientific Ltd. for providing the Raman instrumentation required to complete this research (with numerous trips up and down the M6 for their troubles), along with plenty of help and support along the way. This extends to Dr. Paul Slavin from GSK for many things throughout the last few years including recrystallisation of the COA particles, providing the PIMS instrumentation, setting targets and giving advice from the view-point of the pharmaceutical industry.

Thank you to all the GSK employees at RTP who were very welcoming and made my time there extremely enjoyable, particularly Rahn McKeown for taking me under his wing and finding the time to teach me so much in a short space of time, but also Pascal Toma and Kim Anderson for all their help and support.

I also acknowledge the University of Strathclyde, EPSRC collaborative training account, GSK, and Clairet Scientific for providing funding, without which, none of this work could have been carried out. Other thanks go to Natalie Driscoll, Neil Hodgson and John Dunsieth for various help throughout my Ph.D.

Lastly, I would like to thank all the members of the analytical group, both past and present, for creating a special environment to work in, and all my friends, family, loved ones, and not-so loved ones for sticking in there throughout all the trials and tribulations, the highs and the lows, and all the laughs (and tantrums) along the way!!

Abstract

The attrition of needle-shaped cellobiose octaacetate (COA) particles during drying was studied using particle size analysis and *in situ* spectrometry techniques. Firstly, three particle size analysis techniques were evaluated for their efficacy relating to needle-shaped particles. Laser scattering techniques provided qualitative information on average particle size, however, it was shown that the Feret Max dimension obtained from dynamic image analysis was the best indicator of needle length, and allowed quantitative observations to be reported.

A bespoke lab-scale drier was used to determine the effect of varying the process conditions on drying time and the extent of attrition using two approaches, with non-invasive wide illumination Raman measurements recorded *in situ.* A design of experiments was carried out to determine the effect of three drying parameters on the total drying time and extent of attrition. All the parameters had an effect, however, attrition was mainly affected by the agitation strategy. Variation of the pressure filtration time prior to vacuum agitated drying produced a range of particle wetness that allowed the relationship between particle wetness, agitation and attrition rates to be examined.

In situ Raman spectrometry allowed the drying curves from both the solvent and the particles to be monitored in real-time. The magnitude of the Raman signal of COA during drying was affected by changes in the bulk density of the particle bed. By interpretation of the COA drying curve, it was possible to detect the onset of aggregation and then the break-up of the aggregates to powder. It was not possible to estimate the particle size from the Raman spectra during drying as changes in the particle bed's bulk density dominated the variation in the Raman signal. In the final part, the learning from the laboratory experiments was applied successfully to an industrial case study at GSK.

Table of contents

Journal articles and main external presentation titles

Journal articles

"*Studies of particle drying using non-invasive Raman spectrometry and particle size analysis*", Hamilton, P., Littlejohn , D., Nordon, A., Sefcik, J., Slavin, P., Andrews, J., Dallin, P., Analyst, 2011, **136**, 2168 – 2174.

"*Validity of particle size analysis techniques for measurement of attrition of needle-shaped particles that occurs during vacuum agitated powder drying*", Hamilton, P., Littlejohn , D., Nordon, A., Sefcik, J., Slavin, P., Analyst, 2012, **137**, 118 – 125.

Main conference presentations

"Studies in powder drying using *in situ* Raman spectrometry and off-line particle size analysis", oral presentation, EuroPACT, Glasgow, UK, April 2011.

"*Fundamental studies in powder drying using in situ Raman spectrometry and particle size analysis*", oral presentation, FACSS, Raleigh, NC, USA, October 2010.

"*Study of particle drying using in situ Raman spectrometry and particle size analysis*", oral presentation, APACT 2010, Manchester, UK, April 2010.

"*Detection of attrition in moving cellobiose octaacetate particles in real-time by near-infrared spectroscopy*", poster presentation (2^{nd} prize), APACT 2010, Manchester, UK, April 2010.

"*Evaluation of particle size measurement techniques in relation to powder drying"*, poster presentation (1^{st} prize), APACT 2009, Glasgow, UK, May 2009.

List of Abbreviations

AES	Acoustic emission spectroscopy
API	Active pharmaceutical ingredient
BD	Bulk density
CCD	Charge coupled device
CLD	Chord length distribution
COA	Cellobiose octaacetate
DEM	Discrete element method
DoE	Design of experiment
EQPC	Equivalent projection of a circle
FBRM	Focused beam reflectance measurement
FDA	Food and drug administration
IMO	Immersion optic
LD	Laser diffraction
LOD	Loss on drying
MeOH	Methanol
MIR	Mid-infrared
NIR	Near-infrared
NIRS	Near-infrared spectroscopy
PAC	Process analytical chemistry
PAT	Process analytical technology
PCA	Principal components analysis
PD	Polydispersity
PI	Particle Insight
PIMS	Particle imaging measurement system
PLS	Partial least squares
PSD	Particle size distribution
PTFE	Polytetrafluoroethylene
SLOD	Solvent loss on drying
TBD	Tapped bulk density

1 Powder drying

1.1 Introduction

In powder drying, volatile substances are removed during thermal processing to yield a solid product. It is one of the oldest unit operations in solids processing and is crucial in the chemical, pharmaceutical, agricultural, biotechnology, food, polymer, pulp and paper, ceramics, mineral processing and wood processing industries.[1] Despite industry's reliance on the operation, drying has historically been overlooked for both industrial and academic research due to other processes such as crystallisation receiving a higher priority.[2] More recently, however, the situation has changed as a result of the International Drying Symposia being established in the late 1970s along with the creation of two dedicated journals: Drying Technology and Advances in Drying. Nowadays, a worldwide forum to share research and experience exists that has generated increasing amounts of academic interest in the subject; this in turn has provided chemical engineers with a wealth of drying literature at their disposal.

Improvements in industrial unit operations have traditionally been driven by profit for the given application. Drying is an extremely energy intensive process owing to the high latent heat of vaporisation for many solvents coupled with the inefficiency of the drying media being used. In industrialised countries such as the USA or UK, 10 – 15% of the national industrial energy consumption is used for drying operations. As energy costs have risen considerably over the years, the necessity for industry to keep processing costs to a minimum in order to maximise profits has further widened the interest for research into drying operations, predominantly in developing more energy efficient operations such as fluidised bed drying, where the moist solids are suspended in the drying medium.[3] This upturn was predicted in 1986 by Majumdar who cited 'the energy crisis of the last decade for providing a serious impetus to take a close look at the conventional techniques of drying employed in industry'.[4] Shortly before this, the UK's Energy Technology Support Unit published results of a study into the economic benefits from retrofitting of energy saving equipment or new plant

design across 12 industries that consumed high amounts of energy in their drying, evaporation and distillation processes.[5]

Whereas energy costs appear to have generated the initial raise in interest for solids drying research, changes in the economic climate have perhaps led industries to reduce manufacturing costs across the board. This has prompted further research into drying processes for many reasons such as: reducing the cost of transport, increase preservation and storage time, ensure that materials are free flowing and easy to handle, and ultimately achieving the correct quality of product at the first attempt. The attention has stemmed from the fact that poor drying can lead to permanent damage to product quality and thus an unusable, unsellable product.[1] An unsellable product, as with high energy consumption has a direct effect on the profitability of a company, and therefore, there is a high potential gain associated with the implementation of full process control through increased understanding.

The objective of this research, driven by industry, has been to investigate powder drying from a pharmaceutical view point in order to facilitate the transfer of knowledge back into the industry. A model compound identified by industrial colleagues was chosen to represent a typical active pharmaceutical ingredient (API), and analytical instruments were employed to analyse the physical and chemical events that occurred during drying. There were two main aims: i) to learn more about the factors affecting drying and ii) develop *in situ* measurements procedures to allow better control of drying so that the desired particle properties are achieved.

1.2 Powder drying in the Pharmaceutical industry

In drug manufacturing, consumer safety is of paramount importance meaning that product quality cannot be compromised. Oxidation, decomposition, contamination or microbial infection must all be avoided at any cost as a single batch failure can have a significant impact in terms of manufacturing costs and lost revenue.[6] Furthermore, if a product is re-called after initial release the costs can be significantly more; for

example, legal action may be taken, where paying any damages is typically accompanied by a subsequent loss of credibility.

Drugs in solid dosage forms are manufactured in three stages:

i) Synthesis of intermediates

ii) Final synthesis of the API

iii) Manufacture of the dosage forms

Drying can take place at the end of stages i) and ii) and at the end of specific unit operations in iii) such as wet granulation where water added in order to form granules is removed to below a specified percentage wetness. Selection of the correct drier for each stage depends on the physical properties of the material being dried, for example, their form, sensitivity to oxygen and heat or drying kinetics may be considered. Table 1-1 shows the drier selection guidelines for the four main drier types used within global manufacturing services (GMS) at GlaxoSmithKline (GSK). These are termed filter, conical, pan and tray driers. Schematic diagrams are also shown for each drier type in Figure 1-1 a) – d), respectively.

Table 1-1 Selection guidelines for driers used at GSK.[7]

Parameter	What is required from a pharmaceutical drier	Filter-Drier	Conical Drier	Pan Drier	Tray Drier
Physical properties	Constant particle size distribution, bulk density (avoid balling or attrition)	No, agitation studies required			No (agglomerates formed)
	Potential use for reslurry/ dissolution	Yes	Yes	Yes	No
	Potential use for desolvation (not recommended)	Yes	Yes	Yes	Yes
	Potential use for relative humidity control	Yes	Yes	Yes	Yes
	Ability to handle wide range of solvents	Yes	Yes	Yes	No mainly high volatility solvents
	Wide range of starting loss on drying	Yes	Yes (no agitator heigh adj.)	Yes	Yes (caking)
Mass transfer	Good mass transfer through agitation	Yes	Yes	Yes	No
	No material segregation	Yes	Yes (except when sparging and risk of core flow)	Yes	(no variable moisture content)
	Minimised leaks	Yes	Yes	Yes	No (rapid seal wear)
Heat transfer	Good heat transfer coefficient	Yes (esp. with heated blade)	Yes	Yes (esp. with heated blade)	No (convection only)
Health and Safety	Good cleanability	Limited (moving parts)			Yes
	Good dust recovery	Yes	Yes (except when sparging)	Yes	Yes
	Multipurpose (filtration and washing)	Yes (but can generate process bottleneck)	No	No	No
	Good containment	Yes	Yes (manual operations)	Yes (manual operations)	No
Process Monitoring	PAT can be retrofitted	Yes	Yes	Yes	Yes
	Dynamic powder sampling	Yes (sampler may cause attrition and interfere with agitator)			Yes (vacuum has to be broken)
	Accurate pressure monitoring	Multiple usage requires *p* measurement range and thus decreases absolute accuracy	Yes	Yes	Yes

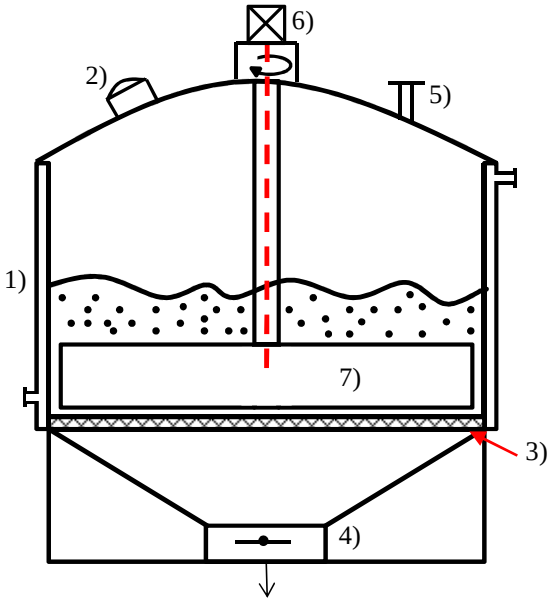

Figure 1-1: a) Vacuum filter drier: 1) jacket, 2) hatch, 3) filter base plate, 4) solvent exit port and valve, 5) feed tube, 6) motor and 7) agitator.

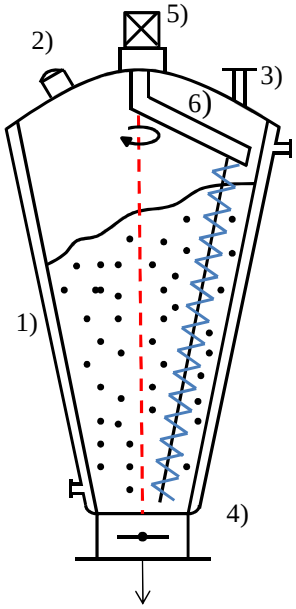

b) Conical Vacuum drier with epicyclic screw mixer: 1) jacket, 2) hatch, 3) feed tub, 4) exit port and valve, 5) motor, and 6) drive arm.[8]

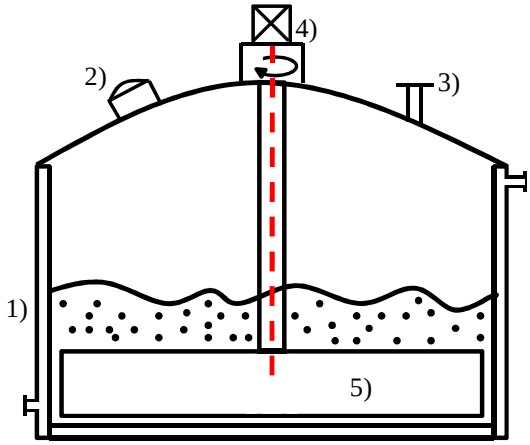

c) Pan drier: 1) jacket, 2) hatch, 3) feed tube, 4) motor, 5) agitator.

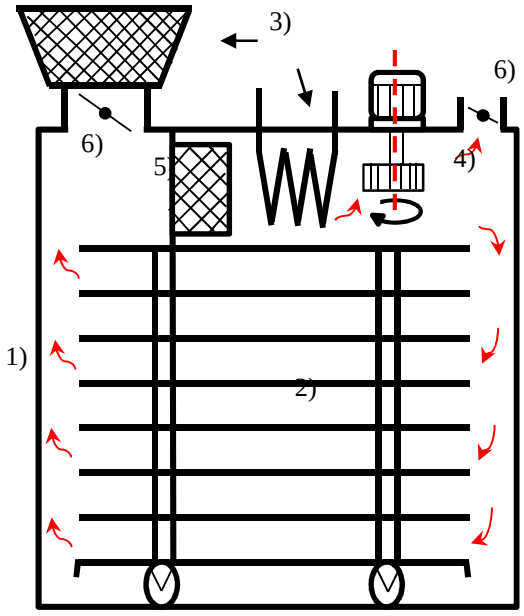

d) Batch tray drier: 1) shell, 2) truck with shelves, 3) heater, 4) fan, 5) air filters 6) valve.[8]

The selection of a drier is largely dependent on the properties of the material being dried. For example, fluidised bed driers (not included in Figure 1-1) are usually used when spherical particles that are easily dispersed (such as those after granulation) are dried. When adequate dispersion is not easy to achieve, for example when non-spherical particles such as flakes, needles, or platelets are dried, a fluidised bed drier is often not suitable and contact driers like those in Figure 1 a) – c) are used.[9] Contact drying uses heat transferred to the material from the hot surface of the vessel by conduction. The ability to work under vacuum makes contact driers very popular in the pharmaceutical industry as heat sensitive material can be dried at lower temperatures. At low pressures, the vapour pressure of the solvent is reduced and, therefore, the temperature required to remove the solvent is also reduced, making the drying of heat sensitive materials possible.[10] Furthermore, in order to reduce the number of production steps, a filter drier (Figure 1: a)) is often used as the filtration step can be carried out in the same vessel as the drying step.[9]

In this report, the focus is on the drying of pseudo API. Drying of an API can be challenging as many are sensitive to oxygen atmospheres or harsh environmental conditions such as high temperature, or can often be toxic in its pure form or explosive. Furthermore, many API have non-spherical geometry and are sensitive to mechanically induced shear from the impellers used in agitated powder drying. The API drying step usually follows crystallisation and filtration. Crystallisation is ideally a highly controlled process that aims to obtain a product with desired size, shape and purity, therefore, the preservation of the initial size and shape of the particles is equally as important as the removal of solvent. Proper control of these properties ensures that the flow and compaction properties of a material are correct for downstream processes such as blending, granulation or tableting and that the bioavailability is correct for proper action in the body.[11] Poorly controlled drying can thus result in the loss of the physical characteristics implemented during crystallisation, resulting in the re-crystallisation and re-drying of a material or ultimately the termination of a campaign. Currently in the pharmaceutical industry, there are no established techniques to monitor the physical processes that occur during drying *in situ*; all analysis techniques are currently carried out at the end of a

given drying process, meaning that any significant changes in particle size, shape, or distribution are unknown until these tests are carried out.

1.3 Physical processes during drying

The development of the penetration theory in the 1970s has meant that drying processes can be modeled relatively successfully using empirical calculations and knowing only a few parameters.[12-14] Furthermore, as computing power has increased, modern methods such as the discrete element method (DEM) have allowed for particle-solvent and particle-particle interactions to be calculated for experimental data sets containing larger numbers of particles.[15-20] What is far less understood, however, are the physical processes that occur throughout drying and have an effect on the particles, such as attrition, where a reduction of particle size occurs, or agglomeration, where an increase in particle size occurs. In some cases of agglomeration, large dense agglomerates can form in the drier, which cause great damage to the vessel, this is known as balling. Other processes that can occur during drying are chemical degradation caused by over drying of a material, or changes to the polymorph or hydrate state of the material.

Modes of attrition have been studied extensively by Ghadiri *et al*. and Grof *et al.*,[21-25] and can be classified into two main types: chipping, where fine daughter particles of material break away from the larger parent particle on impact; and fragmentation, where larger particles break down into several smaller fractions during a series of collisions with other particles, the impeller, or the walls of vessels. The formation and break-up of aggregates has also been studied.[26, 27] Conversely, the relationship between particle breakage and crystal wetness during drying is an area that is still relatively unstudied. The few examples in the literature that do exist show that the attrition caused during drying is a result of shear from the work put into the system by the impeller,[9, 28, 29] however, they are by no means extensive and highlight the need for further study into particle attrition and agglomeration in driers. With this, an opportunity presents itself to evaluate process analytical technologies to monitor these processes *in situ* in near real-time as a process is carried out.

1.4 Process analytical technology

The US Food and Drug Administration (FDA) 2004 "PAT initiative" has led to a boom in pharmaceutical companies investing in process analytical technology (PAT) to improve process understanding and control, with the ultimate goal of achieving quality by design.[30] In addition, the emergence of concepts such as six sigma and lean manufacturing has further augmented the interest of the pharmaceutical industry in PAT applications.[31] PAT is the application of process analytical chemistry (PAC) to pharmaceutical processes, and although PAT and PAC are relatively new to the pharmaceutical industry, they are by no means new concepts in other industries. On-line gas chromatography has been used in the oil and gas industry since the 1980s [32] and near-infrared spectroscopy has been utilised in the food industry for quite some time.[33] In fact the term PAC has its origins in the mid-1930s when British intelligence reported that the German chemical industry was using specialised instrumentation for process control.[34]

Traditionally in the pharmaceutical industry, process parameters such as temperature, pressure and flow rate were monitored for process control, and chemical analysis was only applied to intermediate and final drug products. By implementing PAT, process analysers are located in or next to a process as it is carried out, therefore, chemical analysis can be performed throughout manufacturing, in addition to the analysis of intermediates and drug products. Consequently, PAT has the capability to reduce the number of rejected or re-worked batches produced during routine manufacturing. In light of this, many pharmaceutical companies now have dedicated PAT groups whose role is to identify the opportunities that exist within an organisation to implement PAT, working closely with instrument vendors to design, develop and validate more robust analysers to work in harsh environments. These analysers are ideally operated automatically or by non-technical staff on plant, producing real-time data in a timely manner for process control and optimisation.

There are many challenges for the successful implementation of PAT into the equipment predominantly used in pharmaceutical manufacturing. Many reaction

vessels, blenders, driers etc. were purchased at a time when the implementation of PAT was not exploited as actively as it is today, and often, they must be retrofitted with ports or windows so that measurements can be made. Furthermore, scale up of processes from lab to plant scale can exacerbate difficulties observed at the smaller scale, meaning that representative sampling at the larger scale can be extremely challenging. Likewise, proving to the regulatory authorities that such samples are representative can pose an even bigger test. For these reasons, pharmaceutical companies have, until now, predominantly used PAT to improve understanding of their processes rather than to control them. This allows steps to be taken to rectify any problems that may be encountered, and consequently reduce the likelihood that a batch will fail quality testing. PAT is now a widely researched area across industry and academia, and although it is known that pharmaceutical companies are reluctant to publish articles for fear of losing competitive advantage, review articles in the literature such as the Process Analytical Chemistry series by Workman *et al.* demonstrate the strength and depth of the field across the industry.[34]

The application of PAT can be classified by five different terms established by Callis *et al.* namely: off-line, at-line, on-line, in-line or non-invasive.[35] Off-line analysis involves manual sampling of a process before transferring a sample to a remote or centralised laboratory. At-line analysis also requires manual sampling; however, only local transport is required to a dedicated analyser in the manufacturing area. On-line analysis has automated sampling and transfer to an automated analyser, a re-circulation loop can also be utilised that re-introduces the sample to the vessel after analysis. In-line PAT has a sample interface located in the process, typically by using insertion probes. Non-invasive analysis does not involve direct contact with the sample, but requires the analyser to be located on or beside the process. In this report, *in situ* measurements were performed using predominantly non-invasive probes (with some in-line NIR measurements), whereas reference measurements were performed off-line.

1.5 *In situ* PAT for pharmaceutical API drying processes

As mentioned, the theory and modeling of powder drying processes have featured extensively in the literature since the mid-1970s,[12-14, 17-19, 36-38] and furthermore, the modes of particle attrition are also well known.[21-26, 39] Currently PAT has been successfully implemented to measure particle size and shape in other unit processes such as crystallisation,[40-43] and fluidised bed processes.[44-46] The application of PAT to API drying processes, however, is much less documented and, at present, limited to measuring the drying curve rather than the physical processes that can occur to particles during drying. For example, both Parris *et al.*[47] and Burgbacher *et al.*[48] used NIR spectrometry to measure the drying curve of organic solvents during vacuum agitated drying of an API. Parris *et al.*[47] used an NIR gas cell to measure the concentration of organic solvent in the off-gas of a drier and, therefore, the NIR probe had no direct contact with the API particles. Using a principal components analysis (PCA) method, they were able to monitor the drying curve and also detect the agitation points during intermittently agitated drying. Similarly, Tewari *et al.* monitored the solvent concentration of the off-gas using a gas cell and mid-infrared spectrometry.[49]

Burgbacher *et al.* used an in-line NIR probe to monitor the removal of solvent directly from a bed of particles.[48] The probe was fitted with an integrated cleaning system that meant that the probe could be cleaned between measurements or batches without being removed from the vessel. A PLS calibration model was established that successfully predicted the solvent concentration in validation drying experiments using NIR spectra recorded during drying and off-line loss on drying (LOD) analyis for reference. They concluded that the *in situ* method of analysing the drying curve would reduce the overall drying time as the process could be stopped at an NIR determined time point measured *in situ* rather than by the off-line method. Thus, further time was saved by removing the need for traditional off-line analysis to be carried out.

In these examples, the focus is purely on the solvent removal, and therefore, the API is not commented on. However, NIR is known to be sensitive to physical properties such as particle size,[50-54] or polymorphism.[41, 55] Whereas in the given examples, there is no mention of whether or not the API were susceptible to attrition or agglomeration, it follows that if these processes were to occur, it would result in a change in the NIR contribution from the API that could be detected *in situ*. Furthermore, other *in situ* spectroscopies are known to contain particle size information in their spectra such as Raman, or acoustic emission spectroscopy (AES). AES is an alternative to more conventional spectroscopies and is known to contain particle size information in broadband frequency spectra.[56] AES has already been used to study particulate processes such as powder blending,[57] granulation,[58] and drying.[59, 60]

Raman spectroscopy is an established PAT tool and has some advantages over NIR spectroscopy. Raman spectrometry can be used to monitor polymorphism *in situ*, and spectra generally have sharp, well resolved peaks, often allowing for univariate rather than multivariate calibration, which is nearly always necessary with NIR spectroscopy. Furthermore, with developments in NIR lasers for Raman spectrometry, fluorescence is now less of a problem, and more efficient detectors coupled with wide illumination non-invasive probes have made the measurement of Raman scattering molecules easier, as much shorter integration times are required to collect a spectrum. It follows that Raman spectroscopy has been used extensively to monitor pharmaceutical unit operations other than drying such as crystallisation,[61, 62] fluidised bed granulation,[63, 64] blending,[65] or tablet analysis.[66, 67]

Walker *et al.*[63] used Raman spectrometry to correlate *in situ* measurements with granule density and particle size during the fluidised bed granulation of glass beads.[63] Measurements were recorded of the process in a 5 L granulator with a bespoke framework positioned around the vessel to house the Raman probe. In these experiments, the authors observed a decrease in Raman signal as granule size increased which correlated well with independent granulation experiments where particle distribution analysis was carried out. Furthermore, by monitoring the process

at different bed heights, the distribution in particle density could also be inferred from the Raman data, where a greater Raman signal was obtained from denser areas of particles in the bed.

The dependence of Raman signal intensity on particle size observed by Walker *et al.* has also been described previously for crystal powders by Pellow-Jarman *et al.*,[68] Wang *et al.*[69] and has also been observed in work completed at the University of Strathclyde.[70] The findings in these reports, however, are in direct contradiction to the previous theoretical calculations from Kubelka-Munk[71] and Schrader *et al.*[72] where an increase in Raman signal was calculated to occur with increasing particle size.

1.6 Research goals

The FDA's PAT initiative has motivated pharmaceutical companies to implement process analysis and control throughout their organisations, and furthermore, challenged them to assess the capability of the wide range of technologies for these measurements. The manufacture of solids and their processing has been identified as an area that can benefit significantly from the implementation of PAT. Unit operations that contain solids are inherently more difficult to understand and control than liquid systems, and as such, makes for an extremely challenging research area.

The aims of this research were:

- To evaluate the suitability of particle size analysis techniques as a reference method to determine the extent of attrition that occurs during a drying process for needle-shaped particles.
- To determine the relationship between drying parameters on the length of drying time required and the extent of attrition that occurs during drying.
- To assess non-invasive instrumentation to monitor the physical and chemical processes that take place during drying *in situ*.
- To apply *in situ* instrumentation to an industrially relevant drying process.

1.7 References

1. A. S. Mujumdar, *Handbook of Industrial Drying*, CRC Press, London, 2006.

2. J. C. Ashworth, *Research and development priorities for solids drying and related heat treatment operations*, I.Chem.E., 1982.

3. R. B. Keey, *Drying of Loose and particulate materials*, Hemisphere Publishing Corporation, New York, 1996.

4. A. S. Mujumdar, *Future trends in drying technology - a viewpoint*, 1986.

5. ETSU, *Drying, evaporation and distillation: the potential for improving energy efficiency in 12 industrial sectors*, Energy publications, 1985.

6. Z. Pakowski, Mujumdar, A. S., *Drying of pharmaceutical products*, CRC Press, London, 2006.

7. F. Ricard, Oxley, P., Collier, A., Patience, D., *GlaxoSmithKline guideline GUI-CDW-0018 v01*, 2007.

8. A. S. Mujumdar, *Handbook of industrial drying*, 2006, 689 - 712.

9. A. Lekhal, K. P. Girard, M. A. Brown, S. Kiang, B. J. Glasser and J. G. Khinast, *Powder Technol.*, 2003, **132**, 119-130.

10. P. K. Kom, W. Cook and E. Kougoulos, *Org. Process Res. Dev.*, 2011, **15**, 360-366.

11. Z. Q. Yu, J. W. Chew, P. S. Chow and R. B. H. Tan, *Chem. Eng. Res. Des.*, 2007, **85**, 893-905.

12. F. Heimann, F. Thurner and E. U. Schlunder, *Chem. Eng. Process.*, 1986, **20**, 167-174.

13. E. U. Schlünder and N. Mollekopf, *Chem. Eng. Process.*, 1984, **18**, 93-111.

14. E. Tsotsas and E. U. Schlunder, *Chem. Eng. Process.*, 1986, **20**, 339-349.

15. I. Figueroa, W. L. Vargas and J. J. McCarthy, *Chem. Eng. Sci.*, 2010, **65**, 1045-1054.

16. A. Hassanpour, H. S. Tan, A. Bayly, P. Gopalkrishnan, B. Ng and M. Ghadiri, *Powder Technol.*, 2011, **206**, 189-194.

17. M. Kwapinska, G. Saage and E. Tsotsas, *Powder Technol.*, 2008, **181**, 331-342.

18. T. Metzger, M. Kwapinska, M. Peglow, G. Saage and E. Tsotsas, Modern modelling methods in drying, presented in part at the 11th Polish Drying Symposium, Poznan, POLAND, 2005.

19. E. Tsotsas, M. Kwapinska and G. Saage, *Dry. Technol.*, 2007, **25**, 1377-1391.

20. R. R. Zhu, W. B. Zhu, L. C. Xing and Q. Q. Sun, *Powder Technol.*, 2011, **210**, 73-81.

21. M. Ghadiri, Z. Ning, S. J. Kenter and E. Puik, *Chem. Eng. Sci.*, 2000, **55**, 5445-5456.

22. M. Ghadiri, K. R. Yuregir, H. M. Pollock, J. D. J. Ross and N. Rolfe, *Powder Technol.*, 1991, **65**, 311-320.

23. M. Ghadiri and Z. Zhang, *Chem. Eng. Sci.*, 2002, **57**, 3659-3669.

24. Z. Zhang and M. Ghadiri, *Chem. Eng. Sci.*, 2002, **57**, 3671-3686.

25. Z. Grof, C. M. Schoellhammer, P. Rajniak and F. Stepanek, *Int. J. Pharm.*, 2011, **407**, 12-20.

26. D. G. Bika, M. Gentzler and J. N. Michaels, *Powder Technol.*, 2001, **117**, 98-112.

27. J. Subero and M. Ghadiri, *Powder Technol.*, 2001, **120**, 232-243.

28. A. Lekhal, K. P. Girard, M. A. Brown, S. Kiang, J. G. Khinast and B. J. Glasser, *Int. J. Pharm.*, 2004, **270**, 263-277.

29. C. L. Hare, M. Ghadiri, R. Dennehy and A. Collier, in *Powders and Grains 2009*, eds. M. Nakagawa and S. Luding, Amer Inst Physics, Melville, 2009, vol. 1145, pp. 851-854.

30. FDA, *Guidance for Industry; PAT - a framework for innovative pharmaceutical development, manufacturing and quality assurance*, 2004.

31. B. Swarbrick, *Vib. Spectrosc.*, 2007, **44**, 171-178.

32. K. R. Beebe, W. W. Blaser, R. A. Bredeweg, J. P. Chauvel, R. S. Harner, M. Lapack, A. Leugers, D. P. Martin, L. G. Wright and E. D. Yalvac, *Anal. Chem.*, 1993, **65**, R199-R216.

33. H. B. Huang, H. Y. Yu, H. R. Xu and Y. B. Ying, *J. Food Eng.*, 2008, **87**, 303-313.

34. J. Workman, B. Lavine, R. Chrisman and M. Koch, *Anal. Chem.*, 2011, **83**, 4557-4578.

35. J. B. Callis, D. L. Illman and B. R. Kowalski, *Anal. Chem.*, 1987, **59**, A624-&.

36. E. U. Schlunder, *Dry. Technol.*, 2004, **22**, 1517-1532.

37. E. U. Schlunder, *Chem. Ing. Tech.*, 1993, **65**, 174-&.

38. A. Kharaghani, T. Metzger and E. Tsotsas, *Aiche J.*, 2011, **57**, 872-885.

39. Z. M. Ning and M. Ghadiri, *Chem. Eng. Sci.*, 2006, **61**, 5991-6001.

40. E. Kougoulos, A. G. Jones, K. H. Jennings and M. W. Wood-Kaczmar, *J. Cryst. Growth*, 2005, **273**, 529-534.

41. X. S. Liu, D. Sun, F. Wang, Y. J. Wu, Y. Chen and L. H. Wang, *J. Pharm. Sci.*, 2011, **100**, 2452-2459.

42. S. G. S. Cesur, *Cryst. Res. Technol.*, 2008, **43**, 720-728.

43. A. S. Zidan, Z. Rahman and M. A. Khan, *Aaps J.*, 2010, **12**, 254-262.

44. J. Huang, G. Kaul, J. Utz, P. Hernandez, V. Wong, D. Bradley, A. Nagi and D. O'Grady, *J. Pharm. Sci.*, 2010, **99**, 3205-3212.

45. A. Tok, X. P. Goh, W. Ng and R. Tan, *AAPS PharmSciTech*, 2008, **9**, 1083-1091.

46. J. Rantanen, H. Wikstrom, R. Turner and L. S. Taylor, *Anal. Chem.*, 2005, **77**, 556-563.

47. J. Parris, C. Airau, R. Escott, J. Rydzak and R. Crocombe, *Spectroscopy*, 2005, **20**, 34-41.

48. J. Burgbacher and J. Wiss, *Org. Process Res. Dev.*, 2008, **12**, 235-242.

49. J. Tewari, V. Dixit and K. Malik, *Sens. Actuators, B. Chem.*, 2010, **144**, 104-111.

50. S. B. Abebe, X. Z. Wang, R. Li, K. J. Roberts and X. Lai, *Powder Technol.*, 2008, **179**, 176-183.

51. M. J. Barajas, A. R. Cassiani, W. Vargas, C. Conde, J. Ropero, J. Figueroa and R. J. Romañach, *Appl. Spectrosc.*, 2007, **61**, 490-496.

52. L. J. Bellamy, A. Nordon and D. Littlejohn, *Int. J. Pharm.*, 2008, **361**, 87-91.

53. L. J. Bellamy, A. Nordon and D. Littlejohn, *Analyst*, 2008, **133**, 58-64.

54. D. R. Ely, M. Thommes and M. T. Carvajal, *Colloids Surf., A*, 2008, **331**, 63-67.

55. K. Kogermann, J. Aaltonen, C. J. Strachan, K. Pollanen, P. Veski, J. Heinamaki, J. Yliruusi and J. Rantanen, *J. Pharm. Sci.*, 2007, **96**, 1802-1820.

56. G. Carson, A. J. Mulholland, A. Nordon, M. Tramontana, A. Gachagan and G. Hayward, *Journal of Sound and Vibration*, 2008, **317**, 142-157.

57. P. Allan, L. J. Bellamy, A. Nordon and D. Littlejohn, *Analyst*, 2010, **135**, 518-524.

58. M. Halstensen, P. de Bakker and K. H. Esbensen, *Chemom. Intell. Lab. Syst.*, 2006, **84**, 88-97.

59. L. Briens, R. Smith and C. Briens, *Powder Technol.*, 2008, **181**, 115-120.

60. E. Duff, *Monitoring of powder drying processes using near infrared spectroscopy and acoustic emission*, MSci, University of Strathclyde, 2010.

61. J. Cornel, C. Lindenberg and M. Mazzotti, *Ind. Eng. Chem. Res.*, 2008, **47**, 4870-4882.

62. Y. R. Hu, J. K. Liang, A. S. Myerson and L. S. Taylor, *Ind. Eng. Chem. Res.*, 2005, **44**, 1233-1240.

63. G. M. Walker, S. E. J. Bell, K. Greene, D. S. Jones and G. P. Andrews, *Chem. Eng. Sci.*, 2009, **64**, 91-98.

64. J. Aaltonen, K. Kogermann, C. J. Strachan and J. Rantanen, *Chem. Eng. Sci.*, 2007, **62**, 408-415.

65. T. R. M. De Beer, C. Bodson, B. Dejaegher, B. Walczak, P. Vercruysse, A. Burggraeve, A. Lemos, L. Delattre, Y. V. Heyden, J. P. Remon, C. Vervaete and W. R. G. Baeyens, *J. Pharm. Biomed. Anal.*, 2008, **48**, 772-779.

66. T. R. M. De Beer, W. G. Baeyens, Y. Vander Heyden, J. P. Remon, C. Vervaet and F. Verpoort, *Eur. J. Pharm. Sci.*, 2007, **30**, 229-235.

67. J. Johansson, A. Sparen, O. Svensson, S. Folestad and M. Claybourn, *Appl. Spectrosc.*, 2007, **61**, 1211-1218.

68. M. V. Pellow-Jarman, P. J. Hendra and R. J. Lehnert, *Vib. Spectrosc.*, 1996, **12**, 257-261.

69. H. Wang, C. K. Mann and T. J. Vickers, *Appl. Spectrosc.*, 2002, **56**, 1538-1544.

70. P. Allan, *Studies in Raman, infrared and acoustic emmision spectrometries, and reaction calorimetry for process analysis*, PhD, University of Strathclyde, 2008.

71. P. Kubelka and F. Munk, *Zeitschrift für Technische Physik,*, 1931, **12**, 593–601.

72. B. Schrader, A. Hoffmann and S. Keller, *Spectroc. Acta Pt. A-Molec. Biomolec. Spectr.*, 1991, **47**, 1135-1148.

2 Theory

2.1 Theory and modeling of drying

2.1.1 Drying curves

In solids drying, the production of a drying curve shows the drying kinetics and how they change throughout the process. Typical representations of a drying curve are shown in Figure 2-1 a) for moisture content versus time, and 2-1 b) for drying rate versus time.[1]

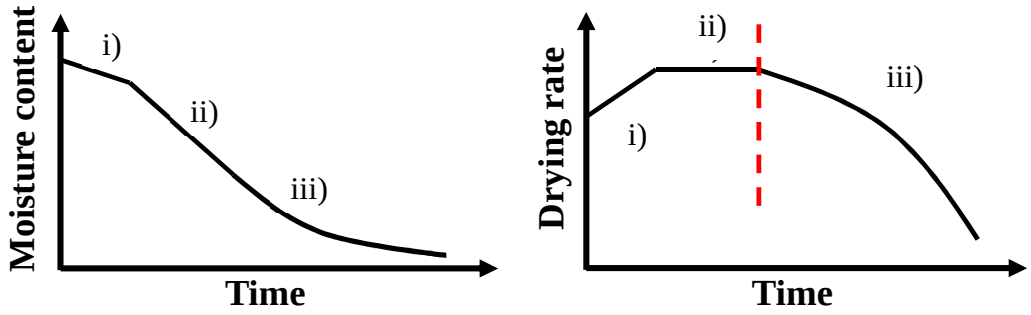

Figure 2-1: a) moisture content as a function of time and b) drying rate as a function of time: i) induction period, ii) constant rate period and iii) falling rate period; - - - critical point.[1]

Figure 2-1 b) best shows that solid drying typically occurs in three separate stages. The first stage (i) in Figure 2-1 b)) is termed the induction period. During an induction period, the drying rate increases while the bed is heated, and this continues until the second stage known as the constant rate phase begins (ii) in Figure 2-1 b)). Throughout the constant rate phase, the surfaces of the particles remain wet enough to maintain a constant vapour pressure of solvent, and therefore, the rate of removal remains constant. Once the surfaces of the particles dries sufficiently, the drying rate begins to decrease and a third phase known as the falling rate period occurs (iii) in Figure 2-1 b)). Figure 2-1 b) also shows that the transition between the constant rate

and falling rate phase occurs at a critical point. This refers to the average moisture content of a material at this transition.[1]

2.1.2 **Vacuum agitated drying (the penetration theory and DEM)**

A model for vacuum (conductive) drying with continuous agitation termed the "penetration theory" was described in the literature by Schlunder and Mollekopf in 1984,[2] which was extended for bi- and poly-dispersed multi-granular materials in 1986 and for hygroscopic material in 1989.[3, 4]

2.1.2.1 **Fundamental drying knowledge**

Before the new penetration theory is described, some fundamentals of solids drying theory are introduced. These are three heat and two mass transfer resistances that can alter the drying rate ($\dot{m}$) of a material when in contact with a hot surface (for this case, the material must be static). The three heat transfer resistances that any heat supplied must overcome are known as: the contact resistance at the hot surface (α_{ws}), the penetration resistance of the bulk (α_{sb}), and the penetration resistance of the particle (α_p). They are described as follows and shown schematically in Figure 2-2.

Contact: $$\frac{1}{\alpha_{ws}} = \frac{T_w - T_0}{q_0} \quad (2\text{-}1)$$

Bulk penetration: $$\frac{1}{\alpha_{sb}} = \frac{T_0 - T_b}{q_0} \quad (2\text{-}2)$$

Particle penetration: $$\frac{1}{\alpha_p} = \frac{T_b - T_s}{q_{z_T}} \quad (2\text{-}3)$$

Where T_w is the hot surface temperature (K), T_0 is the interfacial temperature (K), q_0 is the heat flux into the bed (W m^{-2}), T_b is the bulk temperature (K), T_s is the saturation temperature (K) and q_{z_T} is the heat flux into the drying front (W m^{-2}).

The two mass transfer resistances that the vapour removed must overcome are: the permeation resistance of the particles (β_p) and the permeation resistance of the bulk (β_b), which are also shown schematically in Figure 2-2.

Particle permeation: $$\frac{1}{\beta_p} = \frac{p_s - p_b}{\dot{m}} \quad (2\text{-}4)$$

Bulk permeation: $$\frac{1}{\beta_b} = \frac{p_b - p}{\dot{m}} \quad (2\text{-}5)$$

Where p_s is the saturation pressure at the drying front (bar), p_b bulk pressure (bar), $\dot{m}$ is the drying rate and p is the pressure in the drier (bar).

Figure 2-2 shows the heat and mass transfer parameters schematically for a static bed of particles.

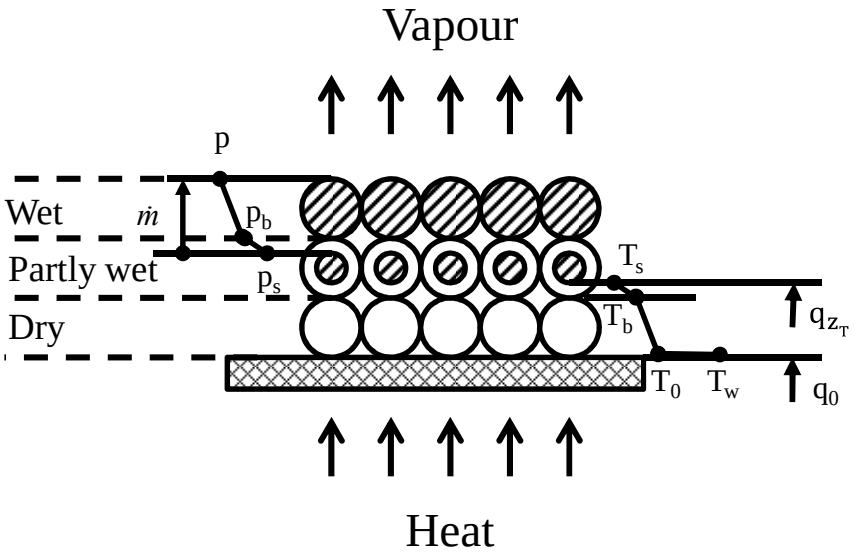

Figure 2-2: Heat and mass transfer resistances in contact drying.[2]

When a static bed of particles is dried, all the described resistances lie in series. However, at the beginning of drying there are no partially wet or dry particles in contact with the hot surface and, therefore, the only resistance that exists is the contact resistance (α_{ws}). The theoretical maximum drying rate ($_{max}\dot{m}$) is thus controlled by the contact resistance and is given by equation 2-6.

$$_{max}\dot{m} = \frac{\alpha_{ws}[T_w - T_s(p)]}{\Delta h_{ev}(T_s)} \tag{2-6}$$

Where T_s is the saturation temperature at pressure p in the drier (K and bar, respectively), $\Delta h_{ev}(T_s)$ is the latent heat of evaporation at the saturation temperature (J kg^{-1}).

Measured drying rates for static beds of particles are much lower than the theoretical maximum rate demonstrating that not only the contact resistance is rate controlling.

In contrast, when material is mechanically agitated during drying, there is a random distribution of wet, partly wet and dry particles present, and because of this, the heat and mass transfer resistances also form a random distribution at any given time in the drier. These resistances now lie partly in series and partly in parallel which lowers the drying rate and makes the application of a suitable model extremely difficult.

2.1.2.2 **The proposed penetration model**

The penetration theory assumes that a continuous mixing process is replaced by alternating imaginary unsteady mixing steps (with fictional static periods followed by instantaneous mixing periods). Each fictional static period (t_R) is followed by instantaneous macromixing of the bulk, again followed by another imaginary static period. During these static periods, a drying front is said to be penetrating from the hot surface (vessel wall) into the bulk (particles), with all particles between the heating surface and the front are said to be dry and all particles beyond the front are wet. At each time t_R the bed is perfectly mixed, however, the number of dry particles behind and beyond the drying front (relative to the previous time t_R) will increase which reduces the drying rate. A schematic representation of the imaginary periods is given in Figure 2-3.

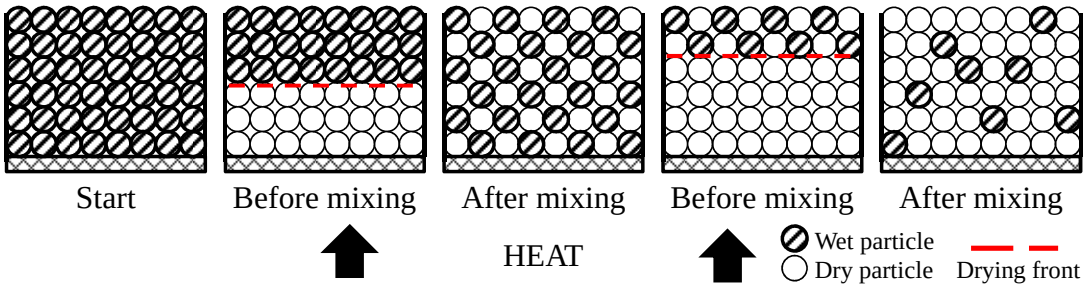

Figure 2-3: Illustration of penetration model.[2]

A second assumption of the penetration model is that when all the liquid has evaporated at the particle surface, only the contact resistance (α_{ws}) and the bulk heat penetration resistance (α_{sb}) remain and that these are rate controlling. These are placed in series to give the overall summed resistance (α_{dry}, equation 2-7).

$$\frac{1}{\alpha_{dry}} = \frac{1}{\alpha_{ws}} + \frac{1}{\alpha_{sb,dry}} \tag{2-7}$$

A normalised drying rate (μ) is then calculated from the ratio of α_{dry} and α_{ws} which is equal to the ratio of the actual maximum drying rate ($\dot{m}_{max}$) and the theoretical maximum drying rate already introduced ($_{max}\dot{m}$). The relationship is shown in equation 2-8.

$$\mu = \frac{\alpha_{\mathrm{dry}}}{\alpha_{\mathrm{ws}}} = \frac{\dot{\mathrm{m}}_{max}}{_{max}\dot{\mathrm{m}}} = \frac{1}{1 + (\sqrt{\pi}/2)\sqrt{\tau_{\mathrm{r}}}} \tag{2-8}$$

The normalised drying rate is then used to describe the process at any given time t_R and can be calculated using the relationship in the 4th term of equation 2-8, where τ_R is the reduced contact time and is given by:

$$\tau_R = N_{therm} N_{mix} \tag{2-9}$$

N_{therm} is derived from predictable quantities such as α_{ws}, the initial moisture content (X_{in}) and initial bulk temperature (T_b). N_{mix} is known as the mixing number, and is the only term that needs to be fitted to experimental results. It is used to determine the number of rotations of an impeller before the material has been ideally mixed. Therefore, using equations 2-8 and 2-9, the drying rate $\dot{m}(X)$ for any given N_{mix} can be predicted by a stepwise calculation as long as the initial moisture content (X_{in}) and initial bulk temperature (T_b) is known.

2.1.2.3 **Discrete element method**

A limitation of the penetration theory, by the authors own admission, is that it does not account for random particle motion. The advent of more powerful computers since the original penetration theory was proposed, however, has made the

calculation of particle motion feasible through the discrete element method (DEM). DEM has since become common place in the literature for processes that require particle motion such as blending or granulation.[5-10] It has also been applied to the modeling of heat transfer to particle beds[11-13] and has been described as "a modern alternative to test and upgrade penetration models" for drying studies.[12]

DEM is well established for purely mechanical processes, however, is less established for thermal processes.[13] In fact, the application of DEM to drying was quoted as "not been treated until now" in 2007, which in the same publication, cited the use of the technique as "having the potential of resolving the motion of every particle of the bed, and in thermal version, also calculating the change of temperature due to every particle-particle or particle-wall interaction".[13] To date, DEM for particle drying applications has largely centered on computational studies of particles in a rotary drum drier with no inserts. There are two parts to the computer code: the mechanical part, which treats particle interactions as dynamic processes with states of equilibrium occurring whenever the internal forces are balanced; and secondly, there is the thermal part, which assigns each particle a heat reservoir, with heat transfer through thermal pipes between individual particles (or walls). These thermal pipes are described by power ($Q^{(p)}$), and thermal resistance per length (η) and length ($L^{(p)}$).[13] Each active thermal pipe is described by the equation 2-10 and the average heat flow per unit volume ($\langle\frac{\partial q_i}{\partial x_i}\rangle$) is given by equation 2-11:

$$Q^{(p)} = -\frac{\Delta T}{\eta \, . \, L^{(p)}} \tag{2-10}$$

$$\langle\frac{\partial q_i}{\partial x_i}\rangle = \frac{1}{V}\sum_{p=1}^{N} Q^{(p)} \tag{2-11}$$

Where T is the temperature (K), V is the volume (m^3), p is the density (kg/m^3), and N is the number of active thermal pipes.

These equations allow calculation of the particle-particle and wall-particle heat transfer coefficients used in the DEM simulations, which, at the time of writing only allowed for the interactions of around 350 particles per simulation.[11, 13, 14] Such small numbers of particles numbers are not representative of even small scale drying processes at present; although, as computer power continues to increase along with general knowledge in DEM, the ability to model a greater number of particles per simulation will also increase, meaning it is likely that DEM theory will eventually become the commonly accepted theory discussed in the literature.

2.1.3 **Physical processes during drying**

Whereas the removal of solvent during drying is well documented, there is currently only limited understanding of the impact of a drying process on crystal properties and moreover, poor control of the phenomena that occur. Complications can arise due to attrition, agglomeration, shrinkage, or over drying which can lead to chemical degradation, and hydrate or solvate changes. In many cases, the occurrence of these effects may lead to a batch being reworked or lost entirely as the particle characteristics are no longer suitable for the intended use.

Attrition is a significant problem in agitated filter driers as particles are subjected to shear while being dried. Attrition causes a reduction in particle size or a change in the particle geometry. There are two main modes of attrition: chipping and fragmentation. Chipping occurs when small segments of the particles break off to form a fine dust. Chipping not only leads to the problems described, but can also generate an explosive dust hazard in a manufacturing area. Particle breakage or fragmentation is more common in needle-shaped particles. Here, the larger parent particles break down into smaller daughter particles during a process. The processes which lead to particle attrition have been studied extensively by Ghadiri *et al.*[15-18], and these authors have also recently began to investigate the effects of particle drying and its relationship with attrition.[14]

Ghadiri *et al*. described a model for the chipping form of attrition caused by impact with another particle or with vessel walls etc. in two parts: theory and experimental.[16, 18] The authors attributed the crystal breakage method to subsurface lateral cracks, and developed a dimensionless attrition propensity parameter (η) to describe the breakage phenomena. In the model, the extent of breakage was related to the material properties and impact conditions. The relationship is given in equation 2-12:

$$\eta = \frac{\rho v^2 l H}{K_c^2} \tag{2-12}$$

Where ρ is the particle density, ν is the impact velocity, l is the characteristic particle size, H is the hardness and K_c is the fracture toughness. The calculation of η allowed for the calculation of the fractional loss per impact (ξ), determined by the relationship:

$$\xi = \alpha\eta \tag{2-13}$$

Where α is a proportionality constant.

The experimental section of the two publications proved that, under a controlled set of conditions (acceleration of single particles through a test rig with fast imaging camera), the model accurately predicted the extent of attrition that occurred in MgO, NaCl and KCl crystals (all cubic). Conversely, in agitated filter driers, the impact conditions cannot be controlled and are far less predictable. Ghadiri *et al*. also understood this was an issueand have begun work to simulate breakage processes that occur during drying, using DEM.[14]

Attrition in filter driers has been investigated by Lekhal *et al.* who published two recent articles. The first describes drying of water from potassium chloride (cubic) crystals and the second, drying of water from an L-threonine (needles) particles.[19, 20] For their work, an 800 ml double jacketed vessel was used to determine the effects of temperature, agitation rate and pressure on drying time and final crystal properties. The results agreed in some respect with the work of Ghadiri *et al.* that attrition was primarily caused as a result of shear; although, they also noted that agglomeration was a competing process in drying systems as a result of capillary forces in the presence of liquid. They concluded that the extent of attrition was correlated to the agitation rate, but also that all three factors investigated contributed to the extent of attrition. This was due to all three having direct effects on drying time (which was directly related to the amount of shear that particles are exposed to).

Typically, in the pharmaceutical industry, a batch will be dried for a length of time under a set of conditions defined by a regulatory filing, with product quality tested off-line in a quality control lab. There are significant disadvantages to this strategy, however, namely the time lag between extracting a sample, transport to the lab, analysing the sample, and conveying the pass/ fail result to the operators. This represents a significant loss in time in determining if the sample is dry or not; further, if the batch is still wet, it will need to be dried for a longer period of time and retested. Also, if the particle characteristics are found to have changed, there are implications for additional energy and materials costs, as well as a delay in manufacturing. There is thus a significant potential gain if: a) the drying end point could be determined in real-time to prevent agitation of the particles that is not required and b) particle attrition could be detected in real-time to avoid significant particle breakage occurring by putting measures in place to prevent it. In this work, the use of non-invasive Raman spectrometry and off-line particle size analysis allowed the investigation of both concurrently.

2.2 Raman spectroscopy

Raman spectroscopy is used to measure the vibrational modes in a system, and has become increasingly popular in the pharmaceutical industry. It allows for rapid, non-destructive measurements with no sample preparation, meaning it can be used on- or in-line to gather real-time information from a process.[21] The Raman effect was discovered in 1928, by Raman and Krishnan, and occurs when monochromatic light from an incident laser beam is in-elastically scattered when directed at matter (solid, liquid or gas).[22] The in-elastically scattered light is dependent on the chemical structure of the molecule analysed and can be either at longer or shorter wavelengths to the incident beam. The Raman processes, however, are inherently weak with only 1 in every 10^6 – 10^8 scattered photons being in-elastically scattered. Furthermore, fluorescence can interfere with the Raman process making spectra difficult to collect. Thus, it was not until advances in computer technology, detector sensitivity, near-infrared lasers and holographic optics in the late 1980s which overcame these fundamental problems that Raman spectroscopy became a commonly used technique. Since then, further developments in optics have also allowed for rapid collection of a large spectral range, with wide illumination of the sampling area.

A Raman spectrum is plotted as scattered intensity against wavenumber shift (from the exciting line), and is obtained by irradiating matter with a laser of visible or near-infrared monochromatic radiation. The laser light then promotes the molecule to a "virtual" excited state for a very short period of time before relaxation produces a photon which is subsequently collected and analysed by a spectrometer. The overall scattered radiation consists of three parts: elastically scattered photons (termed Rayleigh scattering), where the scattered photons have the same energy as the incident beam, and two in-elastically scattered photon components (termed Stokes and anti-Stokes scattering) that bracket the Rayleigh band symmetrically. These processes along with the absorption processes in infra-red and near-infrared spectroscopy are shown schematically in Figure 2-4.

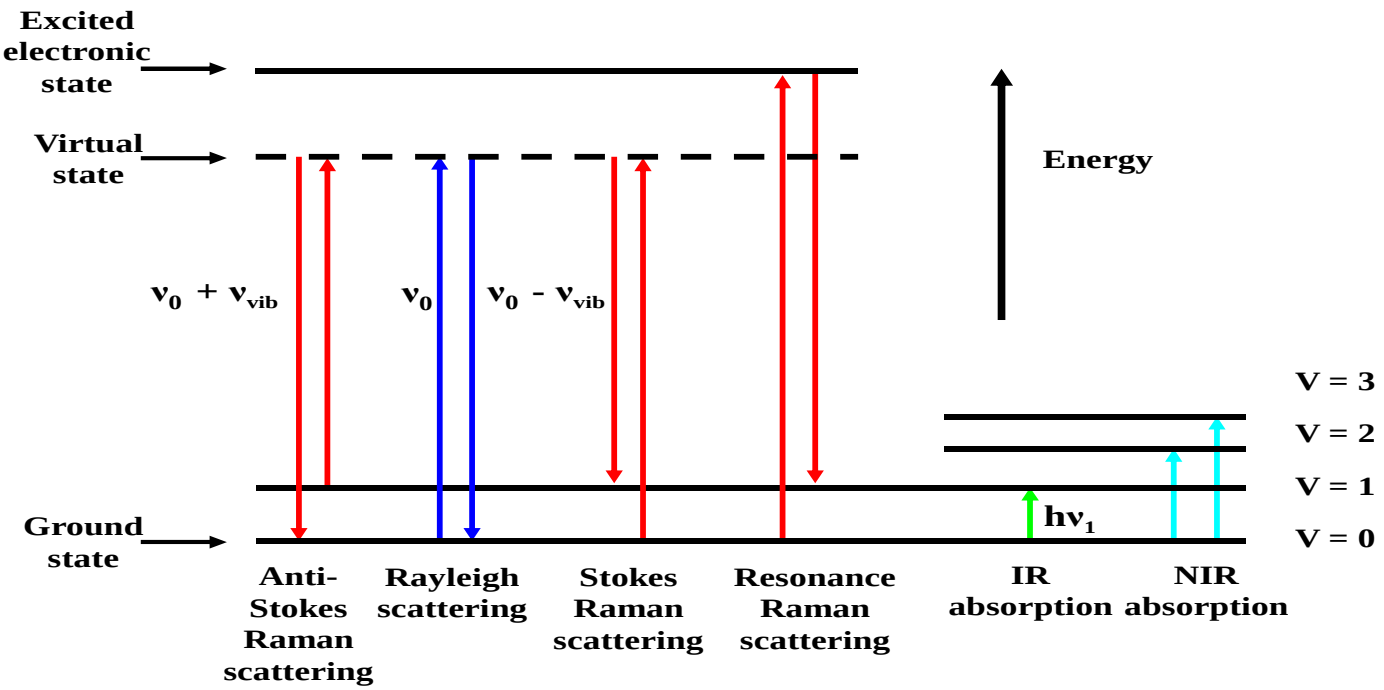

Figure 2-4: schematic representation of spectroscopic transitions for Raman, IR and NIR spectroscopies. ν_0 represents the laser frequency, h is Planck's constant. A virtual state is a short lived distortion of the electron distribution caused by the electric field of the incident laser light.[23] V denotes vibrational energy states, with V = 0 the ground vibrational state

From Figure 2-4, Stokes scattering occurs when molecules in the ground vibration state (V = 0) absorb a photon of energy $h\nu_0$ and re-emits a photon of energy $h(\nu_0 - \nu_{vib})$ where ν_{vib} is the energy of the excited vibrational state (V = 1). If the molecule is in an excited vibrational state (V = 1), the scattered photon can gain energy when emitted ($h(\nu_0 + \nu_{vib})$, leading to anti-Stokes scattering. Stokes scattering is typically analysed in chemical analysis as it is more intense than anti-Stokes scattering due to materials being mostly in their ground states when analysed. The number of molecules in either the ground state or first vibrational energy state at any given time is determined by the Boltzmann distribution and is calculated from equation 2-14:

$$\frac{N_n}{N_m} = \frac{g_n}{g_m} exp\left[\frac{-(E_n - E_m)}{kT}\right] \tag{2-14}$$

Where N_n and N_m are the number of molecules in the excited and ground vibrational energy states, respectively, g_n and g_m are the degeneracy levels of the energy states, E_n - E_m is the difference in the energy between the vibrational levels, k is the Boltzmann constant and T is temperature.[24]

2.2.1 **Classical Raman theory**

Raman scattering is a two photon event, involving an incident and a scattered photon. In contrast to mid- and near-infrared absorption spectroscopies which are single photon processes that induce a change in the dipole-moment of a molecule with respect to particle motion. With classical Raman theory, a change in polarisability (α) of the molecule with respect to its vibrational motion occurs. The incident electric field, E, interacts with the polarisability creating an induced dipole moment, of magnitude P in the molecule (refer to equation 2-15).[23-25]

$$P = \alpha E \tag{2-15}$$

The electric field leads to a distortion of the electron cloud in the molecule, if the field is supplied by electromagnetic radiation of frequency, ν_0 (Hz) then,

$$P = \alpha E_0 \cos(2\pi \nu_0 t) \tag{2-16}$$

where t is the time and E_0 is the maximum electric field strength. Therefore, if the irradiated polarizable molecule is vibrating at frequency ν_{vib} (Hz), then its distortion from its equilibrium position, q, will be given by,

$$q = q_0 \cos(2\pi \nu_{vib} t) \tag{2-17}$$

where q_0 is the maximum possible distortion. If the distortion causes a change in the polarisability, and it is assumed that the variation is linear and the amplitude of the displacement is small, the polarisability of the periodically distorting molecule will become;

$$\alpha = \alpha_0 + \left(\frac{\delta \alpha}{\delta q}\right)_0 q \tag{2-18}$$

Where, the polarisability of the molecule at equilibrium is α_0 and the rate of change of that polarisability with distortion around the equilibrium structure is $(\delta\alpha/\delta g)_0$. Therefore, the variation in polarisability as the molecule vibrates is given by:

$$\alpha = \alpha_0 + \left(\frac{\delta\alpha}{\delta q}\right)_0 q_0 \cos(2\pi\nu_{vib}t) \tag{2-19}$$

Therefore, substituting equation 2-19 into 2-16 gives:

$$P = \alpha_0 E_0 \cos(2\pi\nu_0 t) + \left(\frac{\delta\alpha}{\delta q}\right)_0 q_0 \cos(2\pi\nu_{vib}t)cos(2\pi\nu_0 t) \tag{2-20}$$

Using the product of two cosines rule, equation 2-20 can be rearranged to give:

$$P = \alpha_0 E_0 \cos(2\pi\nu_0 t) + \frac{E_0}{2}\left(\frac{\delta\alpha}{\delta q}\right)_0 q_0 \cos[2\pi(\nu_0 - \nu_{vib})t] + \frac{E_0}{2}\left(\frac{\delta\alpha}{\delta q}\right)_0 q_0 \cos[2\pi(\nu_0 + \nu_{vib})t] \tag{2-21}$$

Equation 2-21 has three terms describing each of the scattering events that are known to occur, the first term contains ν_0 which describes the Rayleigh scattering and is much more intense than the second and third terms that describe the Stokes $(\nu_0 - \nu_{vib})$ and anti-Stokes $(\nu_0 + \nu_{vib})$ processes, respectively. Stokes scattering is typically more intense than anti-Stokes scattering, however this is not explained by classical Raman theory, instead consideration of the Boltzmann distribution is required (equation 2-14).

2.2.2 **Intensity and fluorescence**

The intensity of Raman signal (I_R) observed for a given molecule is given by the following equation:

$$I_R = kI_{ex}\alpha^2\nu^4 \tag{2-22}$$

where k is constant, I_{ex} is the intensity of the excitation beam, α is the polarisability and ν is the frequency of the laser. Therefore, by varying the intensity or frequency of the excitation beam, the measured intensity can technically be optimised. However, fluorescence is often encountered when Raman measurements are recorded, and due to the relatively low number of Raman scattered photons compared to the efficient fluorescence process, fluorescence can often dominate the spectra. Fluorescence is observed when the energy of the incident photon is high enough to promote the molecule above the virtual energy state described in Figure 2-4 into one of the vibrational energy states of the 1st electronic energy level. Internal relaxation processes take place before the fluorescence process occurs, which relaxes the molecule back to its ground state. In order to reduce the effect, modern Raman spectrometers allow users to vary the laser power, and in doing so, reduce the intensity of the incident beam, and thus, reduce the energy of the irradiating photons (reducing the number of molecules excited into the 1st electronic energy level). Of course from equation 2-22, if the laser power (I_{ex}) is decreased then the number of Raman scattered photons (I_R) will also decrease, however, advances in the collection optics efficiency (such as increasing the number of collection fibres) will often compensate for the reduction Raman signal observed. Furthermore, developments in laser technology has produced NIR lasers (785 (diode) – 1000 nm (Nd:YAG)) which has further reduced the degree of fluorescence interference observed in Raman spectra.

2.3 Particle size and shape analysis

In the pharmaceutical industry, particles range in size from nanoparticles in colloidal suspensions to millimeter sized granules, depending on the method of administration of any given product. The size and shape of these particles can have a significant impact on critical parameters such as the manufacturing processability (flow, compaction, blend performance etc.) or quality attributes (dissolution and drug release rate, bioavailability etc.) that ultimately determine the safety and efficacy of the drugs.[26] The typical particle size of powders used in oral dosage forms (like those that are dried in vacuum filter driers) are typically in the 100 – 200 µm range, as these are required for the correct compaction behavior and powder flow properties.[26] An important question then must be asked: what does a 100 – 200 µm range actually mean? The answer: it depends on the particle size analysis technique used to collect and analyse the material. Here, the theories for three commonly used techniques are described (laser diffraction, Focused Beam Reflectance Measurements (FBRM) and dynamic image analysis), however, first some fundamentals of particle size and shape analysis are discussed.

Particle size is typically reported as single values or a range of statistics that are used to represent the measured distribution. There are a number of statistics that can be quoted, such as: means (which vary depending on the way they are calculated), the median, which divides the population into two equal halves, or the mode, which is the most common value of a frequency distribution. For a Gaussian distribution of particles, these three averages are equal. For mean values, two commonly quoted values can be used to describe the same distribution of particles, these are the surface weighted mean (or D(3,2)) or the volume weighted mean (or D(4,3)). Therefore, for a range of spheres of say 1, 2 and 3 µm, each mean can be calculated using:[27]

$$D(3,2) = \frac{1^3 + 2^3 + 3^3}{1^2 + 2^2 + 3^2} = 2.72\ \mu m \quad (2\text{-}23)$$

$$D(4,3) = \frac{1^4 + 2^4 + 3^4}{1^3 + 2^3 + 3^3} = 2.57\ \mu m \quad (2\text{-}24)$$

Further to this, values such as the D(0,1) and D(0,9), corresponding to the 10^{th} and 90^{th} percentiles of a measured distribution, are often quoted alongside the calculated averages in order to describe the polydispersity of the distribution.

Consideration of particle shape is also of extremely high importance, as for non-spherical particles there are a range of diameters than can be used to describe any given distribution of particles. With laser scattering techniques like laser diffraction and FBRM it is not possible with current algorithms to obtain information on particle shape from the scattering patterns. With image analysis, however, a range of diameters can be used. For example there are equivalent sphere diameters, which can be based on the same minimum, maximum or average length, the same volume, or the same specific surface etc. Although for particles with a high degree of asymmetry, these may not be particularly suitable. For these particles, distributions based on the maximum (and or minimum) dimension of the particles would prove more representative. The measured dimensions from image analysis can be used to quote averages/ percentiles etc., as these are calculated independently of the technique used to generate the data.

2.3.1 **Laser diffraction**

Laser diffraction (LD) is commonly used in the pharmaceutical industry for particle size analysis as measurements are generally simple and quick, and instrumentation is also cheap. For LD measurements, the scattering patterns of particles are measured

onto a semi-circular detector made up of concentric light sensitive diodes, with a measured scattering pattern being inversely proportional to the mean diameter of the scattering particle.[28] Figure 2-5 a) and b) shows an example energy distribution of a spherical particle with radius *r*, and a schematic representation of a LD semi-circular detector.

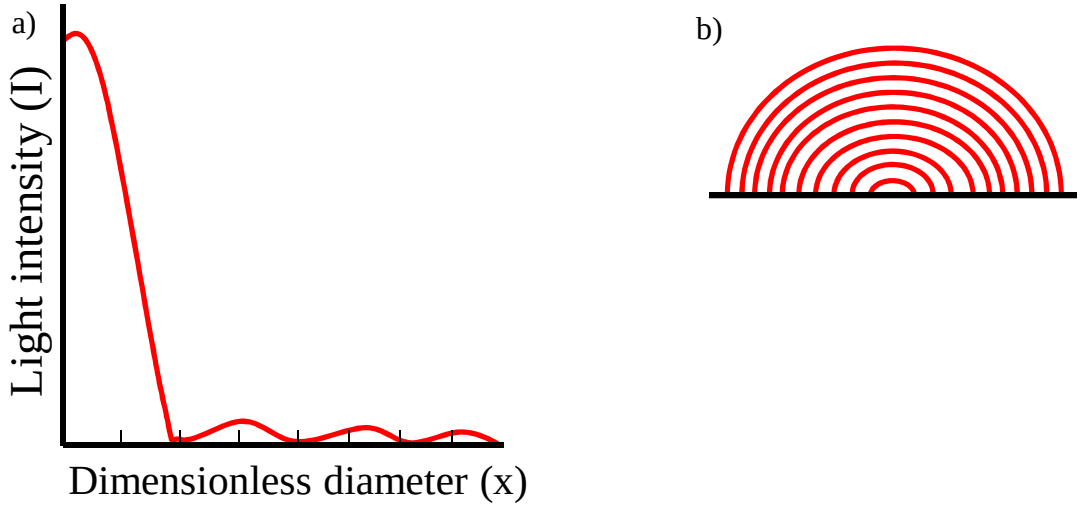

Figure 2-5: a) Energy distribution of spherical particles with radius *r*, and b) schematic representation of semi-circular detector made up of concentric rings.[29]

Once the scattering patterns are collected, a combination of Mie (for fine material) and Fraunhofer (for coarse material) theories are then used to convert the measured signal into particle size distribution data. Both theories are mathematically complex, and as such have limitations such as the consideration of spherical particles only. Fraunhofer diffraction theory is valid if the following are met: i) the wavelength of the illuminating light is much smaller than the size of the particles, ii) the intensity of the illuminating light is homogeneous over the particle, iii) the measured particle is opaque, and iv) the refractive index of the particle differs significantly from the surrounding medium (the refractive index of both must be known for accurate

analysis).[30] For a single particle, the dimensionless diameter (x from Figure 2-5 of the measured pattern) described by Fraunhofer theory is given from:

$$x = \frac{2\pi rs}{\lambda F} \tag{2-25}$$

Where *r* is the particle radius, *s* is the radial distance in the detection plane measured from the optical axis, λ is the wavelength of light and *F* is the focal length of the lens. Figure 2-5 and equation 2-25, however, only relate to the measured scattering pattern of one particle, whereas, in reality, the light energy falling onto the semi-circular detector at any given time is the sum of contributions from all the individual particles. This makes the scattering patterns actually observed in LD measurements more complicated, and therefore, the total light energy distribution for a suspension containing a collection of particles of different sizes is expressed in matrix form, as is described by equations 2-26 and 2-27:

$$L(j) = W(i).T(i,j) \tag{2-26}$$

Where *L(j)* is the light energy falling on the ring, *W(i)* is the weight fraction of the particles in the size range *i*, and *T(i,j)* is the scattering matrix for spherical particles containing the coefficients which define the light energy distribution (similar to Figure 2-5 a)) for each particle size range. Equation 2-26 is solved by assuming a value for *W(i)* and calculating a theoretical value for *L(j)* using the appropriate *T(i,j)* matrix for a given set of experimental parameters. The theoretical *L(j)* is compared with the experimentally measured value and the weight distribution is then iteratively adjusted until the sum of the squared errors in *L(j)* reaches a minimum:

$$min\left|\sum(L(j)-W(i).T(i,j))^2\right| \quad (2\text{-}27)$$

The weight distribution is then determined by inversion of the *T(i,j)* matrix, and hence the success of the approach is dependent on the accuracy of the inversion step and the accuracy of the light scattering model.[28]

Mie theory is applied to the diffraction data from fine particles that are similar in size or smaller than the laser wavelength. Mie theory is also subject to some assumptions, namely: i) the particles are spherical, ii) the suspension is dilute (no multiple scattering effects), iii) optical properties of the particles and surrounding medium are known, and iv) the particles are homogenous. The theory, first developed in 1908 is based on solving the mathematically complex Maxwell equations and describes the scattering pattern of the measured particles based on their absorption and scattering coefficients. To achieve this, the refractive index difference between the particle and the dispersing medium is used to predict the intensity of the scattered light. The theory also describes how the absorption characteristics of the particle affect the amount of light which is transmitted through the particle and either absorbed or refracted.[31]

The limitation of that LD theory, namely it was developed for only spherical particles is well documented;[28-30, 32-35] however, anisotropic particles are also commonly analysed by LD techniques, but scattering patterns differ greatly from those of spheres. Figure 2-6 shows examples of calculated scattering patterns for a) a spherical particle and b) a square shaped particle.[34]

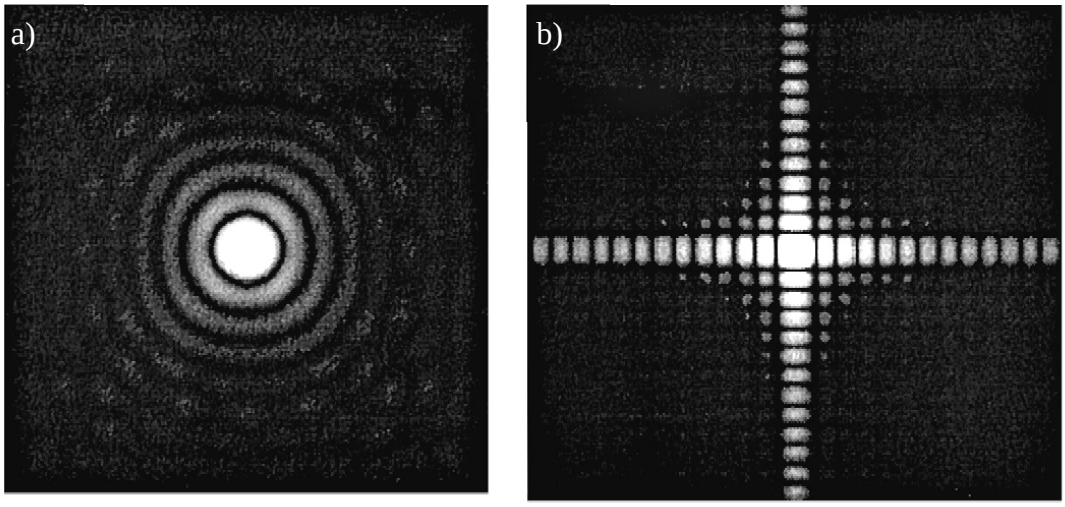

Figure 2-6: Calculated scattering patterns of a) spherical particle and b) square shaped particles taken from 34.

These scattering pattern differences creates significant ambiguity in relation to the matrix *T(i,j)* used to determine the measured scattering patterns for anisotropic particles, however, this is often overlooked due to the simplicity of the measurements. Although, there has been work carried out to develop methods for LD measurements of anisotropic particles,[30, 34-38] at the time of writing, there is no commercially available algorithm that allows for particle shape to be considered as well as particle size for LD measurements.

2.3.2 **Focused beam reflection measurements**

FBRM can be used to measure the chord length distribution of a suspension of particles. In the pharmaceutical industry, it is predominantly used to monitor crystallisation processes *in situ*, however, it can also be used as a laboratory analysis technique.[39-42] Furthermore, recent developments in FBRM technology have also allowed FBRM probes to be inserted into processes where the particles are not in suspension, such as granulation.[43-46] A visual representation of the measurement principle of FBRM is given in Figure 2-7.[47]

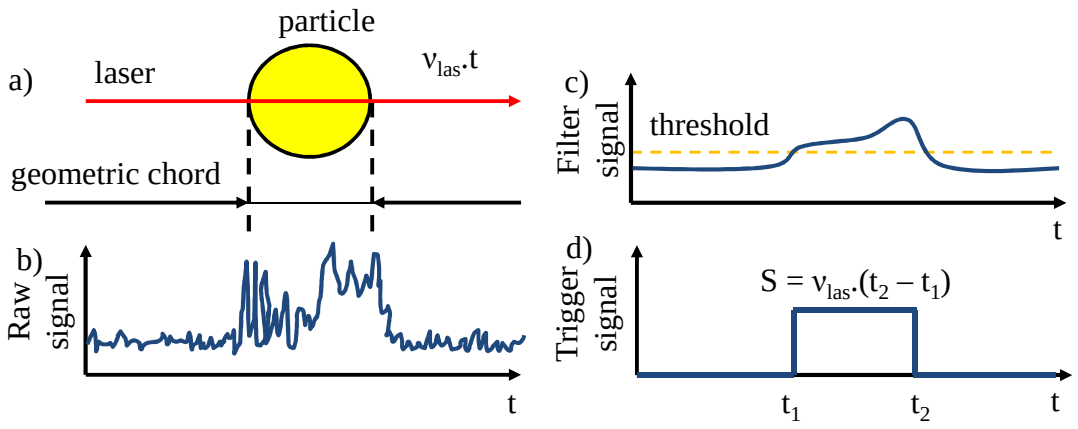

Figure 2-7: Visualisation of a) chord discriminations and b) – d) signal processing for FBRM measurements.[47]

When laser light interacts with a particle, light scattering occurs. The principle of FBRM relies on some of the scattered light travelling back into the measurement system where it is detected. For this to happen, a particle moves perpendicularly into the view plane of the laser beam (a) in Figure 2-7); when this occurs, spot light reflections on the particle surface cause variation in the light scattering intensity (b) in Figure 2-7). In order to minimize these effects, the scattered light intensity is filtered which results in a mean scattering signal where a threshold scattering intensity can be set (c) in Figure 2-7). The trigger is activated when the scattering intensity rises above the set value and is reset when it falls back below the threshold intensity (d) in Figure 2-7). The time difference between these two events ($t_2 - t_1$) is recorded and multiplied by the laser velocity to result in the path length (S). An assumption is then made that the particle velocity is low compared to the laser's rotational velocity (described in section 3.3.3), and therefore the path length of the laser is identical to the chord length of the measured particle. Each of the measured chord lengths are then sorted into a histogram, with each measurement given after a certain predefined time interval.[47] Results can then be interpreted in counts per second or total counts per measurement. As FBRM reports the chord length distribution of particles, particles are thus measured independent of their shape. However, anisotropic particles are known to adopt average orientations when suspended in solution, and hence, particle shape can have a significant impact on the

measured results. There has been significant research into modeling the effects of particle shape in FBRM,[48-51] however, as with LD measurements, at the time of writing there is no known commercial software that incorporates the influence of particle shape on the measured chord length distributions obtained by FBRM.

2.3.3 **Dynamic image analysis**

Dynamic image analysis is emerging as a popular technique for particle size analysis, as it allows for simultaneous size and shape analysis. In terms of theory, the basis of measurement is simple: particles are suspended in a dispersing medium (which can be carrier gas or solvent), and then passed through a measurement zone where images of the particles are recorded. The imaging software calibrates the length of individual pixels of the recorded images to particle size and then evaluates each recorded image based on user defined inputs (usually in close to real-time). In this study, three common statistics were evaluated, namely: i) the equivalent projection of a circle (EQPC) with the same 2-dimensional area as the projected particle, ii) the longest maximum dimension between two parallel tangents (Feret Max), or iii) the shortest possible dimension between two parallel tangents (Feret Min). These are shown pictorially in Figure 2-8.[52]

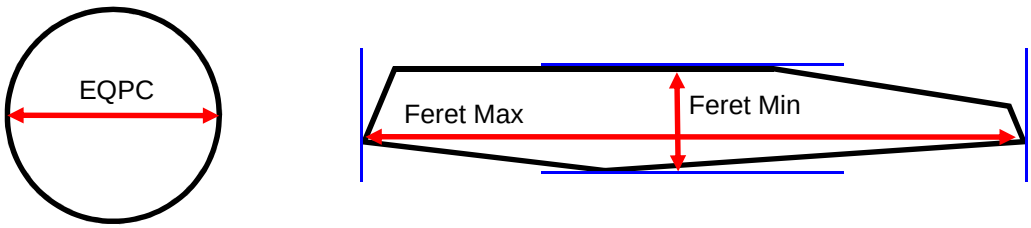

Figure 2-8: Schematic representations of the size descriptions used for image analysis. The EQPC diameter is estimated as the diameter of a sphere with the same 2-dimensional area as the projected particle in the recorded image. The Feret Max and Feret Min diameters are the longest and shortest distances, respectively, between two parallel tangents on opposite sides of the projected particle.[53]

2.4 Design of experiments

2.4.1 Factorial design

During the completion of this work, a 2-level, 3-factor, full factorial design of experiments with two categorical centre points was carried out. Full factorial designs are mainly used for screening, determining the influence on a number of effects on a response, or to eliminate factors that are not significant for future analyses. For each factor, a high and a low level are selected (e.g. considering temperature, 40 and 60 ºC could be selected for the low and high levels, respectively) and then a standard design is formed varying each of the defined factors which creates a design space. A standard 2-level, 3-factor design with categorical centre points is shown schematically in Figure 2-9.

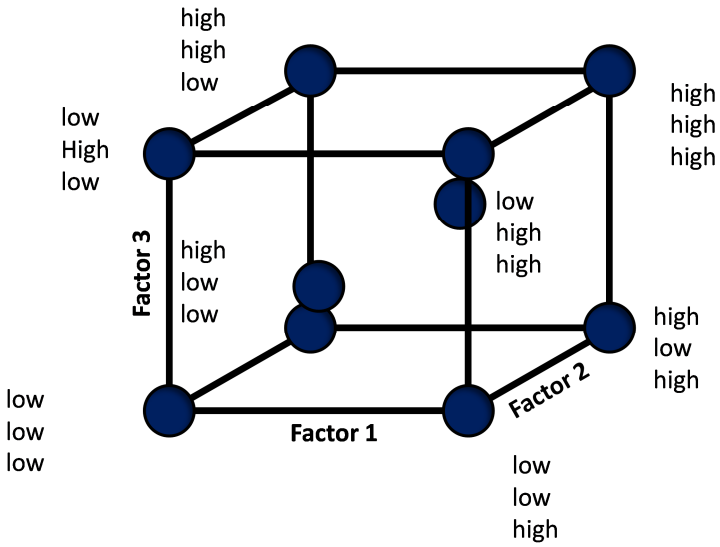

Figure 2-9: Schematic representation of 2-level, 3-factor full factorial experimental design with 2 categorical centre points.

Categorical centre points are used when one of the factors being analysed is not numerical (i.e. such as agitation type, which can only be continuous, intermittent or not employed). Therefore, the centre points cannot be placed directly in the centre of the design space cube.[54]

2.5 Data Analysis

2.5.1 1st derivative transformation

Throughout the duration of this work, a 1st derivative transformation was generally applied to any spectral data to reduce baseline effects in the spectra. In spectroscopy, derivatives are used to measure the rate of change in the gradient of the slope in a spectrum, which acts to resolve overlapping peaks (e.g. in NIR spectra). In this work, derivatives were applied to remove any baseline shifts (1st derivative) or baseline slope (2nd derivative) that are present in a given data set (only data using a 1st derivative transformation is reported).[55] The 1st and 2nd derivative transformations are illustrated for a single spectrum in Figure 2-10.

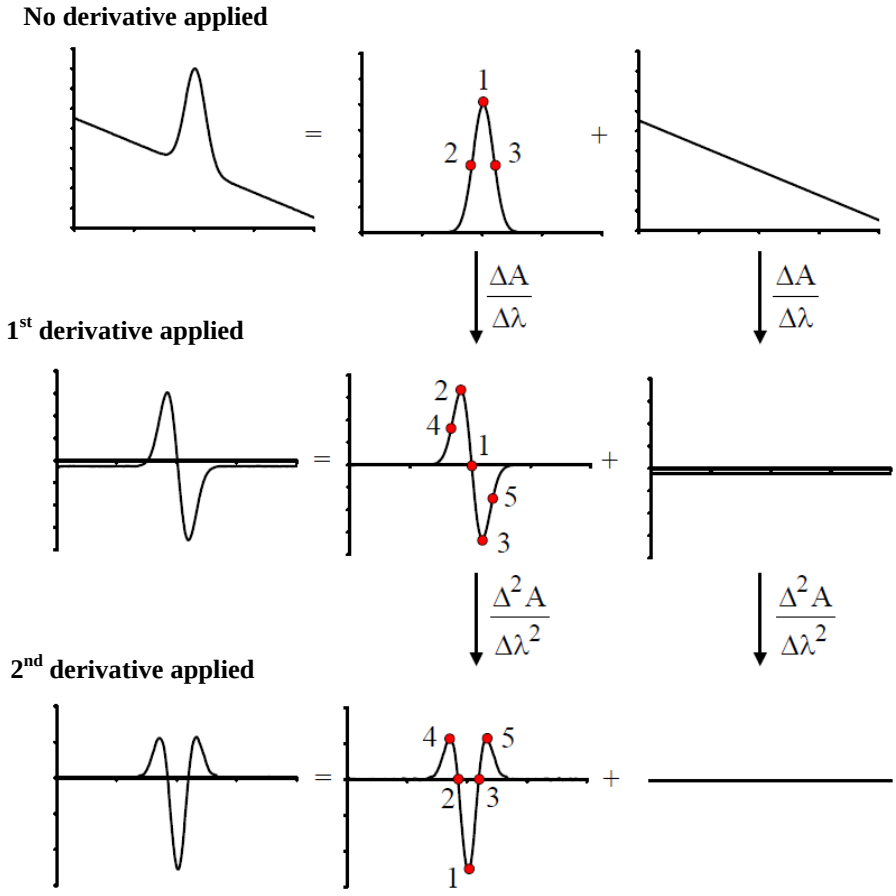

Figure 2-10: Schematic representation of 1st and 2nd derivative transformation processes.

2.5.2 **Principal components analysis**

Principal components analysis (PCA) is a multivariate chemometric technique that is used to reduce the number of variables in large data sets into a smaller number of abstract, latent variables, known as principal components (PCs).[54] The PCs are calculated from the original data and must reflect its underlying structure, both in terms of the relationships between the different samples and the measurement variables. For any given matrix (*X*), the data can be considered as two separate component matrices, these are: the underlying structure of the data, or "model" matrix (*M*) and associated error matrix (*E*); with both *M* and *E* matrices having the same dimensions as *X* (equation 2-28). The result of successful PCA decomposes the model matrix *M,* into two smaller matrices known as the scores matrix (*T)* and loadings matrix (*P*), where superscript T represents the transpose of the matrix, as is described by equation 2-28:

$$X = M + E \xrightarrow{\textbf{PCA}} X = (TP^T) + E \tag{2-28}$$

The scores matrix (*T*), describes any sample patterns that are present in the data set and the loadings matrix (P^T) describes any relationships that exist between the individual measurement variables. The number of PCs required to describe X is often far fewer than the number of measurement variables which results in a score (t_i) and loadings (p_i) vector for each PC and the residual error matrix, as is described by equation (2-29):

$$X = t_1 p_1^T + t_2 p_2^T + \cdots + t_A p_A^T + E \tag{2-29}$$

PCA is usually applied to data which has been mean centered, which is the subtraction of the column mean from each column in the data matrix (in spectral data, the mean spectrum is thus subtracted from each individual spectrum).[56] By mean centering data prior to the application of PCA, the absolute intensity

information from each variable is effectively normalised, allowing the algorithm to focus solely on describing the variation between the spectra in the data set.

In this project, the techniques described here have been applied to a drying process of an excipient material (cellobiose octaacetate) and to the unit operations of an active pharmaceutical ingredient in development. For example, *in situ* Raman spectrometry was used to monitor the processes in real-time with particle size measurements applied off-line as reference measurements. A design of experiments approach was employed to create a design space, so that three variable drying parameters could be examined to determine their effect on the length of drying time and extent of attrition that occurred. Derivatives were typically applied to the measured spectroscopic data so that effects in the baselines of the spectra were reduced. PCA was applied to the measured Raman data to determine if physical information could be extracted from the spectra that was not derived from univariate analysis methods. Before the results of the experiments are discussed, the equipment, instrumentation and materials used to carry out the work are described in Chapter 3.

2.6 References

1. D. W. Green, Perry, R. H., *Perry's chemical engineer's handbook*, McGraw-Hill Professional, New York, 2007.

2. E. U. Schlünder and N. Mollekopf, *Chem. Eng. Process.*, 1984, **18**, 93-111.

3. E. Tsotsas and E. U. Schlunder, *Chem. Eng. Process.*, 1986, **20**, 339-349.

4. R. Forbert and F. Heimann, *Chem. Eng. Process.*, 1989, **26**, 225-235.

5. A. Hassanpour, H. S. Tan, A. Bayly, P. Gopalkrishnan, B. Ng and M. Ghadiri, *Powder Technol.*, 2011, **206**, 189-194.

6. A. S. Persson, G. Alderborn and G. Frenning, *Eur. J. Pharm. Sci.*, 2011, **42**, 199-209.

7. S. S. Manickam, R. Shah, J. Tomei, T. L. Bergman and B. Chaudhuri, *Powder Technol.*, 2010, **201**, 83-92.

8. F. Mahmoodi, G. Alderborn and G. Frenning, *Powder Technol.*, 2010, **198**, 69-74.

9. W. R. Ketterhagen, M. T. A. Ende and B. C. Hancock, *J. Pharm. Sci.*, 2009, **98**, 442-470.

10. R. R. Zhu, W. B. Zhu, L. C. Xing and Q. Q. Sun, *Powder Technol.*, 2011, **210**, 73-81.

11. M. Kwapinska, G. Saage and E. Tsotsas, *Powder Technol.*, 2008, **181**, 331-342.

12. T. Metzger, M. Kwapinska, M. Peglow, G. Saage and E. Tsotsas, Modern modelling methods in drying, presented in part at the 11th Polish Drying Symposium, Poznan, POLAND, 2005.

13. E. Tsotsas, M. Kwapinska and G. Saage, *Dry. Technol.*, 2007, **25**, 1377-1391.

14. C. L. Hare, M. Ghadiri, R. Dennehy and A. Collier, in *Powders and Grains 2009*, eds. M. Nakagawa and S. Luding, Amer Inst Physics, Melville, 2009, vol. 1145, pp. 851-854.

15. M. Ghadiri, Z. Ning, S. J. Kenter and E. Puik, *Chem. Eng. Sci.*, 2000, **55**, 5445-5456.

16. M. Ghadiri and Z. Zhang, *Chem. Eng. Sci.*, 2002, **57**, 3659-3669.

17. Z. M. Ning and M. Ghadiri, *Chem. Eng. Sci.*, 2006, **61**, 5991-6001.

18. Z. Zhang and M. Ghadiri, *Chem. Eng. Sci.*, 2002, **57**, 3671-3686.

19. A. Lekhal, K. P. Girard, M. A. Brown, S. Kiang, B. J. Glasser and J. G. Khinast, *Powder Technol.*, 2003, **132**, 119-130.

20. A. Lekhal, K. P. Girard, M. A. Brown, S. Kiang, J. G. Khinast and B. J. Glasser, *Int. J. Pharm.*, 2004, **270**, 263-277.

21. T. De Beer, A. Burggraeve, M. Fonteyne, L. Saerens, J. P. Remon and C. Vervaet, *Int. J. Pharm.*, 2011, **417**, 32-47.

22. C. V. Raman and K. S. Krishnan, *Nature*, 1928, **121**, 501-502.

23. R. L. McCreery, *Raman spectroscopy for chemical analysis*, John Wiley and Sons, New York, 2000.

24. E. Smith and G. Dent, *Modern Raman Spectroscopy: A Practical Approach*, John Wiley and Sons, Inc, London, 2005.

25. I. R. Lewis and H. G. M. Edwards, *Handbook of Raman spectroscopy: from the research laboratory to the process line*, Marcel Dekker, Inc., New York:, 2001.

26. B. Shekunov, P. Chattopadhyay, H. Tong and A. Chow, *Pharm. Res.*, 2007, **24**, 203-227.

27. A. Rawle, *Malvern instruments technical paper*, 1-8.

28. N. Gabas, N. Hiquily and C. Laguérie, *Part. Part. Syst. Char.*, 1994, **11**, 121-126.

29. G. B. J. Deboer, C. Deweerd, D. Thoenes and H. W. J. Goossens, *Particle Characterization*, 1987, **4**, 14-19.

30. H. Muhlenweg and E. D. Hirleman, *Part. Part. Syst. Char.*, 1998, **15**, 163-169.

31. Malvern, *http://www.malvern.com/malvern/kbase.nsf/allbyno/KB002050/$file/MRK1304-02.pdf*, November 2011.

32. N. Stevens, J. Shrimpton, M. Palmer, D. Prime and B. Johal, *Meas. Sci. Technol.*, 2007, **18**, 3697-3706.

33. E. D. Hirleman, *Part. Part. Syst. Char.*, 1988, **5**, 57-65.

34. Z. Ma, H. G. Merkus, J. G. A. E. de Smet, C. Heffels and B. Scarlett, *Powder Technol.*, 2000, **111**, 66-78.

35. S. Endoh, Y. Kuga, H. Ohya, C. Ikeda and H. Iwata, *Part. Part. Syst. Char.*, 1998, **15**, 145-149.

36. R. L. Xu and O. A. Di Guida, *Powder Technol.*, 2003, **132**, 145-153.

37. M. Naito, O. Hayakawa, K. Nakahira, H. Mori and J. Tsubaki, *Powder Technol.*, 1998, **100**, 52-60.

38. A. Pankewitz, C. Behrens, U. Kesten and Y. J. Park, Particle size and shape analysis the key to success in metal powder production, presented in part at the Power Metallurgy World Congress and Exhibition 2006, Busan, SOUTH KOREA, 2006.

39. S. G. S. Cesur, *Cryst. Res. Technol.*, 2008, **43**, 720-728.

40. X. S. Liu, D. Sun, F. Wang, Y. J. Wu, Y. Chen and L. H. Wang, *J. Pharm. Sci.*, 2011, **100**, 2452-2459.

41. P. Barrett, *Chem. Eng. Prog.*, 2003, **99**, 26-32.

42. E. Kougoulos, A. G. Jones, K. H. Jennings and M. W. Wood-Kaczmar, *J. Cryst. Growth*, 2005, **273**, 529-534.

43. T. Narvanen, T. Lipsanen, O. Antikainen, H. Raikkonen, J. Heinamaki and J. Yliruusi, *J. Pharm. Sci.*, 2009, **98**, 1110-1117.

44. A. Tok, X. P. Goh, W. Ng and R. Tan, *AAPS PharmSciTech*, 2008, **9**, 1083-1091.

45. J. Huang, G. Kaul, J. Utz, P. Hernandez, V. Wong, D. Bradley, A. Nagi and D. O'Grady, *J. Pharm. Sci.*, 2010, **99**, 3205-3212.

46. C. Fischer, M. Peglow and E. Tsotsas, *Chem. Eng. Sci.*, 2011, **66**, 2842-2852.

47. N. Kail, W. Marquardt and H. Briesen, *Chem. Eng. Sci.*, 2009, **64**, 984-1000.

48. A. Vaccaro, J. Sefcik and M. Morbidelli, *Part. Part. Syst. Char.*, 2007, **23**, 360-373.

49. M. Z. Li and D. Wilkinson, *Chem. Eng. Sci.*, 2005, **60**, 3251-3265.

50. M. Z. Li, D. Wilkinson and K. Patchigolla, *Chem. Eng. Sci.*, 2005, **60**, 4992-5003.

51. N. K. Nere, D. Ramkrishna, B. E. Parker, W. V. Bell and P. Mohan, *Ind. Eng. Chem. Res.*, 2006, **46**, 3041-3047.

52. Sympatec, *www.sympatec.com/ImageAnalysis/QICPIC.html*, November 2011.

53. Sympatec, *http://www.sympatec.com/EN/ImageAnalysis/Fundamentals.html*, November 2011.

54. R. G. Brereton, *Chemometrics: data analysis for the laboratory and chemical plant*, John Wiley and Sons, West Sussex, UK, 2005.

55. K. A. Bakeev, *Process Analytical Technology*, Blackwell Publishing Ltd Oxford, UK, 2005.

56. L. Errikson, E. Johansson, N. Ketteneh-Wold, J. Trygg, C. Wikstrom and S. Wold, *Umetrics AB, Sweden*, 2006.

3 Equipment, instrumentation and materials

3.1 Introduction

The research performed for this work has largely involved the use of a laboratory scale vacuum filter drier, and the application of spectroscopic measurements *in situ* using a range of both in-line and non-invasive techniques. *In situ* spectroscopic measurements obtained during vacuum drying enables investigation of the physical processes that the particles are subjected to during the operation. In addition, off-line particle size analysis was performed after drying was completed using laser diffraction, FBRM, and dynamic image analysis. In this section, the equipment, instrumentation, and materials used throughout the project are described.

3.2 Equipment

3.2.1 Bespoke drier

The design of the bespoke lab scale drier (GPE ltd, Bedfordshire, UK) was based on the other laboratory scale filter driers used at GSK, Stevenage, UK. The chamber of the vessel has an internal diameter of 15 cm and a fill volume of approximately 2 L (with an approximate capacity of 1 kg depending on the bulk density of the material to be dried). The outer wall of the vessel was made of glass and it had a glass jacket (starting around 2.5 cm from the base of the drier and ending approximately 2 cm for the lid) that was filled with circulating silicon oil. External control from a heater-chiller unit (Hakke DC5/ K20, ThermoHakke) ensured the jacket temperature remained constant throughout experiments. The impeller used during drying had two angled retreat blades set 180º apart and was driven by a mechanical stirrer (IKA RW 20 digital, IKA works, Wilmington, USA) through a 10:1 gear box positioned at 90º to the vessel (mixing speeds of 10 or 20 rpm were used in drying experiments). The lid of the vessel was made of PTFE and had five ports available; a sixth port was connected to a nitrogen cylinder so that pressure filtration experiments could be carried out. Spectroscopic measurements could thus be made using either direct insertion probes through one of the free ports in the lid, or non-invasively through a

glass window in the lid or the glass wall of the vessel beneath the jacket. A schematic representation of the drier showing the possible probe measurement positions and orientations is given in Figure 3-1.

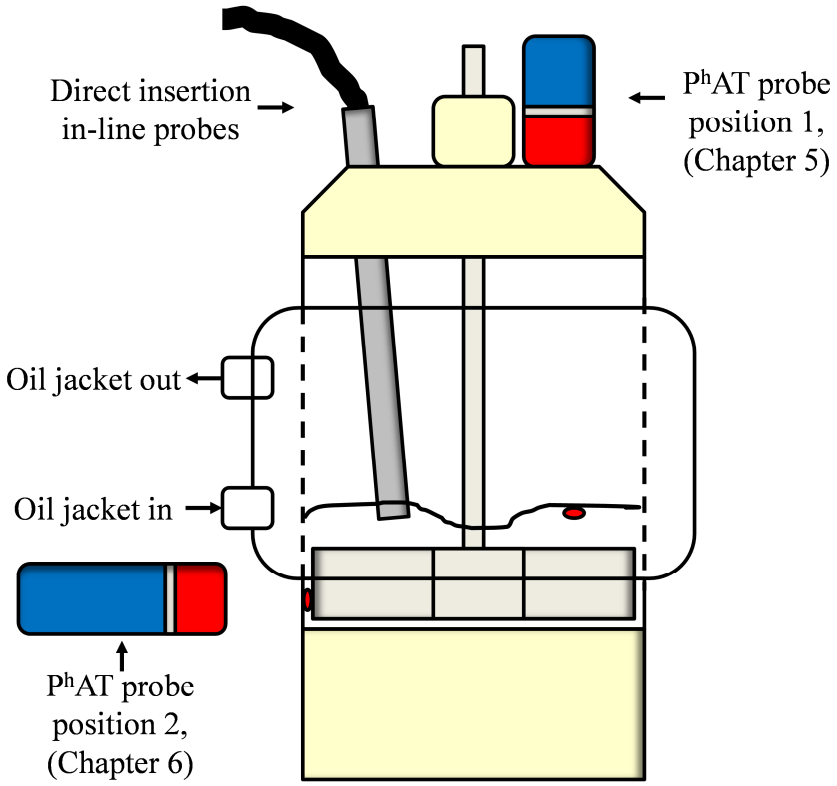

Figure 3-1: Schematic representation of bespoke drier showing the possible probe positions and orientations for the non-invasive Raman P^{h}AT probe or in-line NIR probe.

Due to the adhesiveness of wet particles and the relatively small internal diameter of the vessel, the use of direct insertion probes was not studied in detail due to extensive fouling of the probes and also a baffle effect that disrupted the mixing process of the wet particles. The base of the drier was connected to a vacuum line with a solvent reservoir and cold finger trap; the line could be switched between each using taps that were placed in the line. Vacuum (held between 50 – 100 mbar) was achieved using a vacuum pump (Edwards, Crawley, UK) and the pressure was monitored using a Pirani gauge (Edwards, Crawley, UK) in the line. The set-up of the vacuum line is shown in Figure 3-2.

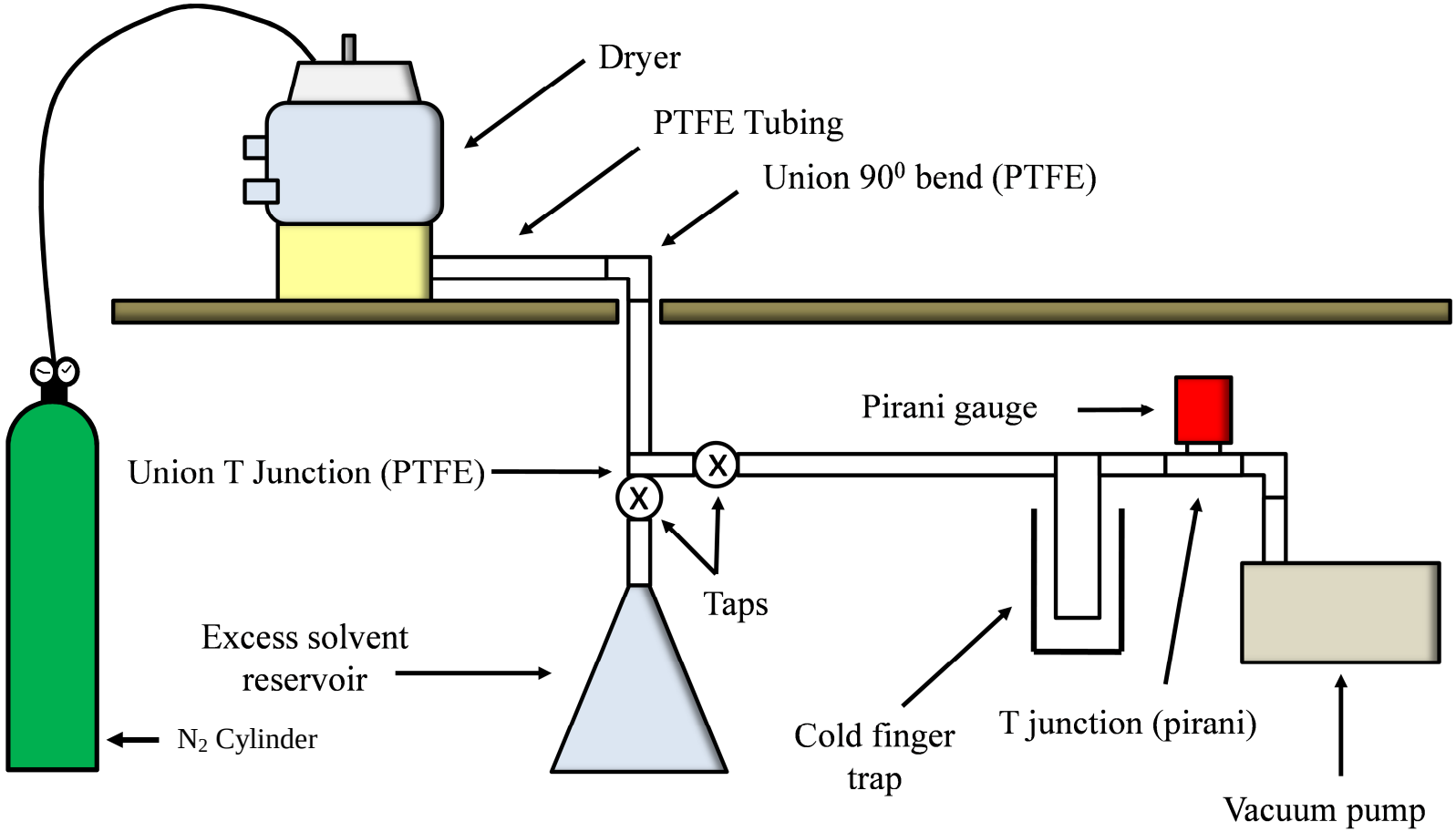

Figure 3-2: Schematic representation of the vacuum line employed for vacuum drying experiments showing the N_2 cylinder, solvent reservoir, cold finger trap, Pirani gauge, taps and vacuum pump.

3.3 Instrumentation

3.3.1 Kaiser Rxn 1 spectrometer

A Kaiser Rxn 1 Raman spectrometer with P^{h}AT probe technology was loaned to Strathclyde University by Clairet Scientific in order to carry out non-invasive measurements of the drying process. A schematic representation of the inside of an Rxn Raman spectrometer is given in Figure 3-3, followed by a short description of the role of each of the important components.

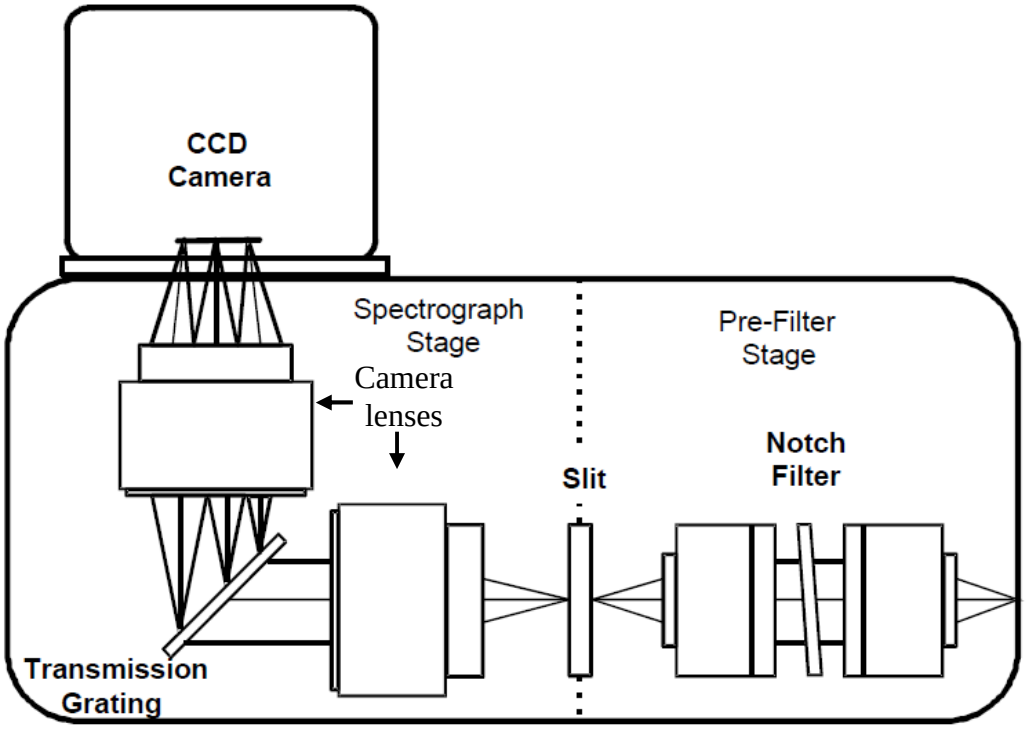

Figure 3-3: Schematic representation of the individual components inside the Rxn Raman spectrometer.[1]

The path that the light from the sample follows through the Rxn 1 P^{h}AT system spectrometer is divided into two sections: firstly, the light passes through a pre-filter stage to remove as much of the Rayleigh scattered and reflected light as possible, and secondly, the Raman scattered photons are then dispersed and detected in the spectrographic stage, using a transmission grating a charge coupled device (CCD).

3.3.1.1 Pre-filter stage

As the collected Rayleigh and Raman scattered photons enter the spectrometer, a notch filter operates as a wavelength selective mirror that reflects a narrow band of wavelengths with high efficiency, while transmitting all other wavelengths, again, with high efficiency. A notch filter has significant advantages over edge filters that were used in older Raman spectrometers such as: good transmission either side of the Rayleigh line, sharp spectral edges, a high damage threshold and good stability. Furthermore, holographic notch filters have a much smoother transmission curve and narrower rejection bands than their dielectric counterparts, giving much superior performance. A typical Rxn 1 holographic notch filter allows bands at around 175 cm^{-1} to pass the filter, however, by tilting the filter, the rejection band can be lowered to lower frequencies that can allow bands as close to 40 cm^{-1} from the exciting laser line to pass. Once filtered, the radiation is then focused onto the spectrograph entrance slit which acts to minimize the transmission of stray light into the spectrograph as it enters the dispersion stage.[1]

3.3.1.2 Axial transmissive spectrograph

As the filtered light enters the spectrograph stage, it passes through a multi-element lens before passing through the second of the holographic components of the spectrometer: a holographic transmission grating. The holographic transmission grating facilitates the instantaneous collection of the entire Raman spectrum with high spectral resolution without the need for moving parts required for scanning grating systems. As a consequence, higher sampling rates, and thus, higher throughputs can be achieved whilst reducing the possibility of sample damage from the laser. As the light enters the grating, it is diffracted at an angle close to 45° so that the diffracted light is forced into the +1 order for highest diffraction efficiency (based on Braggs law of diffraction). The diffracted light then passes through a second multi-element lens where it is simultaneously focused onto a 2 dimensional thermoelectrically cooled CCD detector which records the Raman spectrum.

3.3.1.3 Charge couple device (CCD)

The CCD has 1024 pixels along the spectrograph dispersion axis and 256 pixels along the slit height entrance (each pixel is 26 x 26 µm), which means each spectrum is recorded in 2-dimensions. CCD detectors utilise the movement of electrons from the valence band to the conduction band within a silicon lattice leaving an electron vacancy known as a hole. Whereas the electron and hole would typically recombine rapidly, the recombination is prevented by forcing them apart using an electric field. The electrons are then passed through highly doped silicon electrodes known as gates where they are immobilised in a "potential well". The CCD detector is a 2-dimensionsal array of wells (or pixels), where the number of electrons collected in each well is directly proportional to the number of photons incident on a given pixel. In spectroscopic CCD detectors, one dimension of the CCD chip is used to collect the spectral information whereas the other dimension can be used to determine spatial resolution. Each column of potential wells thus corresponds to a different wavelength. It is often the case that vertical pixels are added together during the "readout" from the array (due to the collected scattered light filling more than one row on the chip), and this results in a larger signal being obtained. For P^{h}AT probe measurements, the 256 pixels are divided into seven bins which are typically summed to give the overall spectrum, but can be looked at individually in newer probes where the n-around 1 probe design (described in section 3.3.1.4) is not randomised. The readout process involves the electrons from each potential well beings digitally converted for storage in a computer.[1, 2]

3.3.1.4 P^{h}AT probe

The P^{h}AT probe has a focal distance of around 25 cm and a variable spot size of 1, 3 or 6 mm depending on the lens positioned the end of the probe optical setup. An image of the probe is given in Figure 3-4.

Figure 3-4: Image of the P^{h}AT probe head. 1) interchangeable lens, 2) fibre optic strain relief connector 3) fibre optic cable.[3]

The P^{h}AT probe system was designed so that it was "easy for a non-specialist to use",[1] this was achieved by intelligent design that allows point-and-shoot sampling without adjustment or alignment of its internal components. The excitation and collection components of the probe are contained within the fibre optic bundle and adopt an 'n-around-1' formation as shown in Figure 3-5 a) for a generic probe. A schematic of the actual internal components of the P^{h}AT probe is then given in Figure 3-5 b) demonstrating the path that the exciting and scattered light follows during a measurement. In the PhAT probe, A single excitation fibre is collimated and passed through a band pass filter where any Raman scattering generated by the silica fibres is eliminated. The laser light is then directed at the samples using mirrors. The collected light is then passed through a notch filter where the Rayleigh scattered light is stopped allowing only light at shifted wavelengths to pass. The Rayleigh scattered light is then focused onto the randomised bundle of 50 collection fibres where it is transferred into the spectrograph along silicon fibre optic cables.[4]

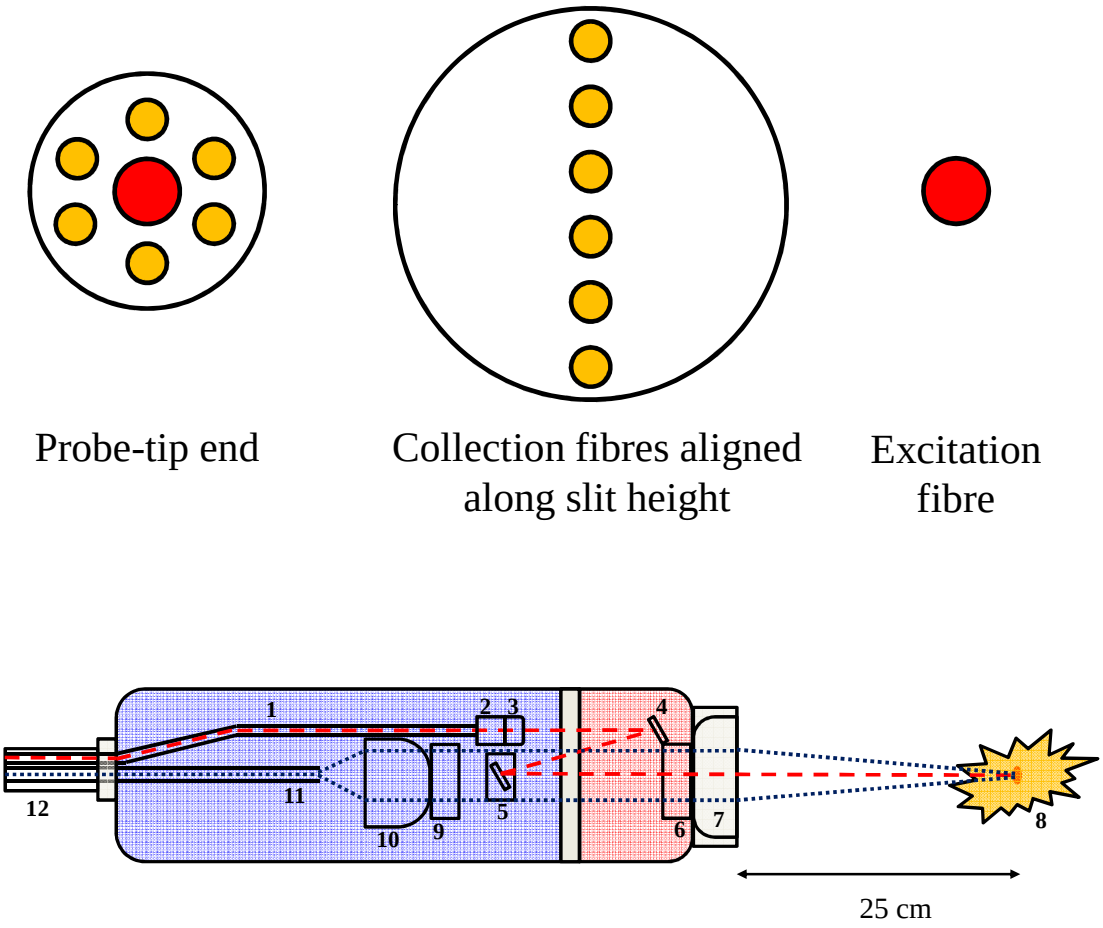

Figure 3-5: a) Schematic representation of an n-around-1 probe design, showing both ends of the fibres (6 collection fibres shown represent the 50 actually contained in the probe.[1] b) Schematic representation of the internal components of the Kaiser P^{h}AT probe. 1 excitation fibre, 2 short focal lens where laser light is collimated, 3 band pass filter, 4 mirror, 5 wavelength selective reflector (edge filter), 6 exit window, 7 Sample lens, 8 sample, 9 notch filter, 10 focusing lens, 11 collection fibre bundle, 12 fibre optic cable, red dashed line is the exciting laser, blue dashed line represents the Raman scattered light.[4]

3.3.2 Malvern Mastersizer (laser diffraction)

For laser diffraction (LD) measurements, a Malvern Mastersizer 2000 was used, however, there are many other manufacturers of LD instrumentation and, therefore, a general overview of the instrumental set-up is provided, rather than the specific contents of the Malvern instrument. A schematic representation of a typical laser diffraction instrumental set-up is thus given in Figure 3-6.

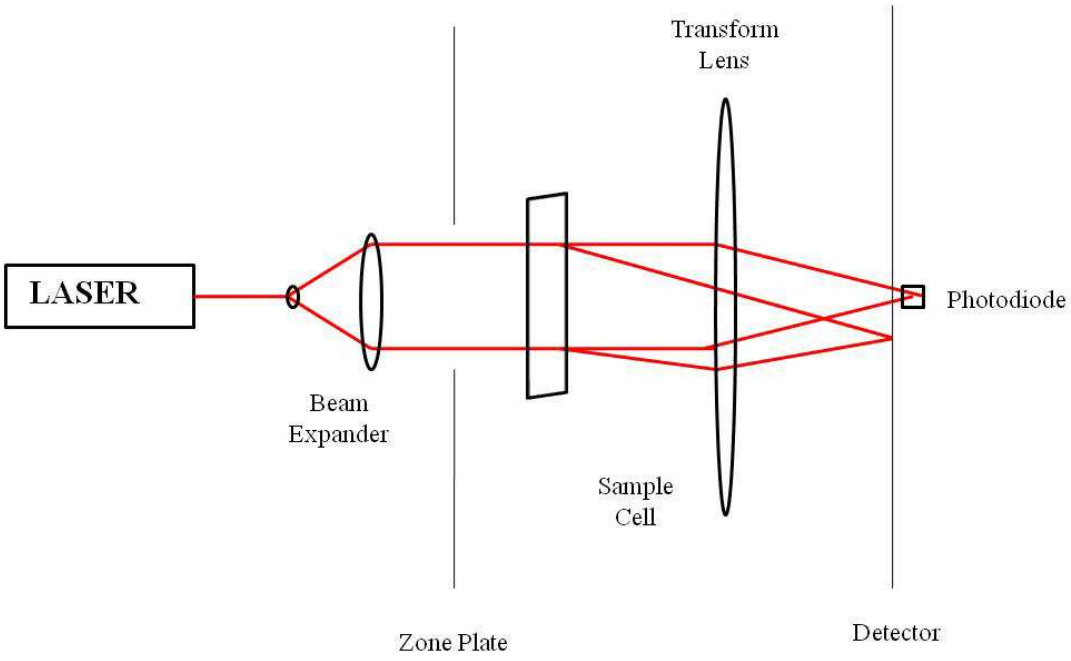

Figure 3-6: Schematic representation of a typical laser diffraction instrumental setup.[5]

In LD instrumentation, the light source is invariably a 632.8 nm HeNe laser with power ranging from 2 – 10 mW. The beam must first pass through a beam expander to ensure a uniform beam of about 5 – 10 mm in diameter allows an adequate sample volume to be illuminated (the beam diameter at the source is around 1 mm). The widened beam then passes through a zone plate to eliminate unwanted scattering and diffraction (aberration) generated by the optics, and transmit the central intensity maximum of the incident laser beam. The expanded beam is then allowed to pass through the sample cell (containing 2 – 20 mm of suspended sample), which is normally mounted at an angle to reduce back reflections from the cell windows. The

scattered light is then passed through a transform lens which images the scattering pattern onto a diode array detector. The signal at a particular position on the detector is determined only by the intensity of the light that has been scattered at a particular angle irrespective of the position of the scattering particle.[5] The theory of LD has already been described in detail in Section 2.2.1 and will not be discussed further here.

3.3.3 Focused beam reflectance measurement

Focused beam reflectance measurements (FBRM) were performed using Lasentec's laboratory scale probe (now produced by Mettler Toledo). A schematic representation of an FBRM probe is given in Figure 3-7.

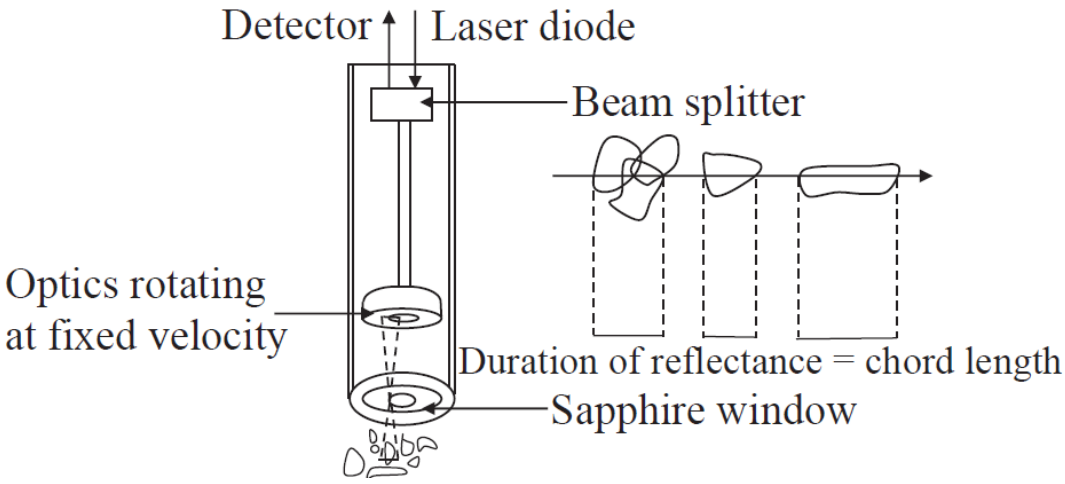

Figure 3-7: Schematic representation of the FBRM probe and measurement principle.[6]

In FBRM instrumentation, light from a diode laser (780 nm) passes through a beam splitter when entering the probe. The laser light then encounters probe optics that are rotating at a fixed velocity (normally 2 – 6 ms^{-1}) which focuses the laser at a point near the probe window. The reason for the rotating optics is to ensure that the laser spot is moving faster than the particles in suspension, and in doing so significantly reduces the probability of multiple measurements of the same particle. The probe then collects the back scattered light from the particles, with the duration of each

collected backscatter translated to give the chord length of each particle. Each measurement is carried out for a defined amount of time and data are presented either as the chord length distribution, the total counts per measurement versus time, or the counts per second versus time.[7, 8] The theory of FBRM has already been described in detail in Section 2.2.2 and will not be discussed further here.

3.3.4 Sympatec QICPIC (dynamic image analysis)

The majority of dynamic image analysis particle size measurements were performed using Sympatec's QICPIC, a schematic representation of the QICPIC instrumental set-up is given in Figure 3-8 (Micromeretic's Particle Insight and the Particle Imaging Measurement System (PIMS), which was developed at GSK, were also used for dynamic image analysis in some experiments).

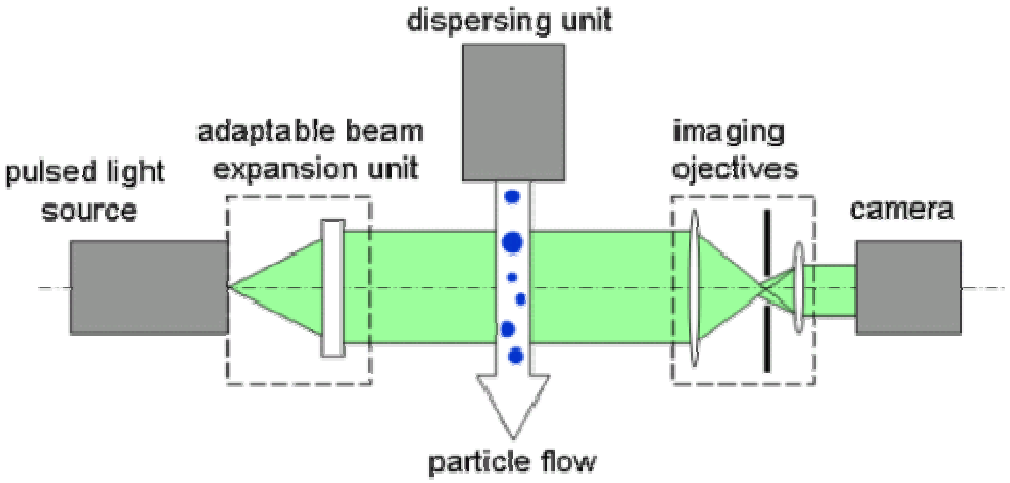

Figure 3-8: Schematic representation of Sympatec's QICPIC dynamic image analysis particle size analysis instrument.[9]

For image analysis measurements, a dispersion of particles is created either using a flow through cell as with LD measurements (wet dispersion), or by accelerating the particles through the measurement zone using a differential in air pressure (ranging from 0.2 – 3 bar, dry dispersion). As the particles pass through the measurement zone, 2 dimensional images are focused onto and recorded by a CCD detector (1024 x 1024 pixels) at frequencies of up to 500 frames per second. The imaging lenses used to focus the particles onto the CCD only transmit light that is nearly parallel to

the optical axis, which ensures that edges of the particles are detected precisely. Furthermore, to ensure that the particles appear static during analysis, a pulsed light source with exposure times of < 1 ns is employed.[9] The theory of dynamic image analysis has already been described in detail in Section 2.2.3 and will not be discussed further here.

3.4 Materials

3.4.1 Cellobiose octaaceate

D-(+)-Cellobiose octaacetate (COA) was selected by and obtained from GSK, UK to be used throughout the duration of this work (as a pseudo active pharmaceutical ingredient (API)). COA particles exist as white, odourless needles with high aspect ratio (length divided by width). The physical characteristics of COA (such as low bulk density and crystals of needle-shape morphology) are similar to typical APIs, however, the powder is not active and does not require any specific controls in order to be handled in a laboratory. Furthermore, COA only has one known polymorph and no known hydrates, and therefore, the effects of attrition and agglomeration during drying could be solely investigated. This made COA an ideal candidate for the work described here and had previously been studied internally at GSK in early attrition trials (not reported). The chemical structure of the compound is given in Figure 3-9.

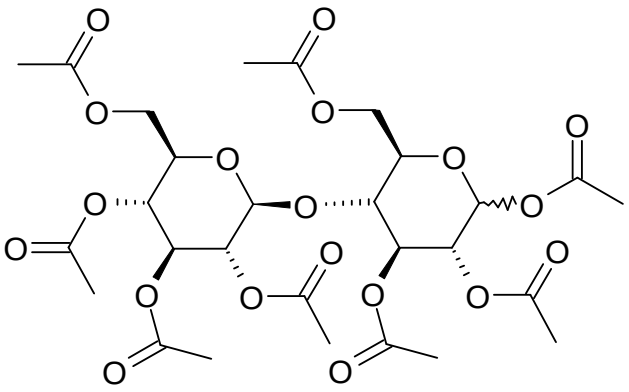

Figure 3-9: Chemical structure of D-(α)-cellobiose octaacetate.[10]

3.4.2 Microcrystalline cellulose (Avicel PH-101)

Avicel PH-101 microcrystalline cellulose is purified, partially depolymerised cellulose that occurs as a white, odourless, tasteless, crystalline/ granular powder composed of porous particles. The granular nature of the compound made sieving possible into well-defined size ranges using mechanical agitation and 10 cm diameter brass pan sieves (Endcotts Ltd, UK). This meant that Avicel could be used as a reference material in the comparison of particle size analysis techniques when applied to the measurement of COA (described in Chapter 4).The chemical structure of Avicel PH-101 is shown in Figure 3-10.

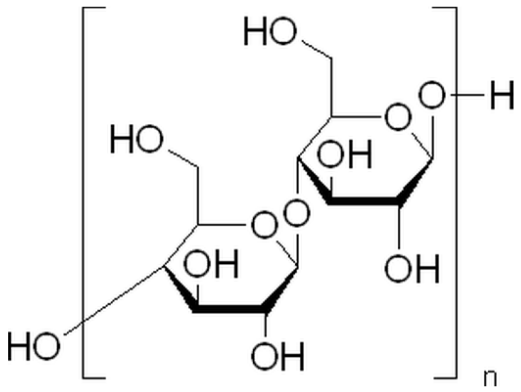

Figure 3-10: Chemical structure of Avicel PH-101 microcrystalline cellulose.[10]

3.4.3 Methanol

Methanol was used as the solvent media in drying experiments due to it being the anti-solvent used in the recrystallisation process for COA (due to the low solubility of the powder in the solvent). Methanol is a volatile alcohol with a boiling point of 65 °C at atmospheric pressure.

3.5 References

1. KOSI, *PhAT system operations manual (2008487 V2.0)*, 2004.

2. R. L. McCreery, *Raman spectroscopy for chemical analysis*, John Wiley and Sons, New York, 2000.

3. KOSI, *http://www.kosi.com/Raman_Spectroscopy/phat-probehead.php*, 2011.

4. *USA Pat.*, US007148963B2, 2006.

5. C. Washington, *Particle Size Analysis in Pharmaceutical and other Industries*, Ellis Horwood Ltd, Chinchester, 1992.

6. E. Kougoulos, A. G. Jones, K. H. Jennings and M. W. Wood-Kaczmar, *J. Cryst. Growth*, 2005, **273**, 529-534.

7. E. Kougoulos, A. G. Jones and M. W. Wood-Kaczmar, *Powder Technol.*, 2005, **155**, 153-158.

8. A. R. Heath, P. D. Fawell, P. A. Bahri and J. D. Swift, *Part. Part. Syst. Char.*, 2002, **19**, 84-95.

9. Sympatec, *http://www.sympatec.com/EN/ImageAnalysis/ImageAnalysis.html#DIA*, 2011.

10. SigmaAldrich, *www.sigmaaldrich.com*, 2011.

4 Comparison of particle size analysis techniques for measurement of pharmaceutical powders

4.1 Introduction

Particle size and shape are often critical quality parameters in pharmaceutical manufacturing. This is because both can have an influence on a variety of physical properties, quality attributes and manufacturing processability. Factors such as flow and packing, mixing and segregation, and even rheological characteristics are related to the particle size distribution and all have an effect on drug product properties. For instance, dissolution rate, bioavailability, and content and dose uniformity can all be affected by a change in the particle size characteristics of a given product. Thus, these properties ultimately determine the efficiency and safety of the drugs released and if not properly controlled can come at a great cost to a company.[1] Particle size measurement techniques are, therefore, of great importance to the industry, however, with many options available, it can be challenging to ascertain the most suitable technique for the particles under investigation.

4.1.1 Laser diffraction

Laser diffraction (LD) is a commonly used procedure for measurements of particles ranging from 0.1 – 2000 µm.[2] Early instruments were based solely on the Fraunhofer diffraction approximation, which is only applicable to particles that are large relative to the wavelength of light. Nowadays, however, LD instruments normally use a combination of the Fraunhofer approximation and Mie scattering theory which can handle small particles properly. Both theories are mathematically complex and have been developed considering only spherical particles. Furthermore, when Mie theory is considered, the refractive index of both the particles and dispersing liquid must be known as they can have a critical effect on the distribution of the light energy at the detector.[3, 4] In LD, a laser beam scatters light in all directions upon interaction with a particle. The intensity of this scattered light is measured as a function of the angle through which it was scattered, where both intensity and scattering angle are dependent on the size of the particles and their optical properties.

LD methods are known to have limitations, for example, when non spherical particles are analysed, the complexity of the maths involved is significantly increased and, as a consequence, almost all light scattering techniques (and not only LD) assume that the particles being measured are spherical and give diameters equivalent to this shape.[5] Thus, when irregular shaped particles are evaluated, the measured particle size distribution results in errors. The fundamental influence of particle shape on LD measurements has featured extensively in the literature.[6-9] Gabas *et al.*[8] used LD to analyse the surface area output for three common particle geometries of known shape and size, these were: cubic, tablet (platelets), and cylinders.[8] The authors calculated number distributions for each particle shape from the LD measured volume distributions, and then calculated the mean surface areas for each geometry based on the diffraction diameters recorded before comparing them to the real values. An assumption was made that particles were randomly orientated when diffracting the beam. The LD software, strictly valid for spheres where orientation is not a factor, performed reasonably well for cubic crystals with an error of 9%, however, the surface areas were considerably underestimated for tablets and cylinders, 31% and 70%, respectively. Gabas *et al.*[8] concluded that the surface area was not measurable for non-spherical geometries as the particles adopted a preferential rather than random orientation in the measurement cell. Another limitation is that particle concentration has to be controlled in LD measurements as a photon of light may interact with many particles rather than only one if the concentration is too high, which means the scattering pattern cannot be analysed accurately.[10] This is termed multiple scattering and is generally overcome in modern instrumentation by the calculation of the "optical concentration", where the operator is instructed by the instrument if the concentration of sample is too high (or too low). The problems associated with LD are well documented, however, they are more than often compensated by the simplicity of use of the instruments and as such, LD is a popular choice for analysis.

LD has been an industry standard for some time and is covered comprehensively in the literature for analysis of solid dose oral formulations, suspensions, inhalation products, and to assess batch-to-batch variability of an active pharmaceutical

ingredient (API) through the effect of particle size on packing density. [11-15] Tinke *et al.*[11-13] have reported a series of studies where the limitations of LD have been tackled by performing static image analysis in tandem with the LD method. The problems associated with the technique are discussed without bias and even the relationship between LD and image analysis was scrutinised. The authors argue that the limited understanding of the principles of LD for non-spherical particles is mainly due to confidential data analysis algorithms from LD manufacturers.[11] Therefore, by making some assumptions, the authors were able to calculate LD patterns based on the image analysis data. In the initial article of the series, the authors used the method to correlate the particle size distribution of an API to the dissolution profile of the drug product of a suspension formulation.[12] Based on theoretical calculations supplemented with experimental data, the authors were able to conclude that the volume weighted mean (d (4,3)) was related to the *in vivo* release profile of the drug.

Hagsten *et al*.[14] used LD to measure batch-to-batch variation in 131 5-aminosalicylic acid batches. They argued that, although the technique has known problems associated with particle shape, LD allowed quick evaluation of the similarity of batches. From their study, they concluded that screening of batches using particle sizing data allowed the rational selection of representative samples for further investigation. They concluded that the use of multivariate principal components analysis of the API LD data allowed the authors to correlate differences in particle size (described by PC 1) and polydispersity (described by PC 2) to packing density in downstream processing.

4.1.2 FBRM

LD is predominantly used as an at-line or off-line technique in the pharmaceutical industry, however, the US food and drug administration's 2004 "PAT Initiative"[16] encouraged companies to invest in *in situ* process analytical technologies in order to build quality by design into their processes rather than measuring quality by end product testing. LD can be implemented *in situ* in a pharmaceutical process; however, problems often arise when the presentation of a sample to the analyser is

considered. Currently for LD, analysis must take place in either a dilute wet dispersion or completely dry dispersion. Therefore, in-line analysis is near impossible for many processing steps due to the nature of pharmaceutical manufacturing, and on-line analysis would incur significant costs to fit an analyser into a recirculation loop which would likely require a dilution step also. A popular alternative to *in situ* LD measurements is focused beam reflectance measurement (FBRM) which can measure particles in the range from 0.25 – 1000 µm.[17] FBRM is also a light scattering technique, although, rather than measuring the diffraction pattern of a particle and applying a sophisticated algorithm to give a volume based distribution as in LD, back scattered light from a diode laser focused on the outside of a sapphire window is measured. The laser is passed through a beam splitter before being rotated at 2 – 6 ms^{-1} by the probe optics so that multiple measurements of single particles are prevented. The back scatter is generated by the laser energy being reflected from particles on or near the measurement window and the duration of the back scattered light is measured and translated to give a chord length distribution (CLD) for the particles being analysed. All particles are thus analysed irrespective of shape.[17]

As with LD, FBRM has known problems. For example, although the CLD generated is related to, it is not a direct measurement of the particle size distribution (PSD), which has a direct effect on product quality.[18] In addition to this, anisotropy of the particles being measured is widely discussed in the literature, because as in LD, the chord length measured is dependent on the orientation of the particle as it cuts the laser beam.[19-22] For example, Li *et al.* studied the relationship between CLD and particle size distribution for non-spherical particles.[20, 21] When needle shape particles were considered, the CLD measured was in fact the average dimension of the object orthogonal to the dominant dimension, in this case, the width of the particle rather than the length. Nonetheless, FBRM has featured extensively in the pharmaceutical particle analysis literature, particularly for crystallisation monitoring.[23-27] Initial FBRM probes required particles to be present in dilute slurry in order to give reliable measurements, however, more recently the C35 probe was developed which allowed FBRM to be implemented into other unit operations such as granulation or drying

processes.[28-31] The C35 probe allows FBRM to be implemented into processes that were previously inaccessible owing to the incorporation of a scraping mechanism on the probe window. Any particles stuck to the analysis window are removed between each measurement, and with this the need for the particles to be in slurry is also removed.

Huang *et al.*[28] used the C35 FBRM probe to measure particle size *in situ* during high shear wet granulation. A design of experiment (DoE) approach was employed to assess how wet massing time and water added for granulation affected the final product particle size. The authors then used the knowledge gained from the DoE to evaluate eight clinical batches. They concluded that FBRM was useful for in-line particle characterization; however, this assessment was subject to some limitations. For example, the probe position had an effect on the median chord length recorded. The authors hypothesised that this was due to larger particles being located in the lower part of the granulator.

FBRM is not alone in its ability to measure particle size *in situ* in processes that have a high solid to solvent ratio. The Parsum probe from Malvern Instruments offers an alternative where pressurised air is used to disperse/ dilute and remove particles from a measurement window where Spatial Filter Velocimetry determines the CLD.[32] The Parsum probe measures particles larger than 50 µm and thus is not likely to be suitable for needle-shaped particles with a width < 50 µm.

4.1.3 Image analysis

In contrast to laser scattering techniques there are also many dynamic imaging techniques such as Sympatec's QICPIC, Micromeritic's Particle Insight (PI), and the Particle Imaging Monitoring System (PIMS) developed in house at GlaxoSmithKline. For wet dispersion of the particles, a similar method is employed by all three techniques. The particles are propelled round a recirculation loop either by means of agitation (PIMS) or a peristaltic pump (PI and QICPIC). A stroboscopic light source is then used to "arrest" particle motion while a fast camera records digital images of the particles. Proprietary algorithms are then used to analyse the images based on user defined statistics for PI and QICPIC or instrument defined

characteristics for PIMS (more detailed information is given in the experimental and results sections). For QICPIC analysis, a second dispersion method is available: dry dispersion using the RODOS system. Particles are accelerated through a measurement window by a differential in air pressure. The measurement process is then identical to when wet dispersion of particles is carried out. Another leading imaging particle size analysis technique is the Morphologi G3 from Malvern instruments which has the capability to analyse wet or dry dispersions of particles. For dry dispersion, particles are dispersed onto the imaging stage using compressed air; the analyser then records the position of every particle in view giving a distribution.

There are many pharmaceutical examples in the literature where image analysis has been applied to powders.[33-39] With the ever increasing computer power available, traditional imaging microscopy where an operator would sit and manually count particles, has been replaced with automated analysis, significantly reducing the analysis time and increasing the number of particles analysed. Furthermore, errors introduced by varying operators have been significantly reduced.[40] Yu *et al.*[41] compared QICPIC digital image analysis with LD diffraction to measure spherical and rod shaped microcrystalline cellulose particles of differing size and aspect ratios, respectively.[41] In addition to analysis of the two individual particle morphologies, digital image analysis was performed on binary mixtures of the spherical and rod shaped particles. For spherical particles, the authors found that QICPIC and LD measurements were in good agreement; however, the respective outputs for the two techniques differed significantly for rod shape particles owing to the fundamental differences in measurement. In LD measurements, the distribution obtained is that of spherical particles with the same diffraction pattern as the measured particles, whereas for the QICPIC measurements, the distribution given was based on the diameter of an equivalent sphere that has the same area of the particles measured (EQPC). EQPC was used in this example so that the two techniques could be directly compared; however, the so called Ferret diameters (max and min length) would have been more appropriate dimensions to analyse the rod shaped particles. For the binary mixture measurements, the authors found that the QICPIC system gave excellent

agreement with calculated distributions of each volume fraction. The authors concluded that QICPIC could provide valuable insights into pharmaceutical processes where the impact of size and shape are coupled such as in powder mixing or segregation.

Digital image analysis has also been successfully implemented *in situ*, although mainly in combination with FBRM for crystallisation monitoring.[17, 26, 27, 42-46] Liu *et al.* combined *in situ* image analysis with FBRM and near-infrared spectrometry (NIRS) to monitor an anti-solvent mediated crystallisation process.[27] *In situ* digital imaging gave information of the particle shapes and dimensions while FBRM was used to measure the chord lengths and give particle counts, a partial least squares NIRS model was established to give the concentration information of the solute throughout the crystallisation process. The authors found that NIRS could accurately determine the concentration profile for the process and this correlated well with the FBRM's chord count profile; however, without the use of video imaging, the morphology, which is a critical parameter when polymorphism is considered, could not be determined. They argued that FBRM combined with digital imaging could provide the concentration trend, particle distribution and polymorphic transition without NIRS, however, their general conclusion was that PAT technology selection should be coupled with scientific knowledge for crystallisation processes.

Currently, *in situ* digital imaging cannot be used to analyse processes where the ratio of solvent to solid is low due to significant overlap of the particles making them extremely difficult to distinguish in a 2D image (even with modern day computing power). As with LD, an online solution would require a dilution step with significant implementation costs.

In the following section, laser scattering techniques (LD and FBRM) and dynamic image analysis techniques (QICPIC, PI and PIMS) were utilised to analyse increasing size fractions of two materials whose morphology are common in the pharmaceutical industry. The aim of the study was to determine a best practice set of guidelines for particle size analysis of the drying process of needle-shaped particles, typical of active pharmaceutical material. Samples of cellobiose octaacetate needles

of different particle size ranges and sieved Avicel PH-101 were analysed. The results presented consider the basis of each technique while offering a discussion on the relative advantages and disadvantages. The evaluation is divided into two sections: firstly, the various statistics from the range of the techniques are discussed followed by a review of the range of distributions that are at the operators' disposal.

4.2 Experimental

4.2.1 Materials

Avicel PH-101 microcrystaline cellulose (granular) and cellobiose octaacetate (COA) (needles) were obtained from GSK (Irvine, Ayrshire and Tonbridge, Kent, UK, respectively) and were selected for this study due to their differing geometries.

4.2.2 Sieving

Bulk powder samples were separated into the following particle size fractions: <38, 38 – 53, 53 – 106, 106 – 150, and 150 - 212 µm in 10 cm diameter brass-pan sieves (Endecotts Ltd, UK) using a mechanical sieve shaker. Sieves were placed in descending size order (from top to bottom) so that smaller particles were able to pass through each mesh until they reached a sieve where they were too big and thus retained in the particular size fraction.

4.2.3 Microscopy

Digital microscope images were recorded using a standard Nikon Eclipse TE2000-U microscope with a magnification factor of 150. The images were recorded using a Nikon CoolPIX 5400 5.1 megapixel camera that was attached through a screw-on port on the microscope. The images were focussed manually by moving the stage in the Z direction using the microscope eye piece to check the focus. Once focused, the stage was moved on the X, Y plane to identify particles of interest. Particles were placed on a microscope slide using a spatula and excess particles were removed by tilting the slide to avoid significant overlap. The images were then extracted to PC using a standard USB connection to the camera.

4.2.4 Laser diffraction

Laser diffraction measurements were carried out using a Malvern Mastersizer 2000 (Malvern Instruments, Worcestershire, UK). Powder samples were dispersed in 0.1% Tween 80 in water (Sigma-Aldrich, A5376, Dorset, UK) using a Hydro2000SM cell. Powder was added to the cell until a laser obscuration (internal parameter of the instrument to prevent multiple scattering effects) of ~3% was reached. Laser diffraction measurements generate a variety of particle size data: the volume distribution, which is given in 100 logarithmically spaced size bins from 0.01 – 10,000 μm, and d (0,5), the particle diameter corresponding to 50% of the volume distribution, were used in this study. Other diameters such as d (0,1) and d (0,9) corresponding to 10% and 90% of the volume distribution, respectively, d (4,3), the volume weighted mean, and d (3,2), the surface weighted mean, are also generated but not discussed here.

4.2.5 Focused beam reflectance measurement (FBRM)

FBRM measurements were made using a Lasentec FBRM PI-14/206 probe and attached control computer. The powder samples were made dispersed into slurries using 0.1% Tween 80 (Sigma Aldrich) at around a concentration of 2% w/w. Each slurry was then stirred at 400 rpm in a beaker using the FBRM standard setup apparatus supplied with the probe. Each individual measurement had an acquisition time of 15 s (approx 4 measurements per min) and data was collected for 10 min per sample. The specific data sets were then exported into Excel as un-weighted number distributions.

4.2.6 Sympatec QICPIC

Sympatec QICPIC image analysis was performed on dry powder samples using the RODOS dry dispersion unit and wet samples using the LIXEL wet dispersion unit, data was analysed using WINDOX 5 software (Sypmatec LTD, Bury, BL9 7BR). For dry powder measurements, samples were placed in the RODOS dispersion unit, which uses vibrations to transport the sample in small volumes into the analyser. The particles were then accelerated through the measurement window where a fast

camera records images of the particles that are analysed. As these particles are accelerated through the measurement window, a pulsed nano-second (ns) light source is used to ensure that no motion blur occurs. This ensures that static images of the particles are obtained where shape analysis can be performed. For wet dispersion measurements, powders were dispersed in 0.1% Tween 80 and water and circulated through a flow cell using a peristaltic pump. WINDOX 5 software performed an auto focus on the particles before measurements were recorded. For analysis of wet dispersions, the pulsed light source and image recording speed were reduced due to the slower velocity of the particles and each measurement lasted for 30 s.

4.2.7 Particle Insight

Particle insight is a flow cell imaging technique where a stroboscopic light source was used to illuminate and arrest particle motion as they pass through a flow cell. The camera was focused inside the glass of the flow cell. The samples were dispersed in 0.1% Tween 80 in water and then introduced to the instrument in a sample well before being re-circulated through the flow cell using an internal pump of the instrument. A small spatula tip of particles were added to the sample well (volume approx. 30 ml) and measured until 5000 “in focus” particles were analysed. Data was analysed using Particle Insight software (version 1.73) before being exported to Excel.

4.2.8 Particle Imaging Measurement System (PIMS)

PIMS has been developed in house at GSK Tonbridge and uses a stroboscopic pulsed light source that arrests particle motion for a camera to record images of particles in a flow cell (similar to QICPIC LIXELL and PI). The camera was focused just inside the glass window of the cell. The samples were dispersed in 0.1% Tween 80 in water using a low speed impeller and circulated through the flow cell using a peristaltic pump. A spatula tip of particles were added to 70 ml of dispersant and then each sample was analysed until the software had counted 30,000 “in focus” particles. The data was exported to Origin software where proprietary algorithms developed at GSK were used to analyse the images based on needle length and width. Standard MATLAB (Mathworks, Natick, USA) functionality was then used to convert this

information to give number distributions and circularity data. The software was calibrated daily using a saved image of a 100 µm grid. For these experiments the instrument was set up to provide a magnification of x20.

4.3 Results and discussion

4.3.1 Sieving of COA particles

For needle-shaped COA particles, it was apparent that sieving was not suitable to obtain ranges of particles of defined size. COA particles are high aspect ratio (length divided by width) needles that when sieved can pass through the mesh in two orientations: either by length or width. The particle size analysis performed on the sieved COA particles suggested that separation based on the length dimension had not been achieved and this was confirmed by imaging microscopy (Figure 4-1). The width of COA particles (~20 µm) is generally less than that of the smallest sieve size (38 µm) and therefore a large number of long needles passed through to smaller sieves. This was due to a randomly orientated multi-particle layer being present in each sieve with particles being sieved based on their length or width.

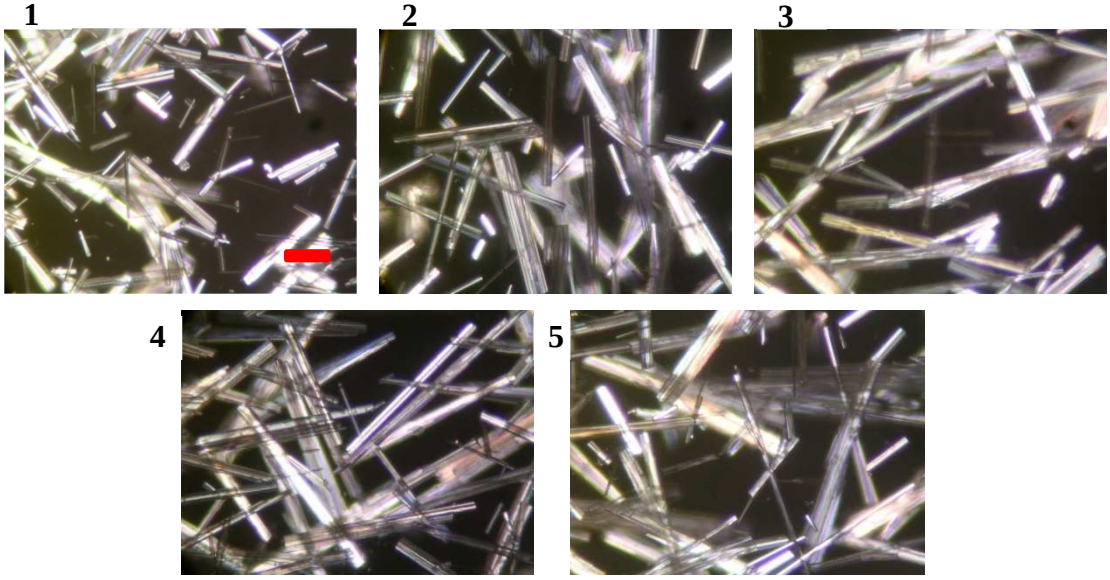

Figure 4-1: Microscopy images of the sieved COA fractions in the nominal ranges: 1) < 38, 2) 38 – 53, 3) 53 – 106 4) 106 – 150 and 5) 150 – 212 µm at 150x magnification (scale bar = 100 µm) ___.

A range of particle sizes was obtained for COA by subjecting bulk material to different levels of attrition caused by shear in an agitated vessel during powder drying (see Chapter 5 for additional details). Imaging microscopy was performed to identify the best samples that produced a range of particle sizes. Microscopy images of the COA particles obtained in the drying experiments are shown in Figure 4-2.

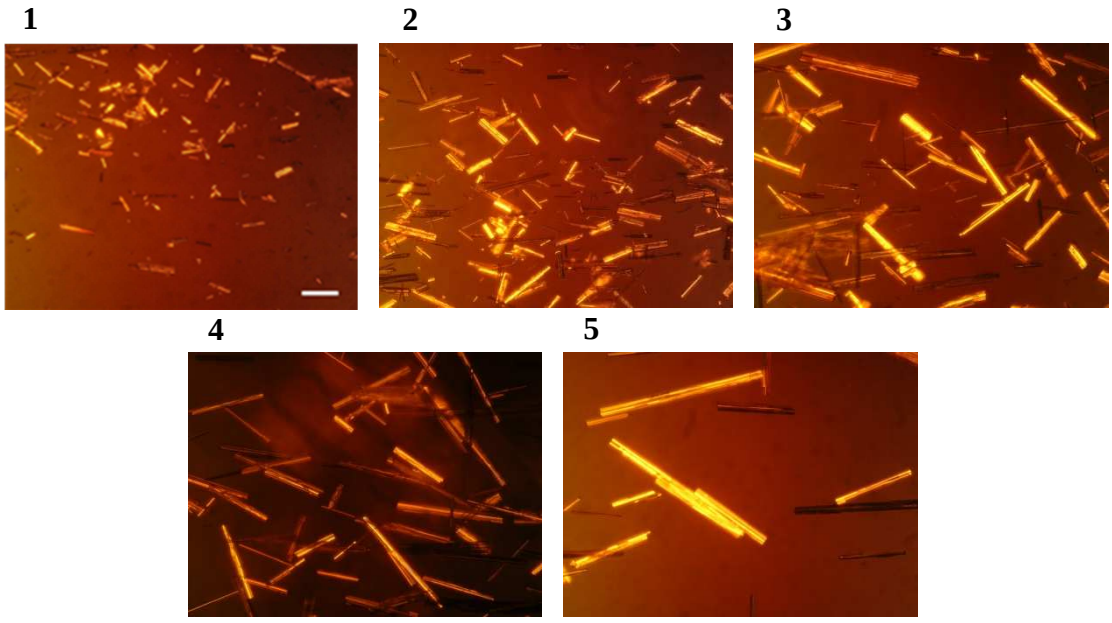

Figure 4-2: Microscopy images of the COA samples obtained from particle attrition during powder drying: increasing size order from 1 – 5 with a magnification factor of 150x (scale bar = 100 µm).

4.3.2 Single value particle size analysis

In the particle size analysis literature, there are several "single value" statistics cited in order to describe a given particle distribution. Commonly used variables (or variations of) are the surface weighted mean (d (3,2)), the volume weighted mean (d (4,3)), the 10% and 90% percentiles (d (0,1) and d (0,9)), respectively), or the median (d (0,5)). Furthermore, when image analysis and particle shape are considered, percentile and median values can be obtained for specific attributes such as particle length, width, area, aspect ratio, convexity or circularity. The median diameter is perhaps the most common diameter referred to in the literature for most particle size analysis techniques. Tables 4-1 (Avicel) and 4-2 (COA) show the median particle diameters obtained for each analytical technique. For LD

measurements, the median value reported is equal to the diameter of spherical particles that have the same diffraction pattern as the median of the distribution of patterns measured. For FBRM, the median value is the un-weighted median chord length obtained. For QICPIC, the median equivalent sphere (volume distribution) is given. For PI, the median equivalent sphere (volume distribution), and for PIMS, the median length dimension obtained (number distribution) are given. As already stated, PIMS is a proprietary GSK technique designed with needle-shaped particles in mind and therefore does not report an equivalent sphere diameter. The length dimension is included for completeness.

Table 4-1: Median particle sizes given from each sieved fraction of Avicel.

	Avicel PH101				
Size Fraction/ µm	**LD/ µm**	**FBRM/ µm**	**QICPIC/ µm**	**PI/ µm**	**PIMS/ µm**
< 38	26	17	45	41	41
38 – 53	38	19	63	59	91
53 – 106	69	24	84	81	117
106 – 150	78	25	102	96	95
150 – 212	145	35	158	96	59

LD: median volume weighted particle diameter, FBRM median number un-weighted median chord length, QICPIC: median volume weighted equivalent sphere diameter, PI: median volume weighted equivalent sphere diameter, PIMS: median particle length.

The median values obtained for each technique show that for granular shaped Avicel, sieving of the particles successfully separated the particles into fractions of increasing particle size. The values in table 4-1, however, show significant variation of median values across the techniques which was expected when the basis of each measurement technique was considered. Comparing LD and FBRM, the values obtained result in a positive correlation; however, as FBRM produces a number based chord length distribution rather than a volume based particle size distribution, the median values do not appear to reflect the actual size of the particles. The probability of the FBRM measuring the particle diameter as a chord even for

spherical particles is particularly low and further, the un-weighted distribution is given purely on the number of particles counted, which places the emphasis on fine particles. In order to put more focus on coarser particles the distributions can be square or cube weighted, which in turn increases the median chord lengths obtained.

When the median values for laser scattering methods were compared to digital image analysis, a general increase in equivalent sphere diameter was observed with QICPIC and PI measurements as expected, with excellent agreement between the techniques, except for the 150 – 212 µm size fraction. However, when PIMS measurements were analysed, a different trend was observed. Here, an increase for the initial three samples was followed by a decreasing trend for the two largest size ranges. The PIMS data is given only as a number distribution whereas both QICPIC and PI have the capability to output both number and volume distributions. Number distributions are weighted heavily towards fine particles, which in general, far outnumber the coarse particles. Although the larger sieve sizes retained the bigger particles, a far greater number of fine particles were still present in each sieve. Furthermore, fine particles are very adhesive and are known to stick to larger particles, which when placed in dispersion, break away leaving one coarse and many fine particles. The number of fine particles measured relative to the number of coarse particles is likely the reason that the PIMS measurements did not display the same trend as the other techniques, rather than the samples were very different or instrument error. Furthermore, with image analysis techniques, the particles must be in focus (depending on the criteria for each individual technique) and all out of focus particles are disregarded. With the PIMS measurements, it was noted that a large number of coarse particles were not analysed due to failing the focus criteria owing to the low depth of field of the PIMS instrument.

Table 4-2: Median particle sizes given from each analytical measurement for COA fractions obtained from drying experiments.

	COA				
Sample No.	**LD/ µm**	**FBRM/ µm**	**QICPIC/ µm**	**PI/ µm**	**PIMS/ µm**
1	25	11	42	65	17
2	32	12	55	79	20
3	37	14	63	84	29
4	50	18	84	113	44
5	58	22	98	104	61

LD: median volume weighted particle diameter, FBRM median number un-weighted median chord length, QICPIC: median volume weighted equivalent sphere diameter, PI: median volume weighted equivalent sphere diameter, PIMS: median particle length.

The median values obtained for the needle-shaped COA particles show a general increasing trend with each technique. Comparing the laser scattering methods, an increasing correlation is present as was observed with Avicel. Needle-shaped particles are known to orient themselves when dispersed in moving liquid. Therefore, the CLD length distribution from FBRM is predominantly formed by measurement of the width of the needles (depicted in Figure 4-3); here, the data suggests that needle thickness increases slightly as needle length increases.

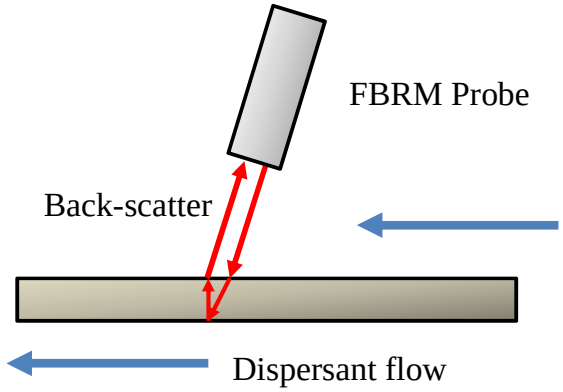

Figure 4-3: Schematic illustration of FBRM measurement of needle-shaped particles oriented in direction of flow.

The LD volume distribution given is that spheres with the same diffraction pattern of the particles measured. Non-spherical particles generate vastly different diffraction patterns to those of spheres,[8] however, LD analysers evaluate each sample as spheres regardless of morphology. The internal algorithms of the instrumentation are vendor specific and confidential making a reasonable hypothesis to the generation of the median values challenging without consideration of the entire distribution. Nonetheless, LD was effective in analysing an increase in needle length as an increase in particle size. For digital imaging techniques, orientation of the particles is much less of a factor for measurements as analysis is performed based on a recorded image that can be treated in several ways rather than an isolated scattering incident that can be measured only once (an assumption is made that the particles are parallel to the imaging plane).

Comparing laser scattering techniques to digital imaging techniques for needles is not a straightforward task, for the purposes of this evaluation, the equivalent sphere diameters are reported for QICPIC and PI rather than the more appropriate length and width dimensions (needle length is reported for PIMS as there is no option to generate equivalent sphere data). This was to make the comparisons as similar as possible; however, the length and width of needles are discussed more fully in later sections. The equivalent sphere data for QICPIC and PI show an agreement with the laser scattering methods, however, the largest fraction in the PI data does not conform to this trend. There are two likely explanations for this anomalous value. Firstly, at the time the evaluation was performed, PI was a relatively new technique to the market. A software glitch that disregarded particles that were longer than 500 µm was present (since removed in later versions) and could have skewed the results as a significant number of longer needles may have been excluded. The second reason is that a poor subsample may have been obtained for analysis. The PIMS data shows reasonable agreement with the LD data obtained, however, as LD is a volume distribution and PIMS is a number distribution, the correlation is likely coincidental.

4.3.3 Particle size distribution evaluation

Although examination of the median particle diameters gives an initial indication of the particle characteristics, a vast amount of information is overlooked regarding the distribution or polydispersity of the sample, and thus, interpretation of the data may be incorrect. A simple example of an incorrect interpretation is the analysis of a bimodal distribution. By only examining the median value, an average value of the two size distributions present is obtained rather than the key information that an overall bimodal distribution is present.

The following section describes the distributions obtained for the techniques evaluated in this study beginning with the laser scattering measurements. This is followed by discussion of the image analysis techniques, and a comparison of their strengths and weaknesses for the samples studied.

4.3.4 Laser diffraction

Figure 4-4 a) and b) shows the volume distributions obtained for the sieved fractions of Avicel and experimentally obtained fractions of COA, respectively.

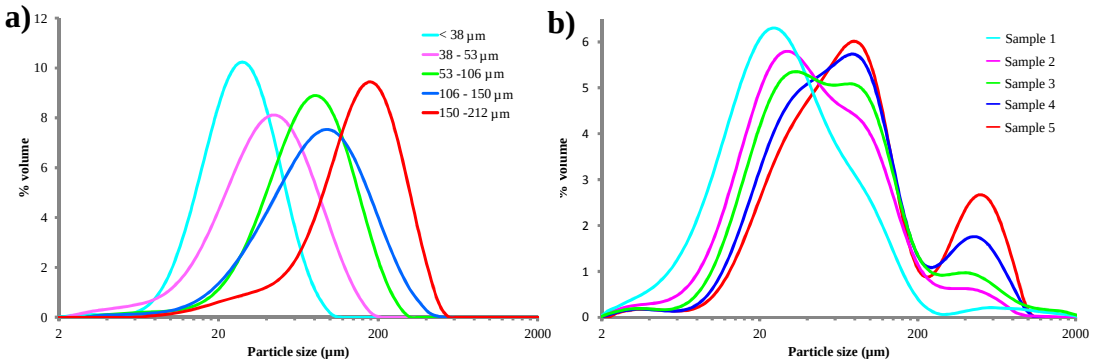

Figure 4-4: Laser diffraction generated volume distributions for a) sieved fractions of Avicel and b) experimentally obtained fractions of COA.

For the sieved samples of Avicel, a positive shift in particle size was observed for the distributions of each particle size fraction. In some of the samples, the Gaussian shaped distribution was skewed and tails were observed corresponding to a high number of fines present in the samples. These fines are attributable to incomplete sieving in the samples or by small fragments breaking off from larger particles.

When volume based distributions are considered, the data are weighted towards large particles as one bigger particle will have the volume of many smaller ones, and can sometimes lead to distributions that are not Gaussian shaped curves. This is outlined in the data obtained for COA where a tri-modal distribution is obtained owing to three populations of the particles. In the smallest fraction, there is a mode centred at ~20 μm which can be attributed to the laser beam being diffracted predominantly by the needle width. Also, in the data for the smallest sample, a second mode is observed at around 90 μm that is likely a result of diffraction by the length dimension of short needles. As needle length is increased, this mode becomes the most prominent one in the distributions for larger particles, as in these samples there is a higher number of longer needles so the probability of diffracting the laser beam by length also increases. For the largest particles, there is also a third mode (at around 800 μm), which is due to the length of the longest needles observed. The mode at 800 μm is most likely caused by a smaller number of particles which nevertheless, contribute a significant volume, especially for samples 4 and 5. It has been shown previously that non-isometric particles such as needles (or platelets) have distinct scattering patterns corresponding to both maximum and minimum particle dimensions.[47, 48] Therefore, when the LD instrument software fitted the scattering data measured for needles from this data set using the scattering patterns of spheres, it follows that the modes in the resulting distributions corresponded to both the maximum and minimum dimensions of the particles actually present in measured samples. In the case of granular Avicel, the distribution was simpler to understand as an increase in particle size resulted in a positive shift in the distribution which signified greater average particle size. The data presented here shows that LD measurements are suitable for analysis of both granular and needle-shaped particles, however, in order to understand the distributions obtained for needle-shaped particles, it is important to understand the method that needle shape changes first, and furthermore, determine the effects that these changes have on the volume distribution. This is a limitation of laser diffraction in that particles that are not spherical or granular will diffract the laser beam depending on the orientation of the particles in the beam; in the case of needles, the probability of diffracting the beam

based on needle length rather than width is small and therefore the effect on the data generated by differing needle lengths would also be expected to be small. However, as the data suggests in Figure 4-4 b), this is not entirely the case as the distribution changes with increasing size and therefore an averaging effect based on the needle populations is observed.

4.3.5 FBRM

The chord length distributions for sieved samples of Avicel and the experimentally obtained fractions of COA are shown in Figure 4-5 a) and b), respectively.

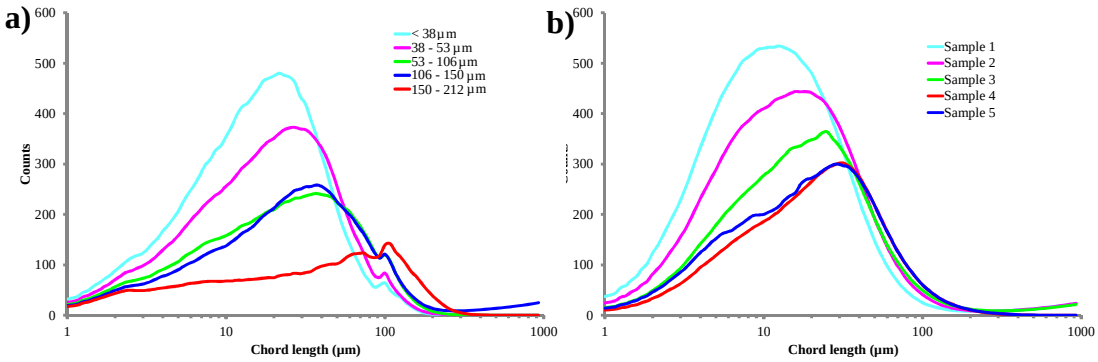

Figure 4-5: Chord length number distributions of the FBRM data for a) sieved Avicel fractions and b) experimentally obtained fractions of COA.

The FBRM data for Avicel shows an increase in chord length distribution (CLD) with increasing particle size. A dampening effect was also observed as particle size was increased, which is easily explained by considering the effects of individual particle volume as particle size was increased. For this study, slurries of 2% w/w were made up for FBRM analysis, a 2% w/w sample of say <38 µm will have many more particles than an equivalent sample of 150 – 212 µm particles, simply because the mass of a single <38 µm particle is much less than the mass of a single 150 – 212 µm particle owing, to its much lower volume. Therefore, the dampening effect observed was due the lower number of particles in the bigger fractions of Avicel. For the COA samples, the FBRM data shows a similar dampening effect to that observed for the Avicel particles. This is once again due to the number of particles in samples with larger particle sizes based on their mass. The data for COA also demonstrates a

general increase in chord length distribution as particle size of the samples was increased. The un-weighted CLDs obtained have median values that are generally smaller than the other techniques, however this is expected when the basis of the measurement is considered, especially for the needle-shaped particles. Here, the dimension that is predominantly measured is through the shortest axis (the width), and this is due to the low probability of the particle being in the correct orientation to be measured along the length dimension. The increase in CLD with increasing needle length suggests that needle width increases as needle length increases, this hypothesis can be scrutinised when then results from image analysis are discussed. Nonetheless, the FBRM measurements shown here demonstrate that changes in particle size for both granular and needle-shaped particles can be observed.

The next three techniques that are discussed are based on image analysis. A comparison is made between the data obtained from these measurements with the laser scattering techniques.

4.3.6 QICPIC

With QICPIC measurements, the Avicel fractions were analysed using the dry dispersion RODOS system (1.5 bar air pressure causing acceleration of the particles through the measurement window). The COA samples, however, were measured using the wet dispersion LIXELL system at a flow rate of 15 ml/ min. With QICPIC, the measurement principle is the same regardless of dispersion method, and therefore, dispersion should not have an effect on the distributions obtained. The reason for using different dispersion techniques was due to the brittleness of the COA particles. When COA particles were analysed using the RODOS system, the particles were instantaneously fragmented into much smaller particles on entering the air stream, this resulted in distributions that were not representative of the sample which did not vary for increasing particle size. This fragmentation occurred at an air pressure of 1.5 bar and to a lesser extent at 0.2 bar, and example distribution data showing this effect for COA sample 5 are shown in Figure 4-6. Avicel particles did not suffer fragmentation on entering the air stream and therefore dry dispersion at 1.5 bar was appropriate for the analysis.

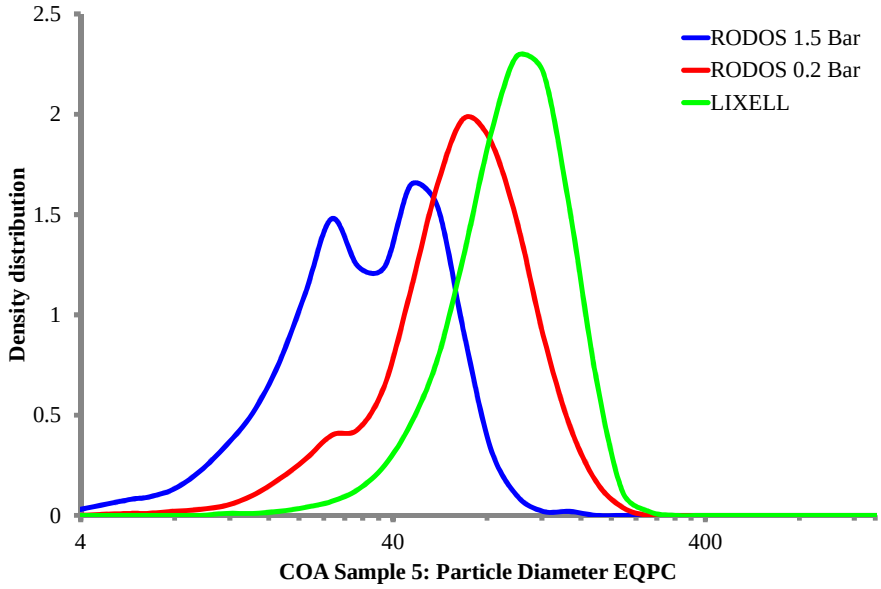

Figure 4-6: QICPIC EQPC distributions obtained for COA sample 5 with varying dispersion method.

The volume distribution plots for Avicel and COA are shown in Figure 4-7; equivalent sphere (EQPC) data is shown in a) and b), and Feret Max data in c) and d), respectively.

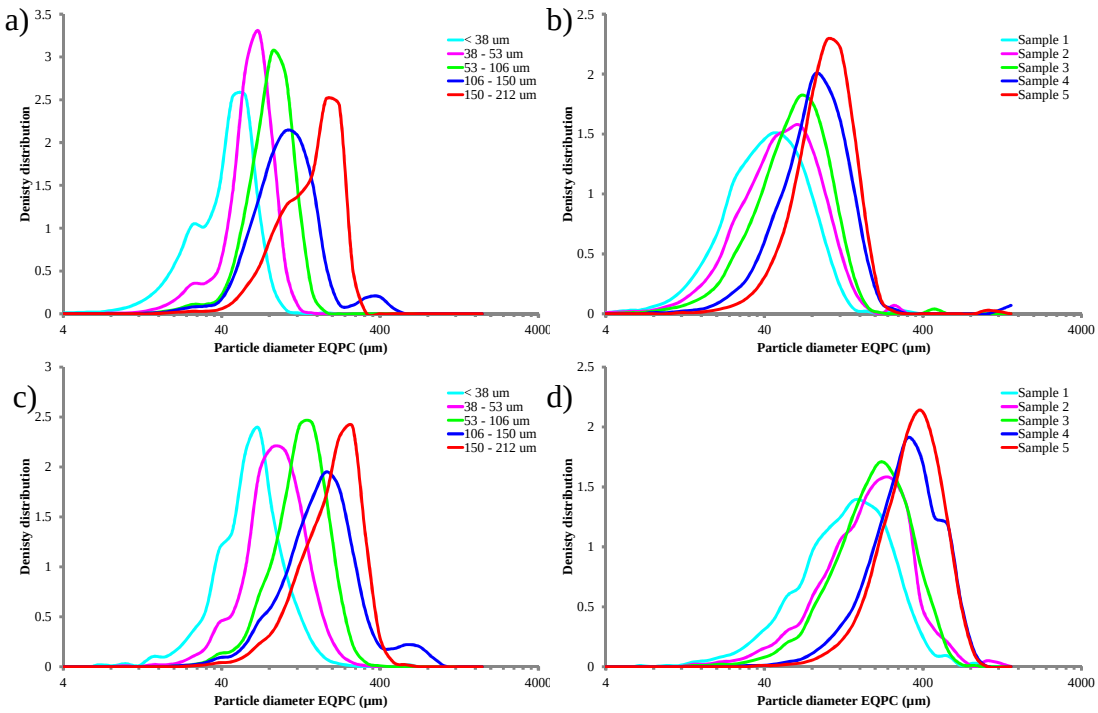

Figure 4-7: QICPIC volume distributions for a) EQPC of Avicel fractions, b) Feret Max of Avicel fractions, c) EQPC of COA samples, d) Feret Max of COA samples.

The EQPC data for both Avicel and COA display the same increasing trend as with the laser scattering methods as expected and can be directly compared with LD measurements. From Tables 1-1 and 1-2, the d (0,5) QICPIC measurements for both materials display an excellent correlation with LD, although, the QICPIC EQPC diameters are systematically higher than the equivalent LD measurement. With QICPIC, the EQPC value given is equal to the diameter of a spherical particle with the same area as the projected particle measured, whereas for LD measurements, the diameter given is that of a sphere with the same diffraction pattern as the measured one. For granular Avicel particles, it was expected that the LD and QICPIC measurements would be in closer agreement to that obtained, however, inspection of the Feret Max data implies that the particles present some anisotropic character. A significant advantage of digital imaging techniques over laser scattering is the ability to investigate more thoroughly the particle size and shape data than is possible from

the given distribution and associated statistics. By analysis of the individual particles in the "QICPIC particle gallery", the shape of each particle measured can be analysed, and further, filters can be set in order to probe user defined problems such as contamination or investigation of a single particle shape in a blend. Figure 4-8 shows an example gallery for the Avicel fraction 106 – 150 µm and demonstrates some anisotropy in the Avicel particles. It is known that LD measurements do not give a quantitative measure for non-spherical particles and therefore the underestimation of the Avicel fractions is not surprising.

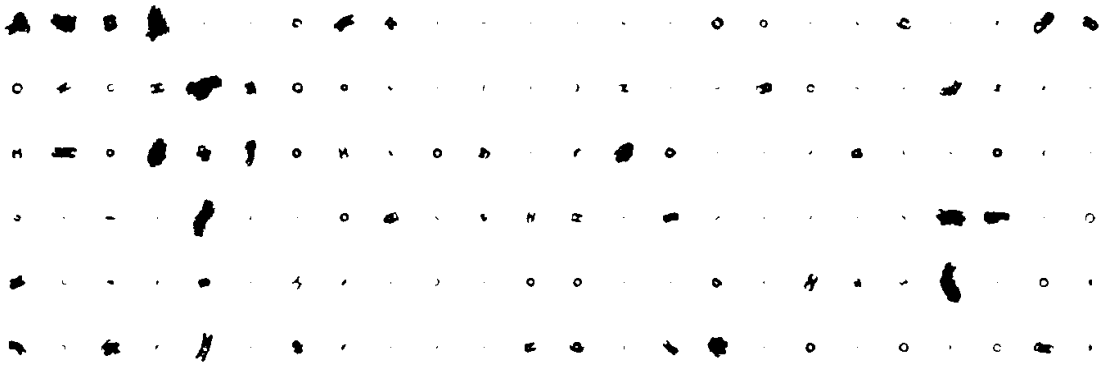

Figure 4-8: QICPIC particle gallery for Avicel fraction 106 – 150 µm.

For needle-shaped COA, the deviation in the EQPC data from the LD data is difficult to compare. As already discussed, the generation of a scattering pattern for a needle is dependent on the orientation of the needle when diffraction occurs. For image analysis, orientation is not a factor as the area used for the EQPC calculation is based on the number of pixels taken up on the camera for any given particle. What is evident, however, is that the use of the EQPC diameter is not ideal for needles and that a more appropriate diameter such as Feret Max should be used. When the EQPC distribution data for COA is compared with the Feret Max distribution data, a significant shift to larger dimensions is observed in the latter. This is because the Feret Max diameter is the longest dimension of a measured particle between two parallel tangents and does not involve a calculation to give an equivalent diameter like in EQPC measurements. Therefore, for changes in particles such as needles where the shortest diameter (Feret Min) does not vary significantly from particle to particle, Feret Max gives the best description of the distribution. This demonstrates

that the QICPIC EQPC, equivalent sphere LD and FBRM CLD data should only be considered as a qualitative description for analysis of needles as they are inaccurate representations of the actual needle length. This is highlighted in Figure 4-9 where an example image of COA is shown with the EQPC, Feret Max and Feret Min dimensions noted.

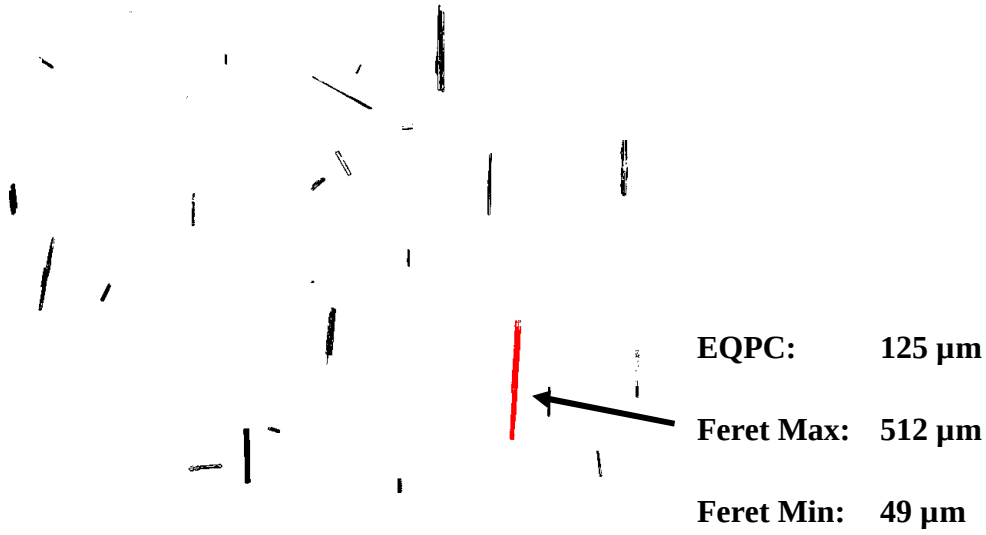

Figure 4-9: Digital image of COA particles in QICPIC analysis software. The EQPC, Feret Max and Feret Min dimensions are given for the marked red particle.

The Feret Min diameter was also investigated for the COA particles, however, a potential limitation of digital image analysis was encountered when this was performed. Overlap of very few needle-shaped particles (with respect to the total particle count) can have a significant effect on the distribution obtained when the volume distribution is considered. When overlap occurs, the dimension which is actually the Feret max of the shorter needle is measured as the Feret Min of the larger one resulting in a significantly increased value. When the Feret Max dimension is evaluated, the shorter needle is disregarded by the analysis software and thus is not problematic.

To remove overlapping particles from affecting the Feret Min distribution, filters can be applied so that particles with a Feret Min greater than a user defined dimension

are disregarded resulting in a more representative distribution. However, in order to apply these filters with confidence, a pseudo Bayesian approach must be applied. The use of Bayesian statistics applies prior knowledge to a data set in order to determine the probability of a given result; in this case, the prior knowledge applied is that the needle width is typically less than 100 µm (from imaging microscopy and previous imaging experiments (not reported)).

Examples of overlapping particles and the Feret Min COA volume distribution for Sample 4, with and without a filter at 100 µm, are shown in Figure 4-10 and 4-11, respectively.

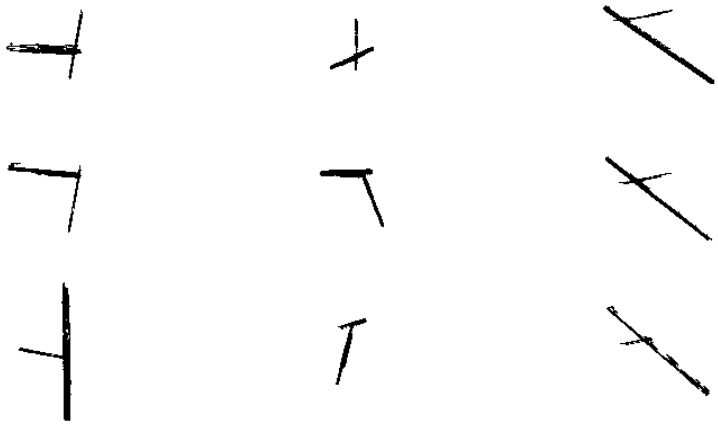

Figure 4-10: Examples of overlapping particles from the QICPIC particle gallery for COA Sample 4 (Filter set at Feret Min ≥ 100 µm).

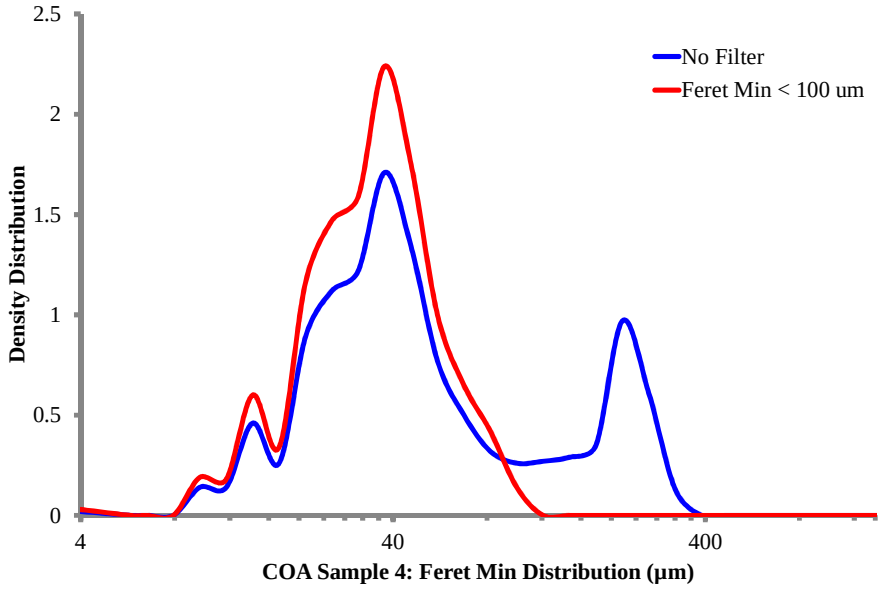

Figure 4-11: Feret Min volume distribution data for COA Sample 4 a) no filter and b) Feret Min ≤ 100 µm.

With QICPIC image analysis, one pixel on the CCD camera is equal to 1 μm^2 (with the optical setup used for this analysis), it follows that a threshold should be determined for the analysis of Feret Min data that constitutes the minimum number of filled pixels required to be considered a particle. Therefore, a second filter was added to the analysis of Feret Min data that removed particles with a Feret Min length less than 5 µm (corresponding to 5 pixels in width).

The filtered Feret Min distributions from QICPIC were compared to the CLD distributions obtained by FBRM. Due to the orientation of needle-shaped particles for FBRM measurements, the un-weighted CLD should, in theory, be comparable to the QICPIC Feret Min data for COA. For direct comparison, the number distribution for the QICPIC data was calculated. The number distributions for the Feret Min COA data are shown in Figure 4-12 followed by the d (0,5) data for both COA and FBRM in Table 4-3.

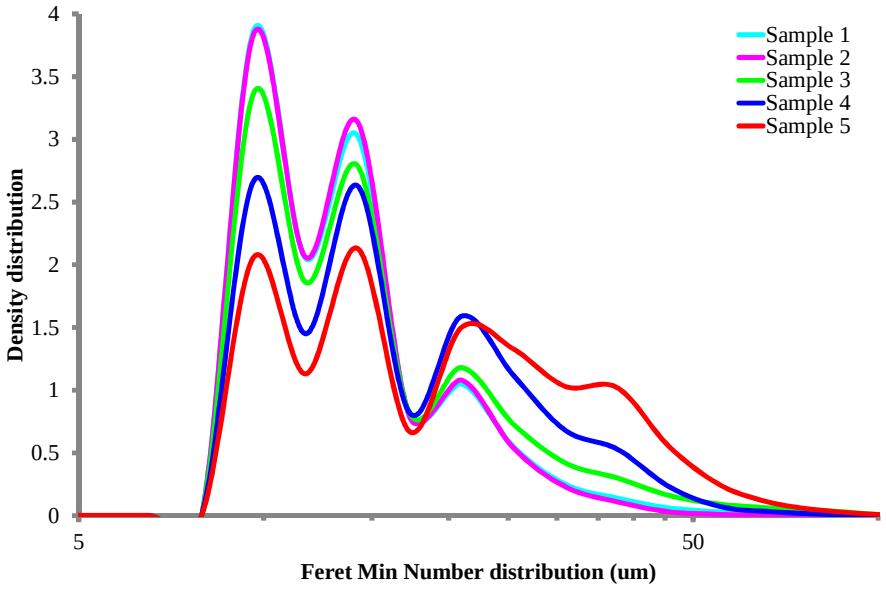

Figure 4-12: QICPIC Feret Min number distributions for COA samples 1 – 5.

Table 4-3: d (0,5) values for FBRM CLD and QICPIC Feret Min number distributions for COA samples.

Sample	FBRM/ µm	QICPIC/ µm
1	12	13
2	12	13
3	14	14
4	18	15
5	22	19

The d (0,5) Feret Min data for the COA needles showed very good agreement with the un-weighted FBRM CLD d (0,5) data discussed previously. This agrees with the hypothesis that average needle thickness increases with increasing needle length for COA particles and shows that FBRM data is in fact a measure of the needle thickness when samples are suspended in solution. Thus, the Feret Min data for COA needles shows that the FBRM CLD can be used as an indirect qualitative measurement of average needle length provided the thickness increases with needle length.

4.3.7 Particle Insight

Particle Insight (PI) is an analogous technique to QICPIC, however only wet dispersion of the particles was possible. With PI measurements, the Feret Max distribution is given as a number distribution rather than a volume distribution as is standard with QICPIC. As already discussed, number distributions give a heavier weighting to fine particles meaning that larger particles have far less of an effect on the distribution. Furthermore, The PI software has much smaller bin sizes than the other techniques and therefore it appears much noisier than other particle size analysis techniques (it is not known if the bin sizes can be altered). The PI Feret Max number distributions for the Avicel and COA fractions are shown in Figure 4-13.

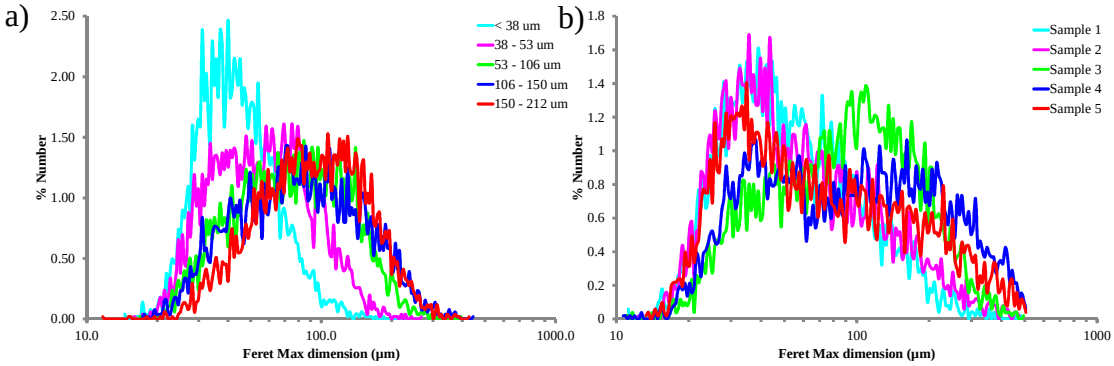

Figure 4-13: PI Feret Max number distributions for a) Avicel fractions and b) COA samples.

For Avicel, the Feret Max distributions shift to larger particle sizes with increasing fraction size. This means that the number of coarser particles increased as size fraction was increased. With COA particles however, the distributions obtained were not as expected based on previously evaluated data. Here, an increase in the number of longer needles is observed for samples 1 – 4, however, sample 5 does not continue to display an increase in the number of longer needles, but rather, an increase in the number of shorter needles. As mentioned previously, the PI software used disregarded particles from analysis that had Feret Max dimensions greater than 500 µm. Samples 4 and 5 have a large proportion of needles greater than 500 µm in length (as shown by QICPIC measurements) that would have been disregarded; therefore, the number distributions for the longer needle samples are not necessarily

reliable for analysis. For this reason, PI data was considered unsuitable for analysis of long needles and will not be discussed further.

4.3.8 PIMS

PIMS is a technique developed at GSK specifically for analysis of needles. The proprietary software is thus developed with needles in mind and automatically generates a report with a number distribution based on the length dimension of a bounding rectangle of the particles, circularity data, and a length vs. circularity plot. The user can set bin sizes for the number distribution, however cannot alter any other of the parameters other than the magnification of the particles. This makes PIMS the least versatile of the digital imaging techniques discussed; however, it does not mean that it should be disregarded as unsuitable for analysis. Figures 4-14 a) and b) shows the shape vs. circularity plots for the Avicel fractions and COA samples, respectively.

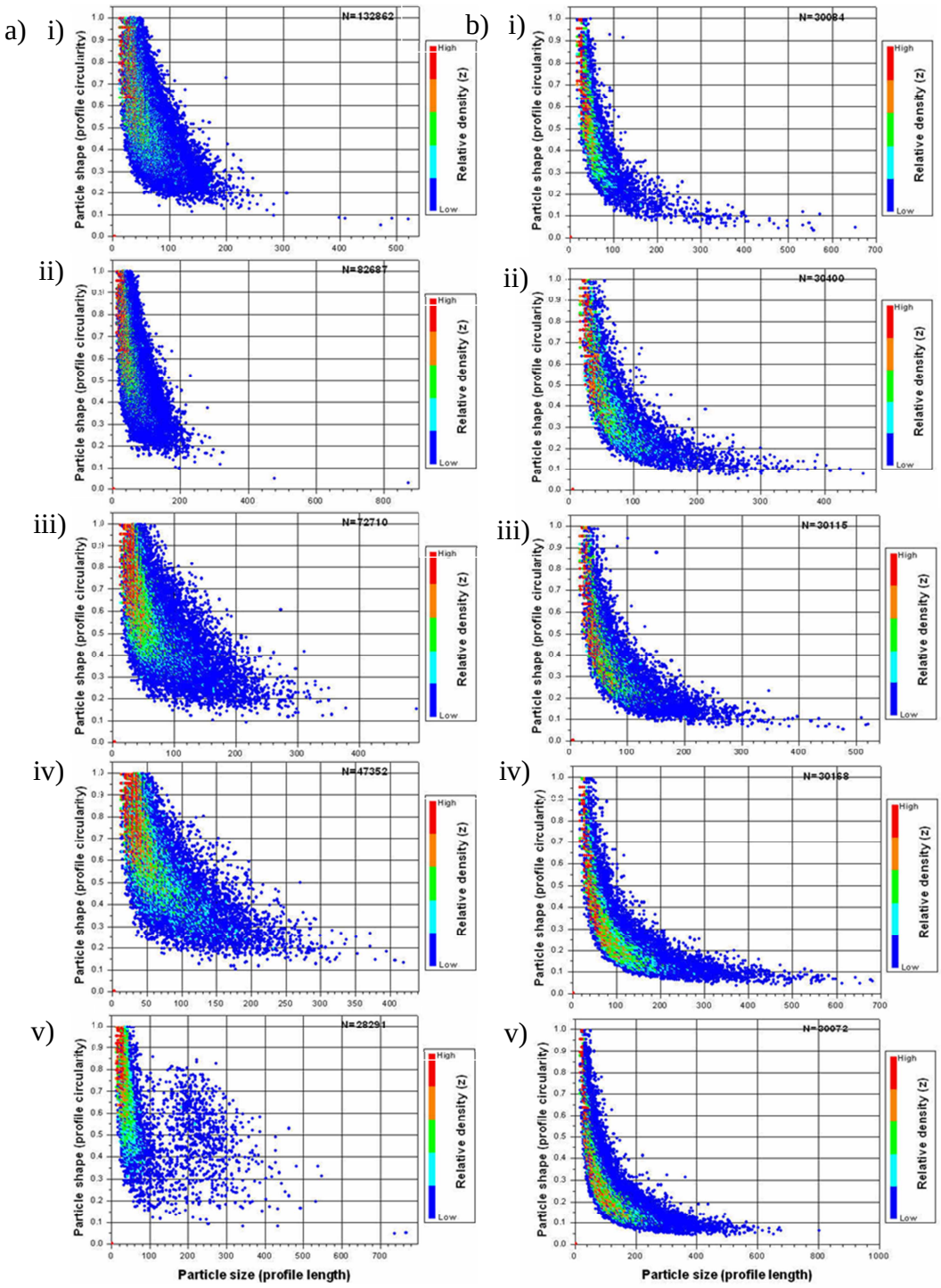

Figure 4-14: PIMS Particle shape vs. particle length data for a) sieved fractions of Avicel: i) <38 µm, ii) 38 – 53 µm, iii) 53 – 106 µm, iv) 106 – 150 µm, v) 150 – 212 µm and b) experimentally obtained fractions of COA: i) Sample 1, ii) Sample 2, iii) Sample 3, iv) Sample 4 , v) Sample 5.

The PIMS analysis for both Avicel and COA show that there is a large number of fine particles present in all samples, as can be seen by the red areas of high density in all the plots. This is common in most samples as fine particles are more adhesive than larger particles and can stick to larger particles during processing; when dispersed, however, these particles can break free and are then counted. Conversely, when a large number of fine particles are observed during image analysis, it is essential to consider the size of the particles in relation to the resolution of the measurement (i.e how many pixels constitute a particle). For example, with PIMS, a 10 µm particle is equal to only a few pixels in an image, making the measurement of fine particles challenging. Filters can be set in the software (although not done for this data set) to ensure that a minimum number of pixels are required for a particle to be counted.

PIMS measurements use particle recognition algorithms to identify particles and then measure those particles based on their length and their width. Therefore these measurements are ideally suited to needle-shaped particles. In Figure 4-14, particle length is plotted against particle circularity for the measured samples, for granular Avicel particles (Figure 4-14 a) i) – v)) there are areas of high density of highly circular particles, and as the particle size fractions increases, there are many irregular shaped particles (circularity ~ 0.3 – 0.7) as would be expected based on previous image analysis results. For COA (Figure 4-14 b)), there are also a high number of fine particles with high circularity for all samples; however, in addition, there is the presence of many particles with low circularity and a high length as expected for needle-shaped particles. For PIMS measurements, the length (number distribution) and circularity of the particles can also be examined individually as demonstrated for COA particles in Figure 4-15.

a) b)

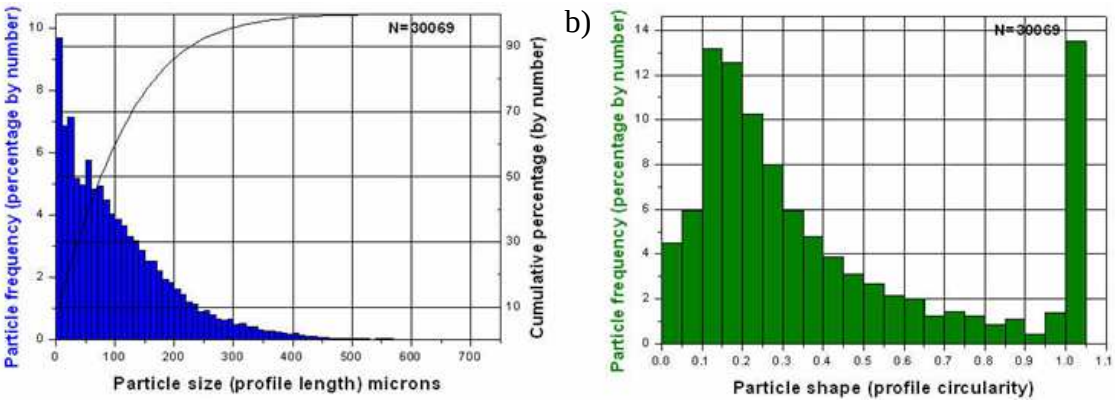

Figure 4-15: PIMS analysis: a) Length based number distribution and b) particle circularity for COA particles (sample 5).

It has been demonstrated that dynamic image analysis has many advantages over scattering based measurements in that particles can be directly viewed and analysed by the operator. Particle geometry is by no means a limitation with modern computing power, allowing for many shape and size parameters to be calculated almost instantaneously. A limitation of dynamic image analysis for PIMS measurements, however, is the depth of field. In dynamic image analysis, a 2 dimensional image is recorded of a 3 dimensional system which can lead to poor resolution of particles that are not in focus. It was noted with the Avicel measurements using PIMS that many of the coarser particles were ignored as being out of focus meaning that the calculation of the number distributions may have been skewed. Nonetheless, PIMS was a useful technique for the analysis of needles.

4.4 Summary and Conclusions

Five particle size analysis techniques have been evaluated with respect to particle shape by measuring increasing size ranges of granular and needle-shaped particles. Sieving of both particle geometries and subsequent particle size analysis highlighted that sieving to obtain particle size ranges is effective for granular shaped particles but not for needle-shaped particles. This was highlighted by microscopy images and particle size analysis. Size ranges of needle-shaped particles were obtained by exposing samples to different amounts of shear in an agitated vessel. The performance of all five techniques was evaluated for both particle geometries and

each technique was shown to successfully differentiate between different particle size ranges of both geometries. Whereas dynamic image analysis techniques had advantages over laser scattering techniques for needle-shaped particles, due to the ability to evaluate a sample based on needle length rather than an equivalent sphere or CLD, both laser scattering techniques gave a good indication of a change in particle size range for these shaped particles. Although not allowing for quantitative analysis of the particles, the laser scattering techniques did allow a quick, cheap (and in the case of FBRM *in situ*) indication of a change in particle size distribution, if not particle shape. The analysis of the QICPIC data for Avicel and COA, however, emphasized the importance of digital image analysis for evaluation of particle size with respect to particle shape.

For granular Avicel, image analysis showed that there was some anisotropy present in the particles, which resulted in lower median values than expected in the LD data, however, the deviation between the two techniques was small compared to that of needle-shaped COA particles. For COA particles, digital image analysis showed that the d (0,5) values obtained by LD were not representative of the length of the needles and that the Feret Max diameter was more suitable to describe the particles. In addition, the Feret Min diameter was comparable to FBRM CLD showing that needle thickness increased with increasing needle length. For full quantitative analysis of a particle shape and size distribution especially for needle-shaped particles, it is recommended that digital image analysis is performed based on the results in this text.

The main conclusions in summary were:

- Both LD and FBRM provided good qualitative analysis of both granular and needle-shaped particles.
- LD was only quantitative for spherical particles as demonstrated by QICPIC EQPC analysis of Avicel where small deviations from sphericity lowers the LD median diameters.

- The Feret Max dimension is the best measurement of needles as it generates the best data for needle length.
- FBRM data correlates well with the Feret Min data from QICPIC.
    - With these particular measurements, it is known that the average Feret Min increases as average needle length increases

4.5 References

1. B. Shekunov, P. Chattopadhyay, H. Tong and A. Chow, *Pharm. Res.*, 2007, **24**, 203-227.

2. Malvern, *http://www.malvern.com/LabEng/products/Mastersizer/ms2000e/mastersizer 2000e.htm*, November 2011.

3. D. J. Brown, K. Alexander and J. Cao, *Part. Part. Syst. Char.*, 1991, **8**, 175-178.

4. A. Beekman, D. X. Shan, A. Ali, W. G. Dai, S. Ward-Smith and M. Goldenberg, *Pharm. Res.*, 2005, **22**, 518-522.

5. D. L. Syvitski and E. W. H. Hutton, *Priciples, Methods and Applications of Particle Size Analysis*, Cambridge University Press, Cambridge, 1991.

6. H. Muhlenweg and E. D. Hirleman, *Part. Part. Syst. Char.*, 1998, **15**, 163-169.

7. Z. Ma, H. G. Merkus, J. G. A. E. de Smet, C. Heffels and B. Scarlett, *Powder Technol.*, 2000, **111**, 66-78.

8. N. Gabas, N. Hiquily and C. Laguérie, *Part. Part. Syst. Char.*, 1994, **11**, 121-126.

9. S. Endoh, Y. Kuga, H. Ohya, C. Ikeda and H. Iwata, *Part. Part. Syst. Char.*, 1998, **15**, 145-149.

10. E. D. Hirleman, *Part. Part. Syst. Char.*, 1988, **5**, 57-65.

11. A. P. Tinke, A. Carnicer, R. Govoreanu, G. Scheltjens, L. Lauwerysen, N. Mertens, K. Vanhoutte and M. E. Brewster, *Powder Technol.*, 2008, **186**, 154-167.

12. A. P. Tinke, K. Vanhoutte, R. De Maesschalck, S. Verheyen and H. De Winter, *J. Pharm. Biomed. Anal.*, 2005, **39**, 900-907.

13. A. P. Tinke, K. Vanhoutte, F. Vanhoutte, M. De Smet and H. De Winter, *Int. J. Pharm.*, 2005, **297**, 80-88.

14. A. Hagsten, C. Casper Larsen, J. Møller Sonnergaard, J. Rantanen and L. Hovgaard, *Powder Technol.*, 2008, **183**, 213-219.

15. N. Stevens, J. Shrimpton, M. Palmer, D. Prime and B. Johal, *Meas. Sci. Technol.*, 2007, **18**, 3697-3706.

16. FDA, *Guidance for Industry; PAT - a framework for innovative pharmaceutical development, manufacturing and quality assurance*, 2004.

17. E. Kougoulos, A. G. Jones, K. H. Jennings and M. W. Wood-Kaczmar, *J. Cryst. Growth*, 2005, **273**, 529-534.

18. W. Yu and K. Erickson, *Powder Technol.*, 2008, **185**, 24-30.

19. A. Vaccaro, J. Sefcik and M. Morbidelli, *Part. Part. Syst. Char.*, 2007, **23**, 360-373.

20. M. Z. Li and D. Wilkinson, *Chem. Eng. Sci.*, 2005, **60**, 3251-3265.

21. M. Z. Li, D. Wilkinson and K. Patchigolla, *Chem. Eng. Sci.*, 2005, **60**, 4992-5003.

22. N. K. Nere, D. Ramkrishna, B. E. Parker, W. V. Bell and P. Mohan, Transformation of the chord-length distributions to size distributions for nonspherical particles with orientation bias, presented in part at the AIChE Annual Meeting 2005, Cincinnati, OH, 2007.

23. C. Lindenberg, M. KraÌˆttli, J. Cornel, M. Mazzotti and J. r. Brozio, *Cryst. Growth Des.*, 2009, **9**, 1124-1136.

24. Z. Q. Yu, P. S. Chow and R. B. H. Tan, *Org. Process Res. Dev.*, 2008, **12**, 646-654.

25. S. G. S. Cesur, *Cryst. Res. Technol.*, 2008, **43**, 720-728.

26. D. O'Grady, B. O'Sullivan, J. Schoell, T. Redman and M. Barrett, *Chim. Oggi-Chem. Today*, 2008, **26**, 22-24.

27. X. S. Liu, D. Sun, F. Wang, Y. J. Wu, Y. Chen and L. H. Wang, *J. Pharm. Sci.*, 2011, **100**, 2452-2459.

28. J. Huang, G. Kaul, J. Utz, P. Hernandez, V. Wong, D. Bradley, A. Nagi and D. O'Grady, *J. Pharm. Sci.*, 2010, **99**, 3205-3212.

29. T. Narvanen, T. Lipsanen, O. Antikainen, H. Raikkonen, J. Heinamaki and J. Yliruusi, *J. Pharm. Sci.*, 2009, **98**, 1110-1117.

30. A. Tok, X. P. Goh, W. Ng and R. Tan, *AAPS PharmSciTech*, 2008, **9**, 1083-1091.

31. C. Fischer, M. Peglow and E. Tsotsas, *Chem. Eng. Sci.*, 2011, **66**, 2842-2852.

32. D. Petrak, *Part. Part. Syst. Char.*, 2002, **19**, 391-400.

33. S. Almeida-Prieto, J. Blanco-Mendez and F. J. Otero-Espinar, *J. Pharm. Sci.*, 2004, **93**, 621-634.

34. S. Almeida-Prieto, J. Blanco-Mendez and F. J. Otero-Espinar, *J. Pharm. Sci.*, 2006, **95**, 348-357.

35. C. Andres, P. Bracconi, P. Reginault, P. Blouquin, M. H. Rochat and Y. Pourcelot, *Int. J. Pharm.*, 1998, **167**, 129-138.

36. N. Laitinen, O. Antikainen, J. P. Mannermaa and J. Yliruusi, *Pharm. Dev. Technol.*, 2000, **5**, 171-179.

37. N. Laitinen, O. Antikainen, J. Rantanen and J. Yliruusi, *J. Pharm. Sci.*, 2004, **93**, 165-176.

38. N. Laitinen, O. Antikainen and J. Yliruusi, *Eur. J. Pharm. Sci.*, 2002, **17**, 217-227.

39. A. Realpe and C. Velazquez, *Powder Technol.*, 2003, **134**, 193-200.

40. C. Washington, *Particle Size Analysis in Pharmaceutical and other Industries*, Ellis Horwood Ltd, Chinchester, 1992.

41. W. L. Yu and B. C. Hancock, *Int. J. Pharm.*, 2008, **361**, 150-157.

42. S. B. Abebe, X. Z. Wang, R. Li, K. J. Roberts and X. Lai, *Powder Technol.*, 2008, **179**, 176-183.

43. P. A. Larsen and J. B. Rawlings, *Aiche J.*, 2009, **55**, 896-905.

44. P. A. Larsen, J. B. Rawlings and N. J. Ferrier, *Chem. Eng. Sci.*, 2006, **61**, 5236-5248.

45. L. L. Simon, Z. K. Nagy and K. Hungerbuhler, *Chem. Eng. Sci.*, 2009, **64**, 3344-3351.

46. A. S. Zidan, Z. Rahman and M. A. Khan, *Aaps J.*, 2010, **12**, 254-262.

47. R. Fartaria, N. Javid, R. A. Pethrick, J. J. Liggat, J. Sefcik and M. B. Sweatman, *Soft Matter*, 2011.

48. O. Glatter and O. Kratky, *Small angle X-ray scattering*, Academic Press London, 1982.

5. Studies in powder drying using *in situ* Raman spectrometry and particle size analysis

5.1 Introduction

Drying of powders is a common unit process in many pharmaceutical manufacturing processes and is one of the final steps in active ingredient production, usually following the filtration step performed after crystallisation. Crystallisation is ideally a highly controlled process which aims to obtain a product with desired shape, size distribution, and purity. Proper control of these properties ensures that the flow and compaction properties of a material are correct for downstream processes such as blending, granulation or tableting and that essential attributes like the bioavailability is correct for the intended action in the body.[1] The impact of the drying process on crystal parameters is thus of great importance to the success of a manufacturing campaign, however at present, this is not well understood and poorly controlled. Complications can arise such as: attrition, where a reduction of particle size occurs; agglomeration or aggregation/ balling, where an increase in particle size is observed; over drying; and hydrate or polymorph changes. In many cases, these effects can lead to the batch being reworked or lost entirely due to the particle characteristics no longer being suitable for the intended use.

Attrition is a significant problem in agitated filter driers as particles are subjected to shear while being dried. This shear force can cause a reduction in the size of the particles or a change in the particle geometry depending on the shear sensitivity of the material. These changes can occur, depending on the nature of the particles, by two main methods. There is chipping, where small sections of the particles break off to form a fine dust, which not only leads to the problems described previously, but also generates a dust hazard in a manufacturing area. The second method is particle breakage or fragmentation, which is more common in needle-shaped particles. Here, the particles break down into smaller particles during a process; this may also produce fines which are similar to the method of chipping but represents less of a hazard and is less common. The processes which lead to particle attrition have been

studied extensively by Ghadiri *et al.*,[2-5] and these authors have also recently began to investigate the effects of particle drying and its relationship with attrition. [6]

Lekhal *et al.* published two studies investigating attrition in drying processes, the first describes a potassium chloride (cubic crystals) and water system and the second, an L-threonine (needles) and water system.[7, 8] The authors studied the effects of temperature, agitation rate and pressure on drying time and final crystal properties in a 800 ml double jacketed vessel. They agreed in some respect with the work of Ghadiri *et al.* in that attrition was primarily caused by a result of shear; however, they also noted that agglomeration was a competing process in their system as a result of capillary forces in the presence of liquid. The authors went on to describe that the extent of attrition was correlated to the agitation rate, although, lower drying times resulted in less attrition as the particles were exposed to less shear from the impeller. Thus, all three factors investigated contributed to the extent of attrition in the system, as all three had direct effects on drying time.

Typically, in the pharmaceutical industry, a batch will be dried for a length of time under a set of conditions defined by a regulatory filing, with product quality tested off-line in a quality control lab. There are significant disadvantages to this strategy, however, namely the time lag between extracting a sample, transfer to the laboratory, analysing the sample, and conveying the pass/ fail result to the operators. This represents a significant loss in time in determining if the sample is dry or not; further, if the batch is still wet it needs to be dried for a longer period of time and retested. Also, if the particle characteristics are found to have changed, there are implications for additional energy and materials costs, as well as a delay in manufacturing. There is also the fact that no in-process information is gained while the particles are being dried, so if there are any special causes of variation in a specific batch, they will remain unknown to an operator until it is too late to rectify the problem.

The Food and Drug administration's "PAT initiative" in 2004[9] led to a boom in pharmaceutical companies increasing their investment in process analytical technology (PAT). The aim was to improve process understanding and control, with the ultimate goal of improving "right first time manufacturing" and building "quality

by design". Along with this came a significant drive from instrument vendors to provide better, more robust process analysers, with a wider range of sample interfaces at more competitive prices. The combined effort has seen many successful applications of PAT arise in unit operations such as powder blending,[10-14] crystallisation,[15-17] granulation and fluidised bed drying,[18, 19] and tablet analysis[20] to name a few.

There appeared to be a gap in the literature, however, when the application of PAT for drying was investigated. Of course, it is widely known that pharmaceutical companies are sometimes reluctant to publish some of the work they do with PAT out of a fear of losing a competitive advantage, however, the examples in the literature that do exist focus primarily on monitoring the drying curve in order to prevent over drying. For example, Tewari *et al.* have demonstrated that MIR can be used to monitor the solvent concentration in drying off gas and used this information to describe the drying curve in a cellulose and isopropyl alcohol system.[21] For this study, a tray drier was used and thus attrition of the particles was not considered. Burgbacher and Wiss, described a method to monitor the drying curve in an agitated filter drier by near-infrared spectrometry (NIRS), displaying a good agreement between *in situ* NIR data and their chosen reference analysis (in this case, Karl Fischer titration or GC headspace analysis depending on the solvent).[22] A diffuse reflectance NIR probe was placed flush with the internal wall of a drier and the process contained an active substance and two organic solvents. Partial least squares (PLS) regression models were developed to successfully determine the individual concentrations of both solvents in the system throughout the process by recording an NIR spectrum once every 10 min. In doing this, the authors demonstrated that a possible reduction in cycle time of approximately 50% was attainable for the specific process. Although success was achieved in both studies with respect to the drying curve and cycle time, a vast amount of spectral information was overlooked regarding the particles. Furthermore, in both studies there is no mention of whether or not attrition was a problem, however, by measuring the drying cake directly there would be scope to investigate whether the particles undergo any changes throughout the process.

NIRS is known to contain particle size information, however, highly convoluted spectra, and matrix effects can make access to such information extremely challenging, especially for complex processes such as powder drying. NIR has been shown to successfully demonstrate particle size information in other unit operations in the pharmaceutical industry.[11, 12, 23] Other spectroscopies are known to demonstrate particle size effects also, for example, Carson *et al.* demonstrated that changes in frequency of the peak position arising from particle collisions with a vessel wall were inversely proportional to a change of particle size with *in situ* acoustic emission spectroscopy.[24]

Another example is Raman spectrometry, with process Raman instruments rapidly becoming one of the most versatile technologies available in the PAT tool kit. The main advantage of Raman over NIR systems is that spectra generally consist of sharp, well resolved peaks, often allowing univariate rather than multivariate calibration, which is nearly always necessary with NIRS. Furthermore, developments in NIR lasers for Raman spectrometry have made fluorescence less of a problem, and with more efficient detectors coupled with wide illumination non-invasive probes, Raman scattering molecules have become easier to analyse requiring much shorter integration times to collect a spectrum. This has resulted in Raman spectrometry being applied to a variety of applications, including crystallisation monitoring,[1, 16, 17, 25] and tablet content uniformity.[20, 26]

Perhaps more appropriately, Walker *et al.* studied a fluidised bed granulation process and found that Raman spectrometry demonstrated accurate correlation with independent granulation experiments describing particle size distribution analysis.[18] Raman spectra were collected of glass beads in a fluidised bed granulation process with the probe mounted using a bespoke framework around the fluid bed drier. The change in Raman signal was monitored at three different positions in the bed and the signal showed a correlation to an increase in granule size. Here, an increase in granule size resulted in a decrease in Raman signal as the process was carried out. Furthermore, the distribution of particle density in the bed was identified, based on

the intensity of the Raman signal, where an increase in Raman signal was observed for denser areas of particles.

Raman spectrometry, also offers another significant advantage over NIR in that there is the potential to monitor polymorphism changes that can occur in some drying processes. A change in polymorph is known to cause a change in the Raman spectrum of a compound and there are examples in the literature where this has been successfully utilised to monitor crystallisation processes.[16, 17, 25] These studies and others [22] highlight the potential for monitoring the physical changes that particles undergo during a process in pharmaceutical manufacturing by *in situ* Raman spectrometry.

Although there are increasing examples in the literature of spectroscopic techniques being used to monitor *in situ* particle size during a process, there are also *in situ* particle size analysis techniques. However, there are many challenges for *in situ* particle size analysis that, at present, make *in situ* monitoring of particles very difficult during all stages of drying. For example, currently for laser diffraction methods, the two main dispersion methods for both laboratory and process measurements require the particles to either be completely dry so that they can be dispersed by a differential in air pressure, or be at very low concentrations in a wet dispersion to prevent multiple scattering effects in a recirculation loop. This does not translate well to drying where the particles are in a partly wet state for most of the operation and therefore on-line sample presentation to an external analyser would be very difficult and expensive to configure.

In situ imaging of a low concentration of particles in a solvent has become very popular in crystallisation monitoring, as particle size can be monitored and physically seen by the human eye on a monitor.[27, 28] In the case of drying, however, image analysis is not suitable with current technology because it is difficult to differentiate between many particles in a 2d image, and therefore, software cannot evaluate the particles in view.

It seems there is most potential for success in drying, with techniques such as Lasentec's focused beam reflectance measurement (FBRM) and Malvern's newly released PARSUM system. FBRM was originally designed for crystallisation monitoring and initial probes were unsuitable for drying monitoring due to major probe fouling and saturation. However, customer demand has led to the release of improved probes with "window wipers" that prevent probe fouling and short measurement times that prevent saturation. This has led to FBRM being used to monitor processes other than crystallisation such as wet granulation.[29, 30] The Malvern PARSUM system is an insertion probe like the FBRM but rather that cleaning the measurement window during analysis, compressed air is used to ensure that particles only enter the measurement zone during analysis.[31]

Although techniques such as FBRM and PARSUM are required for full particle analysis, *in situ* spectroscopic techniques offer some advantages in the monitoring of powder drying if identification of attrition or agglomeration is required. This arises because in addition to providing an indication of a change in particle size, Raman spectrometry, for example, can provide molecular identification, allow generation of a drying curve, and detect changes in polymorphism and state of hydration.

In this study, non-invasive *in situ* Raman spectroscopy was used to monitor the drying process of methanol from cellosbiose octaacetate. A design of experiments approach was used to investigate the effects on particle attrition of three variables that are key in a drying process namely: agitation type, percentage solvent loss on drying and jacket temperature. Off-line Raman analysis of the particles and particle size analysis (by laser diffraction, QICPIC and PIMS) were used as reference measurements for the study.

5.2 Experimental

5.2.1 Equipment

5.2.1.1 Lab scale agitated filter drier

The design of the drier was based on process scale agitated filter driers and has an internal diameter of 15 cm (Figure 3.1). The agitator has two angled retreat blades positioned at 180°. The motor was an IKA RW 20 digital (IKA works, Wilmington, USA) positioned at 90° to the vessel and drove the agitator through a 10 : 1 gear box at a mixing speed of 20 rpm. The vessel was made of glass with an oil jacket meaning that spectroscopic observations could be made using either direct insertion probes or non-invasive probes through a glass window in the lid. A constant flow of oil at either 40 or 60 °C during the experiments ensured a constant jacket temperature. The base of the drier was connected to a vacuum pump and the vacuum was held between 50 – 100 mbar, monitored using a Pirani gauge (Edwards, Crawley, UK) in the line. Also in the vacuum line was a reservoir to collect excess solvent and a cold finger to trap any solvent in the line before reaching the pump. Dry powder was placed into the vessel before the lid was attached and sealed. Solvent was added to the vessel through one of the ports on the lid. The vessel was then sealed and the vacuum subsequently applied.

5.2.2 Materials

Cellobiose octaacetate (COA) was obtained from GSK (Tonbridge, Kent, UK) and has a needle shape with a high aspect ratio and only one known polymorph. COA was selected as a model compound to study as it has similar physical characteristics to many pharmaceutical active compounds, however, is not active and therefore requires no specific controls for handling in a laboratory. Methanol (Sigma-Aldrich, A5376, Dorset, UK) was used as the solvent for the study as this is used as the anti-solvent in the re-crystallisation of COA.

5.2.3 Raman spectrometry

A Kaiser Rxn 1 Raman spectrometer with P^{h}AT probe (Kaiser Optical systems, Ann Arbor, USA) was used to monitor the drying process non-invasively. The P^{h}AT probe has the laser beam optically expanded to give a 6 mm spot size, a working distance of 25.4 cm and a depth of field of 5 cm, and was directed at the process through a glass window in the lid of the vessel. The laser wavelength used was 785 nm produced by an Invictus diode laser operated at 400 mW at the source (equating to ~220 mW at the sample). A 12 channel charged couple device (CCD) detector cooled to -40 °C by a Peltier cooling system was also used. Daily diagnostic tests were performed (which measured relative peak intensity and peak area against known peaks from a cyclohexane standard) using the external sample compartment accessory for the instrument. Raman spectra were recorded using IC Raman software (Metler-Toledo, Columbus, USA) and exported as individual .SPC files to MATLAB version R2007b (Mathworks, Natick, USA) for analysis. Each Raman spectrum was recorded with a 10 s integration time with one spectrum recorded every 15 s. For all Raman experiments, the vessel was wrapped in aluminium foil to remove room and natural light from the spectra. 2 g sub-samples of COA were removed for off-line Raman analysis at the end of drying. The samples were placed in vials and analysed in triplicate (shaken and tapped between each measurement to introduce variability) using the P^{h}AT external sample compartment. A 6 mm spot size and 10 s integration time were used for this part of the study also.

5.2.4 Particle size analysis

Samples were also taken at the end of drying for particle size analysis. About 0.5 g of COA was extracted using a spatula and transferred into vials before being taken for particle size analysis.

5.2.4.1 Laser Diffraction

A Malvern Mastersizer 2000 (Malvern Instruments, Worcestershire, UK) was used to analyse the sub-sampled powder by laser diffraction. The samples were dispersed in 0.1% Tween 80 in water (Sigma-Aldrich, A5376, Dorset, UK) using a

Hydro2000SM cell. Powder was added to the cell until a laser obscuration (internal parameter of the instrument to prevent multiple scattering effects) of ~3% was reached. Laser diffraction measurements generate a variety of particle size data: the volume distribution, which is given in 100 logarithmically spaced size bins from 0.01 – 10,000 μm, and d (0,5), the particle diameter corresponding to 50% of the volume distribution, were used in this study. Other diameters such as d (0,1) and d (0,9) corresponding to 10% and 90% of the volume distribution, respectively, d (4,3), the volume weighted mean, and d (3,2), the surface weighted mean, are also generated but not discussed here.

5.2.4.2 QICPIC

Sympatec QICPIC image analysis was performed on the COA particles before and after drying using the LIXELL wet dispersion unit, and data was analysed using WINDOX 5 software (Sypmatec LTD, Bury, BL9 7BR). For wet dispersion measurements, powders were dispersed in 0.1% Tween 80 and water and were re-circulated through a flow cell using a peristaltic pump. WINDOX 5 software then performed an auto-focus on the particles in the flow before measurement was recorded. A pulsed light source is used to ensure that no motion blur of the particles occurred as they were imaged onto a CCD detector. Each measurement lasted for 30 s and the results quoted are an average of three measurements from the same sub-sample.

5.2.4.3 Particle Imaging Measurement Technique (PIMS)

PIMS has been developed in house at GSK Tonbridge and employs a stroboscopic pulsed light source to arrest particle motion for a camera to record images of particles in a flow cell. The camera is focused just inside the glass window of the cell. Images of particles are then analysed based on their length and circularity. The dispersant used was the same as for laser diffraction. The samples were dispersed using a low speed impeller and re-circulated through the flow cell using a peristaltic pump. A spatula tip of particles was added to 70 ml of dispersant and then each sample was analysed until the software had counted 30,000 “in focus” particles. The

data was exported to Origin software where proprietary algorithms developed at GSK were used to analyse the images based on needle length and width. Standard MATLAB functionality was then used to convert this information to give number distributions and circularity data. The software was calibrated daily using a saved image of a 100 μm grid for the lenses used. For these experiments, the instrument was set up to provide a magnification of x20.

5.2.5 Design of experiments methodology

The reason why attrition occurs in driers is currently not well understood in the pharmaceutical industry. For this reason, a design of experiments approach was used to probe the effects on drying time and extent of attrition of three key parameters in pharmaceutical drying processes, namely, agitation strategy, % solvent loss on drying (SLOD), and jacket temperature. All three parameters are known to influence drying times, however, their effects on the amount of attrition are not so well known. A 2-level full factorial design was performed to determine the effects of these parameters within the design space. In addition to this, two centre point experiments were carried out on each of the two categorical faces of the design. An overview of the low and high levels for each variable is given in Table 5-1.[32]

Table 5-1: Overview of low and high levels for the studied variables.

Variable	Units	Low	High	Cat/num
Agitation method	rpm	intermittent	Continuous	Categorical
%LOD	% v/w	50	100	Numerical
Jacket temp	ºC	40	60	Numerical

5.2.5.1 Monitoring the drying curve for COA – Methanol by non-invasive Raman spectrometry

300 g of COA was placed in the drier and the agitator speed was set to 20 rpm. The vessel lid was then attached and sealed. Raman measurements were collected for a given period of time to determine the signal expected from dry COA. Data collection

was paused to allow the addition of methanol through a port in the lid of the vessel. The powder was then continuously agitated for two minutes to mix the solvent well with the particles. After this addition of the solvent, the vessel was re-sealed and a vacuum applied (ranging between 50 – 100 mbar). Raman data collection was then resumed while the powder dried and ceased when the Raman signal had stabilised for a period of time.

5.3 Results and discussion

5.3.1 Monitoring of COA/ methanol drying curve by non-invasive Raman spectrometry

The Raman spectra of methanol and COA and a mixture of methanol and COA recorded during drying are given in Figure 5-1.

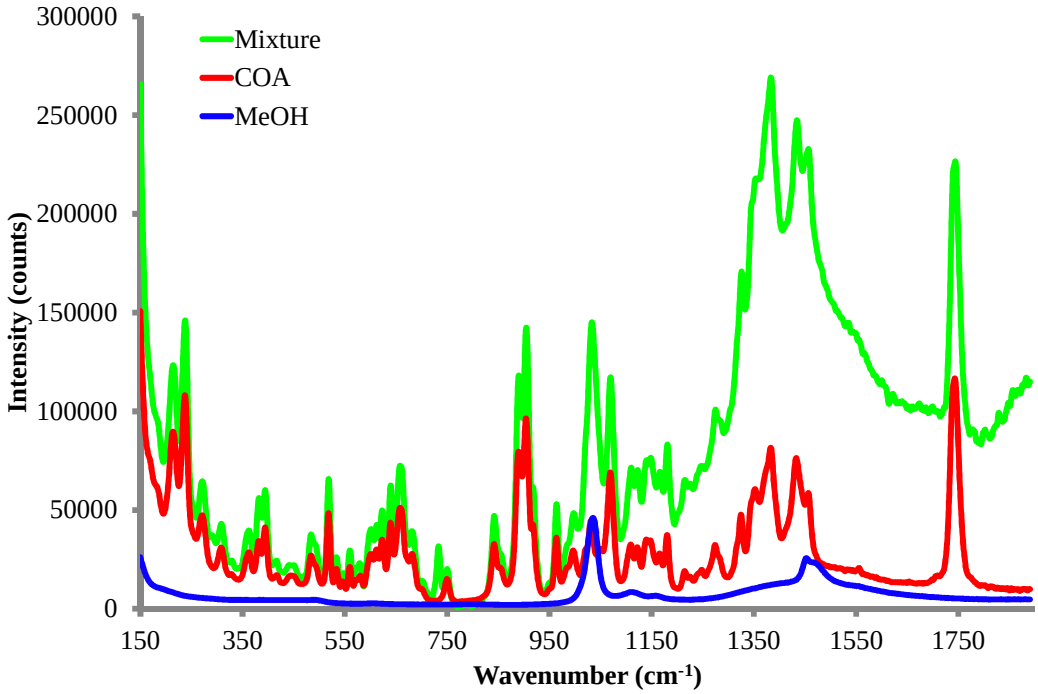

Figure 5-1: Raman spectra of methanol, cellobiose octaacetate and mixture of both compounds (mixture spectrum recorded during drying experiment and therefore glass background was observed from window at wavenumber shifts greater than 1150 cm^{-1}).

The ratio of the methanol peak intensity centred at 1036 cm^{-1} (R-O vibration – peak 2) to the COA peak intensity centred at 1749 cm^{-1} (ROOR vibration – peak 1) was plotted to produce a drying curve. Although, the methanol peak selected occurs at the same wavenumber as a peak in the COA spectrum, the extent of overlap is significantly less than at the alternative methanol peak ~1450 cm^{-1}. Also, COA is a weaker Raman scatter than methanol and so methanol can be detected even at low concentrations.

Figure 5-2 a) – d), shows the drying curves obtained from the 8 design points used in the factorial design.

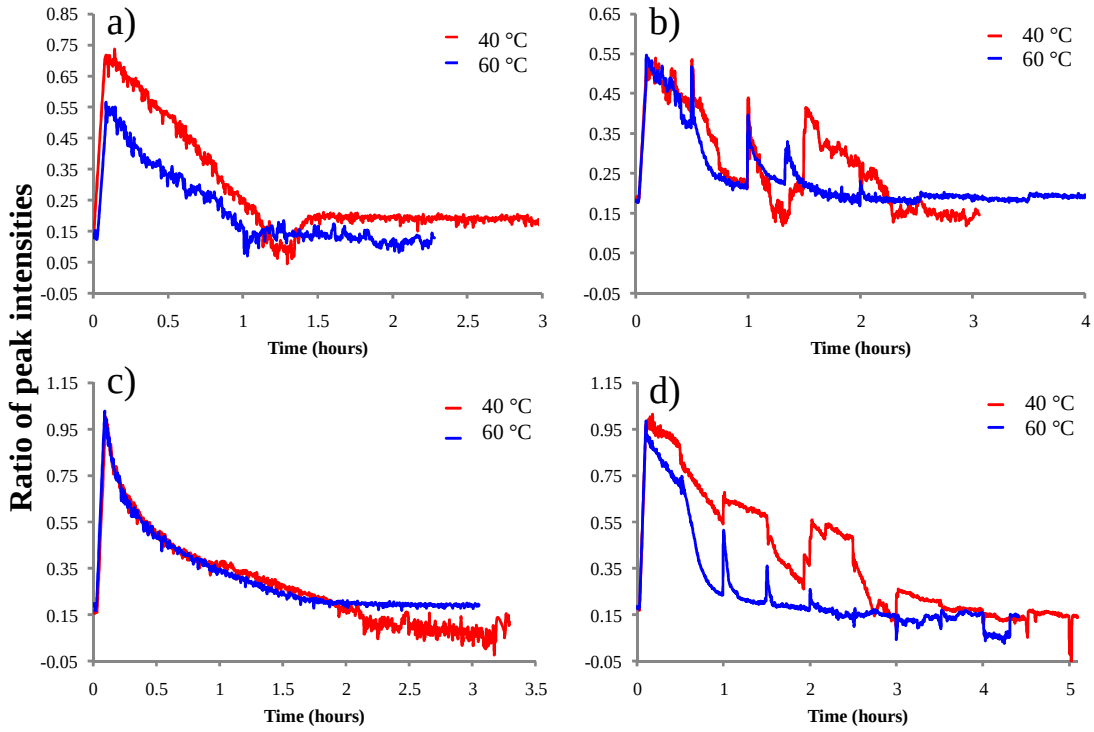

Figure 5-2: Change in the peak intensity ratio of methanol (1036 cm^{-1}): COA (1749 cm^{-1}) under different experimental conditions: a) 50% LOD with continuous agitation, b) 50% LOD with intermittent agitation, c) 100% LOD with continuous agitation and d) 100% LOD with intermittent agitation.

Figure 5-2 shows that after the addition of solvent to the vessel, the ratio of peak 2: peak 1 increased due to the contribution to peak 2 from methanol. Furthermore, this ratio was dependent on the volume of solvent added; with 150 ml (50% LOD) an

increase in the ratio from 0.15 to ~0.55 was observed, whereas when 300 ml (100% LOD) was added, the ratio increased to 0.95. When drying was initiated, the ratio of the two peaks began to decrease as a result of a loss of solvent. The drying curves observed differ greatly depending on the type of agitation employed; however, all three experimental factors investigated appeared to have an effect on drying time. Shown in Table 2 are the conditions used for each of the design and centre point experiments, the drying end point indicated by plots such as those in Figure 5-2, and the median particle size after drying (LD and QICPIC Feret Max).

Table 5-2: Design points for 2^3 factorial design, time of end point of drying and change in d (0,5) for each experiment.

Expt.	Agitation Method[a]	Oil Temp/ °C	% SLOD	Drying end point/ h	LD d (0,5) after drying/ µm[b]	QICPIC Feret Max D50 after drying/ µm[b]
1	CA	40	50 %	1.61	38	246
2	IA	40	50 %	2.61	59	350
3	CA	60	100 %	1.90	30	147
4	IA	60	100 %	2.30	28	201
5	CA	40	100 %	2.15	27	136
6	IA	60	50 %	2.23	51	323
7	IA	40	100 %	4.32	48	272
8	CA	60	50 %	1.32	34	187
CP 1	CA	50	75%	1.90	32	167
CP 2	IA	50	75%	3.27	50	304

[a]CA = continuous agitation, IA = intermittent agitation

[b]LD d (0,5) before drying = 67 µm, QICPIC Feret Max D50 before drying = 443 µm

Considering the agitation method first, the drying rate was significantly greater when the particles in the drier were continuously agitated. This point is demonstrated when experiments 1 and 2 from Table 5-2 are compared. Here, the agitation strategy was

the only parameter varied, however, the drying time was increased by an hour when intermittent agitation was considered over continuous. This occurred due to the particles being exposed to very different conditions during each of the experiments. When intermittently agitated drying is carried out, effective heat transfer from the vessel wall to the particles and from particle to particle will only take place in the particles close to the wall itself. Particles close to the centre of the vessel will only be dried based on the vacuum removing solvent in the same way that a Buchner funnel would work. However, when the mixing steps take place, the dry particles are mixed with wet and partly wet particles, in doing so placing a new set of wet particles by the vessel wall to be dried. These points are analogous with the spikes present in Figure 5-2 parts b) and d). This process was repeated until all the particles were dry. For continuously agitated drying however, the particles are constantly being mixed while drying is taking place and, therefore, particles experience times when they are close to the vessel wall and also times when they are near the centre of the vessel. A smooth drying curve resulted, as all of the particles were dried at the same rate at any given time period.

When SLOD was also considered, it can be seen in Figure 5-2 and from Table 5-2 that the drying time is greater when 100% SLOD was dried rather than 50% SLOD, as would be expected due to the greater volume of solvent to be removed. For example, when considering experiments 1 and 5 (from Table 5-2), the drying time for 100% SLOD was 32 minutes longer than that of 50% SLOD. From this, and also considering the drying curves in Figure 5-2, it appears that the drying rate was not consistent throughout the entire process; there was an initial faster drying period when there was more excess solvent, followed by a slower drying period when more tightly adsorbed solvent was evaporated. This can be seen in Figure 5-2 c) where the gradient of the drying curve changed considerably throughout the experiments and was also consistent with examples in the literature[7, 8] and commonly accepted drying theory.[33]

The effect of varying jacket temperature was also investigated. It should be noted that the cake temperature is lower than the jacket temperature, otherwise at a

temperature of 40 °C and a pressure of 50 mbar all the methanol in the system would be in the vapour phase (B.P 33 °C at 50 mbar).[34] Further, at a jacket temperature of 60 °C, the methanol would be in the vapour phase for the entire limits of the pressure range analysed. It is clear from experimental results that methanol is present in the liquid phase in all experiments and hence the bulk cake temperature is well below that of the jacket temperature. This is due to the fact that heat energy is lost to convert the methanol near the vessel wall from the liquid to the vapour phase, and further energy is lost due to the heat transfer resistances (dominated by wall to solid and solid to bulk resistances) that are present in the system, these effects have been described previously by Schlunder and Mollekopf.[35] In the experiments described here, jacket temperature had the smallest effect on the drying time, but appeared to be a more significant factor when intermittent agitation was employed rather than continuous agitation. As expected, the drying rate at 60 °C was greater than that for 40 °C (shown most clearly in Figure 5-2 d)).

5.3.2 Off-line particle size analysis: LD, QICPIC and PIMS

Dry powder samples were removed at the end of each drying experiment for analysis by LD, QICPIC and also PIMS at GSK. The data were examined to determine the extent of attrition that occurred during each of the drying experiments and to correlate to trends in the Raman data. Figure 5-3 a) – d) shows the volume distribution obtained for each of the 8 design points.

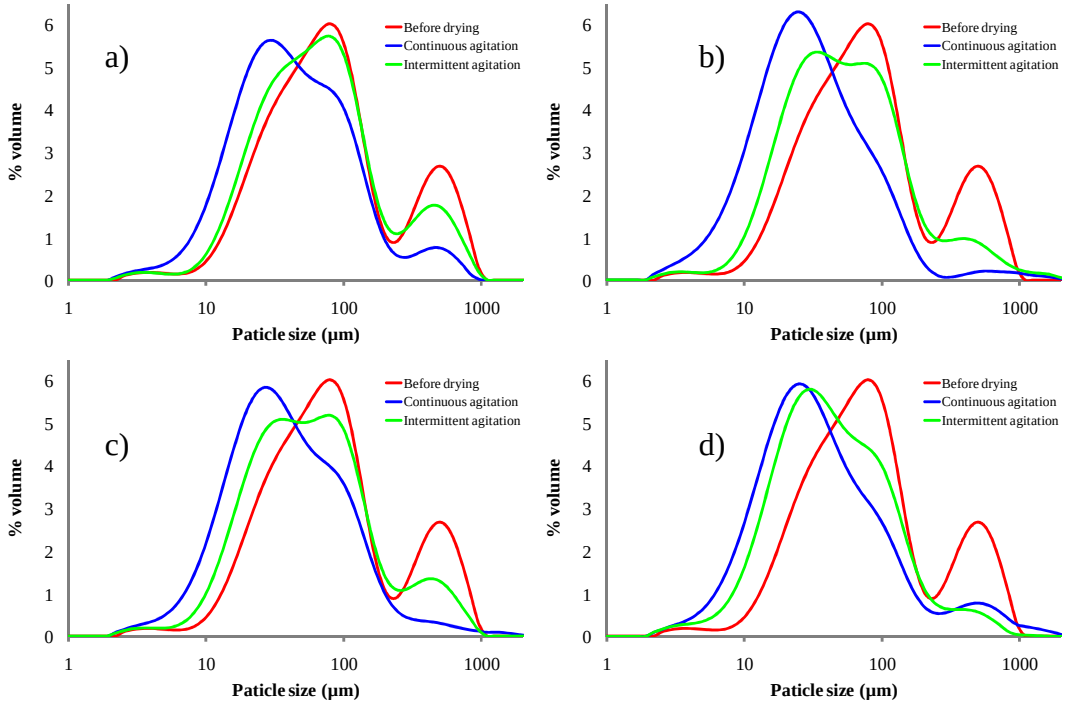

Figure 5-3: Volume distribution of COA particles before drying (red trace) and after continuous (blue) and intermittent (green) agitation for: a) jacket temperature of 40 ºC and 50% LOD, b) jacket temperature of 60 ºC and 50% LOD, c) jacket temperature of 40 ºC and 100% LOD, and d) jacket temperature of 60 ºC and 100% LOD.

The laser diffraction volume distribution for COA can be separated into three distinct peaks. First, there was a mode at around 800 µm in the "before drying" data and the intermittently agitated data (exception is Figure 5-3 d)), which had decreased significantly in size in the data for the continuously agitated particles, signalling that most of the longest needles had been broken into smaller ones. Secondly, there was a mode at around 90 µm, which corresponded to the bulk of the particles (medium length needles) in the "before drying" data and to a lesser extent in the data obtained from intermittently agitated data. This is due to many more medium and long needles being present before drying was commenced, and therefore, the LD instrument detected more of the particles based on their average orientation when diffracting the beam. Lastly, there is a mode at around 20 µm attributable to needle width, which

appeared as a shoulder in the before drying distribution data, but was the prominent mode in the data for continuously agitated particles.

In volume distribution plots, the data are weighted towards larger particles, i.e. one large particle will have a big effect on the data obtained as the volume of one large particle is the equivalent of several hundred or even thousands of fine particles. This means that the peak occurring at around 800 µm is likely to be caused by a small amount of particles and therefore the disappearance of such a peak in the dried particles data does not signify that there has been a large change in the particle size distribution. The change in ratio of the two smaller peaks, however, does indicate that a significant amount of attrition has taken place. The decrease in the peak at around 90 µm is synonymous with an increase in the size of the fines peak at around 20 µm. This indicated that the bulk of particles were fragmented into smaller particles, i.e. attrition had taken place. In each of the plots in Figure 5-3, the continuously agitated particles displayed a bigger proportion of fine particles in relation to the intermittently agitated samples, meaning that the number of particles that had been fragmented was greater in those samples. The reasons for this are discussed in the next section, where Raman data is also considered.

As well as laser diffraction, particle size analysis was carried out using Sympatec's dynamic image analysis QICPIC system and the particle imaging measurement system (PIMS) developed in house at GSK.

The QICPIC Feret Max data shown in Table 5-2 qualitatively agreed with the LD data obtained with a reasonably good correlation (r^2 = 0.92). As previously discussed, the Feret Max diameter from QICPIC offers the best quanititative representation of needle-shaped particles due to the basis of the calculations involved. For this data set, however, LD and PIMS were used to make conclusions based on the drying data as QICPIC was not available at the time the study was carried out (usage of QICPIC instruments was kindly offered by Sympatec Ltd meaning that analysis could only be carried out at certain times throughout the duration of the project). The QICPIC measurements were carried out at a later date to ensure completeness of the study, however, due to the good agreement with the LD

data, did not require a full report here. In later sections, QICPIC and LD measurements of dried samples are discussed equally.

PIMS uses proprietary algorithms to generate a number distribution and particle statistics from images that are recorded in an *in situ* flow cell based on the particle length and width. Figure 5-4 shows an image and length distribution vs. circularity data for samples of COA: a) before drying, b) from experiment 1 and c) from experiment 2. The images in Figure 5-4 show clear differences between the COA particles after continuous and intermittent drying had taken place. Where continuous drying had been carried out, nearly all the particles in the image had been fragmented into much smaller needles and many particles no longer resembled needle-shaped morphology. Conversely, after intermittent agitation had been carried out, the majority of the particles had retained their long needle-shape. This was confirmed by examination of the length vs. shape plots for each of the data sets. In the before drying COA data set, there are a large number of particles that have low circularity with long length dimensions i.e. needles. There is also an area of higher density where the particles have low circularity and length ~60 – 140 µm, which correlates well with the major mode in the LD data. When looking at the data for the continuously agitated sample, the number of particles with low circularity with long needle length had decreased considerably, showing that extensive attrition had taken place. The area of higher density of particles observed in the before drying sample had also decreased and the plot only displays an area of high density of small particles with high circularity, again suggesting that extensive attrition had taken place. The effects observed in the continuously agitated dried sample are not seen in the intermittently agitated dry particle sample and, therefore, suggests that extensive attrition had not taken place in this sample.

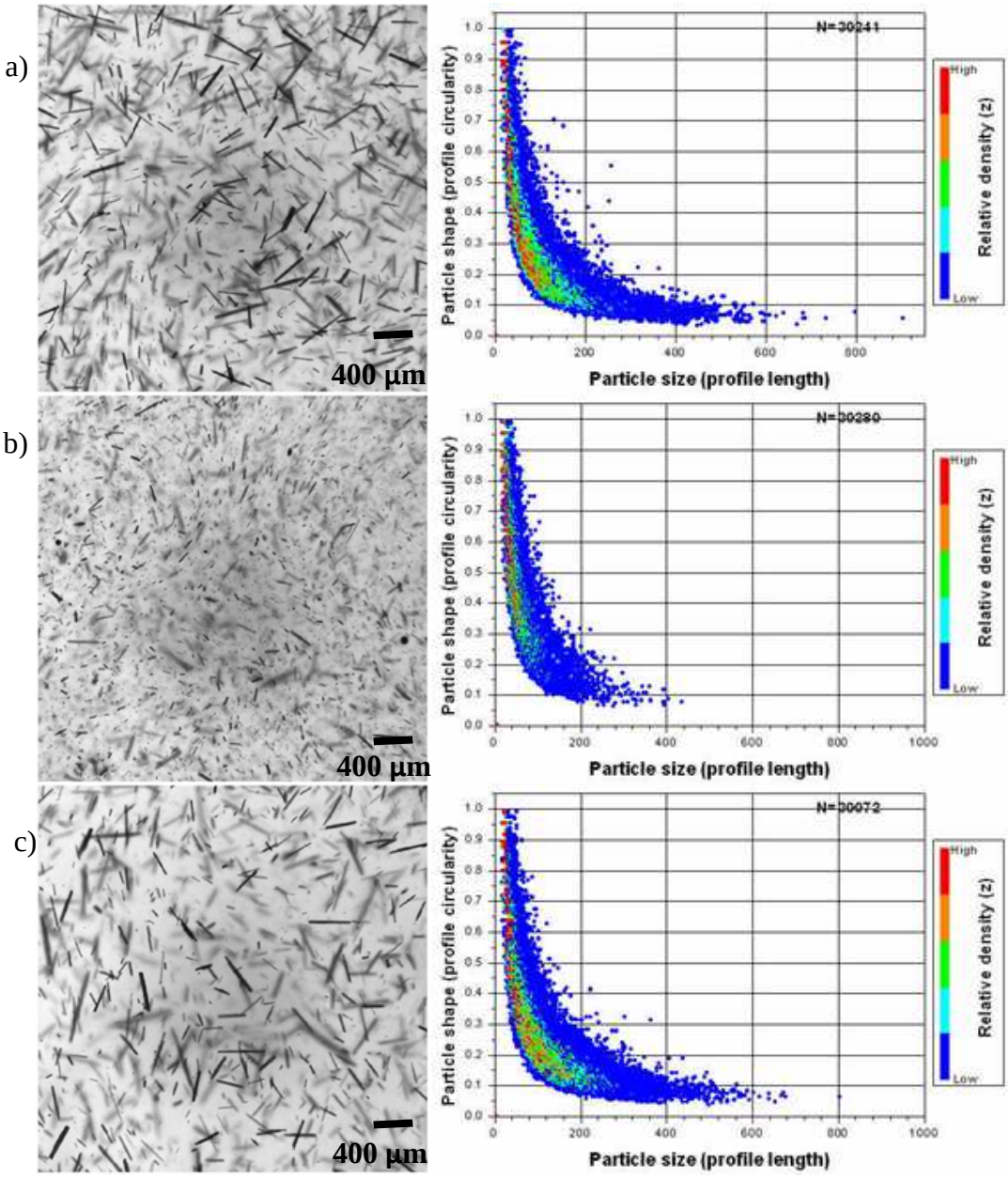

Figure 5-4: Flow cell image of COA and length vs. shape density plot for a) sample of COA taken before drying, b) sample taken after experiment 1 (continuous agitation), and c) sample taken after experiment 2 (intermittent agitation).

The information gained from the particle size analysis of the dried powder samples is an excellent starting point to examine the effects of particle size on the Raman

spectra of COA in real – time during drying. Firstly, the effects of COA particle size on the Raman spectrum was examined off-line using dry powder samples.

5.3.3 Particle size effects in Raman spectra of COA

Raman spectra are known to contain particle size information, although, there has been conflicting articles in the literature as to whether or not the Raman signal increases or decreases with increasing particle size.[36] From previous work carried out at the University of Strathclyde, a decrease in Raman signal has been observed with increasing particle size for needle shaped particles (albeit it for low aspect rather than high aspect ratio needles).[37] In Figure 5-5, the 1st derivative Raman signal at 1749 cm^{-1} is displayed for 2 g samples of dried COA (from experiments 1 – 8 and centre points from Table 2) measured off-line using the P^hAT probe and external sample compartment accessory. In this Figure, Raman data is plotted against median particle size (d (0,5)) measured using laser diffraction.

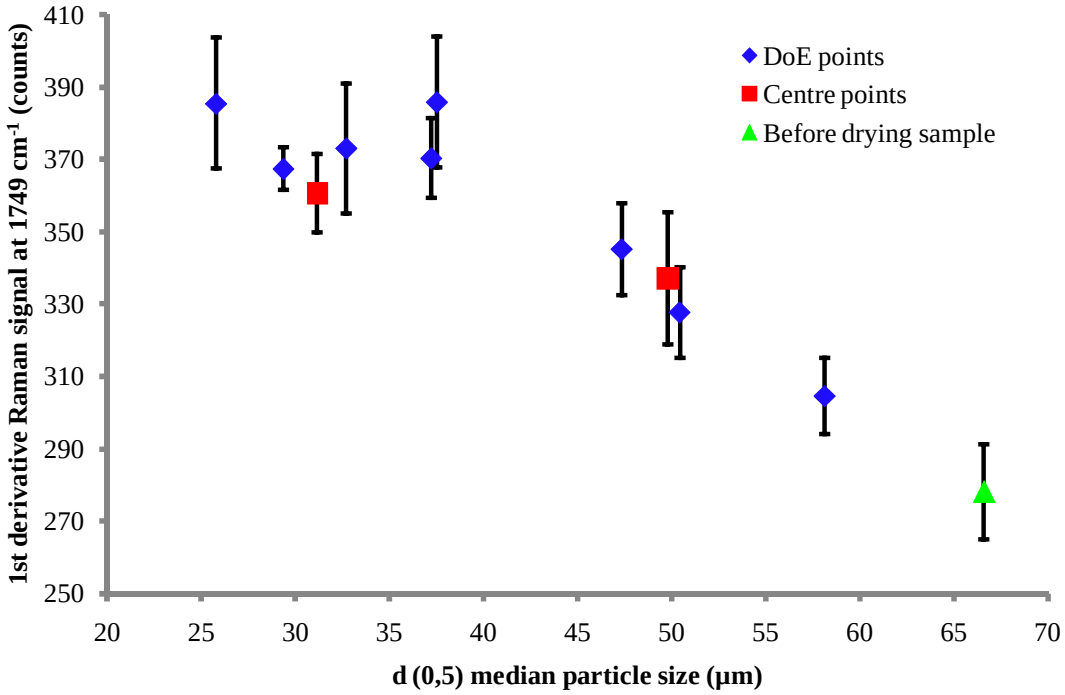

Figure 5-5: 1st derivative Raman intensity at 1749 cm^{-1} for static COA samples measured off-line using the P^hAT probes external sample compartment.

In this data, the Raman intensity appeared to vary with decreasing particle size until a threshold particle size was reached, at which point, the Raman signal no longer

changes with further decreasing particle size. The sample with the biggest particle size (before drying data) displayed the lowest Raman signal and the continuously agitated samples (smallest particle size) displayed the highest signal. As a 6 mm illumination spot size was used, a plausible explanation for this effect is that bigger particles will not pack as efficiently as smaller ones. Therefore, as the median particle size of the samples decreases, there will be a smaller amount of air gaps between the particles and, although, the first layer of particles for all samples will be efficiently excited with laser light, the subsequent layers would be more efficiently illuminated and thus, contribute a higher number of Raman photons back to the detector in better packed samples. It is important to note that only the length of the needles changes while attrition takes place whereas the width remains almost unchanged. Therefore, the overall effect observed is more likely due to the packing density of the bulk rather than from the actual difference in particle size, i.e. a bulk density effect rather than a particle size one.

Looking more closely at Figure 5-5 and Table 5-2, it became clear that the type of agitation had a significant effect on the extent of attrition that occured. With the exception of experiment 4 (intermittent agitation, 60 °C, 100% LOD), the intermittently agitated particles were subject to less attrition than the continuously agitated particles. A plausible reason for this can be rationalised when considering the forces that the particles experienced during the two different methods of drying. Particles that were continuously agitated were subjected to a continuous level of shear throughout the process, meaning that there was infinitely more collisions between particles with the impeller, the walls and themselves than when an intermittent agitation strategy was employed. It is, therefore, reasonable to suggest that these forces were the primary cause of particle fragmentation and therefore a correlation should exist between drying time and extent of attrition. Although an apparent correlation in the data presented does exist, it has to be noted that the samples were extracted for particle size analysis at the end of each experiment and not at the time when drying was complete. However, in future experiments, samples will be taken when the end point of drying has been attained as identified from the

drying curves derived from Raman spectra measured in real-time during the drying process as described in this study (discussed in Chapter 6).

There also appeared to be a relationship between the extent of attrition and % LOD where an increase in loss on drying resulted in an increase in extent of attrition. For example, looking at experiments 1 and 5 from Table 5-2 (continuous agitation, jacket temperature 40 °C, 50% and 100% LOD, respectively), a change in d (0,5) of 29 µm was observed for 50% LOD and a change of 40 µm for 100% LOD. To explain this effect, the forces that the particles are exerted to were considered. When 100% LOD was employed, the particles became saturated with the solvent and, therefore, formed what could almost be considered a slurry or paste. Although the drying rate was quicker at the onset of drying, as solvent is freed much more readily from the particles, it takes longer for the solvent to be removed from the system as the rate decreases and, therefore, longer agitation of the particles resulted in more attrition.

By carrying out two centre point experiments as part of the experimental design for this study, the explanations given above concerning the impact of the drying conditions were scrutinised. If the data obtained from experiments 1 – 8 could be used to predict the outcome of the centre point experiments, it might be expected that the drying end points and extent of attrition for these experiments would be similar to the mean values obtained from the four design points for each type of agitation. Therefore, the mean drying end-points and d (0,5) from LD were calculated and used to predict the outcomes of the centre point experiments. A comparison of actual and predicted drying end points and extent of attrition for the centre point experiments is shown in Table 5-3.

Table 5-3: Predicted and actual drying end points and extent of attrition for intermittent and continuous agitation of COA particles for the centre point experiments.

Agitation type	Predicted End point/ h	Measured end point/ h	Predicted d (0,5)/ µm	Actual d (0,5) for centre points/ µm
Continuous	1.75	1.90	32	32
Intermittent	2.86	3.27	49	50

The data in Table 5-3 shows that both the drying time and extent of attrition can be predicted when the drying conditions are changed within the design space. This suggests that it may be possible to optimise the drier operating conditions to minimise attrition and drying time, although as indicated by the results of this study, these parameters are inter-related. It would be preferable, however, to monitor the particles in real time, so that any changes in the particle size can be known during drying, which may reduce the need for extensive off-line particle size analysis at the end of drying.

5.3.4 More in-depth analysis of the Raman Data obtained during drying

Figure 5-6 shows the initial 10 Raman spectra collected from experiment 1 (continuous agitation, 50% LOD and jacket temperature 40 °C). When methanol was added to the vessel (red spectra), two main effects were observed. First, there was a positive baseline shift of about 2000 counts, and second, the appearance of a significant methanol peak centered at 1036 cm^{-1} appeared. A first derivative transformation was carried out (11 smoothing points, 2^{nd} order polynomial) to remove the effect of the baseline shift so that changes in peak height and shape could be investigated. The region of the first derivative spectra showing the methanol peak at around 1036 cm^{-1} is shown in Figure 5-7 for the initial 10 measurements.

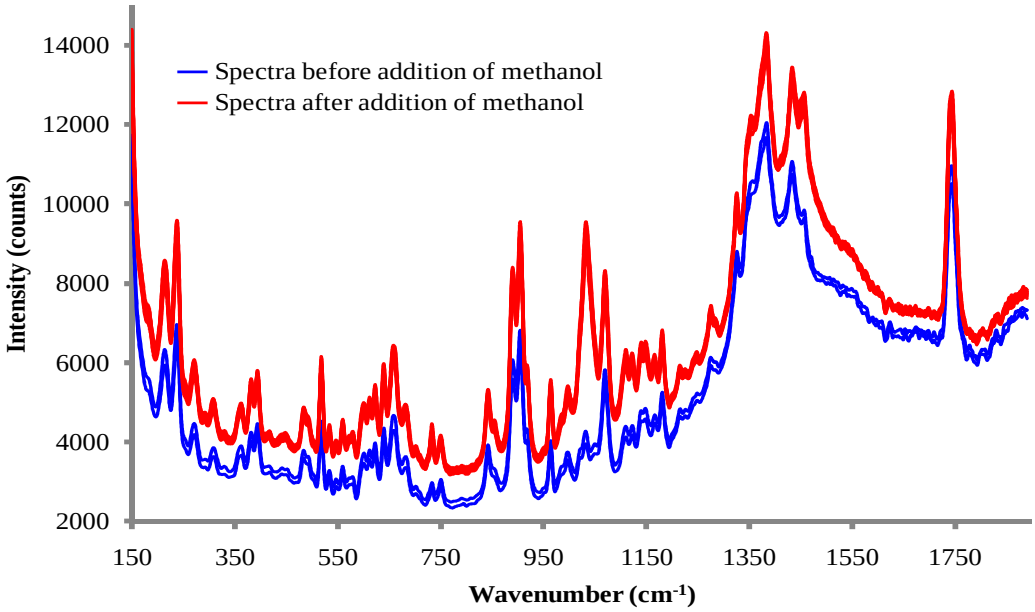

Figure 5-6: Initial 10 Raman spectra of COA drying experiment 1: continuous agitation, 50% LOD, jacket temperature 40 °C (— before addition of methanol data, — after addition of methanol data).

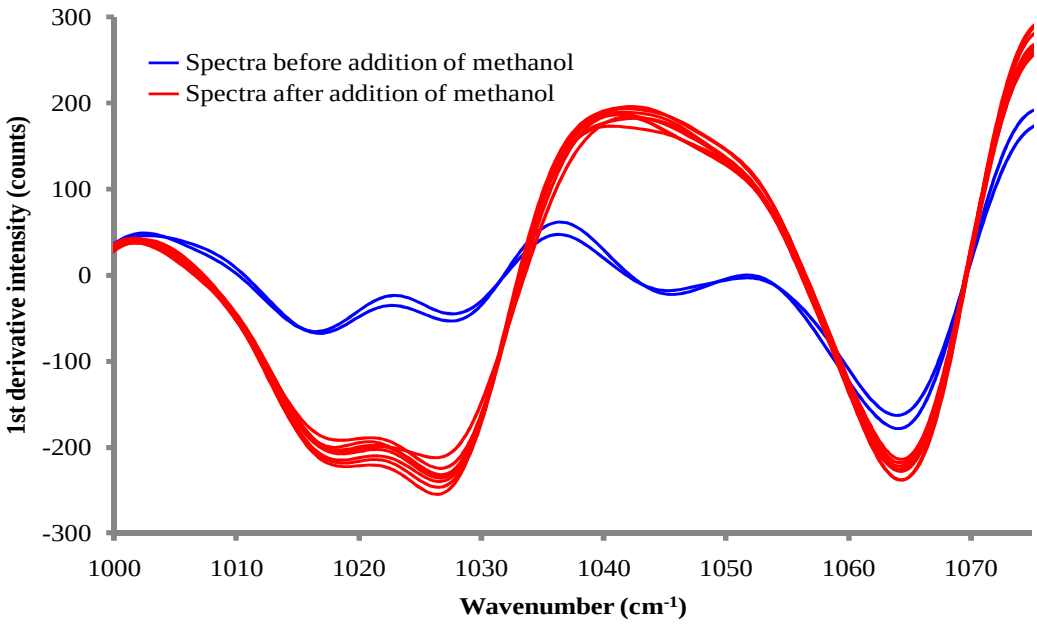

Figure 5-7: Initial 10 1st derivative Raman spectra from experiment 1 (1000 – 1075 cm-1) displaying the changes in peak shape and height due to the contribution of methanol (— before addition of methanol data, — after addition of methanol data).

Figure 5-7 shows a change in the peak height and a significant change in peak shape from the dry COA data upon the addition of methanol. Thus, the rate of removal of methanol during drying could be monitored by plotting a time series plot of the data at 1044 cm^{-1}, where there was minimal interference from the COA particles (as shown in Figure 5-7, where the contribution of COA to the spectrum of the dry particles is approximately 0 at 1044 cm^{-1}). A plot of 1st derivative Raman intensity at 1044 cm^{-1} vs. time is given in Figure 5-8.

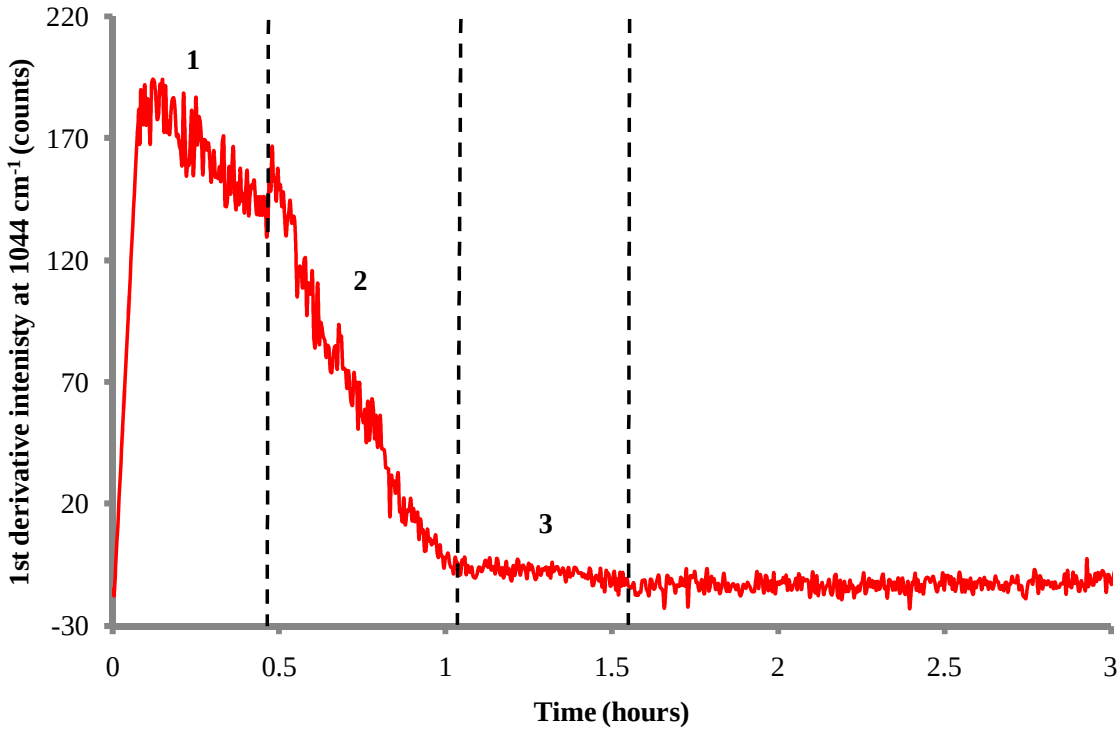

Figure 5-8: Change in the 1st derivative Raman signal of methanol at 1044 cm^{-1} for experiment 1 (continuous agitation, 50% LOD and jacket temperature 40 °C) with three stages of drying identified.

The removal of methanol from the COA particles can be separated into three phases for this data. There was an initial phase (time period **1** in Figure 5-8) where methanol was removed at a constant rate, after approximately 30 min, however, there was an increase in drying rate (time period **2** in Figure 5-8) which lasted for approximately another 30 min. The drying rate then seemed to decrease significantly (time period **3** in Figure 5-8) until a steady state signal was reached after a total of 90 min. At this

point, there is no more removal of methanol from the particles and they are therefore considered to be dry. The observations are consistent with those of Michaud *et al.* who successfully modeled the three (sometimes four) known phases of drying when investigating the vacuum contact drying of potassium chloride and ethanol systems.[38-40]

The three phases were described as: a constant rate phase, where the solvent concentration is above a critical value; a transition phase, where the solvent concentration falls below the critical value and the rate begins to decrease slowly; and a falling rate phase, where the drying rate decreases significantly below a second critical solvent concentration. There is evidence of the constant and falling rate phases in Figure 5-8 (time periods **2** and **3**), however, the drying demonstrated during time period **1** seems to differ from the Michaud model proposed as the drying rate was less than the drying rate for the constant rate phase. This observation was unique to the data of experiment 1 and a similar effect was seen by Lekhal *et al.* in some of their studies of potassium chloride and water systems and is described in the drying literature as an induction period, when the material is being heated early on in drying.[7, 33] The data for the other continuously agitated experiments correspond closer to the model proposed by Michaud *et al.,* as illustrated in Figure 5-9 (Michaud *et al*. did not model the induction phase).

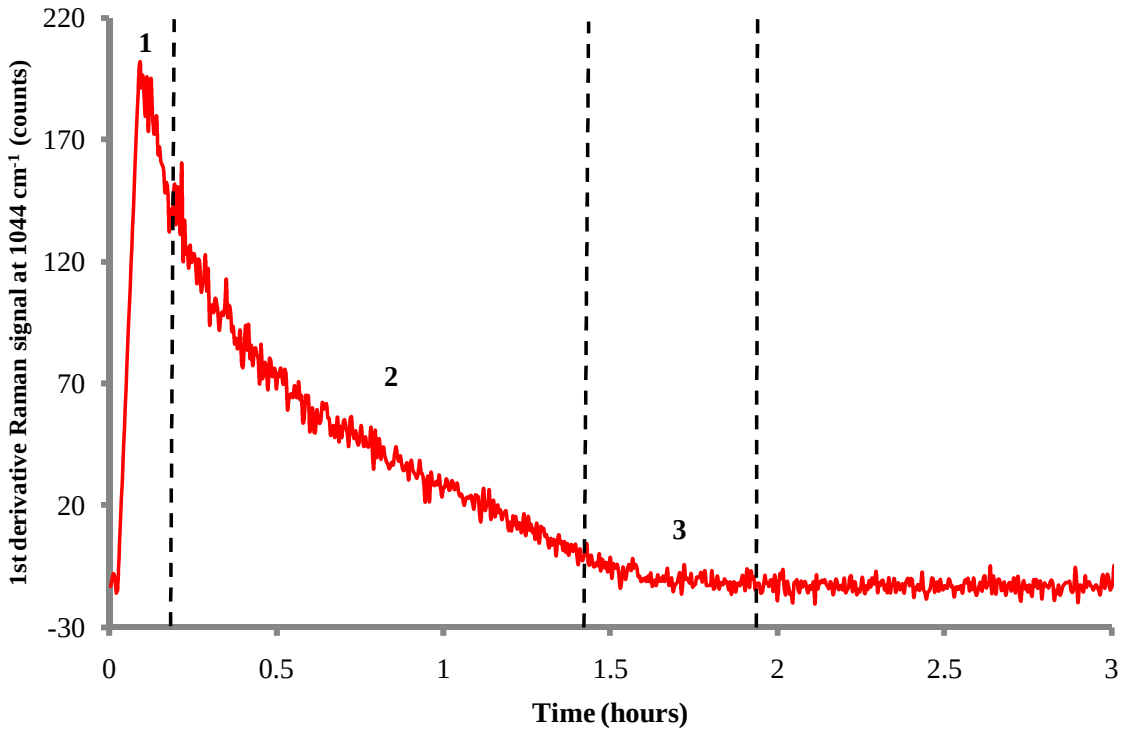

Figure 5-9: **Change in the 1st derivative Raman signal of methanol at 1044 cm^{-1} for experiment 3 (continuous agitation, 100% LOD and jacket temperature 60 °C) with 3 stages of drying identified.**

Monitoring the drying experiments *in situ* by Raman spectrometry has advantages over off-line %LOD measurements as information is not only gained from the drying curve, but also about what is happening to the particles. By studying regions of the spectra where methanol contribution is negligible, the signal arising from only the particles can be recorded. The spectra in Figure 5-1 illustrate that the contribution of methanol should be minimal at 550 – 950 cm^{-1}. Figure 5-10 shows the initial 10 first derivative spectra for that region from experiment 1.

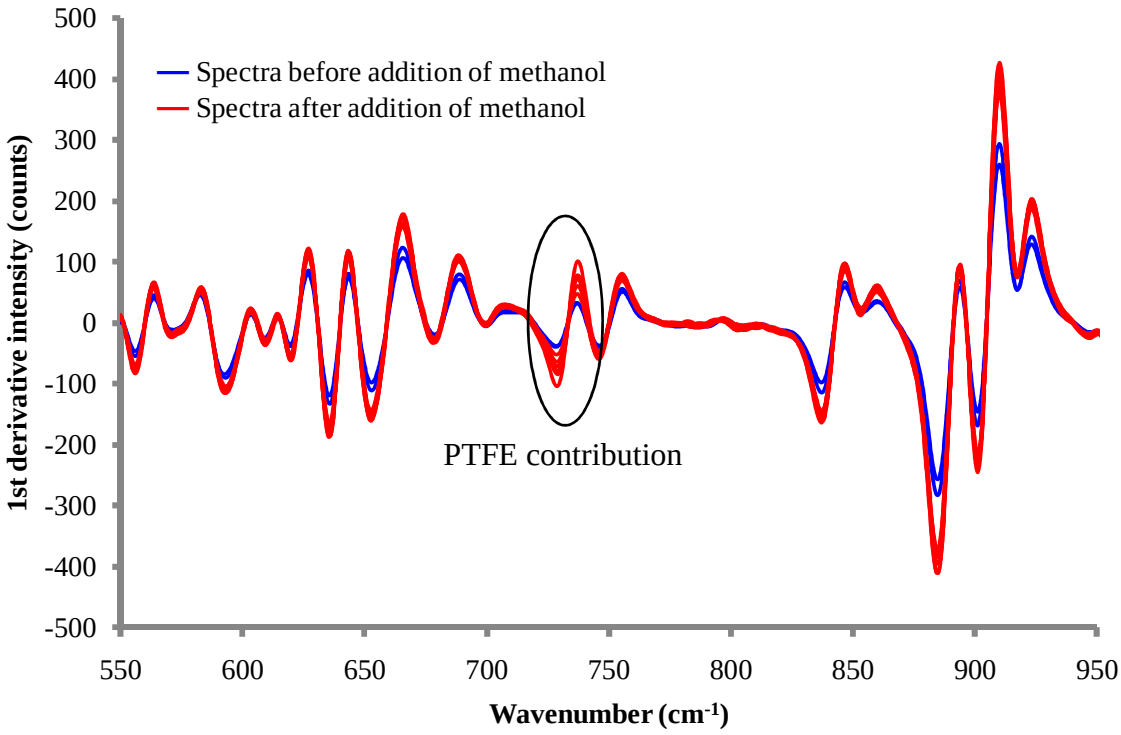

Figure 5-10: Initial 10 1st derivative Raman spectra from experiment 1 (550 – 950 cm^{-1}) displaying spectroscopic information from COA (— before addition of methanol data, — after addition of methanol data).

As methanol does not contribute to the spectra in the region 550 – 950 cm^{-1}, any change in the Raman signal observed was assumed to be due to a change in the signal arising from the COA particles (apart from a small contribution from the PTFE agitator ~740 cm^{-1}). An increase in Raman signal occurred upon the addition of methanol to the vessel (Figure 5-10). Previously in this report, an increase in Raman signal was observed owing to better packing of smaller COA particles, which increased the bulk density of the bed. The increase in Raman signal on addition of methanol, illustrated in Figure 5-10, was attributed to a similar effect whereby there was better packing of the particles. When solvent was mixed with the powder, air gaps between the particles were filled with liquid and this caused the particles to stick together due to liquid bridges being formed. This in turn resulted in a net increase in the bulk density of the powder, which resulted in an increase in Raman signal.

Further to increasing the bulk density of the particles, the addition of methanol may have also resulted in a change in the refractive index of the bulk powder by acting as a lens that focused the laser further onto the particles; it follows that this would also result in an increase in the Raman signal generated from COA as better excitation would be expected. For the analysis of this data set, however, the possible lens effect was not considered and conclusions are drawn based on bulk density effects only. An investigation into these effects may give further insights into the generation of Raman signal from wet particles and should be considered for future study.

Changes in the Raman signal that occur when the bulk density of the powder is altered will limit the ability to monitor changes in particle size caused by attrition using Raman spectrometry. The top of the drying cake is where the most loosely packed particles are located and so Raman measurements made in this region are most susceptible to bulk density changes. A prospective solution is to monitor the particles from a part of the drying cake where bulk density does not vary so greatly, i.e. near the bottom of the cake where the weight of the particles above would help to compress air gaps. The observations from this study are described in Chapter 6, and furthermore it should be noted that many windows in production scale vessels are located on the side near the bottom of a vessel and thus variations in bulk density effects may be less significant. Although changes in the bulk density of the particles have been shown to complicate Raman measurements, a significant amount of information can still be obtained about the status of the particles during drying. A drying curve similar to that produced for methanol was obtained for COA using the region 550 – 950 cm^{-1} shown in Figure 5-11, although the C=O peak at 1750 cm^{-1} could also have been monitored. Multivariate principal component analysis (PCA) was performed on the 1st derivative data obtained for 550 – 950 cm^{-1} during drying. PCA is a data reduction technique that plots the data onto a set of orthogonal axis known as principle components (PCs). Each component has an associated loadings matrix, which describes the weighting of the information that is contained in a PC, and a scores matrix which describes the projections of the data set onto the PC. Figures 5-11 and 5-12 show the scores and loadings plots, respectively, for PC 1 for the spectra recorded from experiment 1.

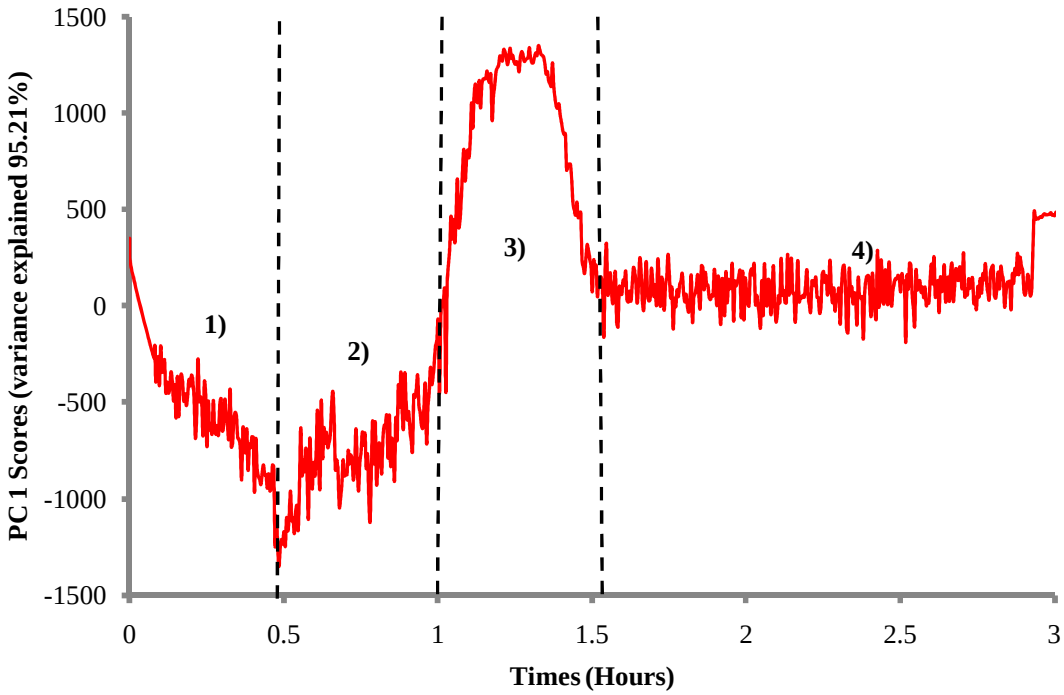

Figure 5-11: PC 1 scores for the COA contribution to the Raman signal (550 – 950 cm^{-1}) for experiment 1 (continuous agitation, 50% LOD, jacket temperature 40 °C).

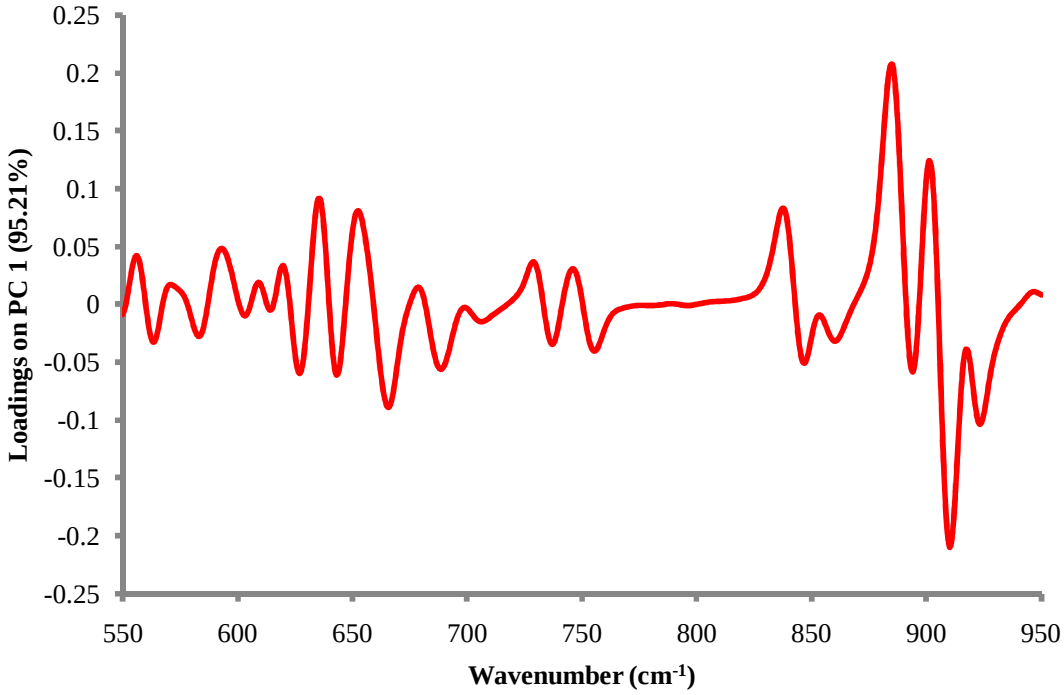

Figure 5-12: Loadings for PC 1 for the COA contribution to the Raman signal (550 – 950 cm^{-1}) for experiment 1.

In Figure 5-11, there are three distinct regions present that coincide with the regions observed in Figure 5-8 when the removal of methanol was monitored. In order to evaluate the data in these regions, the information that is described by the PC must be understood first. To do this, the loadings plot for PC 1 was analysed.

The loadings plot for PC 1 described 95.21 % of the variance observed in the data set and was anti-correlated with the spectra observed. When a loadings plot is anti-correlated to the spectra, an increase in PC score describes a decrease in Raman intensity in the spectra and vice versa for a decrease in PC score. In PC 1 (Figure 5-11), there was a decrease in the scores upon the addition of methanol meaning that there was an increase in Raman signal (time period **1** in Figure 5-11). This was due to the increase in bulk density from the methanol filling the air gaps between the particles as the particles are mixed. A point was then reached where the particles began to aggregate and the PC scores began to increase (time period **2** in Figure 5-11). This resulted in a decrease in the Raman signal due to the effect caused by aggregation, where many particles stick together to form bigger ones which reduces the bulk density (although increasing the density of the agglomerates). If the Raman spot was focused on a single agglomerate, it would be expected that the Raman signal would continue to increase as the bulk density increased. However, the decrease in Raman signal observed was due to the aggregates moving round within the agitator with large air gaps between them. This effect continued into the third phase of drying where the largest aggregates were found (time period **3** in Figure 5-11). A plateau in the Raman signal was seen at this point until a critical point of drying was reached where the solvent concentration had decreased enough so that the aggregates could break up. At this point, the Raman signal increases (decrease in PC 1 scores) due to the fewer air gaps between the particles/ aggregates. The aggregates continue to break up until the particles were dry and a steady state Raman signal was observed (time period **4** in Figure 5-11). The interpretation of the Raman data coincided with observation of changes in the physical state of the power during drying where formation of balls and disintegration of these balls to smaller particles were noted, termed balling. An example of this kind of agglomeration is shown in Figure 5-13.

Figure 5-13: Image of aggregate found in drying experiments.

A similar investigation was performed for the Raman data for experiment 3. Figures 5-14 and 5-15 below show the scores and loading plots for PC 1, respectively, for the data. Here, the loadings plot was correlated with the 1st derivative Raman spectra meaning that an increase in Raman intensity resulted in an increase in PC 1 score (PCA models were constructed individually for each data set as well as collectively using all the data from continuously agitated experiments. The data reported here are the results from the individual PCA data sets, and hence, the reason that the loadings on PC 1 for experiment 1 are anti-correlated to the spectra, which is opposite to the data for experiment 3. In the collective data set, the loadings for PC 1 are anti-correlated to the spectra for all experiments).

In PC 1 (Figure 5-14) there is an increase in scores upon the addition of methanol, again, attributable to an increase in bulk density as before (time period **1** in Figure 5-14). In Experiment 3, the solvent concentration was double that of experiment 1 and therefore the second phase of drying, where aggregates are formed, occurred over a longer time period (time period **2** in Figure 5-14), This is due to the solvent concentration taking longer to decrease to a level where the particles agglomerate in balls. These large agglomerates were formed eventually (time period **3** in Figure 5-14), before breaking up as the solvent concentration decreased further until a point was reached where the particles were dry (time period **4** in Figure 5-14).

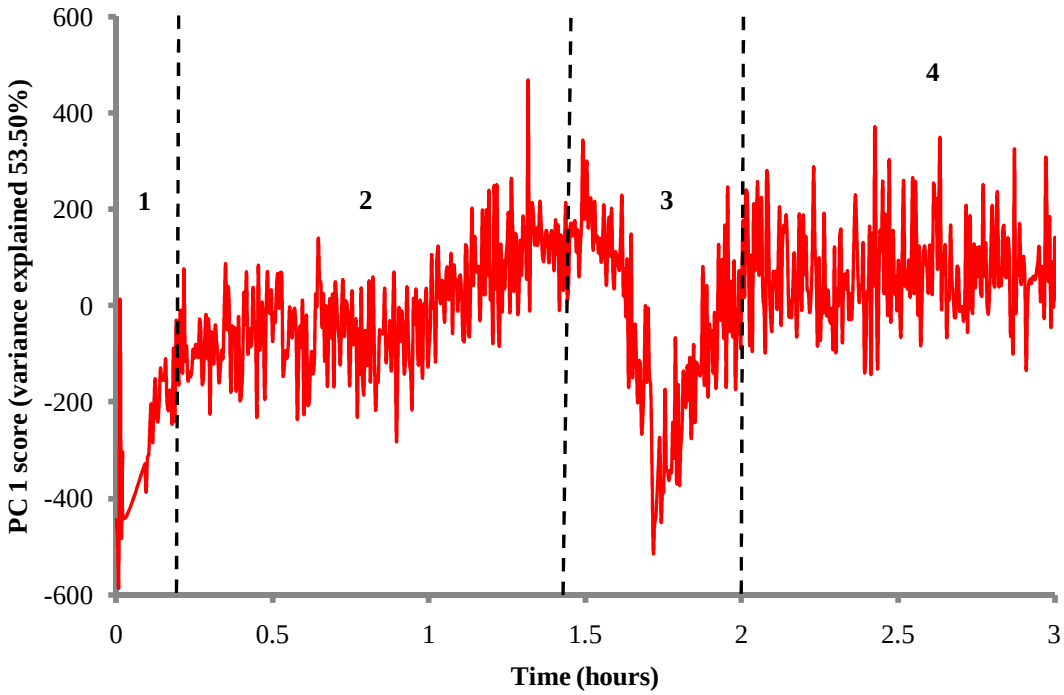

Figure 5-14: PC 1 scores for the COA contribution to the Raman signal (550 – 950 cm^{-1}) for experiment 3 (continuous agitation, 100% LOD, jacket temperature 60 ºC).

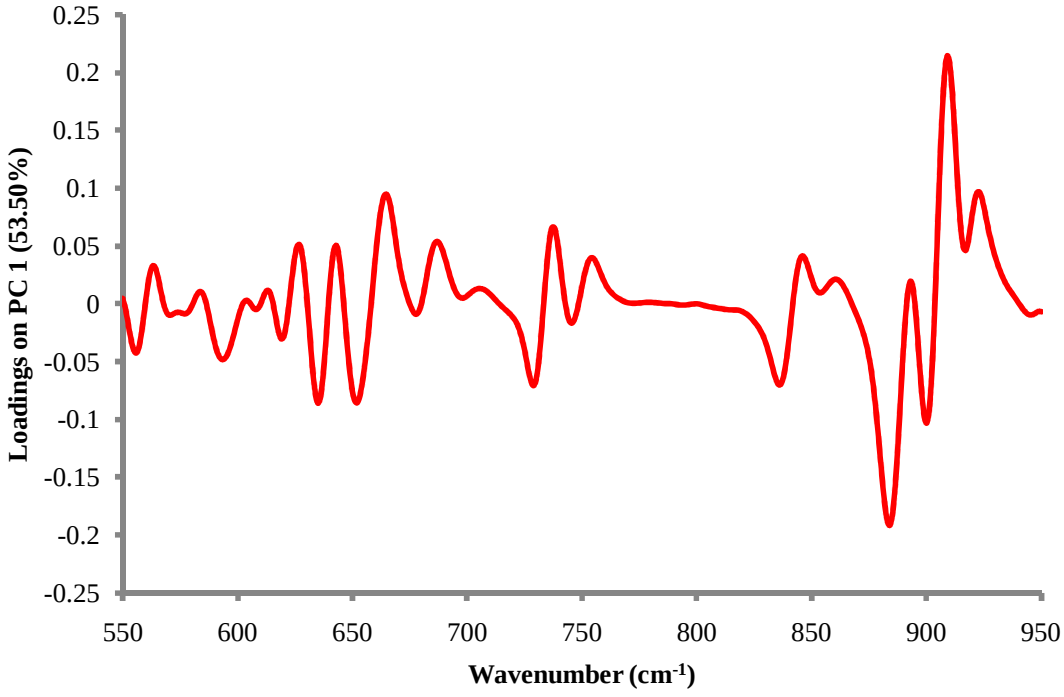

Figure 5-15: Loadings for PC 1 for the COA contribution to the Raman signal (550 – 950 cm^{-1}) for experiment 3.

An objective of this study was to investigate the effects of attrition on *in situ* measurements by Raman spectrometry and monitor these effects in real time. For the experiments conducted in this study, the particle size is only known at the beginning and the end of drying (refer to Table 5-2). Particle size measurements were not made at different stages during these drying experiments, meaning it was only possible to investigate whether the Raman signal was correlated to particle size at the end of drying. Figure 5-16 shows the average 1st derivative spectra for the final 100 spectra for each data set for the continuous agitation experiments as well as the equivalent spectrum for dry COA.

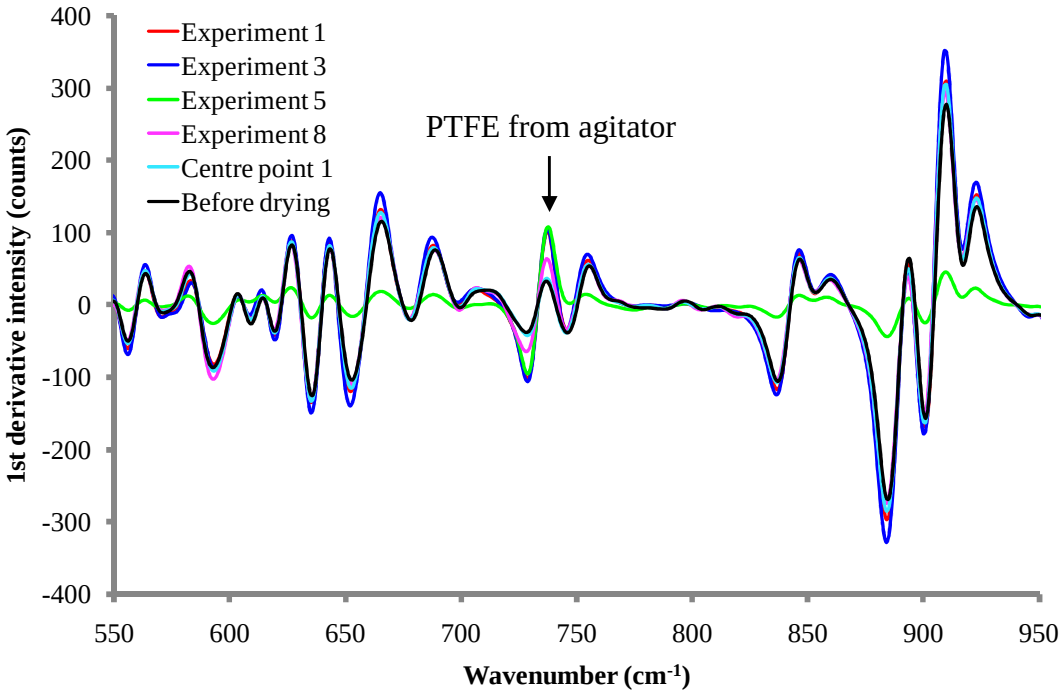

Figure 5-16: Average 1st derivative Raman spectra (550 – 950 cm^{-1}) for the final 100 spectra from each continuous drying experiment for COA before drying. The peak at 725 cm^{-1} is attributable to PTFE from the agitator.[41]

The data for experiment 5 (green spectrum) in Figure 5-16 is different to those of the other experiments because of window fouling that occurred after about 2.1 hours (see Figure 5-2 c) and so was discarded. The other data sets in Figure 5-16 did show some variation, however, this variation was minimal. Previous studies of the Raman spectra of static COA revealed that there was a univariate correlation between the

Raman signal intensity and particle size. However, such a correlation could not be demonstrated for either the continuous agitation or intermittent agitation data sets. PCA was applied to the spectra in Figure 5-16 (other than for experiment 5) and Figure 5-17 shows the scores plot obtained for PC 1 vs. PC 2.

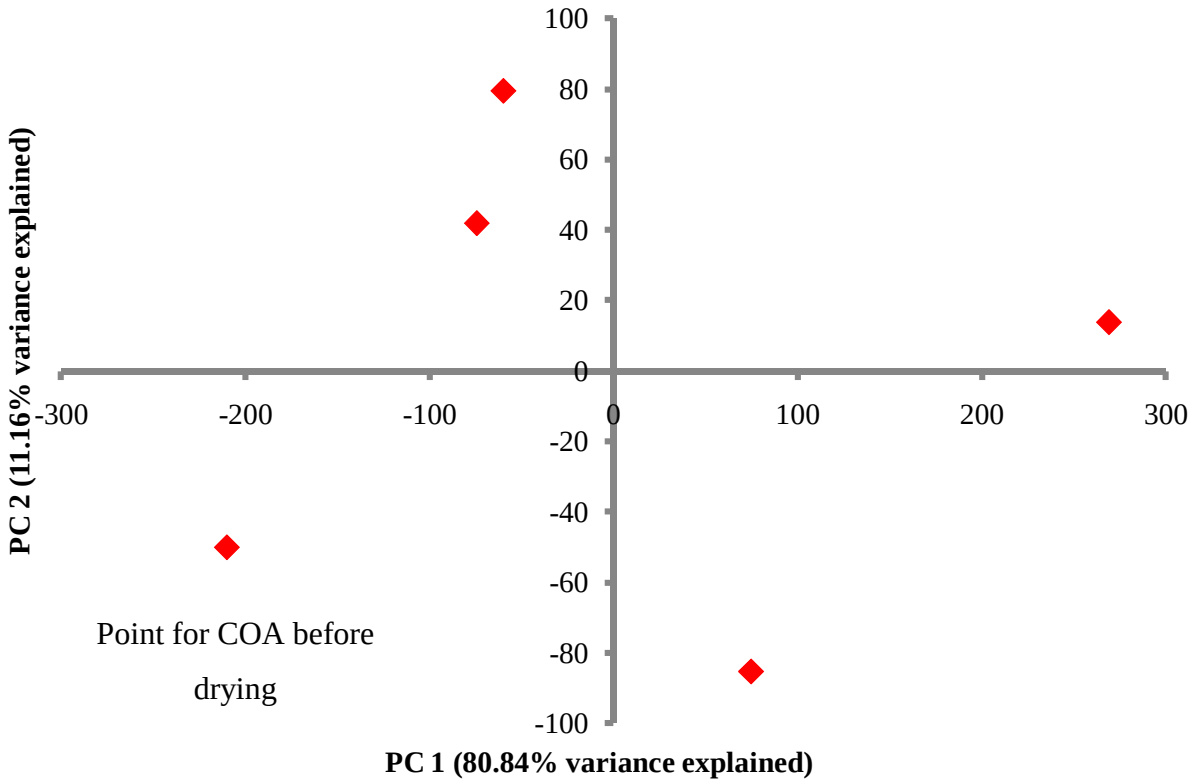

Figure 5-17: Scores plot for PC 1 vs. PC 2 for continuous agitation data set (550 – 950 cm^{-1}).

Figure 5-17 demonstrates that there is not a significant relationship between particle size and the *in situ* continuous Raman signal at the end of the drying experiments for the orientation of the probe used (i.e. through a window in the lid of the drier). Although a significant difference was observed in Raman signal when static off-line samples off different particle size were measured (Figure 5-5), it is likely that the variation in the measured signal caused by the movement of the particles was greater than the variations in the spectra caused by changes in particle size. Also, as mentioned previously, collecting spectra from the top of the drying cake is not the best orientation for *in situ* spectrometry as it is the region of most variance of the powder bed.

A similar investigation was preformed for the data collected from the intermittent agitation experiments (not shown). However, again, the change in Raman spectra could not be correlated to the change in particle size of COA either with univariate or multivariate analysis. Although the particles were static as Raman data was collected, poor mixing of the particles in the agitation periods meant that the cake height and bulk density varied depending on where the laser spot was directed. This, again, demonstrates a limitation of data collection through a window on the top of the vessel, as these effects may be minimised at a lower part of the cake, i.e. through a side window.

Partial least squares regression was performed on both the continuous agitation and intermittent agitation data sets, and also on the two data sets combined. Although, the regression technique could fit models to the data with relatively low root mean standard errors of calibration, the predictive abilities of these models was extremely poor based on the small amount of variation in the data sets and will not be discussed further at this stage.

5.4 Conclusions

In situ Raman spectrometry has been applied to monitor the drying curve of methanol from COA. A drying curve for each experiment was produced by monitoring the ratio of R-OH methanol peak against the C=O peak from COA. By using a factorial design of experiments approach, the effects of three drying variables on drying time and extent of attrition were also determined. It was found that all three variables (method of agitation, % SLOD and jacket temperature) had a significant effect on the drying end point as expected. When extent of attrition was considered, however, the method of agitation had the biggest effect, although both % SLOD and jacket temperature did have some contribution also.

A region of the Raman spectra free from methanol contribution was analysed to monitor the status of the particles during drying. This allowed the identification of the formation and break up of agglomerates that coincided with the various stages of drying. This was verified by visual examination of the particles during drying.

The impact of attrition on the Raman spectra of the dried COA particles was determined using off-line Raman analysis, and an investigation of these effects was also carried out for the *in situ* spectroscopic data. It was determined that particle size effects could not be identified in the *in situ* data due to the greater influence of various effects such as spectral noise created by moving particles for the continuous agitation data, and bulk density effects in the intermittent agitation data. It was concluded that the position of the probe may need to be optimised (e.g. located closer to the bottom of the packed bed) for future analyses to reduce these effects, and allow an indication of particle size changes to be derived from the *in situ* spectral measurements.

5.5 References

1. Z. Q. Yu, J. W. Chew, P. S. Chow and R. B. H. Tan, *Chem. Eng. Res. Des.*, 2007, **85**, 893-905.

2. M. Ghadiri, Z. Ning, S. J. Kenter and E. Puik, *Chem. Eng. Sci.*, 2000, **55**, 5445-5456.

3. M. Ghadiri and Z. Zhang, *Chem. Eng. Sci.*, 2002, **57**, 3659-3669.

4. Z. M. Ning and M. Ghadiri, *Chem. Eng. Sci.*, 2006, **61**, 5991-6001.

5. Z. Zhang and M. Ghadiri, *Chem. Eng. Sci.*, 2002, **57**, 3671-3686.

6. C. L. Hare, M. Ghadiri, R. Dennehy and A. Collier, in *Powders and Grains 2009*, eds. M. Nakagawa and S. Luding, Amer Inst Physics, Melville, 2009, vol. 1145, pp. 851-854.

7. A. Lekhal, K. P. Girard, M. A. Brown, S. Kiang, B. J. Glasser and J. G. Khinast, *Powder Technol.*, 2003, **132**, 119-130.

8. A. Lekhal, K. P. Girard, M. A. Brown, S. Kiang, J. G. Khinast and B. J. Glasser, *Int. J. Pharm.*, 2004, **270**, 263-277.

9. FDA, *Guidance for Industry; PAT - a framework for innovative pharmaceutical development, manufacturing and quality assurance*, 2004.

10. A. S. El-Hagrasy, M. Delgado-Lopez and J. K. Drennen, *J. Pharm. Sci.*, 2006, **95**, 407-421.

11. L. J. Bellamy, A. Nordon and D. Littlejohn, *Analyst*, 2008, **133**, 58-64.

12. L. J. Bellamy, A. Nordon and D. Littlejohn, *Int. J. Pharm.*, 2008, **361**, 87-91.

13. A. S. El-Hagrasy, F. D'Amico and J. K. Drennen, *J. Pharm. Sci.*, 2006, **95**, 392-406.

14. A. S. El-Hagrasy and J. K. Drennen, *J. Pharm. Sci.*, 2006, **95**, 422-434.

15. S. B. Abebe, X. Z. Wang, R. Li, K. J. Roberts and X. Lai, *Powder Technol.*, 2008, **179**, 176-183.

16. J. Cornel, C. Lindenberg and M. Mazzotti, *Ind. Eng. Chem. Res.*, 2008, **47**, 4870-4882.

17. Y. R. Hu, J. K. Liang, A. S. Myerson and L. S. Taylor, *Ind. Eng. Chem. Res.*, 2005, **44**, 1233-1240.

18. G. M. Walker, S. E. J. Bell, K. Greene, D. S. Jones and G. P. Andrews, *Chem. Eng. Sci.*, 2009, **64**, 91-98.

19. A. Peinado, J. Hammond and A. Scott, *J. Pharm. Biomed. Anal.*, 2011, **54**, 13-20.

20. J. Johansson, A. Sparen, O. Svensson, S. Folestad and M. Claybourn, *Appl. Spectrosc.*, 2007, **61**, 1211-1218.

21. J. Tewari, V. Dixit and K. Malik, *Sens. Actuators, B. Chem.*, 2010, **144**, 104-111.

22. J. Burgbacher and J. Wiss, *Org. Process Res. Dev.*, 2008, **12**, 235-242.

23. K. Kogermann, J. Aaltonen, C. J. Strachan, K. Pollanen, P. Veski, J. Heinamaki, J. Yliruusi and J. Rantanen, *J. Pharm. Sci.*, 2007, **96**, 1802-1820.

24. G. Carson, A. J. Mulholland, A. Nordon, M. Tramontana, A. Gachagan and G. Hayward, *Journal of Sound and Vibration*, 2008, **317**, 142-157.

25. Y. Hu, Wikstr, H. m, kan, S. R. Byrn and L. S. Taylor, *Appl. Spectrosc.*, 2006, **60**, 977-984.

26. A. P. Ayala, H. W. Siesler and S. L. Cuffini, *J. Raman Spectrosc.*, 2008, **39**, 1150-1157.

27. E. Kougoulos, A. G. Jones, K. H. Jennings and M. W. Wood-Kaczmar, *J. Cryst. Growth*, 2005, **273**, 529-534.

28. P. A. Larsen, J. B. Rawlings and N. J. Ferrier, *Chem. Eng. Sci.*, 2006, **61**, 5236-5248.

29. J. Huang, G. Kaul, J. Utz, P. Hernandez, V. Wong, D. Bradley, A. Nagi and D. O'Grady, *J. Pharm. Sci.*, 2010, **99**, 3205-3212.

30. T. Narvanen, T. Lipsanen, O. Antikainen, H. Raikkonen, J. Heinamaki and J. Yliruusi, *J. Pharm. Sci.*, 2009, **98**, 1110-1117.

31. Malvern, http://www.malvern.com/ProcessEng/systems/velocimetry/velocimetry.htm.

32. L. Eriksson, E. Johansson, N. Kettanah-Wold, C. Wikstrom and S. Wold, eds., *Design of Experiments: Priciples and Applications*, MKS Umetrics AB, 2008.

33. D. W. Green, Perry, R. H., *Perry's chemical engineer's handbook*, McGraw-Hill Professional, New York, 2007.

34. NIST, NIST Webook, http://webbook.nist.gov/chemistry/.

35. E. U. Schlünder and N. Mollekopf, *Chem. Eng. Process.*, 1984, **18**, 93-111.

36. H. L. Wang, C. K. Mann and T. J. Vickers, *Appl. Spectrosc.*, 2002, **56**, 1538-1544.

37. P. Allan, *Studies in Raman, infrared and acoustic emmision spectrometries, and reaction calorimetry for process analysis*, PhD, University of Strathclyde, 2008.

38. A. Michaud, R. Peczalski and J. Andrieu, *Chem. Eng. Process.*, 2008, **47**, 722-730.

39. A. Michaud, R. Peczalski and J. Andrieu, *Chem. Eng. Res. Des.*, 2008, **86**, 606-611.

40. A. Michaud, R. Peczalski and J. Andrieu, *Dry. Technol.*, 2007, **25**, 1163-1173.

41. S. Firsov, G. Zhbankov, M. Bakhramov, A. Abdukadyrov and A. Gafurov, *J. Appl. Spectrosc.*, 1993, **59**, 644-647.

6 Further studies in particle drying: Isolation of COA particles from COA/ methanol slurries

6.1 Introduction

In Chapter 5, the results of a DoE study that investigated the effects of three controllable drying parameters on the Raman determined end point and the extent of attrition when methanol was removed from COA were described. It was concluded that although an off-line correlation between the 1st derivative Raman signal and LD measured median particle size was established, reductions in particle size could not be detected *in situ* during drying when the powder was analysed through a window in the lid of the vessel. This was attributable to the greater influence of spectral noise for continuously agitated particles and bulk density effects created by the varying particle bed height for intermittently agitated particles. The glass design of the drier, however, allowed the non-invasive Raman probe to be mounted in an alternative orientation that permitted measurement through the glass wall of the vessel underneath the oil jacket, rather than through a window in the lid as described in Chapter 5. Analysis through the side of the vessel may reduce the effect of noise on the Raman spectra created by the motion of continuously agitated particles due to the sample volume potentially being more consistent. Also this orientation may reduce the effect of local bulk density on the spectra recorded of intermittently agitated particles.

In order to mimic an industrial drying process at a laboratory scale, the effects of an initial convective drying period on a packed bed of methanol and cellobiose octaacetate (COA) particles (pressure filtration), and a subsequent conductive agitated vacuum drying period were investigated using Raman spectrometry and particle size analysis. The study consisted of two parts: firstly, the effect that batch to batch variation of the starting bulk density of COA particles had on the drying curve was investigated, followed by a study of the drying of COA-methanol slurries, using non-invasive *in situ* measurement by Raman spectrometry. Various drying periods of pressure filtration were utilised to “blowdown” the methanol concentration of the

mixture with no agitation to different extents. This was done to produce different degrees of particle wetness, as defined by the “loss on drying” measurement prior to the start of the conductive period. Experiments were carried out using both continuous and intermittent agitation strategies.

6.2 Experimental

6.2.1 Equipment

6.2.1.1 Lab scale agitated filter drier

The design of the drier was described in section 5.2.1.1. For the experiments described in this work, the drier was assembled and sealed before methanol-COA slurries were added through one of the ports in the lid, the port was then also sealed. A positive pressure of nitrogen (N_2) at 0.5 bar was applied to the slurry (delivered from a cylinder through another port in the lid) and methanol was collected in a solvent reservoir in the line. At the end of the pressure filtration period, the base of the drier was connected to a vacuum pump and the vacuum was held between 50 – 100 mbar during vacuum drying periods, this was monitored using a Pirani gauge (Edwards, Crawley, UK) in the line. Also in the vacuum line was a cold finger to trap any solvent in the line before reaching the pump. At the commencement of the vacuum drying period, the line was switched to collect the remaining solvent that was not removed during the pressure filtration in the cold finger using a PTFE T-junction with two taps (shown in Figure 3-2).

6.2.2 Materials

The cellobiose octaacetate (COA) particles used for the work described in Chapter 5 were re-crystallised at GSK (Stevenage, UK), the re-constituted material was used to complete the study described in this chapter. Methanol (Sigma-Aldrich, A5376, Dorset, UK) was once again used as the solvent.

6.2.3 Re-crystallisation of COA

The COA particles used for the DoE study in Chapter 5 were re-crystallised on two occasions (spring 2011 (batch 2) and summer 2011 (batch 3)) at GSK (Stevenage, UK). The following is a summary of the process used at GSK for the re-crystallisation of regular grade COA:

COA (1.0 wt.) was added to acetonitrile (3.7 vol.) and heated to dissolution at 70 - 75 ^{o}C. The solution was filtered into a clean vessel heated to 70 - 75 ^{o}C to ensure dissolution and then cooled over 30 mins to 60 - 62 ^{o}C. The batch was then seeded, (0.0008 wt.) at 62 ^{o}C before the slurry was cooled down to 20 – 22 °C at 5 ^{o}C/h. To the slurry, methanol (3.7 vol.) was added over 1 hour maintaining the contents at 20 – 22 ^{o}C and then the slurry was further cooled to 0 - 5^{o}C at 5 ^{o}C/h. The slurry was aged at 0 – 5 ^{o}C for at least 1 hour. The slurry was then isolated by filtration and the cake washed with 5 x (0.8 vols.) of methanol. The product was dried in a vacuum drier with no agitation at 50 ^{o}C (±3 °C)/10 – 75 mbar. The batch was judged dry when residual solvent content was < 0.5% w/w. (Recovery range, 70 to 85%).[1]

6.2.4 Raman Spectroscopy

A Kaiser Rxn 1 Raman spectrometer with P^{h}AT probe (Kaiser Optical systems, Ann Arbor, USA) was used to monitor the drying process non-invasively through the glass wall of the bespoke vessel (for instrumental setup, refer to section 5.2.3). Each Raman spectrum was recorded with a 30 s integration time with one spectrum recorded every 35 s. For all Raman experiments, the vessel was wrapped in aluminium foil to remove room and natural light from the spectra and to aid maximum recovery of Raman scattered photons to the detector.

6.2.5 Loss on drying analysis

Samples were taken at the end of each drying period for loss on drying (LOD) analysis. A sample thief probe was made by cutting the bulb of a plastic pipette tip and for each sample the bulb was filled with powder from the vessel. The total weight of sample was measured on collection and after static drying in an oven. The

LOD is the percentage of weight lost during drying based on the initial weight after extraction from the drier. After oven drying and LOD analysis, the samples were subjected to particle size analysis.

6.2.6 Particle size analysis

6.2.6.1 Laser Diffraction

A Malvern Mastersizer 2000 (Malvern Instruments, Worcestershire, UK) was used to analyse the sub-sampled powder by laser diffraction using the method described in section 5.2.4.1.

6.2.6.2 QICPIC image analysis

Sympatec QICPIC image analysis was performed using the LIXELL wet dispersion unit using the method described in section 5.2.4.2.

6.2.7 Bulk and tapped bulk density

The bulk density (BD) was measured by gently pouring COA into a graduated measuring cylinder until a fill volume of 70 – 100% was reached. BD was then calculated by the dividing the mass of material poured into the cylinder by the fill volume of the powder (quoted in g mL^{-1}). The tapped bulk density (TBD) was measured by performing a series of taps on a wooden surface in defined increments. TBD is defined as the mass of sample divided by the volume (after the volume remained constant for two successive series' of taps). The increments used were as follows (number of taps, **(total number of taps)**): 10 **(10)**, 40 **(50)**, 50 **(100)**, 100 **(200)**, 300 **(500)**, 250 **(750)**. The cylinder was cleaned with water and dried using N_2 gas between measurements.

6.2.8 Monitoring of drying curve for COA-methanol by non-invasive Raman spectrometry

250 g of COA was transferred to a 2 L conical flask before 1 L of methanol was added. The resulting slurry was transferred from a conical flask into the drier through a port in the lid, the conical flask was then rinsed with 100 ml of methanol and

transferred into vessel before the port was sealed. A positive pressure of nitrogen (N_2) at 0.5 bar (measured by the pressure gauge on the cylinder) was then applied to perform a) a pressure filtration resulting in a packed bed of particles and b) a N_2 blowdown convective drying period of the packed bed of particles. After time periods of 0 (no convective drying, cake allowed to filter for 1 hour at atmospheric pressure), 10, 20, 30 and 60 minutes, the N_2 feed was stopped and a sample was extracted for LOD and particle size analysis. Vacuum agitated filter drying with continuous or intermittent agitation at 10 rpm was then started and the powder was deemed to be dry when the Raman signal remained at a steady state for 15 mins (ratio of a COA:MeOH peak). At this point, a second sample was taken for LOD and particle size analysis. The oil jacket temperature was held at 60 °C for all experiments.

6.3 Results and discussion

6.3.1 Comparison of spectra measured from the side and top of vessel

In the previous DoE study (Chapter 5), the Raman probe was positioned at the top of the vessel with analysis of the COA powder achieved through a glass window in the lid with an approximate thickness of 0.5 cm. For the experiments described here, the probe was directed at the sample through the glass wall of the vessel that has a thickness of about 1.5 cm. An example spectrum of COA and methanol recorded through the glass wall is given in Figure 6-1.

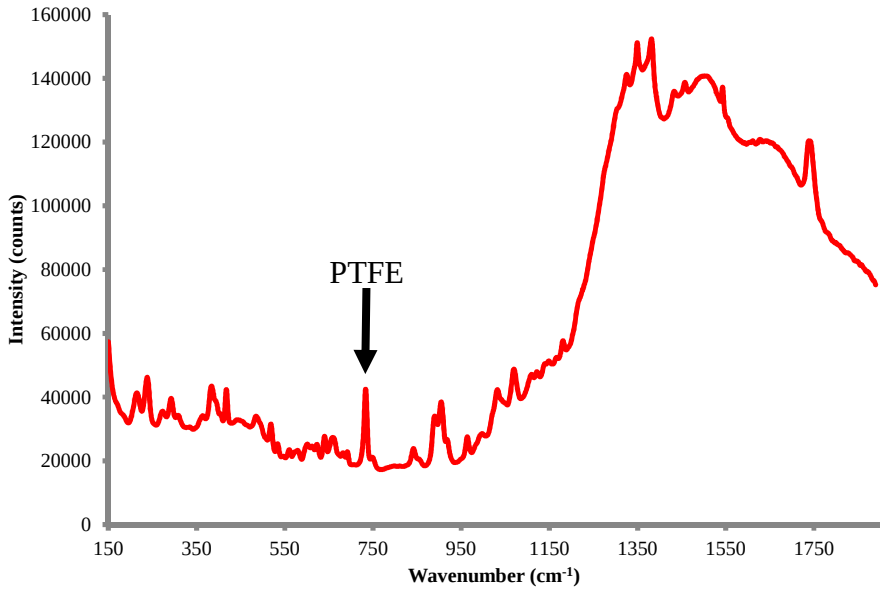

Figure 6-1: Raman spectrum of COA and Methanol recorded through side of glass drier.

A large background in the spectrum is observed at wavenumber shifts greater than 1150 cm^{-1} which was caused by the thick glass wall of the vessel, however, at wavenumbers less than 1150 cm^{-1}, there was very little contribution to the Raman spectrum from the glass. Therefore, all data analysis was performed using Raman intensities at wavelengths lower that 1150 cm^{-1}. Additionally, in the drying experiments, the PTFE agitator passed at approximately 1 mm from the inside wall of the vessel which resulted in a greater PTFE contribution to the Raman signal being observed compared to the experiments reported in Chapter 5. The penetration depth of the $P^{h}AT$ probe (400 mW at source, 6 mm spot size) has been measured previously and was found to be > 3 mm when the Raman signal arising from a TiO_2 disk was measured through increasing depths of Avicel, aspirin or sodium nitrate.[2] When multivariate analysis was performed the part of the spectrum caused by PTFE was omitted from the data.

6.3.2 Comparison of different batches of COA

The average 1st derivative Raman spectra of recrystallised COA batches 2 and 3 are shown in Figure 6-2 and the 1st derivative region from 1500 to 1700 cm^{-1} is shown in Figure 6-3 (average spectra of three 2 g sub samples, each measured in triplicate).

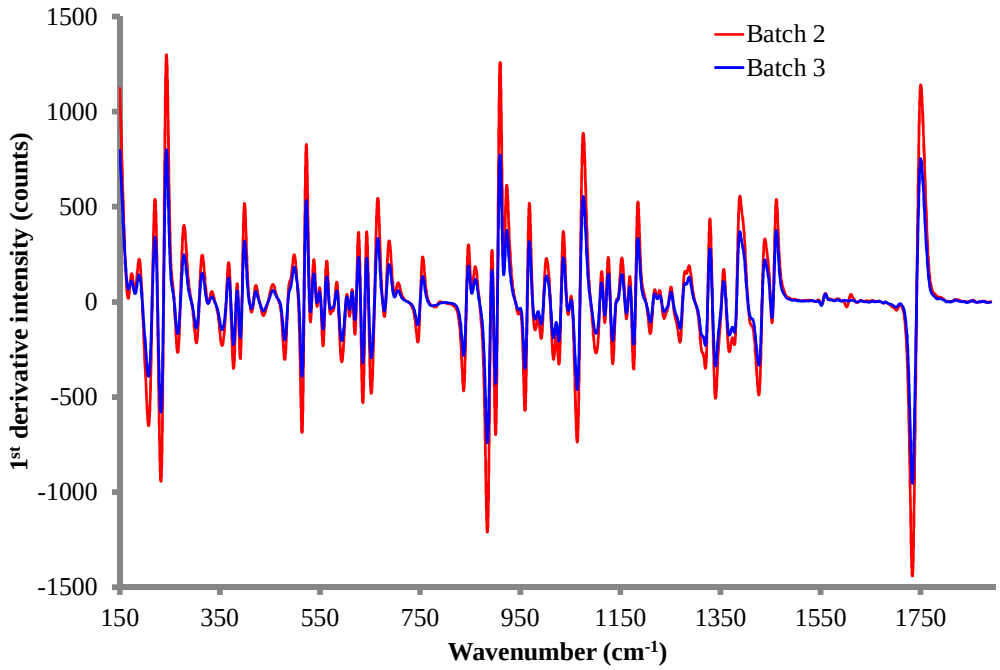

Figure 6-2: Average 1st derivative spectra of batches 2 and 3 of COA.

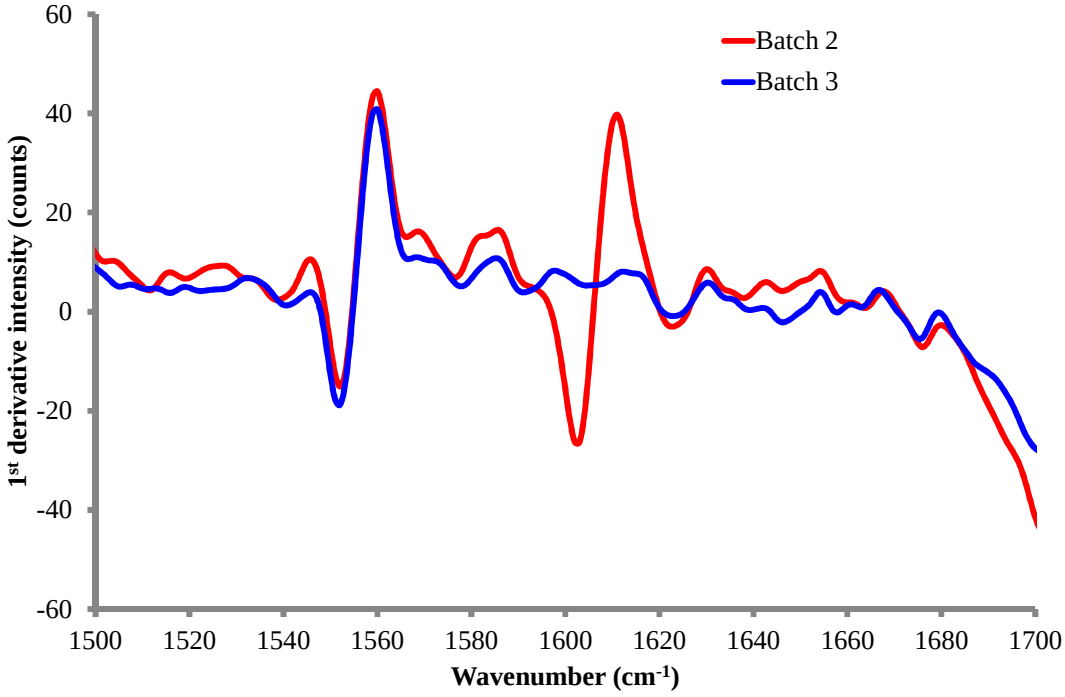

Figure 6-3: Average 1st derivative Raman spectra (1500 – 1700 cm^{-1}) of batches 2 and 3 of COA showing differences between samples.

The 1st derivative Raman spectra for COA batches 2 and 3 were generally similar when the peak positions were considered, as is shown in Figure 6-2. However, there was a small difference between the two samples at around 1600 – 1620 cm^{-1} owing to a peak that is present in batch 2 that is not present in batch 3 (Figure 6-3). The intensity of the additional peak is relatively low and was likely due to an impurity either from the reactor where recrystallisation was performed, or the drier where the batch was dried and was not likely due to a significant chemical difference in the samples. Nonetheless, it must be acknowledged as a difference between the batches. When the intensities of the peaks from batch 2 and batch 3 were evaluated, however, significant differences were observed. The data for batch 2 displays greater peak intensities at almost all peaks across the spectrum indicating that the average particle size for batch 2 was lower than that of batch 3. It follows then that the bulk density of batch 2 was greater than that of batch 3, as bulk density is directly related to particle size and polydispersity (PD). In order to confirm this observation, particle size analysis was carried out using both laser diffraction (LD) and QICPIC dynamic image analysis along with bulk and tapped bulk density measuremnts. The average LD volume weighted distributions, and QICPIC Feret Max distribution are shown in Figure 6-4: a) and b), respectively, with median particle size and PD data given in Table 6-1.

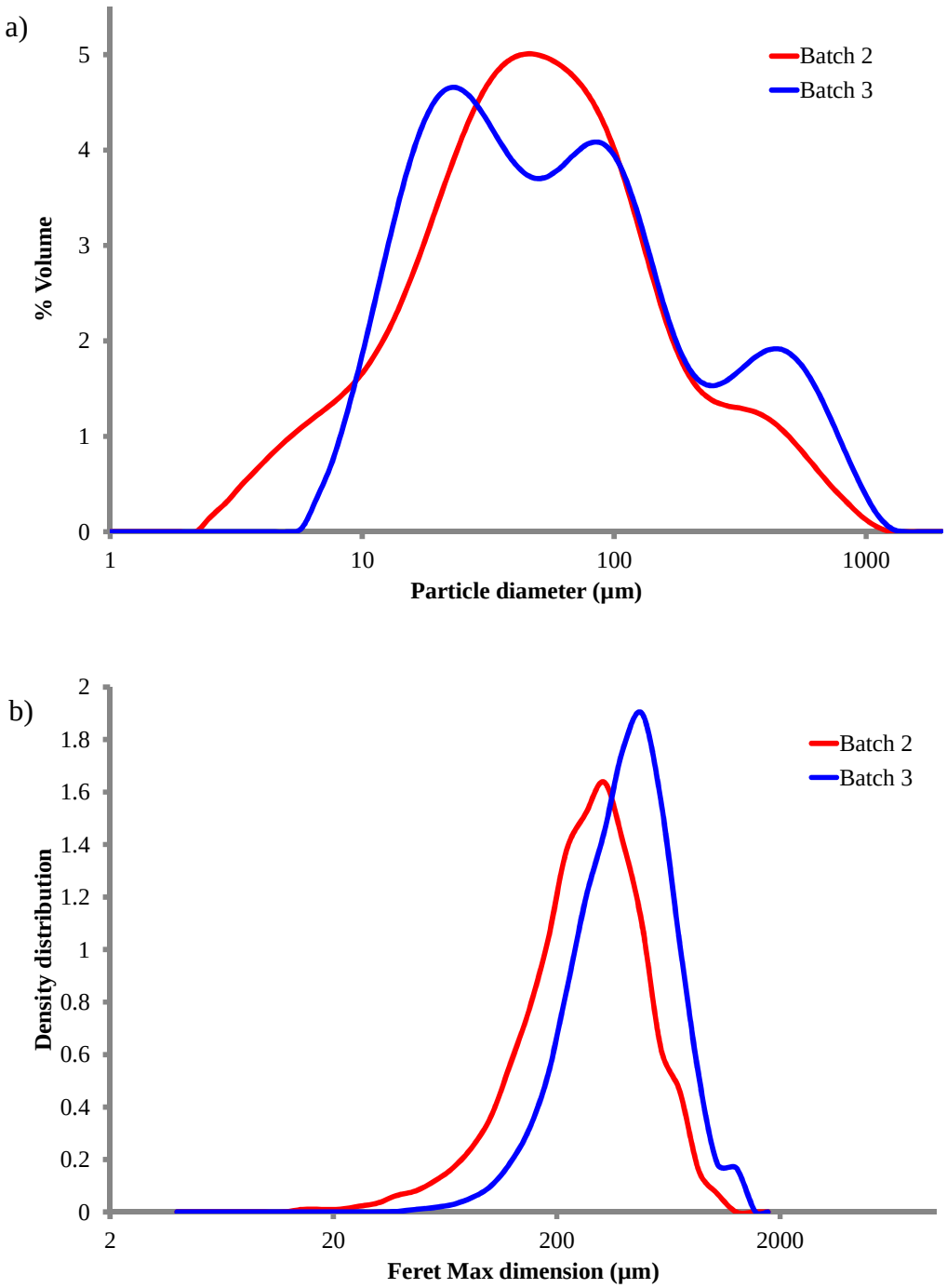

Figure 6-4: a) LD volume distribution, b) QICPIC Feret Max volume distribution for COA batches 2 and 3, respectively.

Table 6-1: Median particle size, polydispersity (PD) (from LD and QICPIC: EQPC and Feret Max), bulk density (BD) and tapped bulk density (TBD) results from measurements of sub-samples of batches 2 and 3.

	LD[a]		QICPIC: EQPC (left), Feret Max (right)[a]					
	D50/ µm	PD/ a.u.	D50/ µm	PD/ a.u.	D50/ µm	PD/ a.u.	BD[b]/ g/mL	TBD[b]/ g/mL
Batch 2	44 ± 1	4.64 ± 0.42	74 ± 2	1.41 ± 0.84	283 ± 20	1.63 ± 0.24	0.27	0.42
Batch 3	51 ± 1	7.11 ± 0.15	84 ± 2	1.23 ± 0.14	413 ± 18	1.31 ± 0.10	0.16	0.25

[a] Particle size values quoted as mean ± 1 standard deviation (n = 3 for both batches)

[b] BD = bulk density, TBD = tapped bulk density (after 750 taps)

The particle size data from both LD and QICPIC image analysis showed that batch 2 had a smaller median particle size than batch 3; however, the two techniques differed when PD was compared. In this case, PD was an approximation of the span of particles in a given sample and was calculated using the following equation, applicable to both LD and QICPIC data:[3, 4]

$$PD = \frac{(D90 - D10)}{D50} \tag{6-1}$$

where D10 and D90 are the 10th and 90th percentiles of the distribution and D50 is the median value. Samples that have higher values for PD will generally pack better than samples with lower PD values for samples of needle shaped morphology. This is because the smaller needles fill the interstices between the longer needles, and in doing so increases the bulk density of the sample. The different trends observed in the PD data from LD and QICPIC are likely due to the different basis of measurement for each technique. For LD, the calculated distribution is that of calculated spheres, generated by the instrument software, which have the same scattering patterns as the particles observed. It has been shown previously that the observed scattering pattern is dependent on the orientation that a given needle

diffracts the beam (either width or length axis) with the reported distribution being an average of all orientations.[5] Therefore, considering the results for LD, batch 2 would appear less polydisperse than batch 3 as the range of needle length in the samples was less than that of batch 3, and as a result, the PD results become weighted towards the increase in aspect ratio in the samples with a higher proportion of longer needles. Conversely for QICPIC image analysis, the particle size distribution is dependent on the number of pixels that each projected particle fills on the imaging CCD. Therefore, the orientation of the particle in the measurement window does not affect the dimensions calculated for each of the particles. The PD of the distributions is, thus, independent of the way that the particles are dispersed, and the distribution is calculated either based on area (EQPC), or length (Feret Max). Consequently, it is likely that the PD calculated by QICPIC is more representative of the sample, as the aspect ratio (length/ width) is not factored into the data. The bulk and tapped bulk density results for batches 2 and 3 confirm this hypothesis as batch 2 displayed both higher BD and TBD results than did batch 3, indicating the particles packed much better for batch 2. It has been shown previously that an increase in bulk density results in an increase in the Raman signal generated from static samples,[6] and similarly for changes in bulk density during a granulation experiment.[7] Taking this into account, it was assumed that the changes in Raman intensity observed were a result of the differing bulk densities between the batches.

The Raman and particle size data were also compared with the initial COA batch received from GSK (Tonbridge, Kent, UK) that was used to complete the previous DoE study (batch 1) described in Chapter 5. It was found that batch 3, although not identical, was not significantly different from 1, with batch 2 displaying considerable differences in particle size and, thus bulk density.

It was important to confirm whether or not the differences between batch 2 and batch 3 had an effect on the drying characteristics of the material, which would determine if the batches could be directly compared. For this, drying experiments were carried out using samples of each batch. Slurries of COA were made using the procedure outlined in section 6.2.8 and drying was carried out with a 60 min convective N_2

blowdown period followed by a continuously agitated vacuum conductive period which was carried out until a steady state had been reached in the Raman signal. Representative drying curves based on the methanol contribution at 1044 cm^{-1} are shown in Figure 6-5 for batch 2 and 3, respectively.

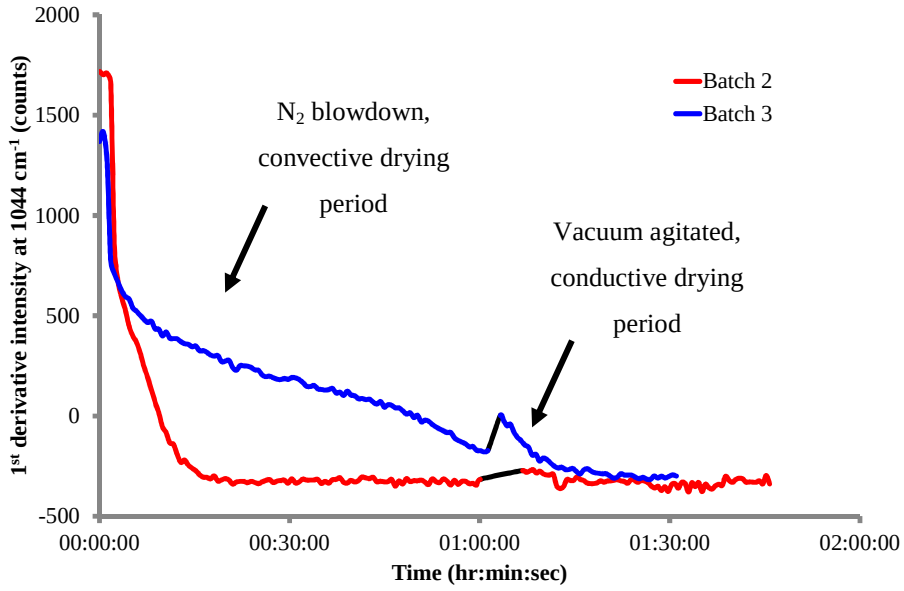

Figure 6-5: Representative drying curves of methanol contribution at 1044 cm^{-1} for batches 2 and 3 based on Raman measurements recorded through the side of vessel; 60 min convective period followed by conductive drying until a steady state was reached.

The drying curves for batches 2 and 3 showed differing drying characteristics during the N_2 blowdown period where the particles from batch 2 appeared to dry at a greater rate during the convective drying period than the particles from batch 3. This observation was consistent for all experiments conducted with particles from batch 2 compared to those from batch 3. The reasons for this can be described by considering the smaller particles (shorter needles) present in batch 2. During the N_2 blowdown period, the drying rate can be affected by two parameters: the contact drying as a result of heat transfer from the surface of the vessel to the particles, and convective drying from the carrier gas to the particles. The difference in drying rate for fine and coarse particles as a result of contact from the vessel walls has been described previously, albeit for mechanically agitated particles by Schlunder and Tsotsas.[8, 9]

Using theoretical modeling and experimental data for spherical particles, these authors determined that fine material dries at a faster rate than coarse material under the same conditions. This occurs as the contact heat transfer coefficient (α_{ws}) increases strongly with decreasing particle diameter via the following relationship:[8, 9]

$$\alpha_{ws} = \phi_A \alpha_{wp} + (1 - \phi_A) \frac{2\lambda_G / d}{\sqrt{2} + (2l + 2\delta)/d} + \alpha_{rad} \qquad 7\text{-}2$$

Where ϕ_A is a plate surface coverage factor, α_{wp} is the heat transfer coefficient for a single particle, d and δ are the particle diameter and roughness, respectively, *l* is the mean free path of the gas molecules, and α_{rad} is the radiative heat transfer coefficient. α_{wp} is also affected by changes in particle diameter.[9]

Conversely, for the experimental conditions described in these experiments, it is likely that the effect on the drying rate of the convective N_2 gas is far greater than that of heat transfer from the walls in a static bed and, therefore, the increase in drying rate from batch 2 to batch 3 was most likely not due to an increase in (α_{ws}) for the smaller particles. Instead, the increase in drying rate was likely attributable to the greater total surface area of the smaller particles (shorter needles), allowing the N_2 gas to carry away the excess methanol at a quicker rate than for larger particles (longer needles). In batch 2, the N_2 gas had removed effectively all the methanol with an LOD of 0.01% wt/wt remaining after 60 min, whereas for batch 3, a higher LOD of 3% wt/wt was present after 60 min N_2 blowdown. In primary manufacturing drying processes, organic solvents are typically dried from API material. Organic solvents generally present a risk to patients, and therefore need to be dried to LOD typically less than 0.5% wt/wt. For these reasons, convective drying is typically employed to remove the majority of solvent from the particles before vacuum agitated drying is utilised to remove the remaining residual solvent. This is in contrast to secondary manufacturing processes (where the drying media is generally water (after wet granulation) that poses no risk to patients) where an LOD of 3% wt/wt can be beneficial for the tableting procedure. In the experiments described

hereafter, the data obtained when drying COA powder from batch 3 are discussed so that better continuity with the DoE study described previously is maintained.

6.3.3 Isolation Data

Table 6-2 shows the drying conditions for each of the seven experiments carried out during the study. In these experiments, an initial N_2 blowdown period was followed by a period of vacuum agitated drying that was terminated when the ratio of two peaks (MeOH: COA) had reached a steady state for 15 min.

Table 6-2: Drying conditions for experimental data set and LOD after each drying stage.

Experiment	N_2 blowdown/ h	LOD after blowdown/ % wt/wt	Agitation strategy [a]	Agitation period/ h	LOD after agitation period/ % wt/wt
1	0 [b]	104 [b]	CA	2.167	0.05
2	0.167	22	CA	1.216	0.05
3	0.333	7	CA	1.750	0.18
4	0.500	4	CA	0.900	0.09
5	1.000	3	CA	0.500	0.35
6	0.167	40	IA	0.100	0.29
7	0.500	15	IA	0.067	0.50

[a]CA = continuous agitation, IA = intermittent agitation (1 min agitation per 30 min of drying)

[b]cake left to filter for 1 h at atmospheric pressure to allow enough methanol to be removed by gravity in order to start drying. LOD quoted is after 1 h period

The LOD at the end of vacuum agitated drying for each experiment was ≤ 0.5% wt/wt (Table 6-2). This confirms that *in situ* Raman spectroscopic measurements are suitable to determine the end point of vacuum agitated drying in real-time. In this work, the drying end point was decided upon by the operator monitoring the Raman signal on a monitor and stopping the drying process once the signal had stabilised for a period of 15 min, however, if the method were to be implemented into a real process, algorithms (such as moving standard deviation analysis) could be established in statistical software that could stop the process without the need for operator approval. The data in table 6-2 also shows that the LOD at the end of the N_2 blowdown for experiments 1 – 5 decreased with increasing blow-down time, however, the relationship was not linear and can be represented by a decaying curve as shown in Figure 6-6.

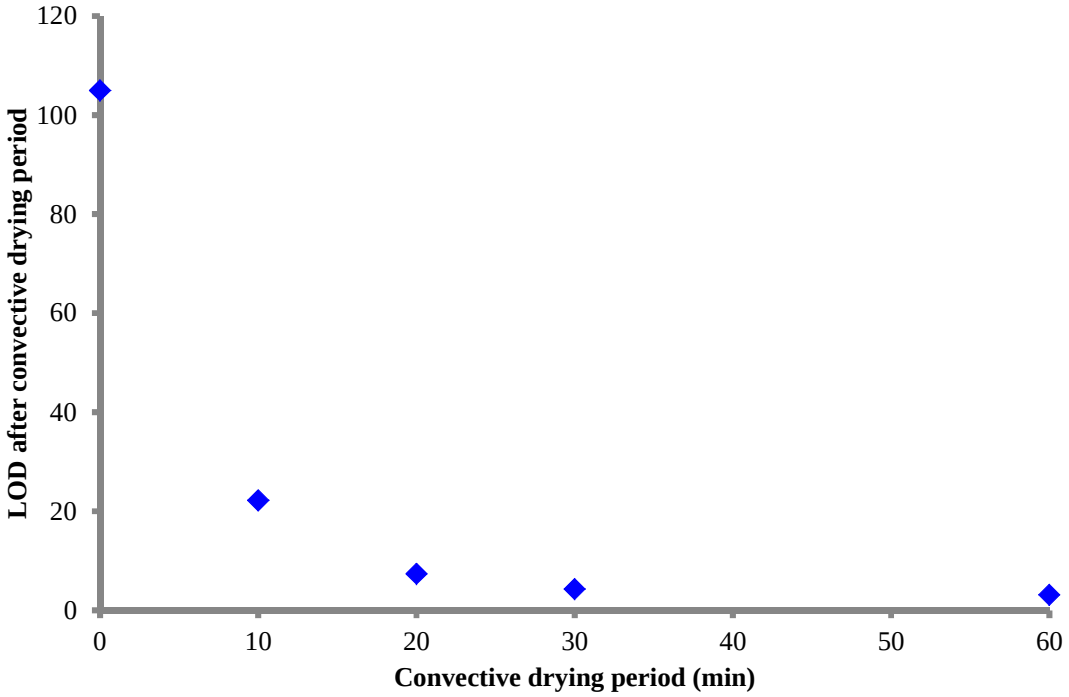

Figure 6-6: Graph showing length of N_2 blowdown vs. LOD after N_2 blowdown for experiments 1 – 5.

Figure 6-6 shows that the initial 0.167 h (10 min) period of blowdown removes most of the excess methanol, however, after this time point, the rate slows significantly as the more tightly bound methanol is removed. The data also indicates that the optimum blowdown period for the data set is 0.5 h as the LOD decrease for an additional 0.5 h is only 1% wt/wt, and therefore was not a significant loss of solvent compared to the energy supplied to the system. In contrast, when experiments 6 and 7 are also considered, greater variability than expected of the LOD after N_2 blowdown was observed when compared with the results from experiments 1 – 5. This effect was likely caused by the seal of the vessel being slightly less tight for experiments 6 and 7 than for experiments 1 – 5. Between each drying experiment, the lid of the vessel was removed in order to remove the dry COA particles from the drier and to clean the glass walls of the vessel, particularly the area where the Raman probe was directed at the powder. It is likely that a small leak had been created between experiment 5 and 6 that meant the N_2 blowdown was not as efficient as for experiments 1 – 5 although the same pressure was recorded on the pressure gauge (as the gauge is located on the cylinder before the vessel). The fact that the LOD values were not repeatable did not present a problem to the data analysis for the *in situ* Raman and particle size measurements discussed in the following sections.

6.3.3.1 Continuous agitation

The purpose of carrying out *in situ* measurements during the removal of methanol from COA particles was twofold: Firstly, Raman measurements were employed to monitor the removal of solvent from the COA particles using two approaches as with previous drying experiments.

i) the change in the ratio of methanol: COA peak was plotted against time in real-time using the IC Raman software (the peaks used for analysis were two point baseline corrected from untreated Raman spectra), where the particles were deemed to be dry when a steady state had been reached for 15 min (Figure 6-7). At the end of drying, the data was exported into MATLAB where further data analysis was carried out.

ii) The second method for monitoring the solvent removal from the COA particles was to plot the 1st derivative signal of a methanol peak vs. time.

Secondly, attempts were made to correlate changes in the Raman spectra to correlate to the measured or observed changes in the physical characteristics of the particles that occurred during drying (described in section 6.3.4.1). This would allow the possibility of real-time detection of attrition (or agglomeration) during drying.

Drying curves based on the ratio of the methanol: COA peaks (1044 cm^{-1}: 911 cm^{-1}) in the untreated Raman spectra, and on the methanol peak centered at 1044 cm^{-1} in the 1st derivative Raman spectra obtained for experiments 1 – 5 are shown in Figure 6-7 a) – e) and 6-8 a) – e), respectively.

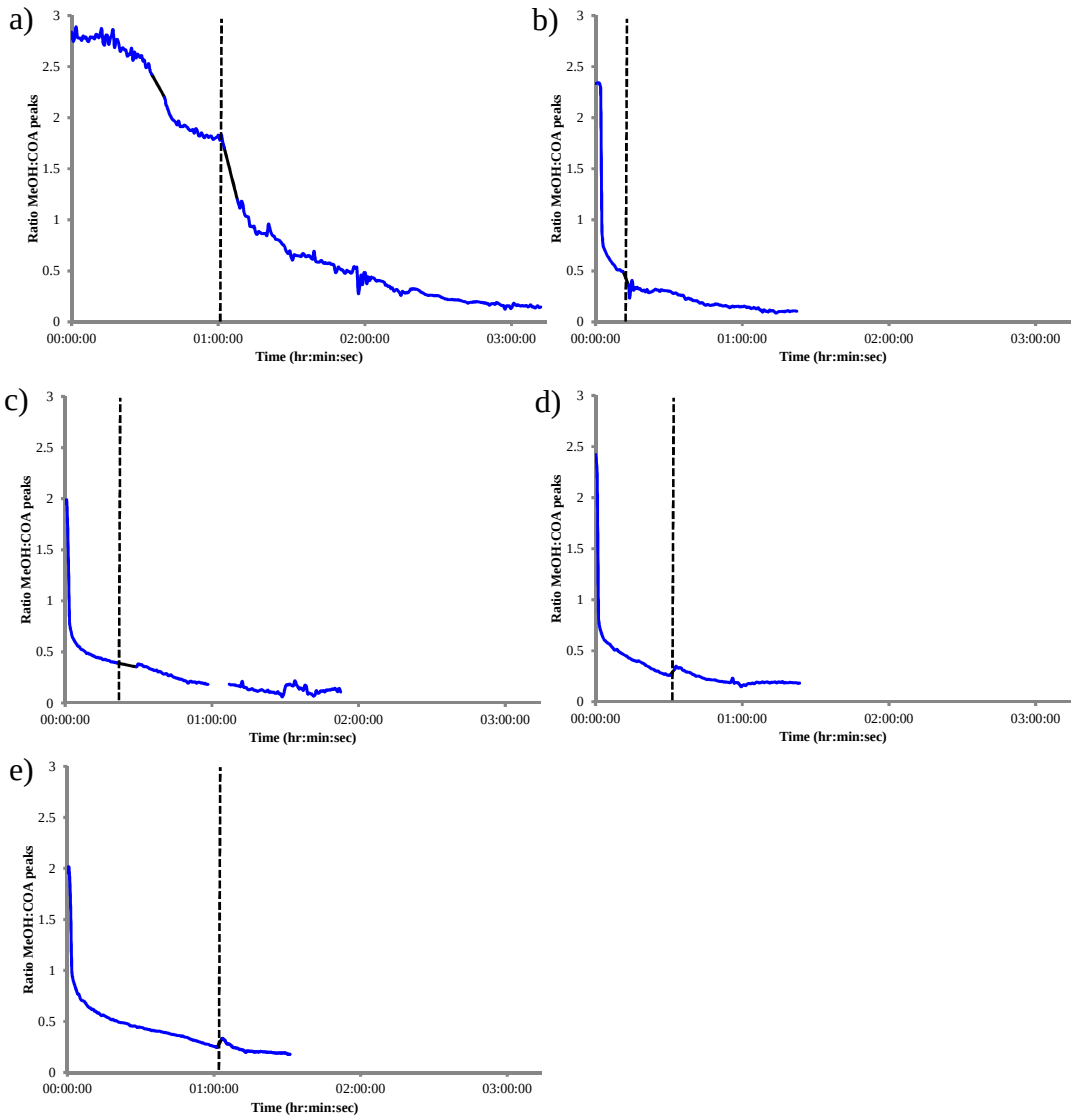

Figure 6-7: combined N_2 blowdown and vacuum agitated period drying curves for experiments 1 – 5, based on the ratio of methanol peak: COA peak (1044 cm^{-1}: 911 cm^{-1}) in the Raman spectra. a) no N_2 blowdown (cake allowed to filter at atmospheric pressure for 1 h), b) 0.167 h N_2 blowdown, c) 0.333 h N_2 blowdown (10 min section of data removed due to Raman probe slipping from original position, the probe was replaced at around 01:07:00 and then adjusted a 01:29:00), d) 0.5 h N_2 blowdown, and e) 1 h N_2 blowdown. Dashed black lines indicate the end of the N_2 pressure filtration.

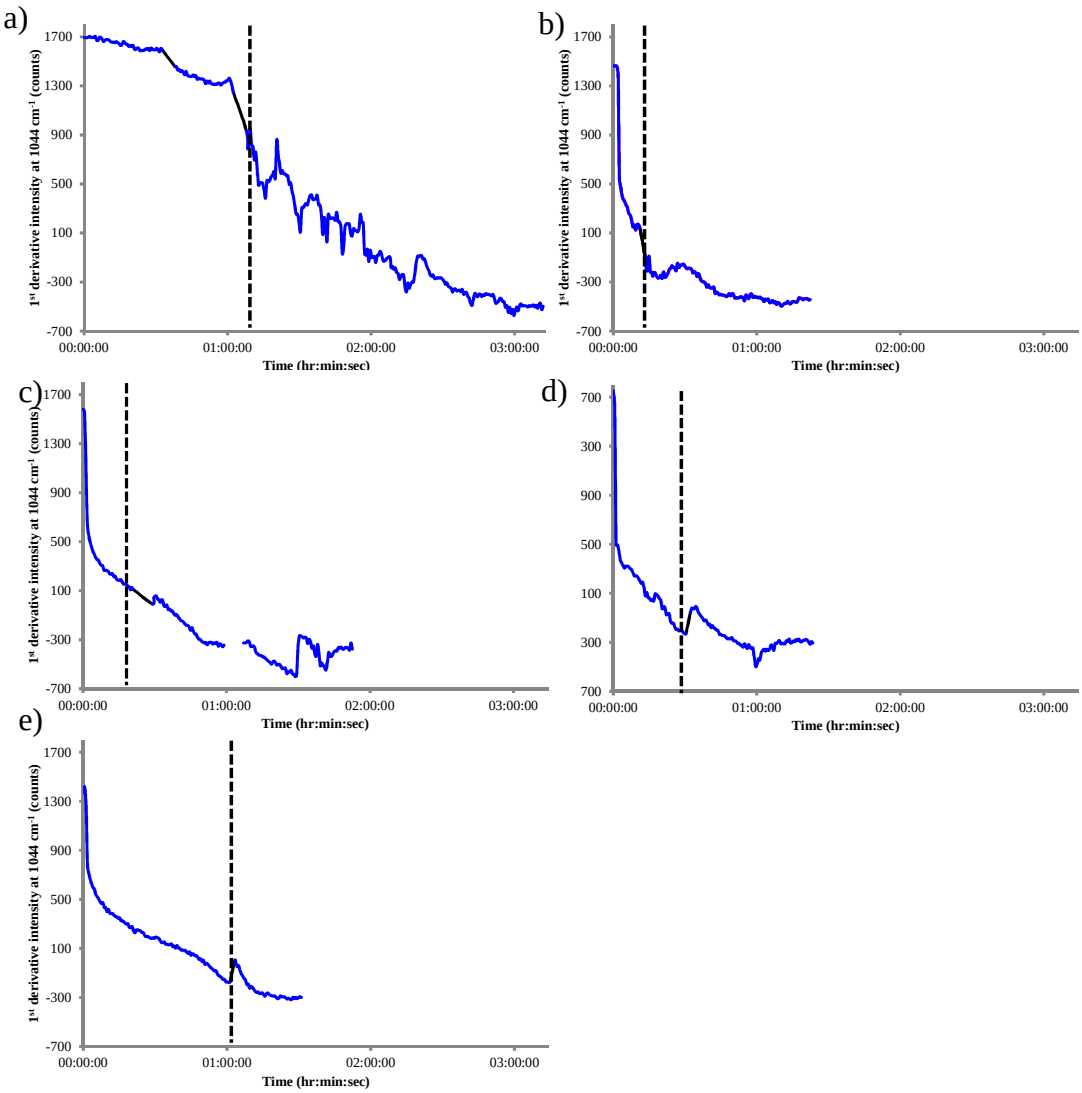

Figure 6-8: combined N_2 blowdown and vacuum agitated period drying curves for experiments 1 – 5, based on the methanol peak centered at 1044 cm^{-1} in the 1st derivative Raman spectra. a) No N_2 blowdown (cake allowed to filter at atmospheric pressure for 1 h), b) 0.167 h N_2 blowdown, c) 0.333 h N_2 blowdown (10 min section of data removed due to Raman probe slipping from original position, the probe was replaced at around 01:07:00 and then adjusted a 01:29:00), d) 0.5 h N_2 blowdown, and e) 1 h N_2 blowdown. Dashed black lines indicate the end of the N_2 pressure filtration.

From Figures 6-7 and 6-8 (also recorded in Table 6-2), there is a general trend that shorter vacuum agitated drying periods are required when the LOD at the start of the

period is lower. This was somewhat expected when the same vacuum agitated drying conditions were employed for each experiment (continuous agitation, jacket temperature: 60 °C and pressure range: 50 – 100 mbar), although the data for the vacuum agitated period after 0.333 h N_2 blowdown (experiment 3 (c) in Figures 6-7 and 6-8) does not conform to the trend. Here, it was expected that a vacuum agitated drying time of around 1 h would be required to remove the remaining methanol (7% wt/wt), however, the time required to remove the solvent was 1.75 h. A small change in the vacuum pressure can have a large effect on the drying rate, as the boiling point of the solvent can change considerably. For example, the boiling point of methanol at atmospheric pressure is 65 ºC, whereas at 50 mbar, it is 33 ºC.[10] Therefore, towards the upper limit of the pressure range used in drying experiments, the drying rate was slower than near the lower limit due to the higher energy required for the transition of the methanol to the gas phase.

6.3.3.2 Intermittent agitation

Drying curves based on the removal of methanol from the COA particles were also produced for the two intermittently agitated experiments. The curves based on the intensity ratio of the COA: methanol peaks for experiments 6 and 7 are shown in Figure 6-9 a) and b) and Figure 6-10 a) and b), respectively.

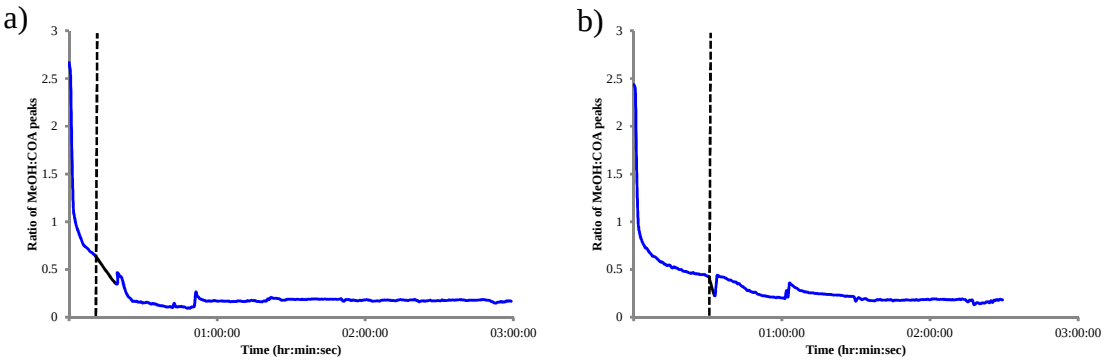

Figure 6-9: Combined N_2 blowdown and vacuum agitated period drying curves for experiments 6 and 7, based on the ratio of methanol peak: COA peak (1044 cm^{-1}: 911 cm^{-1}) in the Raman spectra; a) 10 min N_2 blowdown, and b) 30 min N_2 blowdown. Dashed black lines indicate the end of the N_2 pressure filtration.

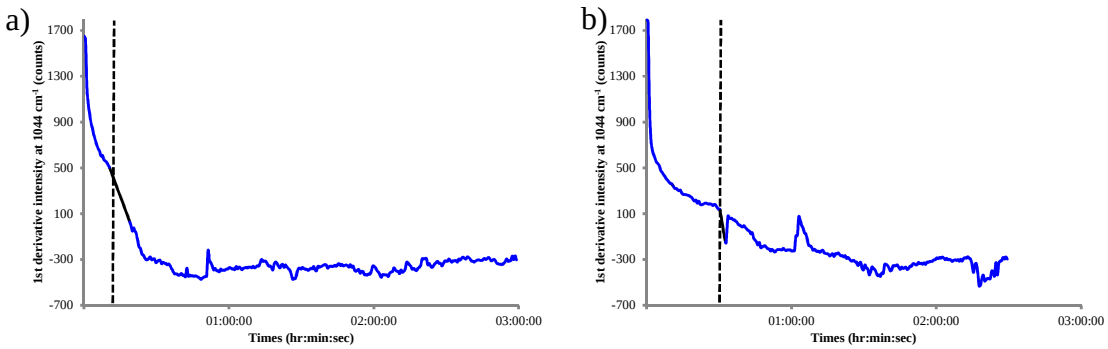

Figure 6-10: Combined N_2 blowdown and vacuum agitated drying period curves for experiments 6 and 7, based on the methanol peak at 1044 cm^{-1} in the 1st derivative Raman spectra; a) 10 min N_2 blowdown, and b) 30 min N_2 blowdown. Dashed black lines indicate the end of the N_2 pressure filtration.

For these experiments, vacuum drying was terminated when the signal obtained when monitoring the ratio of two peaks did not vary significantly during two successive 1 min agitation periods. Furthermore, for these experiments, it appeared that peak ratio method of analysis gave smoother drying curves with less variability when the particles were close to being dry, this is typical of these analyses and is the reason that peak ratio data was used in order to determine the drying end point in this data set.

6.3.4 Physical processes during drying

The Raman data were subjected to more in-depth analysis to determine if changes in the spectra obtained from the particles during drying could be correlated to either changes in the particle size measured at the start and end of each experiment (using LD and image analysis methods) or attributed to physical processes that are known to occur during the operation, for example, balling. The evaluation was carried out in two stages: first, the data from the N_2 blowdown period was investigated, where it was expected that there would not be a significant change in the particle size observed. Secondly, the Raman data obtained during the vacuum drying stages was investigated.

6.3.4.1 Physical processes during N_2 blowdown

Shown in Table 6-3 are the average D50 particle size values obtained when LD and QICPIC (EQPC and Feret Max) analysis was carried out on samples extracted from the drier after the N_2 blowdown period for each experiment.

Table 6-3: D50 particle size values obtained for LD and QICPIC analysis.

Experiment	LD D50/ µm	QICPIC EQPC D50/ µm	QICPIC Feret Max D50/ µm
1	52 [a]	79 [a]	392 [a]
2	56	82	381
3	54	84	411
4	50	78	391
5	58	87	421
6	56	85	405
7	56	87	394

Average D50 values of batch before slurries were made: LD = 51 ± 1 µm, EQPC = 84 ± 2 µm, Feret Max = 413 ± 18 µm. The mean values quoted are the average of duplicate measurements made from 3 sub samples of each batch (as is described in section 6.3.2).

[a] cake left to filter for 1 h at atmospheric pressure to allow enough methanol to be removed by gravity in order to start drying. LOD quoted is after 1 h period

On initial inspection, the data in Table 6-3 suggests that no needle breakage occurred (attrition) during the N_2 blowdown stage of drying. Indeed the LD data suggests that some form of particle agglomeration may have occurred (where an increase in D50 relative to the measured batch mean was observed for all samples subjected to N_2 blowdown). It could be argued that the EQPC results from dynamic image analysis generally agreed with this observation; however, the Feret Max data did not show the same trend. There are two main modes of agglomeration possible when needle shaped particles are considered: side-by-side, where particles form liquid bridges along their length dimensions making thicker needles, and end-to-end, where particles form liquid bridges on their width dimensions resulting in longer needles.

Consideration of the Feret Max data calculated from QICPIC measurements shows that end-to-end agglomeration was not significant, but suggested some minor needle breakage may have occurred during the blowdown process (considering the data from samples 1, 2, 4 and 7). Conversely, the LD and EQPC data suggests that some side-to-side agglomeration had taken place during the blowdown period (a change in needle width would not be represented in Feret Max data).

It has been reported previously in work carried out at AstraZeneca (Macclesfield, UK) that attrition rather than agglomeration was the dominant physical process that occurred during the N_2 blowdown phase during the development a needle shaped API.[11] In their work, a 9% reduction in average particle diameter (measured by LD) was observed after the N_2 blowdown stage rather than a small increase as observed here. The authors attributed the reduction in particle size to the extent of the stress caused by the application of N_2 exceeding that of a critical limit required for needle breakage to occur. However, their work was carried out at an applied N_2 pressure of 1.6 bar which was over three times higher than the pressure applied to the COA particles in the data reported here. Therefore, it is likely that the 0.5 bar applied to the COA particles was not sufficient to reach the critical amount of stress required for significant needle breakage. However, this would need further investigation that is beyond the scope of this thesis.

As previously discussed in Chapter 4, the examination of only median values does not provide an adequate representation of the particle distribution obtained and can lead to misleading interpretation of data sets. Therefore, the distributions obtained from each technique were also examined. The distributions obtained are given in Figure 6-11 a) – c) for LD volume weighted distribution, EQPC volume weighted distribution and Feret Max volume weighted distribution, respectively.

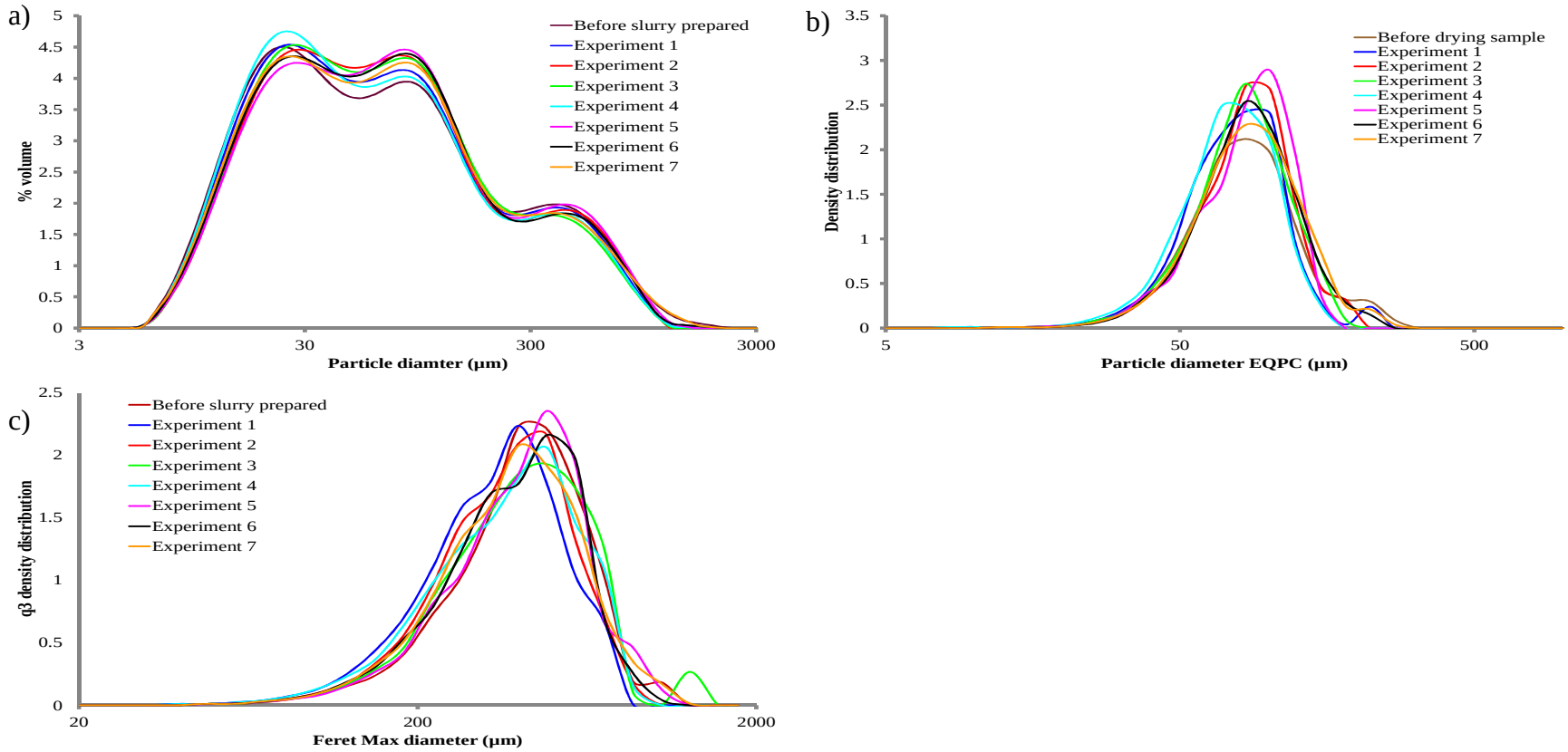

Figure 6-11: Average particle size distributions obtained before and after N2 blowdown periods for experiments 1 – 7: a) LD volume weighted distribution, b) EQPC volume weighted distribution and c) Feret Max volume weighted distribution.

The particle size distribution data obtained from both LD and dynamic image analysis methods indicated that there was not a significant amount of either agglomeration or breakage of the COA particles during the N_2 blowdown stage. As shown previously for LD measurements, a change in average needle length for COA causes a shift in the two main modes present in the distribution with the mode at ~20 µm increasing in % volume as less medium length and long needles are present to diffract the laser light. With the exception of experiment 4 (which had the lowest D50 value for LD), the ratio of the two main modes in the particle size distributions did not vary greatly from the sample measured before the slurry of COA and methanol was prepared. The greater number of fines observed for experiment 4 is likely attributable to a greater number of fines present in the initial slurry rather than a greater amount of needle breakage during N_2 blowdown.

Examination of the Feret Max particle size distributions obtained confirmed that needle breakage was not significant during the N_2 blowdown phase of drying. The distributions, although generally overlaying each other at first glance, were reasonably variable in both coarse and fine tails. Further inspection of the tails indicated that in all of the experimental data for the samples, there were a greater number of fines (short needles) than in the "before drying" sample, whereas there was no indication of less coarse (long needles) being present (with the exception of experiment 1). This indicated that there was some, if not significant, needle breakage during blowdown.

The EQPC data shown agrees with both the LD and Feret Max data discussed where there was no significant shifts in the particle distribution caused by the application of N_2 blowdown.

For all experiments, sampling of the cake was performed using a sample thief inserted through one of the ports in the lid. There are known issues with using thief probes to obtain samples from vessels due to the disruption of the bed and uneven flow of the powder into the probe.[12, 13] For these experiments, it was assumed that the sampling error would be constant from sample-to-sample due to the same thief being used.

In situ Raman measurements were also made during the N_2 blowdown period and shown in Figure 6-12 a) and b) are example 1st derivative spectra (550 – 1250 cm^{-1}) from experiment 5 (longest blowdown period), and the associated univariate drying curves from the methanol peak centred at 1044 cm^{-1} and the COA peak centred at 1076 cm^{-1}.

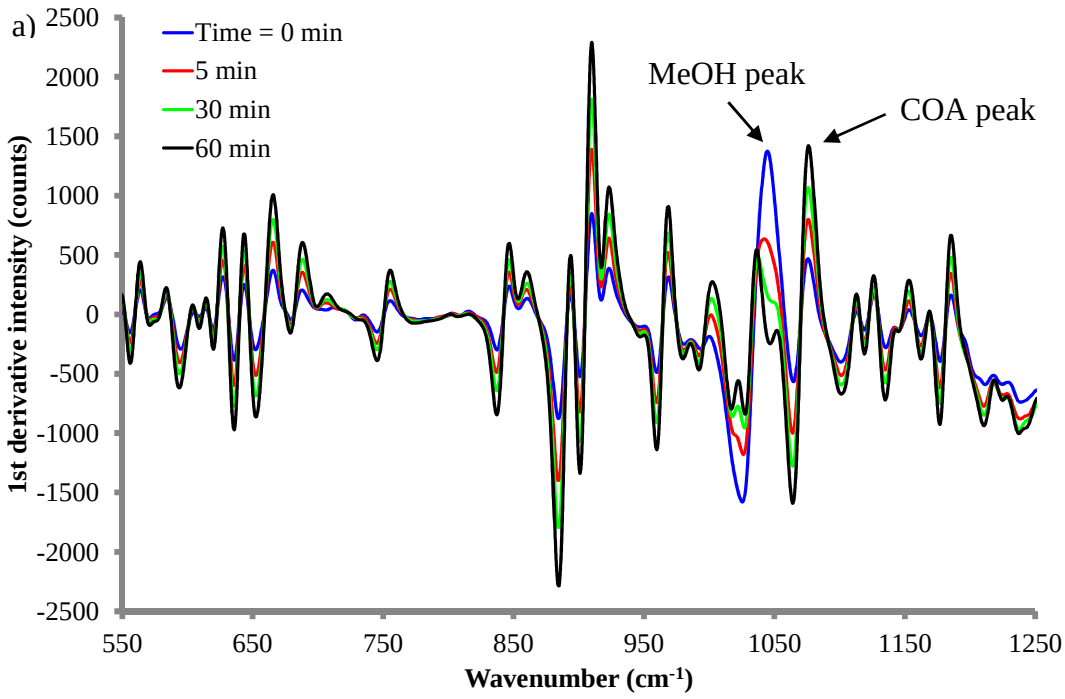

Figure 6-12 a) Example 1st derivative spectra at stated time points (550 – 1250 cm^{-1}) from experiment 5 (longest blowdown period).

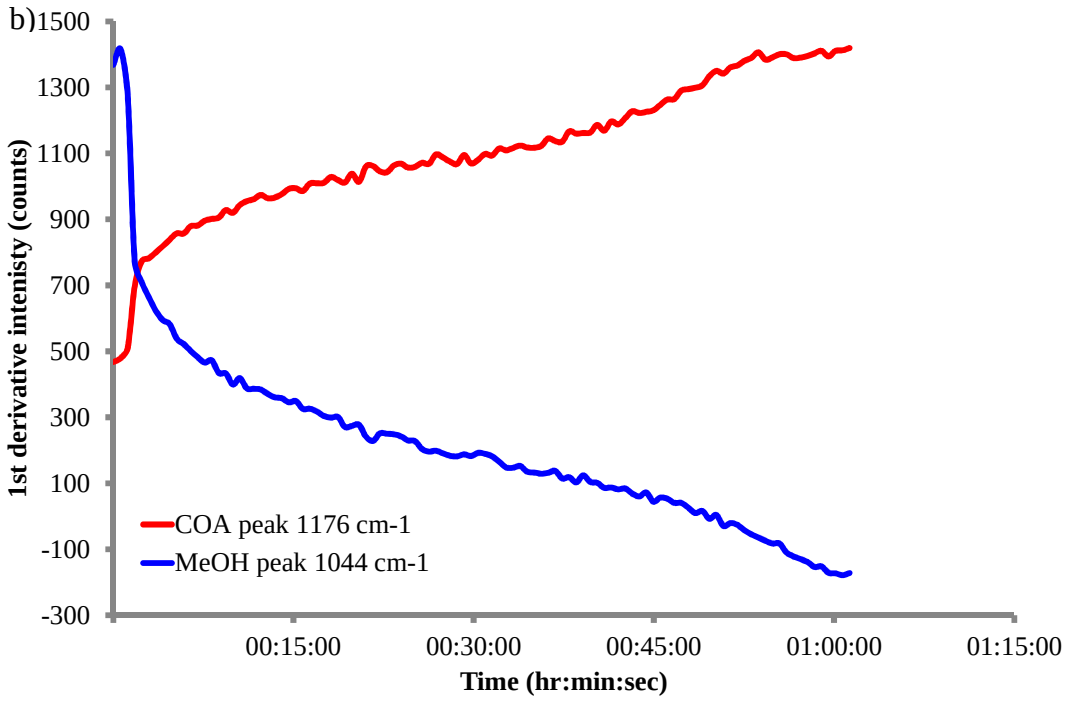

Figure 6-12 b) univariate drying curves from the methanol peak centred at 1044 cm^{-1} and COA peak centred at 1076 cm^{-1}.

The Raman data shown in Figure 6-12 demonstrated the dependence of the signal arising from the COA particles on the contribution from the methanol solvent. The increase in signal arising from COA is attributable to two complimentary processes that occur as the methanol is removed under pressure, i.e. there was less methanol present to contribute to the Raman scattering and the bulk density of the COA particles increased as the static bed of particles became increasingly packed. At the commencement of the N_2 blowdown period there is a great excess of methanol in relation to COA particles in a slurry and thus, the sample volume of the Raman probe is focused on an area with a low number of COA particles, hence, a low signal arises from the COA peak. When the positive pressure is applied, the excess methanol compresses the loose particles in the slurry into a packed bed of wet particles (as it is removed very quickly), resulting in a substantial reduction in the signal arising from methanol and a sharp rise in the signal arising from COA. As the particles become packed, the bulk density of the cake increases as the gaps between the particles that were initially filled with methanol were now compressed. Consequently, an increase

in the number of COA particles in the measurement volume occurred, hence, the increase in signal. This densification process continued as more and more of the methanol was removed and, therefore, the increase in COA signal also continued. At the end of the N_2 blowdown period for experiment 5, the measured LOD was 3% wt/wt and so the majority of methanol had been removed. No further investigation of the Raman data during the N_2 blowdown period was performed due to the particle size evaluation data indicating that there were no significant changes in the average needle length (i.e there was no attrition caused) during the time period.

6.3.4.2 Balling during vacuum agitated drying

In the DoE study described in Chapter 5, the formation and break up of dense aggregates during the drying process, known as balling, caused a significant perturbation to the Raman intensity measured during drying. In the pharmaceutical industry, balling is generally thought to be caused by vacuum agitated drying being commenced at a time when the LOD exceeds a critical point that is required for the aggregates to form. At an industrial scale, these aggregates can be extremely detrimental to the inside of a drier, causing significant damage before the second critical LOD is reached where they begin to break up. Therefore, the ability to detect this phenomena in real-time without the need for an operator to watch the process at all times would be beneficial, as measures could be taken such as stopping agitation until a more suitable LOD had been reached to resume agitated drying. This is not possible by monitoring the off-gas from the drier, either with mass spectrometry or by using an NIR/ MIR gas cell (commonly used to monitor drying processes), as information is only gained regarding the concentration of solvent and not about the state of the particles themselves.

By placing the Raman probe in the orientation described in section 6.2.4, it could not be assumed that the same features would be present in the Raman data if balling were to be observed, as in the previous orientation through the lid of the vessel. Additionally, the mechanisms that lead to balling are still not well understood (other than a high starting LOD), and therefore, design of a suitable experiment was difficult. Experiment 1 had no N_2 blowdown as part of the experimental conditions

and as such, vacuum agitated drying was started at a very high LOD of 104% wt/wt (typical API drying processes at industrial scale would begin vacuum agitated drying at LODs of around 5% wt/wt for shear sensitive materials). The COA particles were then agitated continuously at 10 rpm until the particles were deemed dry based on the Raman signal (ratio of COA/MeOH reaching steady state for 15 min). Whilst monitoring the change in COA signal during this time period (Figure 6-13), a similar feature was observed to that reported previously using either uni- or multivariate data analysis methods; however, in this case the trend was opposite with a sharp decrease in Raman signal followed by a sharp increase in Raman signal, which was thought to be caused by the formation and disintegration of balls/ aggregates. Images recorded during this period of significant signal change are shown in Figure 6-14.

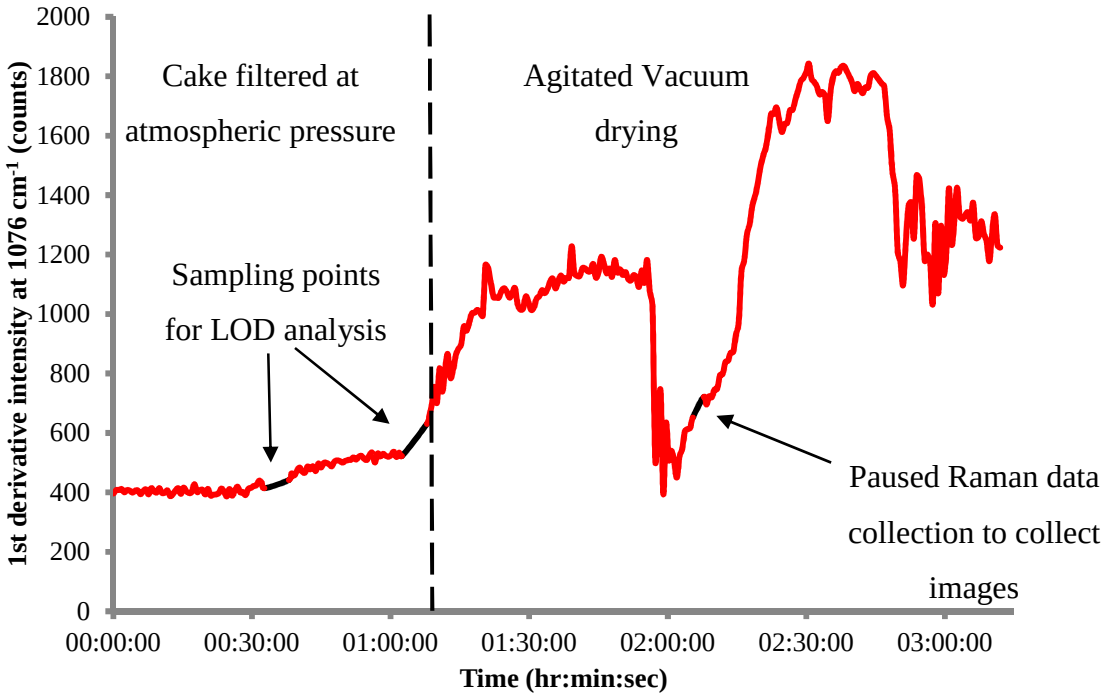

Figure 6-13: 1st derivative intensity at COA peak centred at 1076 cm^{-1} showing the univariate COA drying profile. Also marked on the plot are the sampling points where data analysis was paused (black).

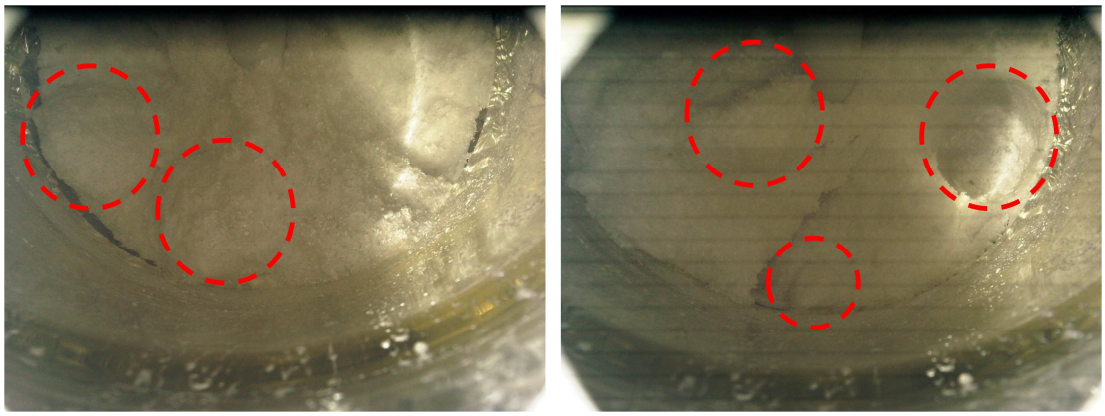

Figure 6-14: digital images recorded through port in the lid of the drier when Raman data acquisition was paused during the assumed balling period (dashed red circles indicated where aggregates are observed in images).

The Raman time series plot shown in Figure 6-13 is best described by dividing the data into two sections. The first section or time period occurs during the first hour when the slurry was left to filter without the application of a positive pressure of N_2. During this time, the COA particles were subjected to sedimentation as the methanol was slowly filtered off. This gave rise to a very different drying curve to those obtained in experiments 2 – 7 where the N_2 blowdown resulted in a packed bed of particles. For these reasons, only a small increase in COA signal was observed over the hour long period rather than the sharp increase associated with an increase in the bulk density as before. The measurement volume of the Raman probe was consequently not subjected to denser areas of COA particles, and therefore, explains why only a small change in COA signal was observed.

The second time period is the remaining drying time when agitated vacuum drying was employed. During this time period, the application of the vacuum removed any excess methanol rapidly in the same manner as a Buchner funnel resulting in the COA particles becoming more densely packed, which caused the sharp rise in the COA signal observed from around 1hr 7 min to 1 hr 25 min. The COA signal then remained relatively constant indicating that conditions in the drier remained saturated with solvent vapour as the particles were agitated. At around 1 hr 45 min, a sudden drop in the Raman signal was observed owing to the formation of aggregates (onset

of balling). It is thought that the Raman signal drops due to the number of COA particles observed during each measurement. As the balls tumble around freely in the drier, the Raman spot is only focused on each aggregate for a small amount of time during the measurement. As the aggregates break up gradually, the bulk density increases rapidly due to the Raman probe then being focused on the densest regions of the particles, however, as drying was continued, the remaining dense aggregates also broke up resulting in the steady state observed at the end of drying. In order to confirm that the observed effects in the Raman data were in fact caused by balling as hypothesised, data collection was paused and the vacuum removed in order to collect digital images of inside the vessel (vacuum and data collection was subsequently resumed). The images shown in Figure 6-14 confirm that balling had in fact occurred at the time point inferred from the Raman data in real-time.

It is difficult to determine from univariate analysis alone if the net increase in Raman signal observed throughout the vacuum agitated drying period for experiment 1 (excluding the data collected during balling) was a result of the bulk density increase caused by attrition of the COA needles or rather other competing drying factors resulting in changes in the bulk density. For example the removal of free methanol from the gaps between the COA particles would lead to a similar increase as the sampled volume would contain more COA particles. The next section investigates the attrition of the COA needles caused by vacuum agitated drying, with examination of the particle size data collected and both further univariate and multivariate analysis of the Raman data. Furthermore, balling was only observed during experiment 1 and therefore, the Raman data observed for experiment 1 was likely not representative of experiments 2 – 5. Furthermore, experiments 6 and 7 employed intermittent agitation, which meant that smaller changes in average particle size were expected as a result of the mode of agitation employed during vacuum agitated drying.

6.3.4.3 Needle breakage during vacuum agitated drying

Shown in Table 6-4 are the average D50 particle size values obtained when LD and QICPIC (EQPC and Feret Max) analysis was carried out on samples extracted from the drier after the vacuum agitated drying period. Table 6-4 is followed by Figures 6-15 and 6-16. Figure 6-15 shows plots of the particle size distributions obtained for each experiment. Figure 6-16 shows plots of D50 vs. agitation time (a) – c)) and LOD at the start of drying (d) – f)) for all analysis methods, respectively.

Table 6-4: D50 particle size values obtained for LD and QICPIC analysis after vacuum drying period.

Experiment	LD D50/ µm	QICPIC EQPC D50/ µm	QICPIC Feret Max D50/ µm
1 [a]	38	57	236
2 [a]	39	60	216
3 [a]	39	55	181
4 [a]	38	63	189
5 [a]	42	61	221
6 [b]	48	76	343
7 [b]	50	79	368

[a] Continuous agitation carried out during vacuum drying period, [b] intermittent agitation carried out during vacuum agitated drying period.

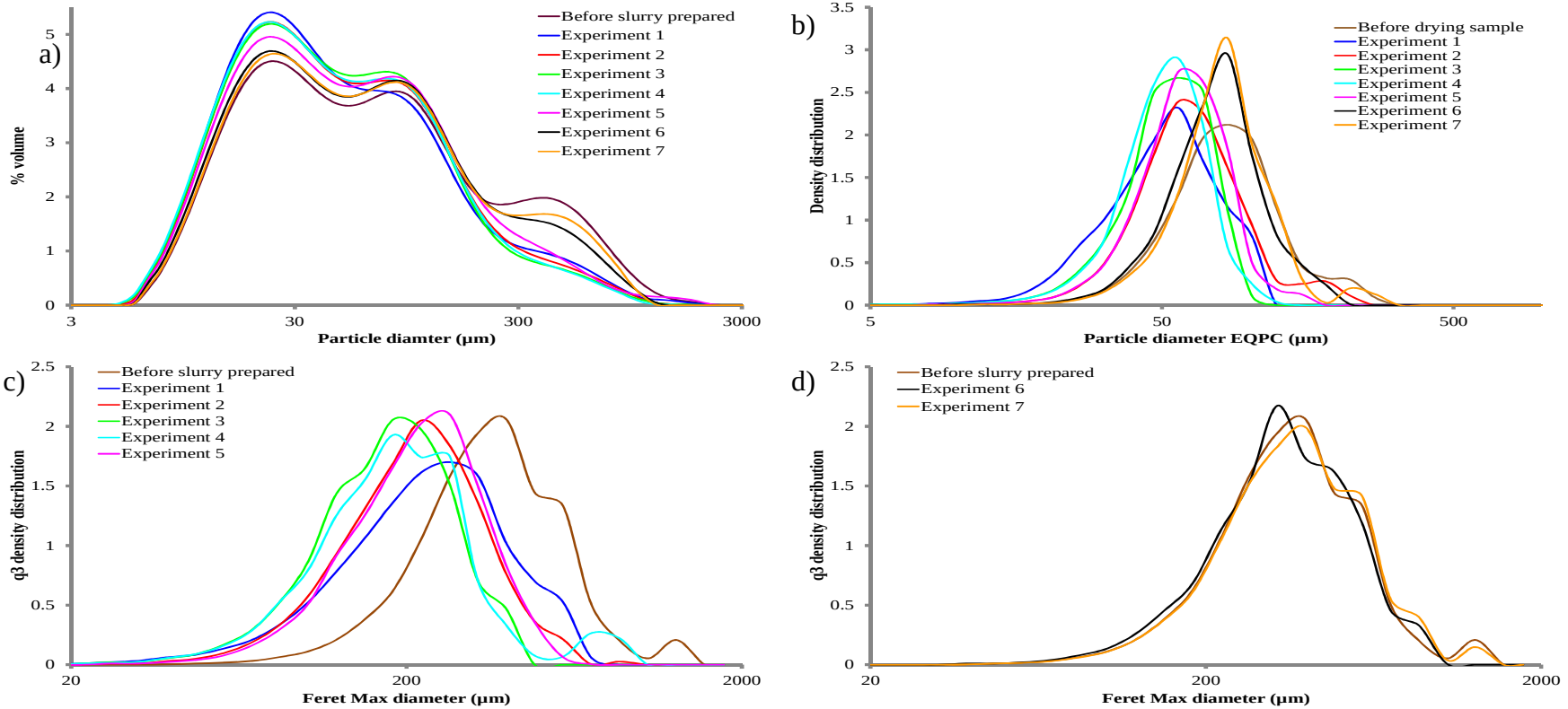

Figure 6-15: Average particle size distribution data obtained before slurry prepared and after vacuum agitated drying periods from experiments 1 – 7: a) LD volume weighted distribution, b) EQPC volume weighted distribution and c) Feret Max volume weighted distribution; i) continuously agitated experiments, and ii) intermittently agitated experiments.

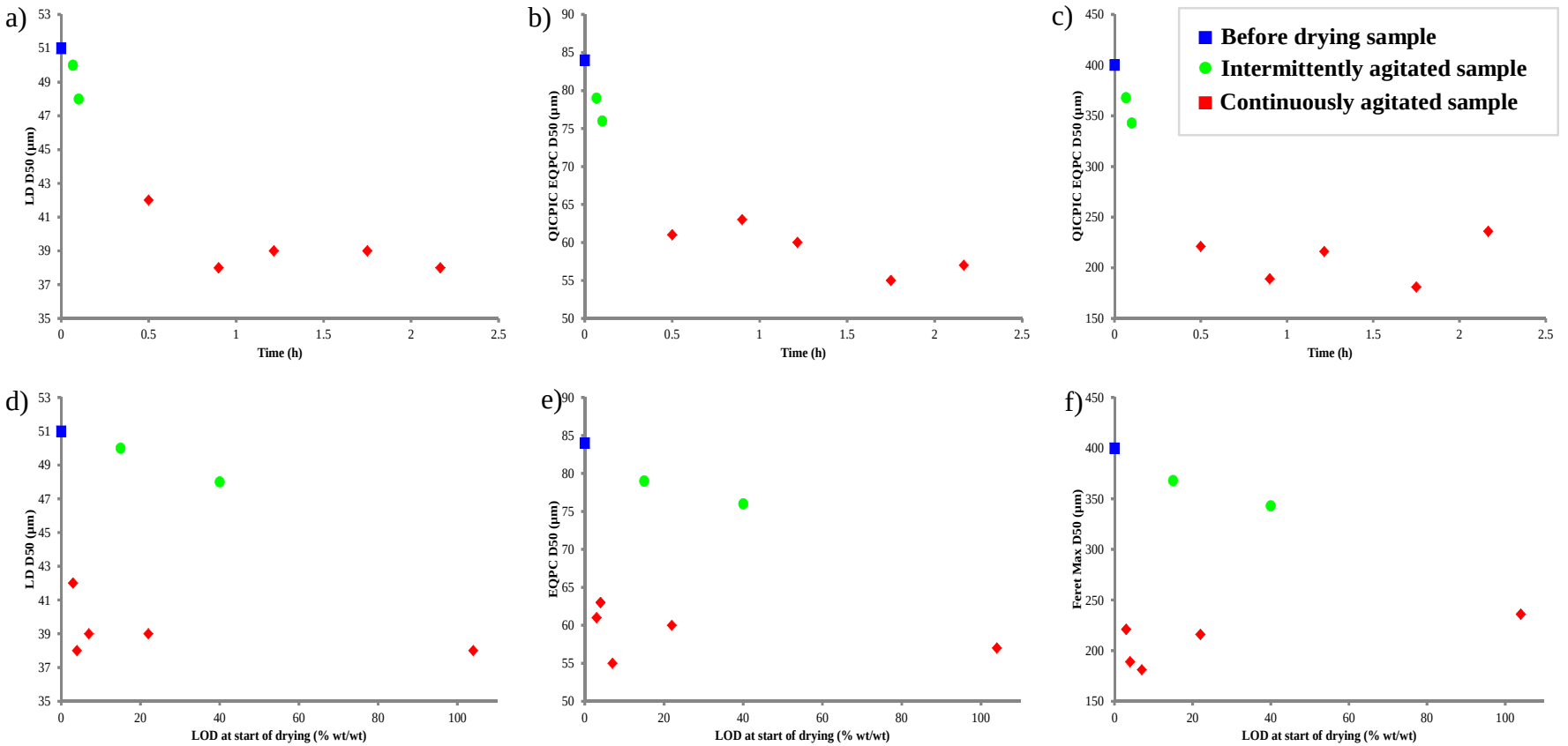

Figure 6-16: Plots of D50 values vs. agitation time for a) LD, b) QICPIC EQPC, c) QICPIC Feret Max and LOD at the start of vacuum agitated drying vs. agitation time for d) LD, e) QICPIC EQPC, f) QICPIC Feret Max.

Considering the data in Table 6-4 and Figures 6-15 first, the D50 values obtained from the continuously agitated experiments are considerably lower than the values obtained from the intermittently agitated experiments. From this, it follows that the distributions obtained for the continuously agitated experiments displayed a greater number of fines (and lower number of coarse particles) than the intermittently agitated experiments. In fact, by examination of the distributions alone, it would be difficult to conclude if any significant change in particle size had occurred at all during intermittently agitated drying. Inspection of the particle size data with consideration of the length of agitation time carried out for each experiment was also performed. Particle attrition is generally attributed to shear induced by the impeller and the data in Table 6-4 and Figure 6-15 support this hypothesis,[14-17] however, the relationship between agitation time, particle wetness and attrition is not fully understood.

As the experiments carried out for this study had a defined strategy to identify the drying end point (and additionally, it was demonstrated by particle size analysis that there were no significant changes to the average needle length during the N_2 blowdown period), the conditions of the experiments allowed an investigation into the relationships of the extent of attrition with agitation time and also the effect of initial particle wetness on the extent of attrition caused. The relationship between needle breakage and agitation time for COA under the defined conditions are given in Figure 6-16 a) – c). Figure 6-16 shows that all three particle size techniques used to analyse the particles are in qualitative agreement, where particle breakage during the initial 0.5 hour period appears to be close to linear (up to 1 hour from LD) at which point it seems a threshold was reached where the rate of particle breakage slowed significantly. At the start of the agitation period, there were a high number of long needles present in all of the samples, and these long needles were most susceptible to fragmentation caused by collisions with either the agitator, the walls or other particles. At this point, the attrition rate is high due to the low density and high friability of the COA particles. The attrition rate then slowed at a time when the majority of the needles had undergone the attrition process, with a corresponding increase in the bulk density and reduction in the shear sensitivity of the particles.

Whereas the data infers that the attrition process occurs in two close to linear sections, the observed trends are more likely due to the low number of data points available to describe the data. If more experiments were to be carried out with agitation times around 0.25 h and 0.75 h, it is likely that the data will appear as a decaying curve, as it is unlikely that the attrition rate changed instantaneously. The attrition process of mixing dry COA in a powder blender at relatively high rpm has been studied previously, where both the results of LD particle size analysis and non-invasive NIR spectrometry indicated that there was an initial period with high attrition rate followed by periods of lower attrition rates.[18] The data presented here is in qualitative agreement with the previously collected data, however, the lower rpm of the agitator in the current study caused a reduction of the initial attrition rate.

The relationship between particle attrition and starting LOD was also investigated and is shown in Figure 6-16 d) – f). For the continuously agitated experiments, the data presented is randomly distributed and doesn't seem to exhibit any trend, which suggests that there was not a relationship between the starting LOD and the particle size measured at the end of drying. For the intermittently agitated experiments, however, the starting LOD was important in relation to the extent of attrition that occurred. In Figure 6-16 a) – c), the attrition rate is highest during the initial 30 mins of agitation, therefore as the number of 1 min agitation periods required to dry samples with greater starting LODs increases, the extent of attrition will also increase. In the data reported by Lekhal *et al.*, the authors found that particle attrition was only dominant over agglomeration at LOD's of <4% wt/ wt,[14] and also, attrition has often been attributed to over-drying of a compound.[19, 20] The data presented here, however, does not agree with these hypothesises and instead indicates that agitation is the only controlling factor in the needle breakage for COA. This highlights, as with many aspects of API synthesis and isolation, that conclusions based on the measurements made for one compound will not necessarily transfer to others as the physical properties of powder materials are so wide ranging. Nonetheless, it is likely that shear sensitive materials like COA will behave in a similar, if not exact way.

In order to examine if the physical changes measured at the end of drying could be observed in real-time during powder drying, an investigation into the Raman data collected *in situ* was performed. The evaluation was performed in two parts: first, a univariate approach was carried out to determine the effects of the individual component's contribution to the Raman spectra (i.e. COA particles, MeOH and PTFE) and secondly, multivariate analysis was carried out in order to investigate the combined effects of the contributing components. Univariate drying curves based on the 1st derivative intensity at 1076 cm^{-1} (COA) are shown in Figure 6-17 a) – e) for experiments 2 – 7, respectively (data for experiment 1 are shown in Figure 6-13).

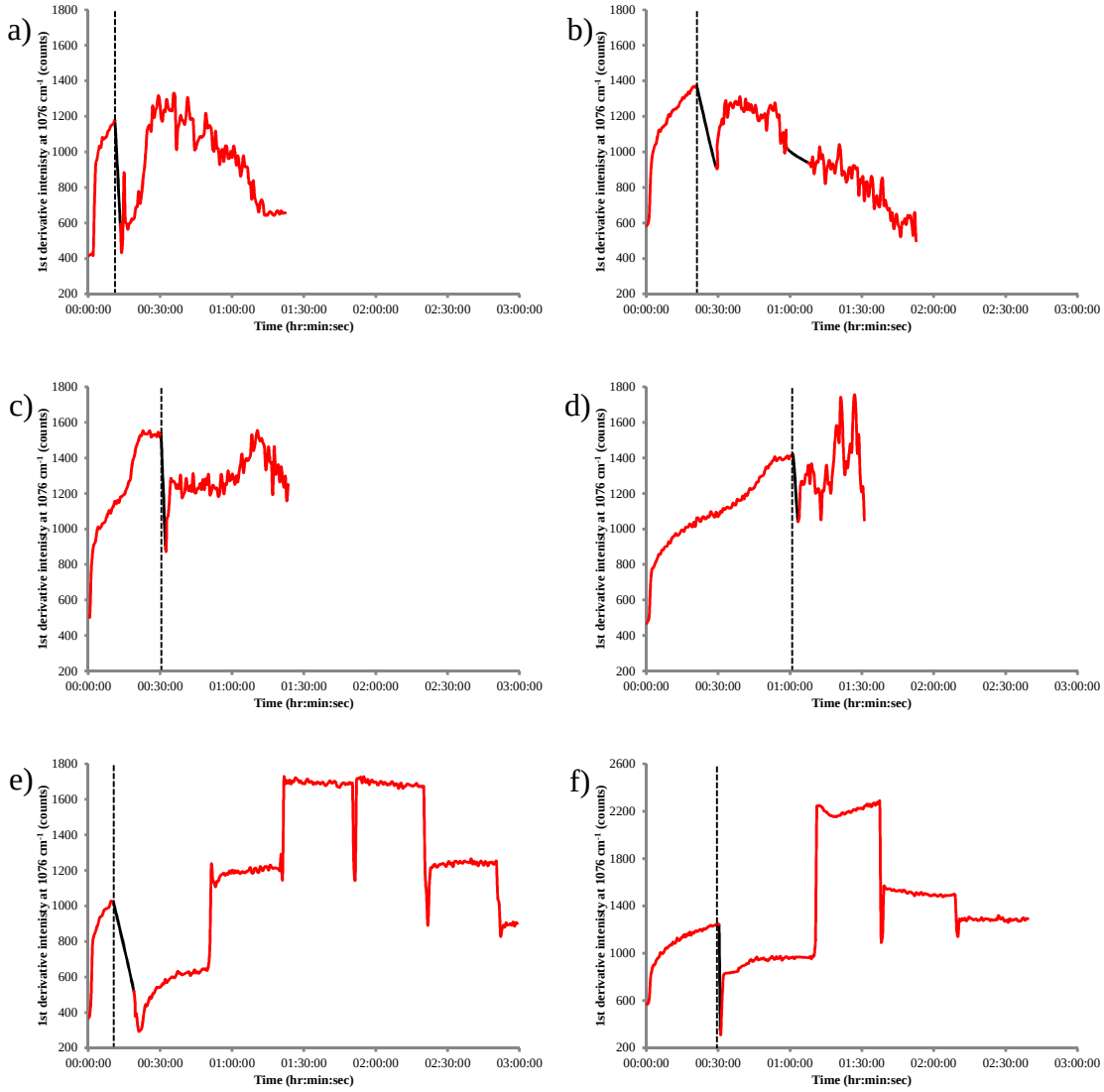

Figure 6-17: Drying curves based on 1st derivative COA peak centered a 1076 cm^{-1} for both N_2 blowdown and vacuum agitated drying periods for a) experiment 2, b) experiment 3, c) experiment 4, d) experiment 5, e) experiment 6 and f) experiment 7 (data for experiment 1 shown in Figure 6-13). The conditions for each experiment are given in Table 6-2. Dashed black lines indicate the end of the N_2 blowdown period. Solid black lines indicate that the data is extrapolated by the data analysis software used to plot the data as no measurements were being collected at these time points.

The Raman data shown in Figure 6-17 can be divided into two sections: the N_2 blowdown pressure filtration period and the vacuum agitated drying period.

Although it has been demonstrated that no significant needle breakage occurred during the N_2 blowdown period, it was important to include the data in order to adequately describe the importance of the bulk density of the COA particles in the measurement volume of Raman probe on the signals obtained. As previously discussed, the application of a positive pressure of N_2 creates a packed bed of particles which in turn increases the bulk density of the powder sampled by the Raman probe. Most of the excess methanol was filtered rapidly when the N_2 was initially applied which accounts for the sudden rise in COA signal during the first couple of minutes, however, after this time, the rate of packing and removal of methanol slowed down, and therefore, the rate of the increase in bulk density observed (and mass of COA in the sampled volume) also slowed down.

Considering now the agitated periods of vacuum drying, in experiment 1, an increase in Raman signal was observed when agitation was commenced (Figure 6-13) due to the sudden increase in bulk density caused by the rapid removal of methanol by the vacuum pump. Conversely for experiments 2 – 7, a reduction in Raman signal was observed at the onset of agitation, which was again attributable to bulk density effects. In these experiments, the motion of the agitator disrupted the packed bed of particles by inducing a shear force into the vessel, and in doing so decreased the bulk density of the particles in the measurement volume at any one time. As the process was completed, the profiles obtained from the continuously agitated experiments were significantly different to those obtained with intermittent agitation. And furthermore, the curves obtained from the continuously agitated experiments do not display any obvious trends. For the continuously agitated experiments, the LOD at the start of vacuum agitated drying appears to be the key parameter that controls the bulk density effects on the COA drying curve. For example, experiments 2 and 3 (a) and b) in Figure 6-17) had starting LODs of 21 and 7% wt/wt, respectively, with both COA drying curves displaying an increase in COA signal that reached a maximum before decreasing as the drying process was carried out. The increase in signal that followed was likely caused by both attrition and aggregation processes occurring at the same time with both acting to increase the bulk density. The maximum COA signal observed for these experiments occurred when the methanol concentration was

at a critical point where the most liquid bridges between particles had formed, and this is supported by examination of the data for experiment 2 where a longer time was required to reach the maximum signal as more solvent needed to be removed. Once the critical point was reached, the aggregates began to break up again, causing the COA signal to decrease, and furthermore, for both experiments 2 and 3, this occurred at a time where particle size analysis results suggested that the majority of attrition had already taken place, and therefore, the decrease in signal (and hence, bulk density) observed was not likely competing with an increase in bulk density from needle breakage.

For experiments 4 and 5, a different process to that described for experiments 2 and 3 occurred, here, it was likely that the starting LOD's of 3 and 4% wt/wt, respectively were too low for sufficient liquid bridges to be formed. Thus, after the initial decrease in bulk density caused by the disruption of the particles in the packed bed, the Raman signal was dependent of local variations in the bulk density of the material that passed through the measurement volume. Therefore, for these measurements, the bulk density effects caused by aggregation of the particles should not have had as large an effect on the Raman data, and this seems to be the case as there is not a significant decrease in the signal obtained that could be attributed to the reduction in bulk density caused by the break-up of aggregates. The Raman signal obtained suggested that there was an increase in the overall intensity observed during drying that may have been caused by particle breakage, however, further experiments would need to be carried out to determine if these effects were caused solely caused by the breakage effect. Experiments 6 and 7, which involved intermittent agitation, displayed completely different characteristics to the continuously agitated curves. In the data for these experiments, it appears that the starting LOD is not a key factor in the bulk density effects observed by the Raman probe; this is because the length of agitation time (1 min) for each 30 min period is not sufficient enough for dense aggregates to form. The Raman signal obtained for these experiments did, however, confirm the role of bulk density of the particles in the measurement zone of the probe to be extremely important when considering any change in the physical properties of a material during drying.

The data from experiment 1 was described previously in detail (section 6.4.3.2), however, the increase in COA signal observed at the beginning of vacuum agitated drying was caused by the vacuum pump pulling most of the excess methanol through the COA particles and filter, which caused a net increase in the bulk density, and hence, the Raman signal obtained from the COA particles.

In order to investigate further the effect of bulk density on the Raman signal obtained, multivariate analysis was applied on the data set. For this, principal components analysis (PCA) was performed on the regions of the Raman spectrum where there was no contribution from PTFE or glass. Furthermore, because the attrition process occurred predominantly during the vacuum agitated drying period, only the spectra obtained during these periods were included in the data set. This meant that the spectra obtained during the N_2 blowdown period and all the spectra from the intermittently agitated drying experiments were excluded at this stage, with the intention of reintroducing them at a later stage if the PCA results revealed any further physical information. The scores and loadings plots obtained for PCs 1 are shown in Figure 6-18 a) and b), respectively.

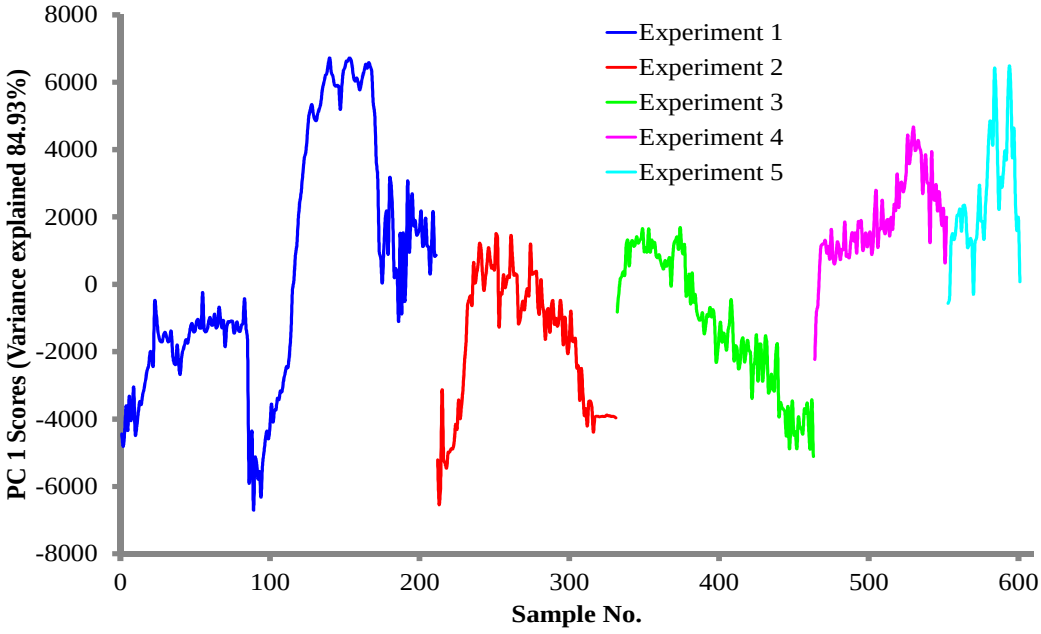

Figure 6-18: a) Scores for PC 1 from PCA performed on the spectra collected during continuously agitated drying experiments.

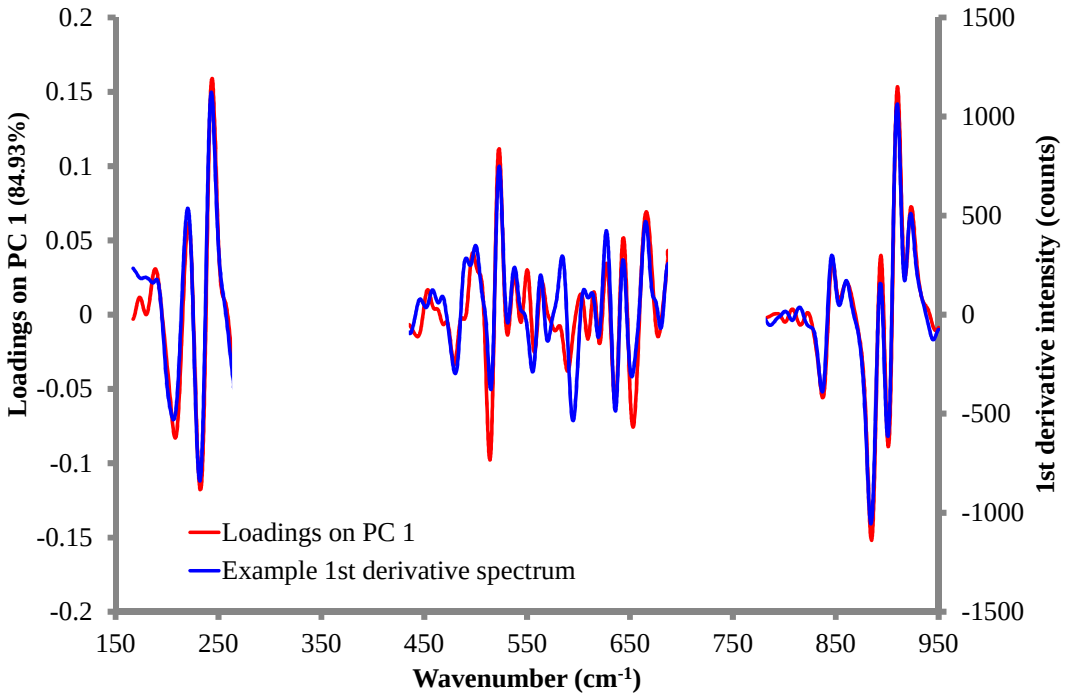

Figure 6-18: b) loadings on PC 1 from PCA performed on the spectra collected during continuously agitated drying experiments (with glass background and PTFE regions excluded).

The loadings for PC 1 are generally strongly correlated with the COA peaks, which means that PC 1 describes the changes that occur to the COA particles during drying. In this case, the data are correlated, and therefore, an increase in PC 1 score resulted when there was an increase in Raman signal. The data displayed is in qualitative agreement with the univariate data described previously and therefore shall not be discussed further

Due to the fact that the multivariate analysis performed on the Raman data did not provide more information about the physical processes that occurred during drying than the univariate analysis described previously, it was decided not to develop the models any further and thus, the spectra obtained during the N_2 blowdown and intermittently agitated drying experiments were not analysed by multivariate methods during this study.

6.4 Conclusions

The isolation (N_2 pressure filtration and vacuum agitated drying) of COA particles from a slurry with methanol has been studied using *in situ* Raman spectroscopy and off-line particle size analysis techniques. Firstly, it was found that variations in bulk density and particle size caused by the poorly controlled recrystallisation process for COA meant that the data generated from batch-to-batch was not directly comparable; therefore, the data from only one batch was used in the study. The removal of methanol during drying was then monitored with an *in situ* Raman probe using two methodologies. For this either the univariate decay of a methanol peak or the ratio of methanol: COA peaks was plotted vs. time. The Raman measurements allowed: i) the detection of balling during the vacuum agitated drying process meaning that in a real process, operators could be alerted to cease agitation. ii) the effects of bulk density caused by particle motion and particle wetness to be monitored in real-time. However, the overall bulk density effect were found to compete with the effects of particle attrition, and therefore, *in situ* Raman measurements did not allow for the needle breakage process to be monitored in real-time. The attrition process is known to effect Raman signal observed from dry particles (due to the increase in bulk density caused when average needle length is reduced (i.e. better packing)) as was reported in Chapter 5. However, for these experiments, the increase in Raman signal that was expected due to the increase in bulk density caused by the attrition process appeared to be masked by competing bulk density effects owing to the formation and break-up of aggregates during drying (caused by liquid bridges between the particles). Instead, data from off-line particle size measurements were required to quantify the extent of attrition that occurred during each experiment. The physical processes that occurred during the isolation process were investigated using particle size analysis. It was shown that: i) the N_2 blowdown period at 0.5 bar did not cause a significant amount of either particle aggregation or attrition. ii) The attrition process caused by vacuum agitated drying was independent of starting LOD for continuously agitated particles and is instead controlled by the length of agitation time. For intermittently agitated drying experiments, the starting LOD was related to the number of 1 min agitation periods employed, and hence correlated to the amount of

shear that was introduced into the system. It was concluded, therefore, that the starting LOD was important in determining the extent of attrition that took place in these experiments.

The general recommendations for drying of shear sensitive materials like COA that have stemmed from this research are as follows:

- The agitation strategy employed is the most critical parameter when attrition is a concern. It is recommended that intermittent agitation at a low mixing speed is carried out in these cases.

- The second most critical parameter that effects the extent of attrition is the starting LOD for vacuum agitated drying (particularly for intermittently agitated particles). It is recommended that particles are subjected to N_2 blowdown (pressure filtration) until an LOD is reached when there is no longer a significant amount of solvent being removed from the particles.

- *In situ* measurements allowed for the drying curve to be monitored in real-time, which allowed for the process to be stopped at the correct end-point, rather than a pre-determined end-point outlined in an SOP. Furthermore, by monitoring the particles directly, the on-set of balling could also be detected in real-time, meaning that the drying strategy could be changed avoiding damage to the drier. Hence, it is recommended that for processes where balling can occur that *in situ* measurements are recorded.

- Many active pharmaceutical ingredients have needle-shaped morphology, it is recommended that the Feret-Max dimension from image analysis is used when particle size analysis is carried out on these samples; this ensures that the measurement is representative of the particles being evaluated.

6.5 References

1. E. Griva, *Working directions for the recrystallisation of regular grade cellobiose octaacetate*, GSK, UK, 2005.

2. P. Allan, *Studies in Raman, infrared and acoustic emmision spectrometries, and reaction calorimetry for process analysis*, PhD, University of Strathclyde, 2008.

3. J. Yang, T.-J. Wang, H. He, F. Wei and Y. Jin, *Ind. Eng. Chem. Res.*, 2003, **42**, 5568-5575.

4. Malvern, *http://www.malvern.com/malvern/kbase.nsf/allbyno/KB000089?opendocument*, October 2011.

5. P. Hamilton, D. Littlejohn, A. Nordon, J. Sefcik and P. Slavin, *Analyst*, 2012, **137**, 118-125.

6. P. Hamilton, D. Littlejohn, A. Nordon, J. Sefcik, P. Slavin, P. Dallin and J. Andrews, *Analyst*, 2011, **136**, 2168-2174.

7. G. M. Walker, S. E. J. Bell, K. Greene, D. S. Jones and G. P. Andrews, *Chem. Eng. Sci.*, 2009, **64**, 91-98.

8. E. Tsotsas and E. U. Schlunder, *Chem. Eng. Process.*, 1986, **20**, 339-349.

9. E. U. Schlünder and N. Mollekopf, *Chem. Eng. Process.*, 1984, **18**, 93-111.

10. NIST, NIST Webook, http://webbook.nist.gov/chemistry/.

11. C. MacLeod and F. Muller, personal communication.

12. F. J. Muzzio, C. L. Goodridge, A. Alexander, P. Arratia, H. Yang, O. Sudah and G. Mergen, *Int. J. Pharm.*, 2003, **250**, 51-64.

13. F. J. Muzzio, P. Robinson, C. Wightman and D. Brone, *Int. J. Pharm.*, 1997, **155**, 153-178.

14. A. Lekhal, K. P. Girard, M. A. Brown, S. Kiang, J. G. Khinast and B. J. Glasser, *Int. J. Pharm.*, 2004, **270**, 263-277.

15. A. Lekhal, K. P. Girard, M. A. Brown, S. Kiang, B. J. Glasser and J. G. Khinast, *Powder Technol.*, 2003, **132**, 119-130.

16. E. Kougoulos, C. E. Chadwick and M. D. Ticehurst, *Powder Technol.*, 2011, **210**, 308-314.

17. P. K. Kom, W. Cook and E. Kougoulos, *Org. Process Res. Dev.*, 2011, **15**, 360-366.

18. E. Duff, *Monitoring of powder drying processes using near infrared spectroscopy and acoustic emission*, MSci, University of Strathclyde, 2010.

19. J. Parris, C. Airau, R. Escott, J. Rydzak and R. Crocombe, *Spectroscopy*, 2005, **20**, 34-41.

20. J. Burgbacher and J. Wiss, *Org. Process Res. Dev.*, 2008, **12**, 235-242.

7 The application of *in situ* Raman spectrometry to an industrial case study

7.1 Introduction and overview

An opportunity to investigate the potential applications of *in situ* spectroscopic and particle size measurements in an industrial context arose within the Particle Generation, Control and Engineering (PGCE) group at GSK (RTP, NC, USA), made possible through the studentship agreement with CPACT and the industrial partners. PGCE is part of the research and development arm of GSK and is located between synthetic chemistry and formulation in its drug manufacturing chain. PGCE's responsibilities encompass all crystal engineering and PAT support to the synthetic and formulation chemists, as well as being accountable for delivering the route to the final API for drug manufacturing. The unit operations performed range from primary operations such as crystallisation and drying, to secondary operations such as granulation, blending or tablet compression. In this work, a phase II antibiotic intended as a treatment for Methicillin-resistant Staphylococcus aureus (MRSA) bacterial infections in humans was studied. MRSA was first reported in the UK in 1961 and is now a worldwide problem causing severe infections in hospitals and nursing homes. Furthermore, MRSA infections are becoming increasingly difficult to cure due to evolving resistance to current antibiotic treatments.[1] The API itself, cannot be named due to the proprietary nature of the compound; it can be referred to as Peptide Deformylase API, however, hereafter; it will only be described in this report as the "API". The form of the API used is "form III" and has needle-shaped morphology.

The work carried out for this study proposed a reduction in the number of production steps (primary and secondary) from crystallisation to tableting from seven to four, creating an API granule during primary rather than secondary manufacturing so that direct compression of the drug substance would be the only operation performed during secondary manufacturing. Currently, the manufacturing process crystallises the desired form by a seeded, anti-solvent, cooling recrystallisation from *n*-butanol

and isooctane. The API is then isolated and dried using an agitated filter drier before being transferred to secondary manufacturing where it is blended with sodium crosscarmellose and Starch 1500, and granulated with water. The granules are then dried to around 3% wt/wt prior to forming an extra-granular blend with Avicel, sodium crosscarmellose and magnesium stearate. Lastly, the extra-granular blend is compressed to form tablets. The proposed manufacturing process performed in this evaluation would reduce the number of steps by performing a wet-milling step with the API, sodium crosscarmellose and Starch 1500 in the crystalliser, and the granulation step during agitated filter drying. Therefore, only the formation of the extragranular blend and compression would be performed during secondary processing. The current and proposed states for primary and secondary manufacturing are shown schematically in Figure 7-1 a) and b), respectively.

a)

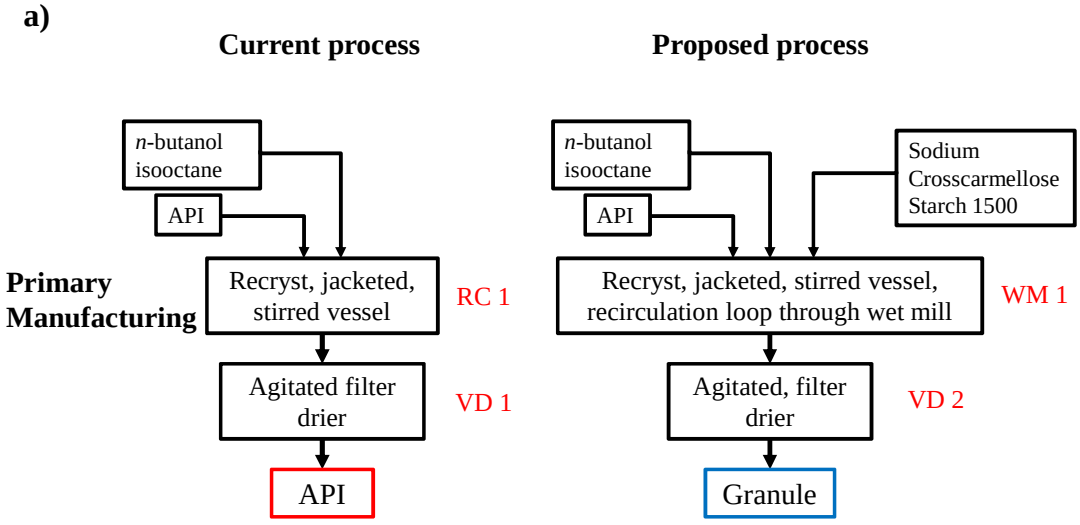

b)

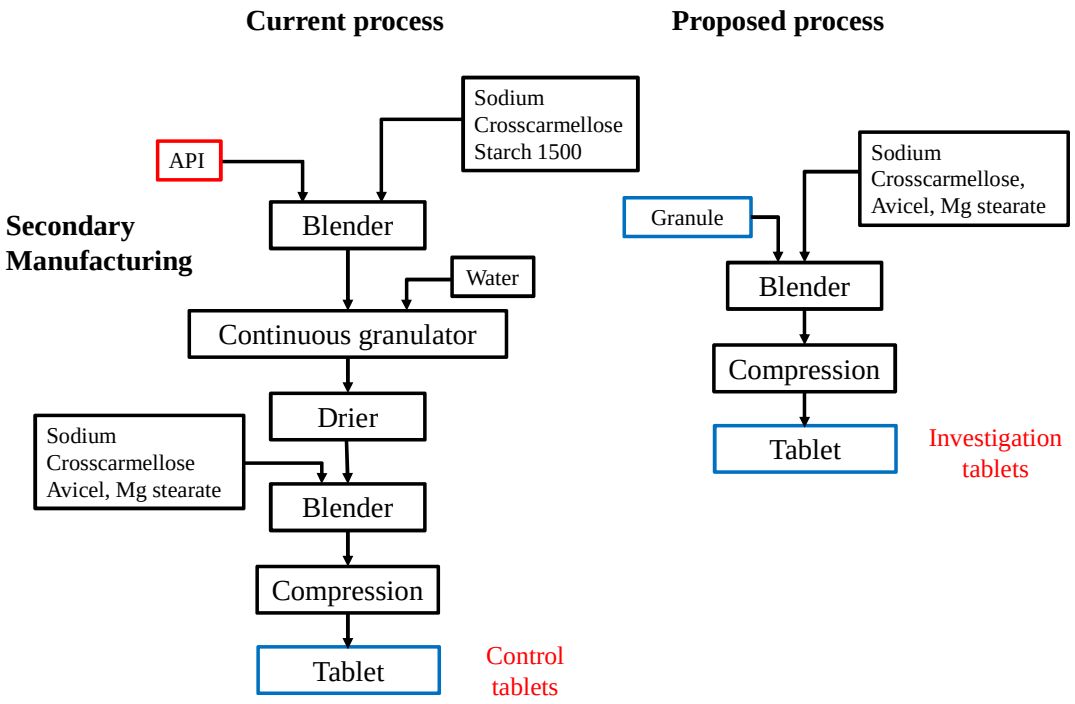

Figure 7-1: Current and proposed process train from API study for a) primary manufacturing and b) secondary manufacturing. Red text indicates the processes described in sections 7.2 and 7.3.

Prior to the reported study, the application of PAT instrumentation to the named processes in Figure 7-1 for the API under investigation had been minimal. FBRM probes had been used to monitor the crystallisation step and mass spectrometry applied to the drying step. The strengths and weaknesses of FBRM for needle-shaped particles have been discussed, in detail, previously in this report (Chapter 4) as well as the disadvantages of using the off-gas to monitor a drying process (Chapter 5). In this case study, the API under investigation has three known polymorphs and each batch is analysed by off-line x-ray diffraction to determine if the desired form has been made. It is well known that polymorph information is contained in Raman spectra and there are many existing examples in the literature where models have been developed to determine a given polymorph *in situ* for crystallisation monitoring.[2-6] It was considered, therefore that the recrystallisation step for the API could be monitored by *in situ* Raman spectroscopy to determine simultaneously the crystallisation profile and polymorph. The process was carried out twice, firstly at a

5 L scale using a Kaiser Rxn 1 Raman spectrometer with an MR immersion optic (IMO) and secondly at a 1 L scale using a Kaiser Rxn 2 Raman spectrometer with P^{h}AT probe to monitor the process non-invasively. Furthermore, in the proposed process train in Figure 7-1, wet milling of the API was employed for two reasons: firstly to increase the bulk density properties of the API, and secondly to attempt to form the API and excipient granule during primary manufacturing. When the particle size of a material is reduced, an increase in Raman signal for that material is generally observed, therefore, Raman spectrometry could potentially be used to monitor this process also. An additional application of Raman spectrometry in the proposed process train is to monitor the drying process of the API, and this was carried out in two driers, using an agitated filter drier with the IMO when the API was dried in the absence of excipients (data not shown), and in a pan drier using the Kaiser Rxn 2 P^{h}AT probe in a pan drier in the presence of the excipients. Here, an increase in granule size is expected to cause a reduction in Raman signal, however, changes in bulk density are also known to affect the Raman signal. These effects have been observed previously by Walker *et al.* while monitoring the granulation process of glass beads using *in situ* Raman spectrometry.[7]

The corporate objective of the project was:

- To evaluate the possibility of creating the API/ excipient granule during primary manufacturing, reducing the total number of production steps from 7 to 4.

The objective of this part of the study from a research perspective was:

- To apply learning from the *in situ* measurement of controlled laboratory drying experiments of a pseudo API to the processing steps of an actual API in development.

It is important to note that it was only possible to carry out proof-of-concept experiments and not full characterisation for each unit operation, and it is the results of these studies that are presented here. The reasons for this are twofold: i) the

studied material was in development at the time that the research was carried out, and therefore, the quantities available in order to carry out each unit operation were limited meaning that a full experimental design was not possible, and only scoping experiments could be carried out. ii) The PAT research was carried out over the duration of a fixed term 2 month placement with the timings of the unit operations determined by the availability of reactors and GSK personnel, and the needs of the company, and thus, there was not time to carry out substantial repeat experiments. This meant that important variables such as probe placement, or optical setup were not always optimised for the unit process being studied. Where this is the case, discussion is offered as to how the measurement system could be improved if further research were to be carried out.

7.2 Experimental

7.2.1 Materials

The API was synthesised in the pilot plant at GSK (RTP, USA). Around 150 g was collected by PGCE to complete this work. *N*-butanol and isooctane (2,2,4-trimethylpentane) (Sigma-Aldrich, USA) were the solvents used when the seeded recrystallisation of the API was carried out. For granulation studies, granules were prepared using the API, starch 1500 and sodium crosscarmellose (all GSK, RTP, NC, USA). After granulation, the granules were mixed to form an extra-granular blend with magnesium stearate, Avicel and sodium crosscarmellose (all GSK, RTP, NC, USA) before tablets were pressed so that hardness, thickness and dissolution/ disintegration tests could be carried out.

7.2.2 Recrystallisation, (RC 1 in Figure 7-1 a))

The API was added to *n*-butanol (6.5 vol.) and heated to dissolution at 87 ºC over 30 min with agitation at 300 rpm. Once dissolution had occurred, the solution was cooled to 80 ºC before being seeded with 0.5% wt/wt of the API in the correct form. After seeding, the solution was cooled to 50 ºC over 300 min at a cooling rate of 0.1 ºC/min at which point the anti-solvent addition was commenced. The anti-solvent used was isooctane (10 vol.) and was added over a further 300 min period at a rate of

5 ml/min. Once all the anti-solvent was added the solution was cooled to and held at 0 ºC at a rate of 0.25 ºC/min. At this point the API was either transferred from the reactor and used for drying, or wet-milled in the reactor with excipients for use in the granulation studies.

7.2.3 Drying, (VD 1 in Figure 7-1 a))

The resulting slurry from the recrystallisation of the API was transferred into a 2 L GL filter drier (GL Filtration Ltd, Doncaster, UK) where it was allowed to settle for 20 min. At this point, a positive pressure of N_2 was applied at 0.5 bar until the top of the cake could be observed through the window in the lid. The positive pressure of N_2 was then paused so that the cake could be washed with a further 300 ml of isooctane. After washing, N_2 was then reapplied (at a constant flow rate of 5 L/min rather than constant pressure) and the cake smoothed using the mechanical agitator, this was carried out until the solvent signal from mass spectrometry remained constant (data were not stored), at which point a sample was extracted for LOD analysis. To remove the remaining solvent from the powder, vacuum drying was performed once again until the signal from mass spectrometry remained constant. *In situ* Raman spectrometry using the Kaiser Rxn 1 with MR probe and IMO was also performed throughout the drying process when the cake height was large enough to allow coverage of the probe optics.

7.2.4 Wet milling/ granulation (crystalliser/ drier), (WM 1 in Figure 7-1 a))

The recrystallised API was passed through a wet-mill (IKA Magic Lab, IKA, Germany) while maintaining the reactor temperature at 0 ºC until a steady state had been reached in the total number of particle counts from *in situ* FBRM measurements. Wet milling was performed with the following reactor contents for each run:

1) API only

2) API, sodium crosscarmellose and Starch 1500

3) API, Starch 1500 (with sodium crosscarmellse added during drying stage)

After wet milling, the intra-granular blend was dried either in the GL filter drier described in Section 7.2.3 or a bespoke pan drier (developed in-house within GSK) to complete the granulation step. For drying of the granules, an N_2 blowdown was employed until an LOD of ~ 5% wt/wt was reached, and afterwards vacuum drying was performed to remove the remaining solvent. At this point, the granulation conditions were altered for the different batches: for batch 1: 30% wt/wt water was added before being dried to 2.8% wt/wt. Batch 2 was divided into two sub-batches, with 2, i) being dried until completion without the addition of water and 2, ii) 30% wt/wt water was added before being dried to 2.7% wt/wt. For batch 3, the granules were dried to completion before 2.5% wt/wt water was added to the sample. The LOD after the addition of water was monitored by Karl Fischer titration. For all granulation drying experiments, agitation was performed continuously at 10 rpm throughout the duration of the process.

7.2.5 Drug product formulation, (control and investigation tableting procedure in Figure 7-1 b))

The target intra-granular blend content was 92% API, 5% starch 1500 and 3% sodium crosscarmellose. In order to test the tableting properties of the granules (hardness, thickness and dissolution/ disintegration), an extra-granular blend was constructed consisting of 84% API, 10% Avicel, 3% sodium crosscarmellose and 1% magnesium stearate. The extra granular blend was then pressed into tablets at increasing pressures before the thickness, hardness and dissolution/ disintegration properties were tested. Furthermore, the tabletting performance from the granules manufactured by the reduced process train was compared with granules prepared using the original process train.

7.2.6 Raman spectrometry

Raman measurements of the API recrystallisation process were carried out using one of two Kaiser spectrometers and probe optical arrangements. Firstly, a Kaiser Rxn 1 with MR immersion optic (long working distance) was inserted directly into the

reaction vessel. Spectra were recorded with an exposure time of 10 s with a measurement every 12 seconds. The data were recorded using HoloGRAMS software (Kaiser Optical Systems, Ann Arbor, USA) and was then exported to MATLAB (Mathworks, Natick, USA) as .SPC files for multivariate analysis using PLS Toolbox version 4.1 (Eigenvector Research Inc., WA, USA). Secondly, a Kaiser Rxn 2 with P^hAT probe was used to monitor non-invasively the recrystallisation process of the API through one of the unused ports in the lid of the vessel. Spectra were again recorded with an exposure time of 10 s with a measurement every 12 s, and the data was also exported to MATLAB as .SPC files to perform multivariate analysis, however, the data were recorded using the IC Raman software (Mettler-Toledo, Columbus, USA) platform rather than HoloGrams.

For Raman measurements of wet-milling, the Kaiser Rxn 2 and P^hAT probe were used to monitor the change in Raman signal through the oil jacket of the vessel. An acquisition time of 30 s was set and measurements were made every 45 s. Data were collected using IC Raman software and exported to MATLAB as .SPC files for data analysis. NIR measurements were also recorded concurrently using a Bruker Matrix FT-NIR spectrometer with a direct insertion probe. Data were collected using OPUS 6.5 software (Bruker, Germany) with acquisition times of ~ 30 s.

Non-invasive Raman and in-line NIR measurements of the granulation step were performed when the process was performed in the bespoke pan drier, through a window in the lid and using a diffuse reflectance immersion probe, respectively. For Raman measurements, an acquisition time of 10 s was set with a measurement was made every 15 s. Data were collected using IC Raman software and exported to MATLAB as .SPC files for data analysis. For NIR measurements, Bruker Matrix FT-NIR spectrometer with a direct insertion probe was used. Data were collected using OPUS 6.5 software (Bruker, Germany) with acquisition times of ~ 30 s. Conversely, neither Raman nor NIR measurements were suitable for granulation experiments carried out in the GL filter drier due to there being no suitable window available for non-invasive measurements, and the cake height being too low (for the mass of granules that were dried) for probes to be inserted.

7.2.7 FBRM measurements

FBRM measurements were carried out during recrystallisation of the API and wet-milling of the API and excipients. The FRBM probe was placed directly into the reaction vessel for both unit processes with measurement times of 30 s for recrystallisation and 10 s for wet milling. Data were collected for the duration of each unit process. Each data set was then exported as both the un-weighted and square weighted distribution as a .CSV file for analysis in Excel.

7.3 Results and discussion

7.3.1 Recrystallisation, (RC 1 in Figure 7-1 a))

The recrystallisation process of the API under investigation was performed and monitored using in-line FBRM and Raman spectrometry. The data obtained from both techniques were evaluated and the strengths and weaknesses of each are discussed. Firstly, the FBRM data collected are discussed. The un-weighted FBRM chord length distribution (CLD) at various time points, and the number of counts (user defined bins) vs. time profile are shown in Figure 7-2 and 7-3, respectively.

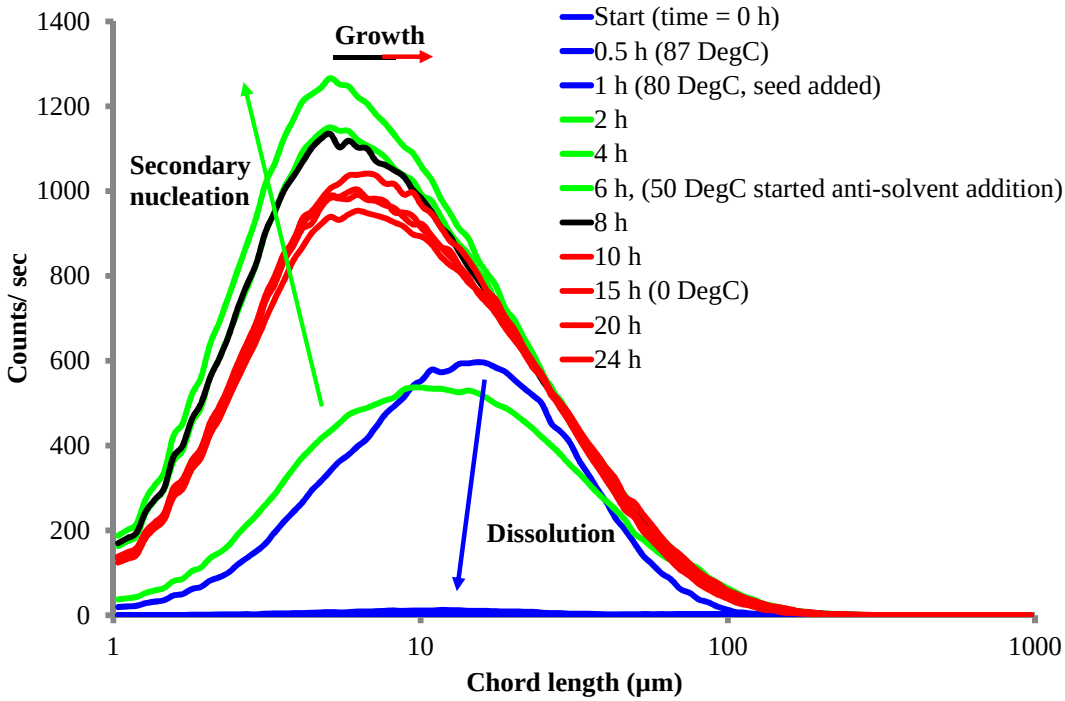

Figure 7-2: Chord length distribution at labeled time points during the recrytsallisation process for the API.

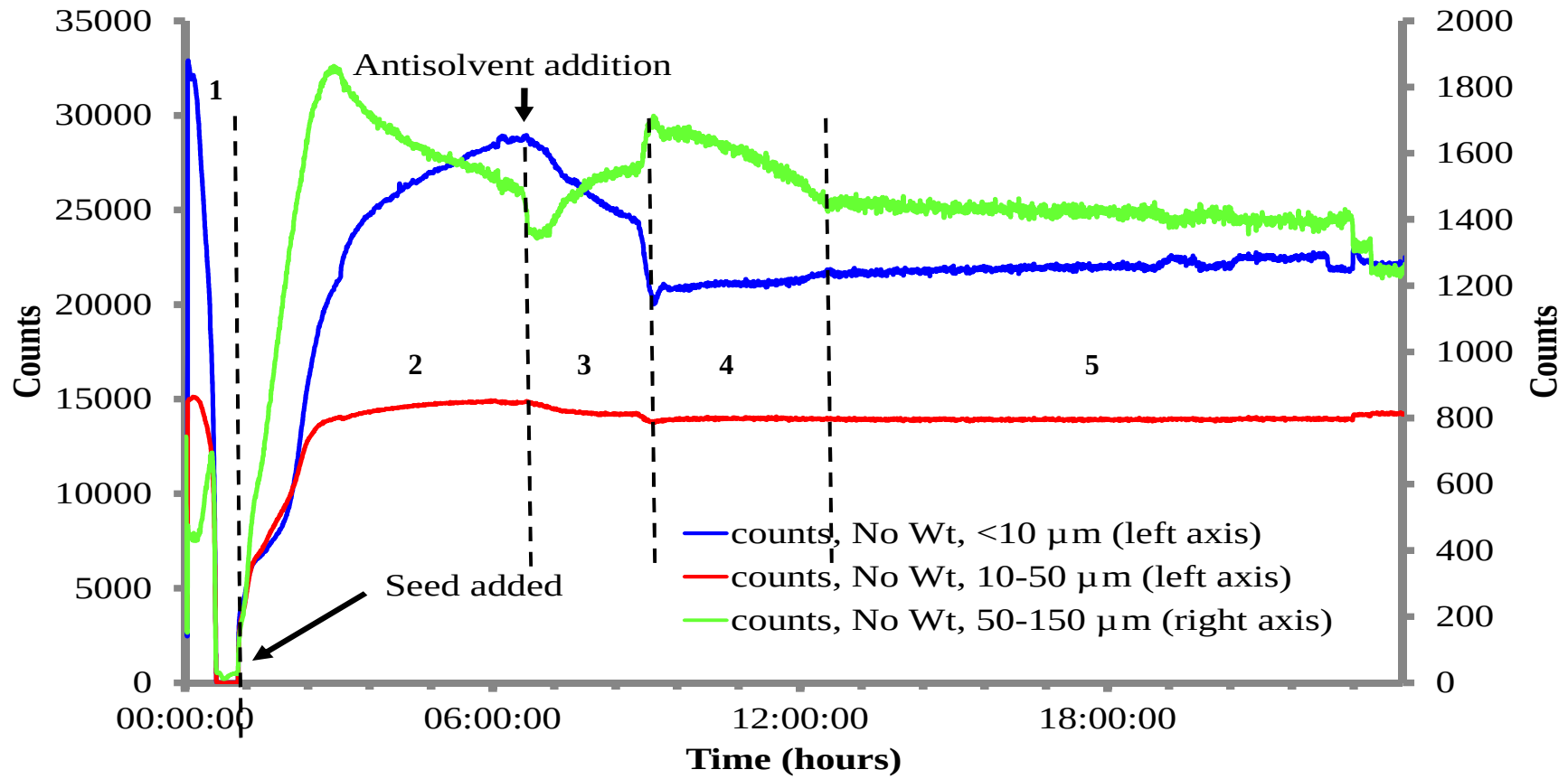

Figure 7-3: Counts vs. time for the defined size ranges observed throughout recrystallisation measured by FBRM (blue: 0 – 10 µm, red: 10 – 50 µm and green 50 – 150 µm).

In the FBRM data shown in Figure 7-2, three distinct processes that occur during recrystallisation are observed. Firstly, dissolution occurred after ~30 min of agitation and heating to 87 ºC (represented in blue in Figure 7-2). The second process that took place was secondary nucleation which occured after the addition of some form III seed particles of the API (green in Figure 7-2). Seeding is commonly used in the process industries to induce crystallisation, this is because supersaturated solutions are known to crystallise more readily in the presence of solute (either already present in the solution or added). Secondary nucleation is the term used to describe nucleation in this way and differs from primary nucleation where no seed is added to the solution.[8] The third process that took place was crystal growth which began after the onset of secondary nucleation. During a crystal growth period, there are competing processes that take place which can affect the data observed by the FBRM probe: secondary nucleation will continue, albeit at a far slower rate than at the onset, however, agglomeration of the particles will also take place. When the anti-solvent addition was started, the solubility of the API decreased, which increased the supersaturation of the solution and also the driving force for crystallisation. The FBRM data obtained after the addition of the anti-solvent displays a decrease in the number of counts per second for each distribution which is accounted for by the reduction of solid caused by the increase solvent concentration caused by the addition of the anti-solvent.

The observations from Figure 7-2 are confirmed by the data displayed in Figure 7-3, where the total number of counts from each measurement for three user defined size ranges (bin sizes) vs. time is shown. In Figure 7-3, the data agrees with the processes observed in Figure 7-2, however, the growth/ agglomeration process appeared more complex than discussed. In Figure 7-3, dissolution was observed after 0.5 h and secondary nucleation occurred after 1 h when the API seeds were added (period 1 in Figure 7-3). Secondary nucleation, growth and agglomeration then continued until 6 h had past for the 1 – 10 and 10 – 50 µm size ranges, however, the 50 – 150 µm size range showed a different trend (period 2 in Figure 7-3). In the bigger size range, growth and agglomeration were observed until a certain critical point was reached where it appears that attrition of the particles/ aggregates was likely caused by the

impeller. This effect has been observed previously when slurries of tyrosine were studied using FBRM.[9] This continues until the addition of the anti-solvent (period 3 in Figure 7-3), where growth and agglomeration were again favored in the largest size range. However, a dilution effect is observed in the two smaller fractions (due to the reduction in solid concentration caused by the increase of anti-solvent combined with agglomeration). After the anti-solvent addition was complete, the aggregates and bigger particles were once again broken up by the shear from the agitator, until equilibrium was reached after ~13 h (period 5 in Figure 7-3).

The FBRM data shown emphasises the already well-established application of *in-situ* chord length measurements to monitor crystallisation in real-time. [10-14] Conversely, *in situ* or non-invasive Raman spectroscopy is an emerging complementary technique to monitor crystallisation and can be used to obtain chemical information as well as the physical information observed by FBRM. In this case study, the butanol, API (dissolved and solid), and isooctane concentration could potentially be monitored by Raman spectroscopy.

The API recrystallisation process described by FBRM was monitored by Raman spectroscopy using a Kaiser Rxn 1 spectrometer with MR probe immersion optic (IMO). The MR probe has a confocal optical setup meaning that the laser spot size is approximately 80 µm and is focused only millimeters from the end of the IMO, this is very different to the wide illumination optics of the non-invasive P^hAT probe described previously that has a 6 mm diameter spot size and is focused 24.5 cm from the end of the probe. Examples of the 1^{st} derivative Raman spectra obtained during the recrystallisation of the API are shown in Figure 7-4.

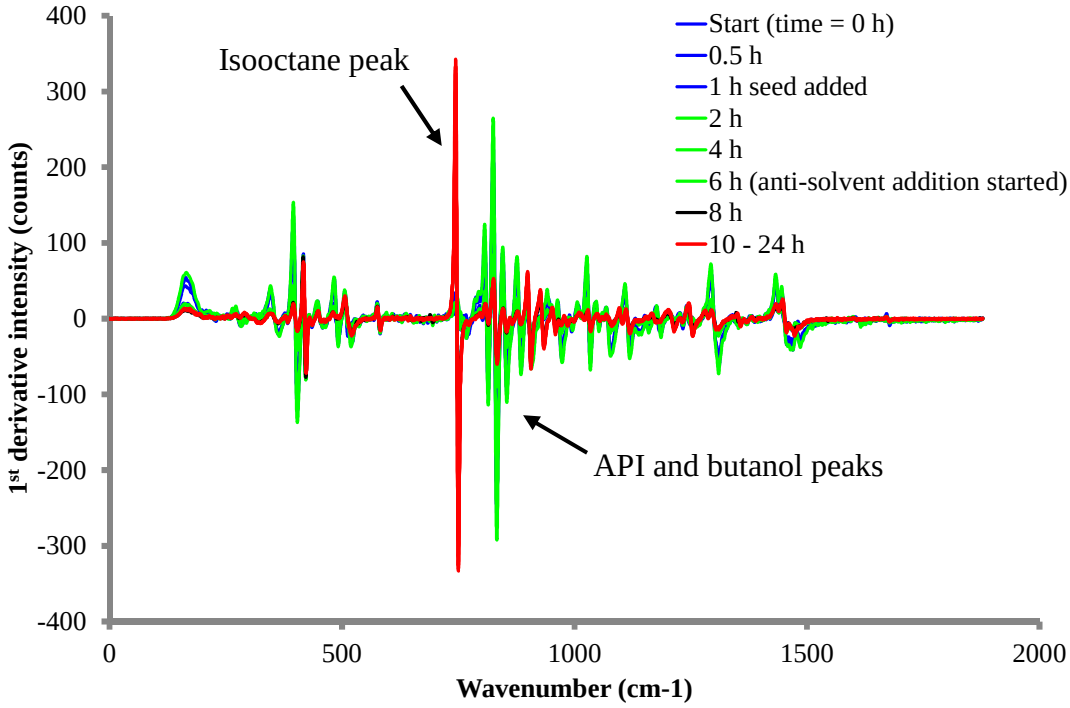

Figure 7-4: 1st derivative Raman spectra obtained during API recrystallisation with the MR IMO probe at stated time points.

The Raman spectra obtained vary significantly with the time point that they were obtained, particularly after the addition of the isooctane anti-solvent. Isooctane has a characteristic peak centered at 744 cm^{-1} that could potentially be used to monitor the anti-solvent addition univariately by plotting the peak intensity versus time. Furthermore, as the isooctane was added, it follows that the signal obtained from the peaks attributable to the API and *n*-butanol decreased due to the dilution caused. This could also be observed by univariate analysis by plotting the intensity of a characteristic *n*-butanol peak (e.g. 480 cm^{-1}) versus time. In general, however, the Raman spectra were difficult to interpret univariately, owing to complications resulting from dissolution and recrystallisation of particles. Instead, multivariate analysis techniques such as principal components analysis (PCA) or multivariate curve resolution were more suitable. For this data set PCA was performed with three principal components using the full spectral range. Any spectral outliers were removed by visual identification. Also, Raman spectroscopy is very sensitive to room lights being switched on, therefore, spectra that were obtained during times when this

was the case were removed. The results from PCA (for PC 1 and PC 2) performed on the recrystallisation data for the entire data set are shown in Figures 7-5 and 7-6, with the scores for PC 1 and PC 2 plotted against time in Figure 7-5 and overlaid plots of the loadings for PC 1 and PC 2 with spectra obtained before and after the addition of the anti-solvent shown in Figure 7-6 (a) – d)).

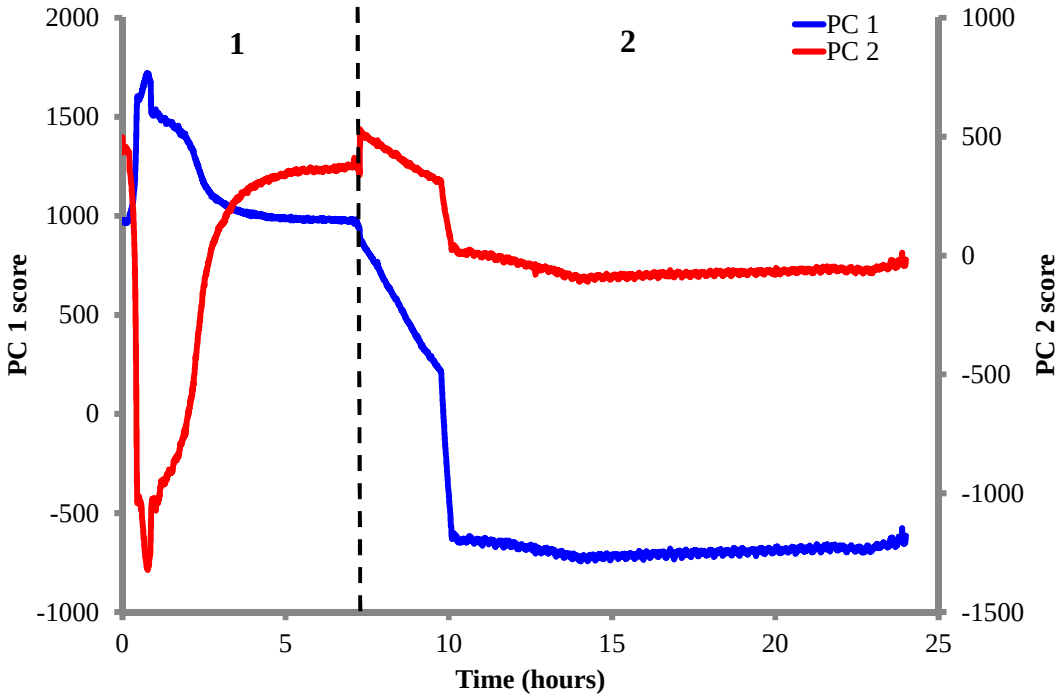

Figure 7-5: PC 1 and PC 2 scores vs. time results from PCA of full Raman spectrum (obtained using the Kaiser Rxn 1 with MR probe and IMO). 1: represents before the addition of the isooctane anti-solvent and 2: represents after the addition of the isooctane anti-solvent.

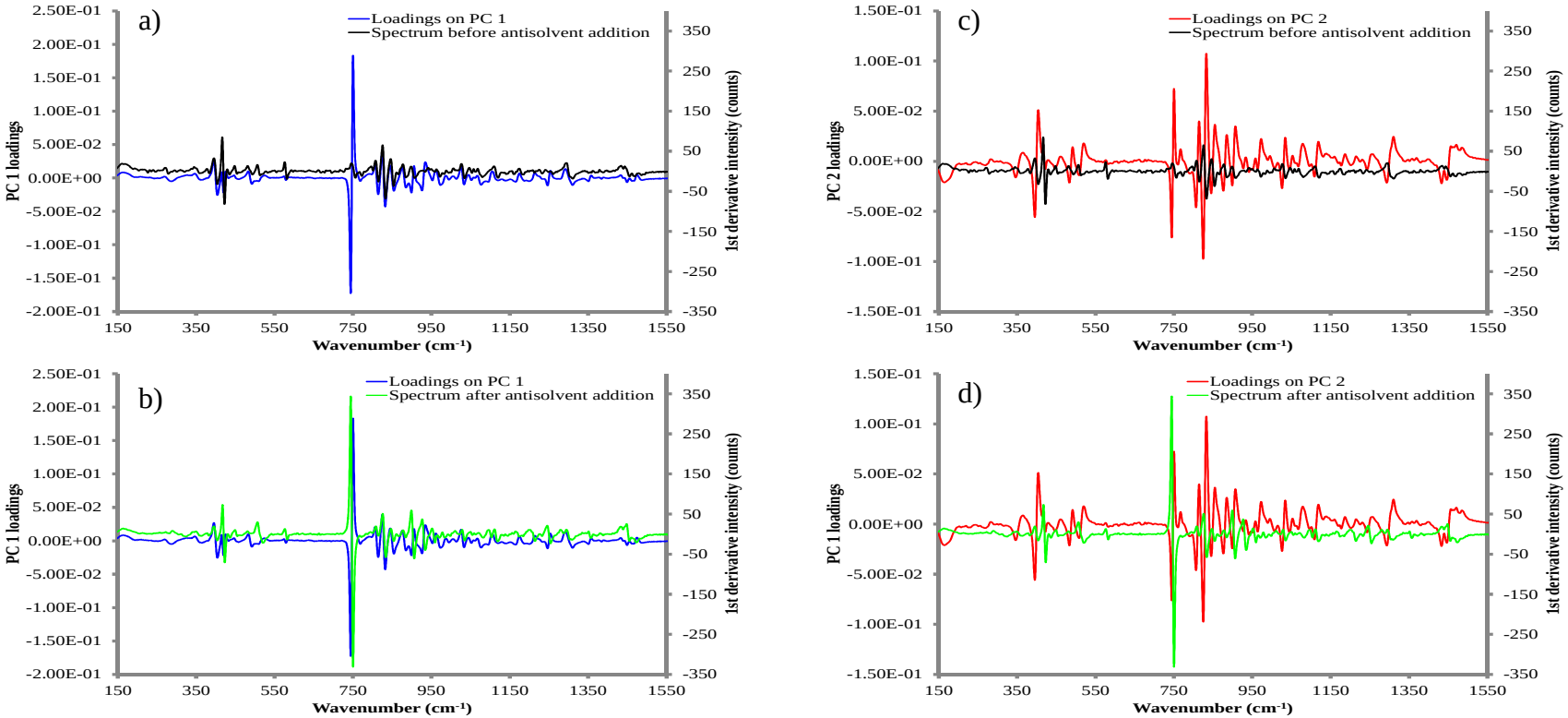

Figure 7-6: overlaid plots of from PCA and Raman spectra obtained during API recrystallisation for a) Loadings on PC1 and spectrum before anti-solvent addition, b) Loadings on PC1 and spectrum after anti-solvent addition, c) Loadings on PC 2 and spectrum before anti-solvent addition and d) Loadings on PC 2 and spectrum after anti-solvent addition.

Considering the PCA data for PC 1, which accounted for 85.3% of the variance in the spectra, the loadings are anti-correlated to the peaks attributed to isooctane and correlated to the peaks from the API and *n*-butanol. However, the isooctane addition only began after 10 hours, and therefore, the data is best interpreted by considering the process in two sections: 1) before the addition of isooctane and 2) after the addition of isooctane (denoted in Figure 7-5 and represented by Figure 7-6 a), c) and 7-6 b), d) for the loadings for PC 1 and PC 2, respectively). During time period 1 in Figure 7-5, dissolution is clearly observed when the scores reach the maximum values after around 0.5 hours; this is followed by a period of cooling and the addition of seed particles (when supersaturation is at 20%, 80 ºC), which is represented as a decrease in PC 1 score as the API precipitates. Upon the commencement of the anti-solvent addition (section 2), the scores for PC 1 decreased as increasing amounts of anti-solvent were added, due to the anti-correlation of the peak centred at 744 cm^{-1} in the Raman signal with the PC 1 loading. Here an increase in Raman signal corresponds to a decrease in PC 1 score. After completion of the anti-solvent addition, at around 10 hours, the PC 1 scores continue to decrease during the cooling period (where crystal growth, agglomeration and breakage are all taking place) until equilibrium is reached after approximately 14 hours.

PC 2 accounted for 13.2% of the variance in the spectra and is anti-correlated to the contributions from the *n*-butanol and API and the anti-solvent. However, the loading on the isooctane peak at 744 cm^{-1} is considerably less than for PC 1 and, therefore, the API and *n*-butanol contribution to the data are greater. Here, a similar trend was observed to the data for PC 1 where dissolution was observed after 0.5 hours (lowest PC 2 score and, therefore, highest Raman intensity), however, the anti-solvent data were also anti-correlated and therefore a decrease in PC 2 was observed when this was added. Comparing the PC 2 data from Figure 7-5 with the FBRM data for the 10 – 50 µm fraction from Figure 7-3, a similar trend is observed. This shows that using the Kaiser MR probe with IMO, the crystallisation profile can be inferred from the effect that dissolution and recrystallisation of the particles has on the Raman information, which is contributed to predominantly by the solvent and anti-solvent. Although, there is a fairly high number of API particles present in the slurry, the

optics of the probe (confocal with a short penetration depth) are not optimised to monitor the solid in the presence of solvent.

The non-invasive Kaiser P^{h}AT probe, with a wide illumination 6 mm spot size, offered the potential to gain more information from the API particles during the recrystallisation procedure. Therefore, a second batch of the API was recrystallised, in this case including a form change from form II to form III of the API. This experiment was carried out at a smaller 1 L scale to the 5 L scale in the previous reaction, and furthermore, the pump used to add the anti-solvent overnight failed, and therefore, the solution was held at 50 ºC overnight as the control software would not begin the second cooling phase until after the anti-solvent addition. The anti-solvent was added the following day manually in small amounts while cooling was carried out. Figure 7-7 shows example spectra obtained during the API recrystallisation obtained with the P^{h}AT probe.

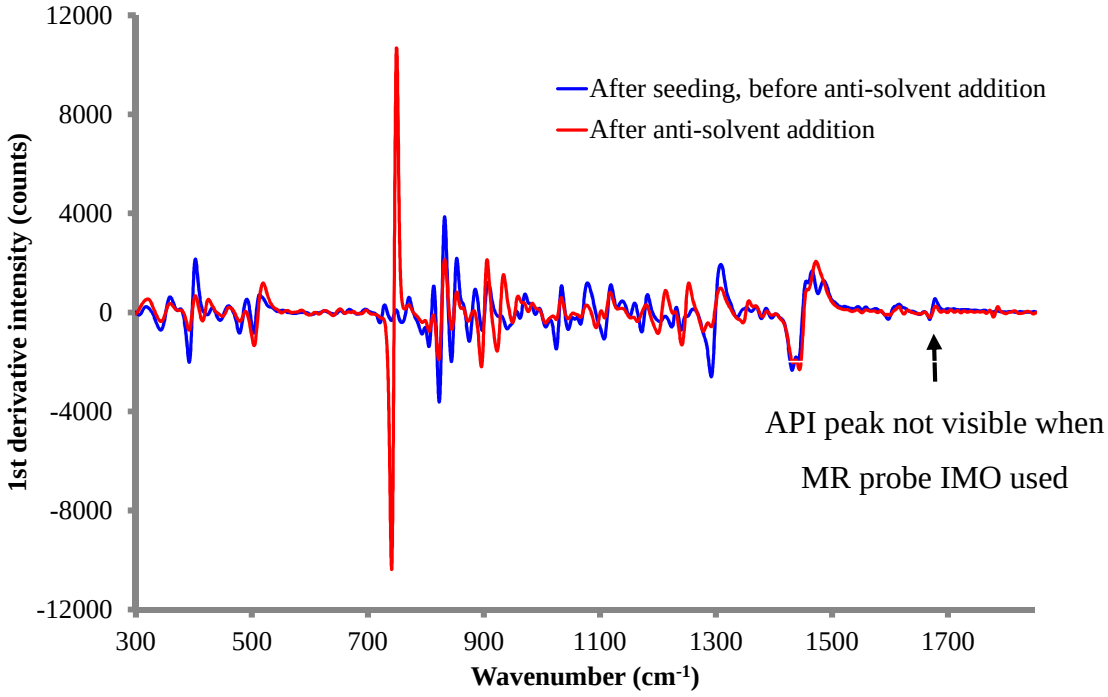

Figure 7-7 Example Raman spectra obtained during API recrystallisation before and after the addition of isooctane (anti-solvent) (obtained using the Kaiser Rxn 2 and P^{h}AT probe).

The Raman data obtained with the P^{h}AT probe were similar to the data obtained with the MR probe IMO setup, however, due to the larger sampling area, peaks attributable to the API that are independent of solvent are visible that were not well resolved previously. For example, the annotated peak centred at 1678 cm^{-1} in Figure 7-7 is attributable to the API and can be used to track the reaction profile univariately. The data for this are shown in Figure 7-8.

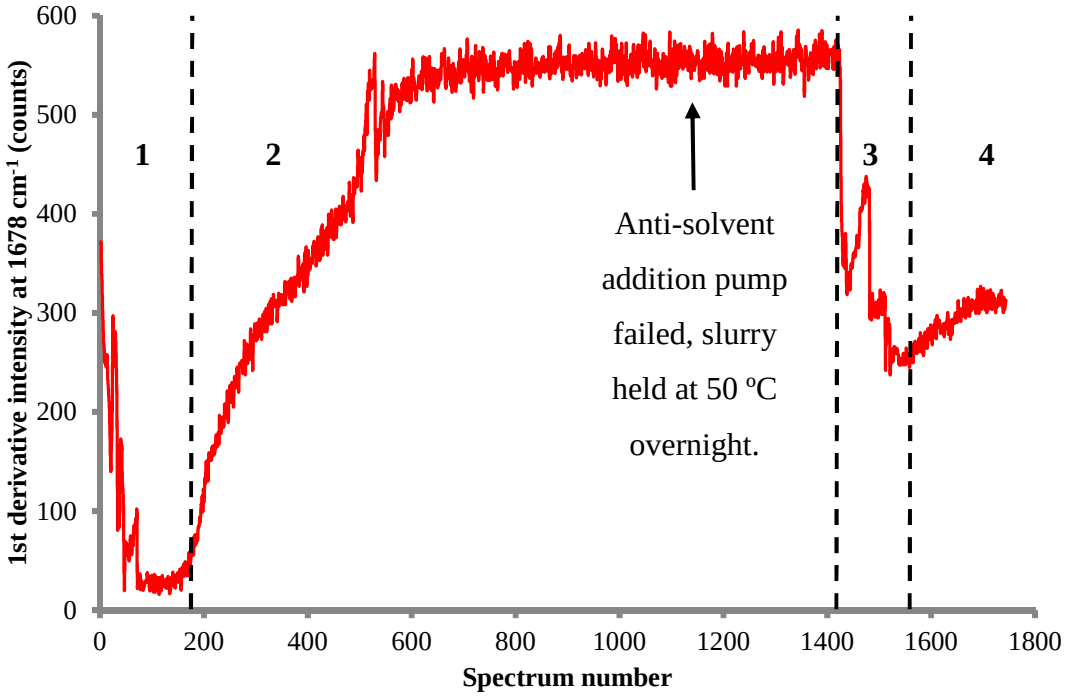

Figure 7-8: 1st derivative Raman intensity at 1678 cm^{-1} vs. spectrum number representing the API contribution to the overall Raman signal during recrystallisation. Section 1: dissolution and seeding, 2: nucleation, growth, agglomeration and breakage, 3: anti-solvent addition and 4: growth and breakage until equilibrium was reached.

The data in Figure 7-8 can be divided into four segments describing the process as before. Section 1 shows the signal arising from the API decreasing due to dissolution before cooling to 80 ºC and seeding takes place. Furthermore, the change from form II to III occurred during the first 50 measurements, this is observed as a sharp reduction then increase in the API signal as the form II particles dissolved rapidly and then precipitated as form III. In section 2, nucleation, growth, agglomeration and breakage of the recrystallised particles took place simultaneously, until equilibrium

was reached with the solution cooled from 80 to 50 ºC. At this point, the pump employed to add the anti-solvent failed which resulted in the slurry being held at 50 ºC overnight until manual override of the control system and addition of the anti-solvent was commenced the following day (section 3). Section 4 shows the final growth and agglomeration period until equilibrium was reached. Multivariate analysis techniques could also be employed to probe the recrystallisation data, however, the univariate approach described here adequately demonstrates the potential to monitor the process successfully using the non-invasive P^{h}AT probe, and further, illustrates the advantages of using wide illumination Raman rather than a confocal optical set-up with a small laser spot size.

7.3.2 Wet-milling, (WM 1 in Figure 7-1 a))

Wet-milling of the API was performed at the 1 L scale in the presence of the excipients in order to investigate the possibility of creating granules without a specific wet granulation step being performed during secondary manufacturing. The contents of the intra-granular blend were: the API (92%), Starch 1500 (5%) and sodium crosscarmellose (3%). The operation was performed three times (results of experiment 1 shown here): firstly, in the presence of both excipients, secondly, in the presence of only Starch 1500, and thirdly, with the API only. In the second experiment, sodium croscarmellose was added during the drying stage as it was found that the dissolution properties of the drug product were poor when it was added during wet milling (in the third experiment, both Starch 1500 and sodium crosscarmellose were added during the drying stage for experiment 3). Sodium croscarmellose is a disintegrent that was added to ensure that tablets break-up correctly in the body. It was found that by wet-milling, the physical properties of sodium croscarmellose were altered, which in turn, had an effect on the dissolution/ disintegration properties of the oral dosage formulation of the drug product. Likewise, with the recrystallisation measurements, during the wet milling, the particles were monitored using FBRM, Raman spectrometry and a Bruker Matrix FT-NIR spectrometer. The FBRM data obtained during wet-milling experiment 1 in the presence of both intra-granular excipients are shown in Figure 7-9.

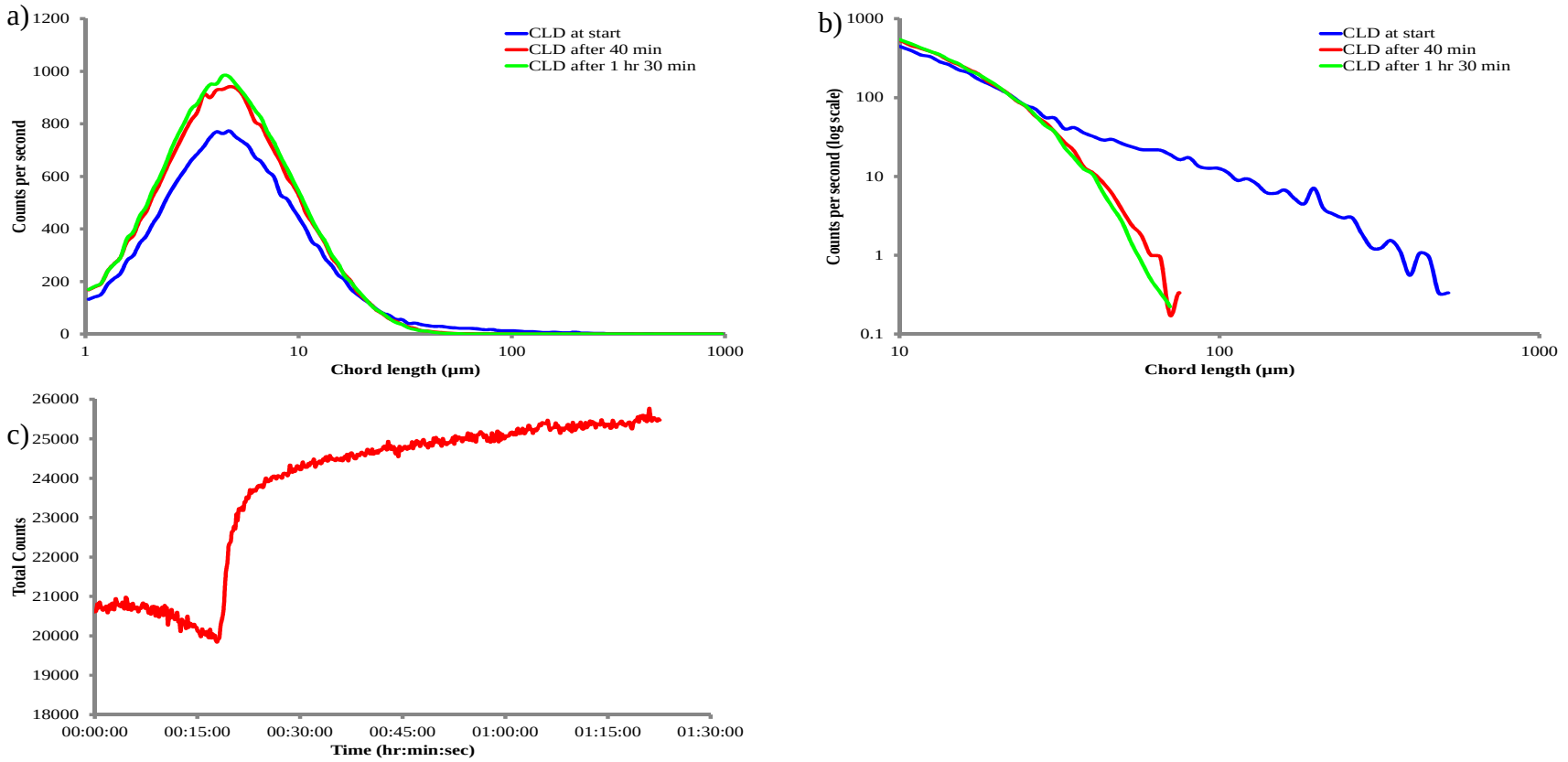

Figure 7-9: a) Chord length distribution data obtained by FBRM at stated time points during milling, b) log/ log plot of coarse tail in FBRM data at stated time points during milling and c) total counts vs. time for milling experiment.

In Figure 7-9 a) the number of counts per second for the measured CLD increased as the milling operation was carried out. This indicated that larger needle particles were being milled into smaller needle fragments, and also that agglomerates were being broken up into primary particles and eventually into fragmented needles. This was confirmed when Figures 7-9 b) and c) were also considered. By studying the log/log plots of FBRM chord length distributions, significant weighting is placed on the coarse tail of the distributions. In this data set, the log/log plot demonstrates the reduction of coarse particles and aggregates owing to a sharp reduction in the number of these particles from the start of milling to after 40 mins and then a further, albeit smaller, reduction in the number of coarser particles from 40 mins to 1 hr 30 min. Additionally, the basis of FBRM meant that the needle width was the dimension predominantly measured throughout the milling process, whereas a change in needle length occurred as the particles were passed through the mill. Therefore, the reduction in average needle length was not significantly reflected by a shift in the mode observed in the distribution plot of CLD vs. counts per sec due to the needle width remaining relatively constant. Conversely, when considering the plot of total counts vs. time for the data set, the increase in the total number of counts per measurement indicates the reduction in the average particle size of the needles measured, and furthermore, the rate of change (or rate of particle breakage) was also observed. Here, a large reduction in the number of coarse particles and aggregates at the onset of milling resulted in a sharp rise in the number of total counts per measurement due to the larger needles or aggregates breaking down into many smaller particles. The breakage rate then slowed at a time point when the majority of particles had passed through the mill at least once, and thus, completed the particle size reduction process.

For Raman measurements, the Kaiser Raman Rxn 2 spectrometer with the P^hAT probe was used to collect data, however, there was no suitable probe position to monitor the process non-invasively through a port in the lid. Consequently, the P^hAT probe was directed at the process through the glass walls and oil jacket of the vessel and this resulted in a significant glass background in the Raman data, with peaks also present that were attributable to the oil used in the jacket. Furthermore, with the sub

optimal position of the probe, it was prone to slipping and needed to be replaced twice during the experiment. Fortunately, NIR measurements were made concurrently with the Raman measurements and can be used here as a more suitable spectroscopic comparison to the FBRM data collected. However, when wet-milling was repeated, a more suitable Raman probe position was used with the probe directed at the slurry through an unused port in the lid of the vessel (data not shown due to the process being performed at much smaller scale, and therefore, the timescale for the reaction was much less and there was only a small number of spectra recorded). Shown in Figure 7-10 a) and b), respectively, are the PC 1 scores and loadings (with example spectrum overlaid) from PCA on the full useable region of the Raman spectra (150 – 980 cm^{-1} due to the glass background). The PCA model was built using four principal components.

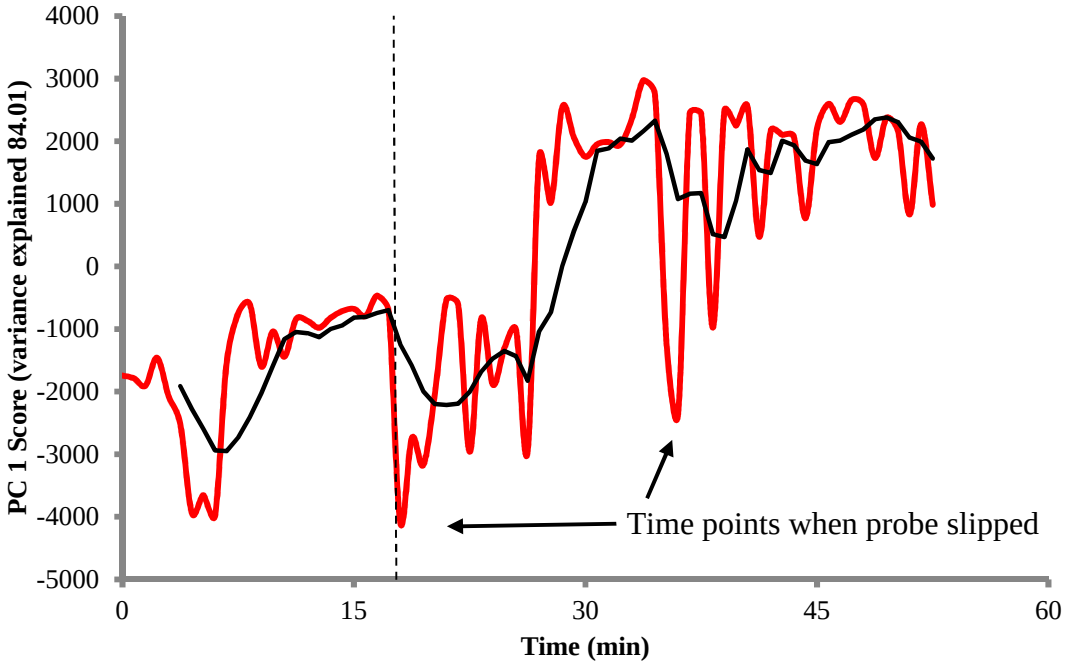

Figure 7-10 a) PC 1 scores vs. time from PCA model constructed using full useable region of Raman data through glass wall of vessel during wet milling of the API and excipients in the crystalliser. Dashed line indicates when wet-milling commenced and solid black line indicated the moving block average over 5 measurements.

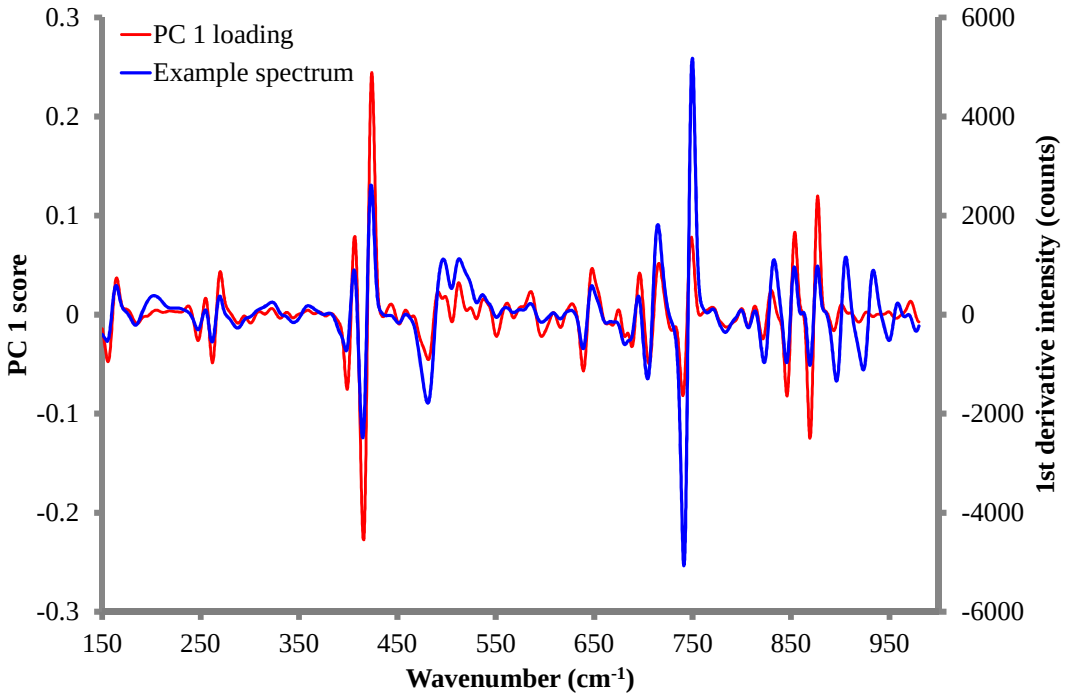

Figure 7-10 b) Loadings on PC 1 with overlaid example spectrum from the PCA analysis carried on the full usable region of the Raman spectra (150 – 980 cm^{-1}) obtained during wet milling experiment 1 (WM 1 in Figure 7-1 a)).

The PCA data obtained demonstrates that Raman spectrometry is suitable to monitor the unit operation, however, optimisation of the probe position would be required to obtain better data with less or reduced glass background and less susceptible to the probe slipping, i.e. a fixed position. From Figure 7-9 b), the loadings for PC 1 are correlated to the Raman spectra, and therefore, an increase in Raman signal was expected as the average particle size decreased during the operation. The scores for PC 1 are consistent with this hypothesis, however, there is a significant amount of noise present in the data, and further, a decrease in the Raman signal was observed at the two time points where the probe had to be re-positioned. The amount of noise present in the data were reduced by plotting the moving block standard average of the data (block size 5 measurements), and this showed that the rate of change slowed after around 25 – 30 min which is in qualitative agreement with the FBRM data in Figure 7-9 c).

Although showing the expected trend for a reduction in particle size, the poor method of measurement for the experiment made the Raman data difficult to interpret, and therefore, will not be discussed further here. However, NIR spectroscopic measurements were made using a Bruker Matrix FT-NIR spectrometer and diffuse reflectance immersion probe in tandem to the Raman measurements. Peaks in NIR spectra are broad and often convoluted, and therefore resolution of peaks can sometimes be a challenge. However, NIR spectra, like Raman spectra, are known to contain physical information, and thus, are a suitable alternative for detecting a change of particle size *in situ*. Figure 7-11 shows examples of 1st derivative NIR spectra obtained during the wet-milling experiment.

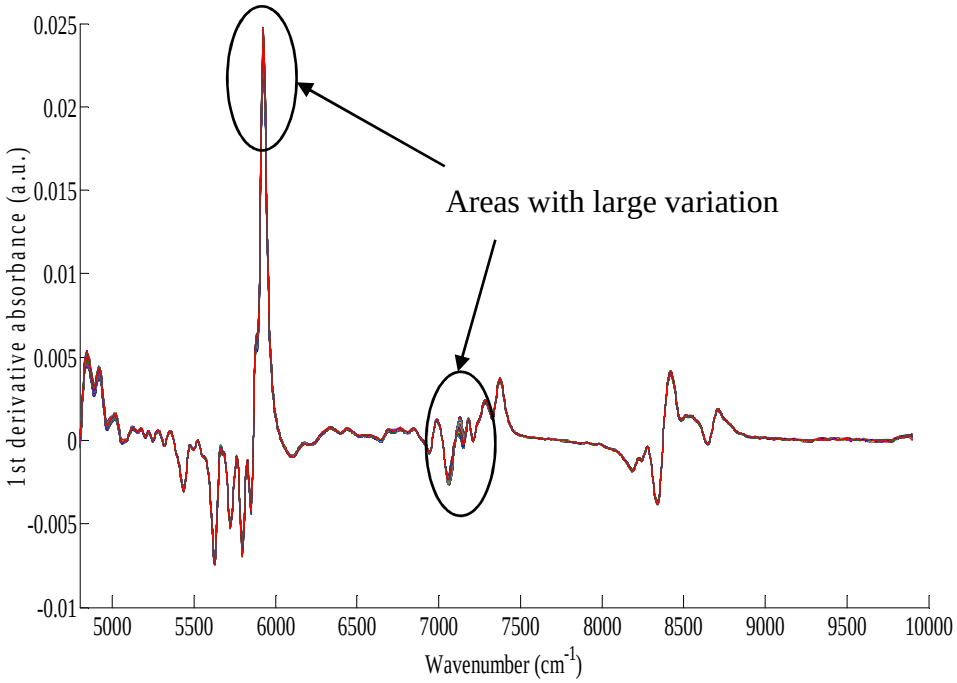

Figure 7-11: Examples of 1st derivative NIR spectra obtained during wet-milling experiment 1.

The NIR spectra shown in Figure 7-11 display two areas where large variation was observed. In the log 1/R NIR data (not shown), particle size affects both the baseline and absorbance from the particles due to both the absorption and scattering coefficients of the NIR signal being susceptible to physical characteristics of the material. These effects have been modelled by Bull, where, based on Kubelka-Munk

scattering theory, the author determined that smaller particles of the same material will scatter incident light more efficiently, and as a consequence have lower baselines in their NIR spectra.[15, 16] By performing a first derivative transformation to the data, the effects caused by varying baseline are reduced, and therefore, variations in the spectra are due to the changes in absorbance. From the literature, it is generally accepted that coarser, larger particles will absorb more incident radiation than smaller particles of the same derived from penetration depth studies with static powders,[17] however, when univariate analysis was carried out, an opposite trend was observed in this work, where an increase of absorbance occurred as the particle size was decreased (data not shown).

PCA was then performed on the full usable spectral region (4800 – 9800 cm^{-1}) in order to determine the regions of the spectra that varied the most as the milling process was carried out. Figure 7-12 a) and b) show, respectively, the PC 1 scores and loadings (with example spectra overlaid) from PCA analysis of the NIR data set, respectively.

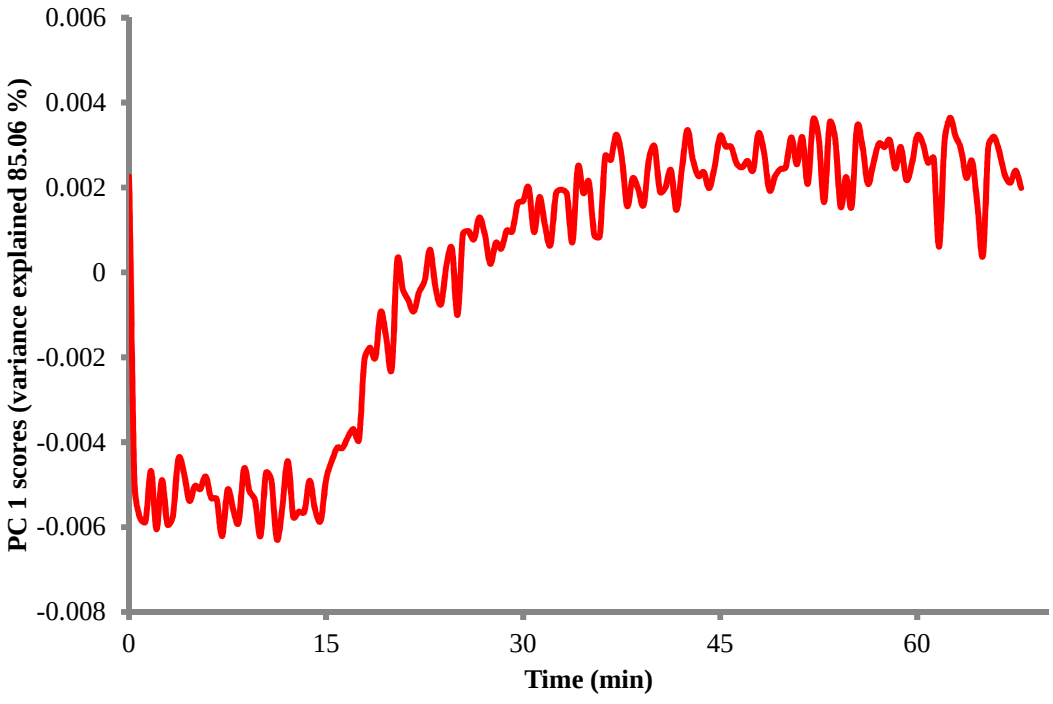

Figure 7-12 a) PC 1 scores vs. time for the PCA model constructed using the NIR data obtained during wet milling experiment 1 (spectral region 4800 – 9800 cm^{-1}).

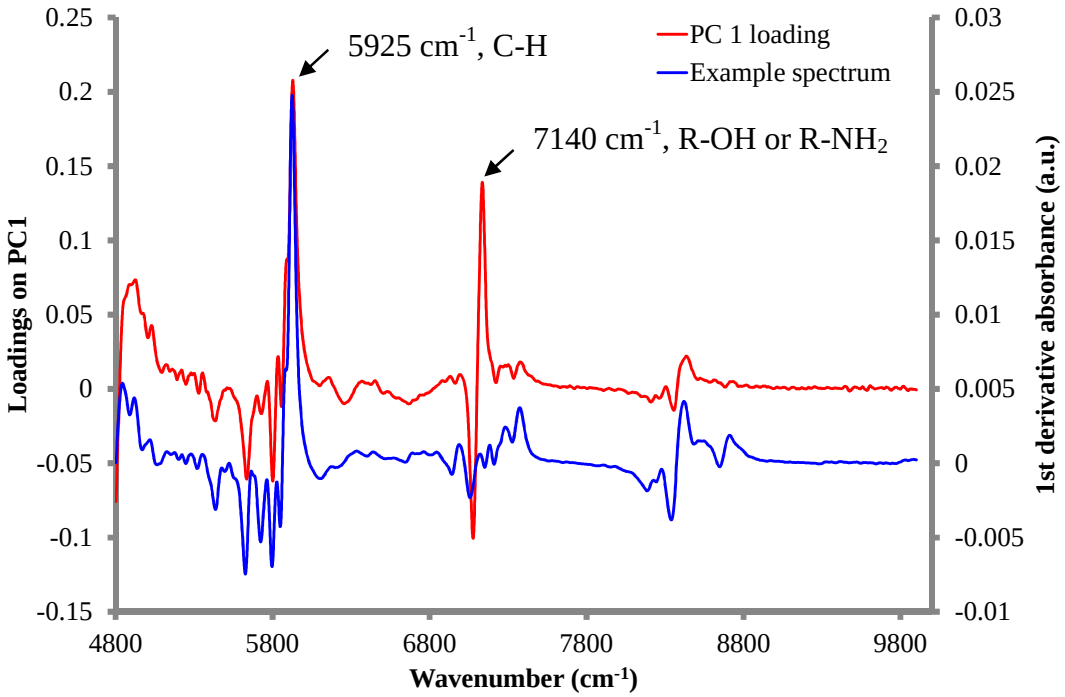

Figure 7-12 b) Loadings on PC 1 with example NIR spectrum overlaid from the PCA carried out on the NIR data set.

The loadings on PC 1 are correlated to the NIR spectra obtained, and therefore an increase in PC 1 scores like those observed vs. time in Figure 7-11 a) occurs as a result of an increase in NIR absorbance. There are two peaks that have particularly strong correlation to the spectra in PC 1. The peak at 5925 cm^{-1} is likely caused by C-H vibrations that are present in the *n*-butanol solvent, the API and both excipients. The second peak (7140 cm^{-1}) can be attributed to either R-OH or R-NH absorptions, with R-OH again being present in both *n*-butanol and the API, and $R\text{-}NH_2$ being unique to the API. It is often difficult to assign peaks in NIR spectra to uniquely identify a single component of the mixture, which is why multivariate data analysis techniques are typically used to analyse NIR data. As mentioned, the trend observed using both uni- and multivariate analysis is opposite to that expected based on NIR diffuse reflectance theory. A possible reason for this is similar to the observations of Nordon *et al.* during NIR monitoring of a fermentation process, where a decrease in NIR signal was observed during a growth period of the bacteria rather than an increase as expected.[18] The authors attributed the reduction in NIR

signal with growth to the reduction in concentration of bacteria that the NIR probe could measure (few bigger bacteria rather than many smaller ones). In the data presented in Figure 7-11 a) and b), the particle size is reduced during the process, and thus, it is rational that the NIR signal increased due to a rise in the number of particles (which is related to concentration) leading to greater absorbance, similar to the effects observed with the FBRM probe where the number of total counts per measurement increased as the particle size decreased. It is also important to note that diffuse reflectance scattering theory was not developed for particles in a slurry, but was instead developed for static dry powders, and therefore would not be expected to be strictly valid to this data set.

The NIR and Raman data presented here have shown the suitability of both spectroscopic techniques to monitor the wet-milling process of the API in the presence of the intra-granular excipients. The sub-optimal positioning of the Raman probe, however, led to poor results being obtained due to the position not being constant throughout the analysis. Nevertheless, the Raman data obtained displayed the expected trends for a reduction in particle size that were consistent with other results in this report and with the literature.

Considering both the wet-milling and recrystallisation processes for the API described, the added chemical information obtained from *in situ* spectroscopic methods compared with the information obtained with FBRM would not really justify the time and expense required to build predictive spectral models for analysis. FBRM has known limitations for needles shaped particles with the technique predominantly measuring needle-width, and therefore, does not give a representative distribution of the needle length (which is the major dimension). For recrystallisation, the Raman data obtained was generated from both the API particles and the solvent, however, the FBRM probe was able to track the process until completion using the total number of counts per measurement, and furthermore, provided in-depth physical information about the process. Similarly for wet-milling, despite both spectroscopies successfully monitoring the process qualitatively, FBRM was able to track the process in real-time giving information about the distribution of

particles and the increase in the number of particles as the milling process was carried out. Conversely, where Raman and NIR spectroscopies demonstrate the most potential, is in unit processes where normal operation of FBRM probes is not suitable, such as in wet granulation or drying. The development of the C35 FBRM probe with a "window wiper" over the probe optics has allowed for FBRM probes to be placed into processes that were previously inaccessible, however, during the completion of this work, a C35 probe was not available for study.

7.3.3 Wet granulation/ drying, (VD 2 in Figure 7-1 a))

The wet-milled API and excipients were dried in an agitated filter drier, however, there were no ports in the drier to allow PAT instrumentation to monitor the operation (the cake height was too low). The granules prepared were blended further with excipients to form an extra-granular blend that was subsequently pressed into tablets, however, the hardness and dissolution/ disintegration properties of these tablets were not suitable for use in the body. It was thought that the absence of water in the granules (hardness) coupled with the change in the physical properties of the sodium croscarmellose (dissolution) caused by addition during the wet milling stage were the reason for the poor tablet properties (see section 7.3.4). Therefore, water was added to the dry granules to determine if the tablet hardness properties were improved. This was performed in a pan drier and water was added to a concentration of 30% wt/wt. The experiment was carried out in two stages: an initial mixing period followed by a period of vacuum agitated drying. Samples were taken at the end of the mixing period and at the end of the vacuum agitated period for LOD analysis. During the experiments, a combination of non-invasive Raman and NIR measurements were performed. The bending and stretching modes of Raman are practically insensitive to water (at 785 nm excitation), whereas, NIR spectroscopy is very sensitive to water concentration. Therefore, Raman measurements were used to monitor changes to the particles as the granulation process was carried out, whereas NIR was used to monitor the water drying curve (not shown). Figure 7-13 shows an example 1st derivative Raman spectra (one during initial mixing period and one

during vacuum agitated drying period) obtained during the removal of water (30% wt/wt) from the API/ excipient granules.

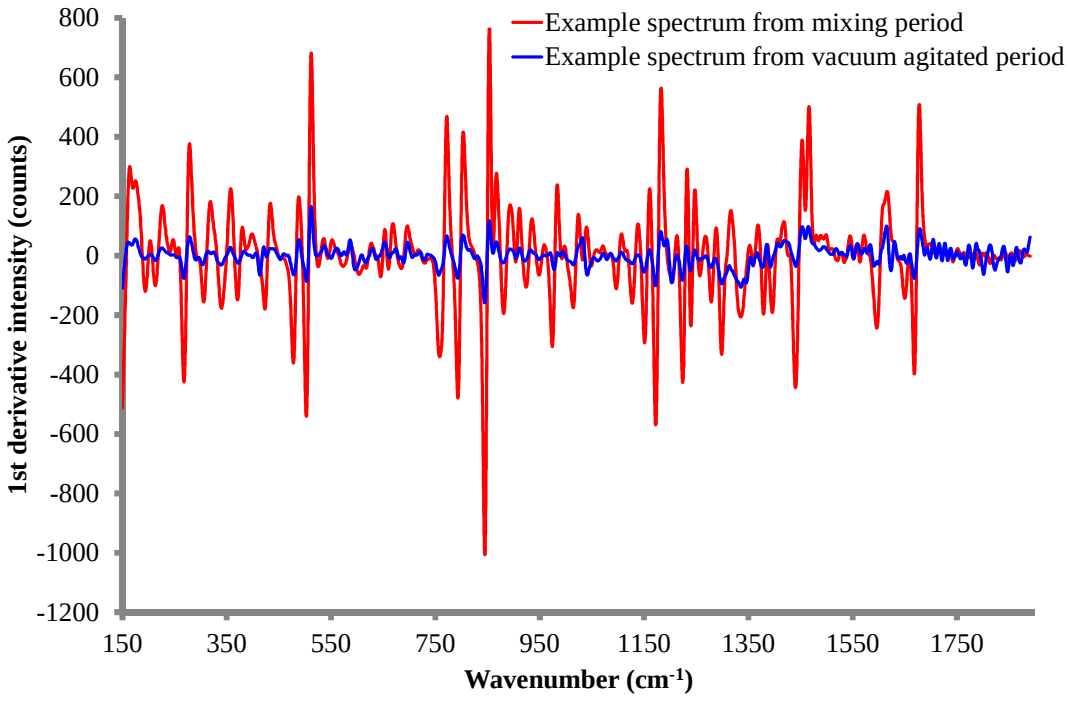

Figure 7-13: Example 1st derivative Raman spectra for initial mixing period (red) and vacuum agitated drying period (blue) for addition of water to the API/ excipient granules.

Figure 7-13 shows a reduction in the Raman signal after the vacuum agitated drying period was commenced. In Raman data, a reduction in the signal observed would be expected with an increase in particle size, however, this effect is related to the bulk density of the material. Granulation processes are designed to increase the bulk density of particles while simultaneously increasing the particle size. The aim is to produce free flowing granules with low polydispersity that can easily be blended with excipients and tableted. This is an opposite effect to the particle size effects described previously during this report where a reduction in particle size (caused by attrition) resulted in an increase in the bulk density of the material. Attrition of needle-shaped particles does not often result in free flowing particles that can be easily be processed downstream, instead, adhesive poor flowing particles is the

typical result. Walker *et al.*,[7] noted that the areas of greatest particle density gave rise to the largest Raman signals during fluidised bed granulation of glass beads, indicating that bulk density has a greater effect on the Raman signal than does particle size. In order to understand the effects observed in the Raman spectra, both univariate analysis (not shown) and PCA was carried out on the data set. Shown in Figure 7-14 a) and b) are the scores from PC 1, and the loadings on PC 1 (with example spectrum overlaid), respectively, obtained from PCA of the full region (150 – 1900 cm^{-1}) using 2 principal components (750 – 1350 cm^{-1} region shown for clarity).

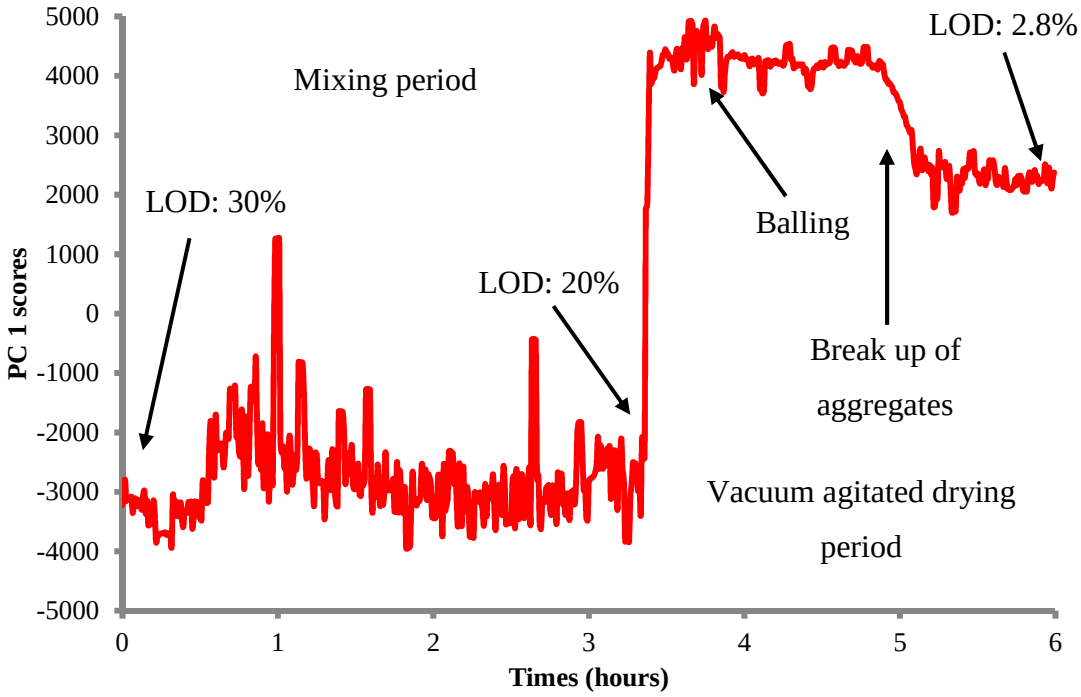

Figure 7-14: a) PC 1 scores from PCA analysis on the 150 – 1900 cm^{-1} region during Raman analysis of the API/ excipient granules as water is removed.

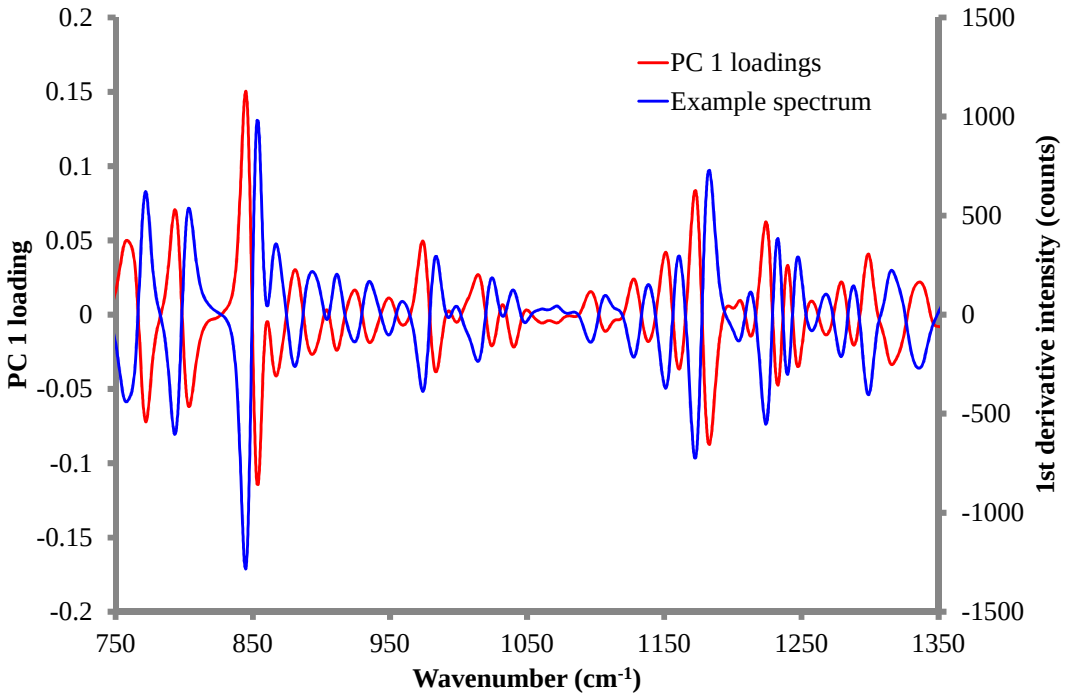

Figure 7-14: b) Loadings on PC 1 (750 – 1350 cm^{-1} region shown for clarity) with example Raman spectrum overlaid from the PCA carried out on the Raman data set.

From the plot in Figure 7-14 b), it can be seen that the loadings are anti-correlated to the Raman spectra, therefore, an increase in PC 1 occurred when there was a decrease in Raman intensity. From 7-14 a), The PC 1 scores appear to take around 1.5 h to reach equilibrium where only random noise generated by the particle motion affected the signal measured. A sample was extracted before the vacuum agitated period so that the LOD was known before and after drying, the LOD at the end of the mixing period was 20% wt/wt. At the onset of vacuum agitated drying, the PC 1 scores increased significantly signaling a decrease in the Raman signal, visual inspection of inside the drier at this point showed that balling had taken place, and therefore, the change in Raman signal was consistent with when balling had been observed previously in vacuum agitated drying experiments. As the balls of particles broke up and drying continued, the Raman scores decreases, which was consistent with an increase in Raman signal and also the bulk density as the process progressed.

A second wet-milling experiment was also performed, using just the API and starch particles to determine if adding the sodium croscarmellose during the drying stage resulted in better tablet dissolution properties. The wet-milled API and starch were then dried in the agitated filter drier before being transferred to a vacuum pan drier, where the sodium crosscarmellose was added along with water (either 2.8% wt/wt, or 30% wt/wt and dried to ~ 2.8% wt/wt). Data were collected for the experiment where 2.8% wt/wt water was added (non-invasive Raman and NIR measurements were performed). For this experiment, there were no significant changes in the Raman data during granulation owing to the majority of the granules being formed during drying, and thus, the addition of a small amount of water and sodium croscarmellose did not have a great effect on the granules themselves or the Raman spectra collected (data not shown).

7.3.4 Hardness and disintegration/ dissolution testing (control and investigation tablets from Figure 7-1 b)

The granules prepared via the proposed reduction in the production train (Figure 7-1 a) and b)) were then subjected to hardness and disintegration/ dissolution testing using standard methods. The bulk density of the granules were measured before they were blended with excipients to form the extra-granular formulation and then pressed into tablets at increasing compression forces (2000 to 5000 psi). The results of the bulk density and dissolution/ disintegration tests are given in Table 7-1. The results of hardness testing are given in the compression profiles shown in Figure 7-15. In Figure 7-15, the x axis is labeled compression force, which was the force exerted onto the blend of excipients and API while it was mounted in a die on a tablet press. The y axis reports the tablet hardness (kPa) and are the results of a destructive test that determines the pressure required in order to break the tablet. Furthermore, the plane in which the tablet breaks is indicative of the robustness of the formulation of the tableting procedure, where breakage on the vertical plane of the tablet suggests that the formulation and tableting procedure is fit-for-purpose.

Table 7-1: Results of bulk density, and disintegration/ dissolution testing for the granules prepared using proposed reduced production train (Figure 7-1 a) and b)).

Reactor contents during wet milling	Granulation conditions	Bulk Density of granule/ g/ mL	Dissolution/ disintegration testing method	Result	Ref in Figure 7-14
API, sodium croscarmellose and startch 1500[a]	dry	0.4-0.45	Disintegration	~ 3 min	Set 1
API, sodium croscarmellose and startch 1500[a]	30% wt/wt water dried to 2.8% wt/wt	0.4-0.45	Disintegration	~ 3 min	Set 2
API[a]	30% wt/wt water added and dried to 2.8% wt/wt	0.5-0.55	Dissolution	91% @ 15 min, 100% @ 60 min	Set 3
API, Starch 1500[a]	2.5% wt/wt Water added	0.15-0.2	Not measured	NA	NA
Control[b]	NA[c]	Information not given	Both	Disintegration: < 45 sec Dissolution: ~ 15 min	Control

[a]Investigation tablets prepared using process train outlined in Figure 7-1 b)

[b]Wet-milling not performed, granules prepared using continuous granulator by formulation chemists (control tablets prepared using process train outlined in Figure 7-1 b).

[c]Granulation carried out in continuous granulator and drier (no further information available in relation to conditions).

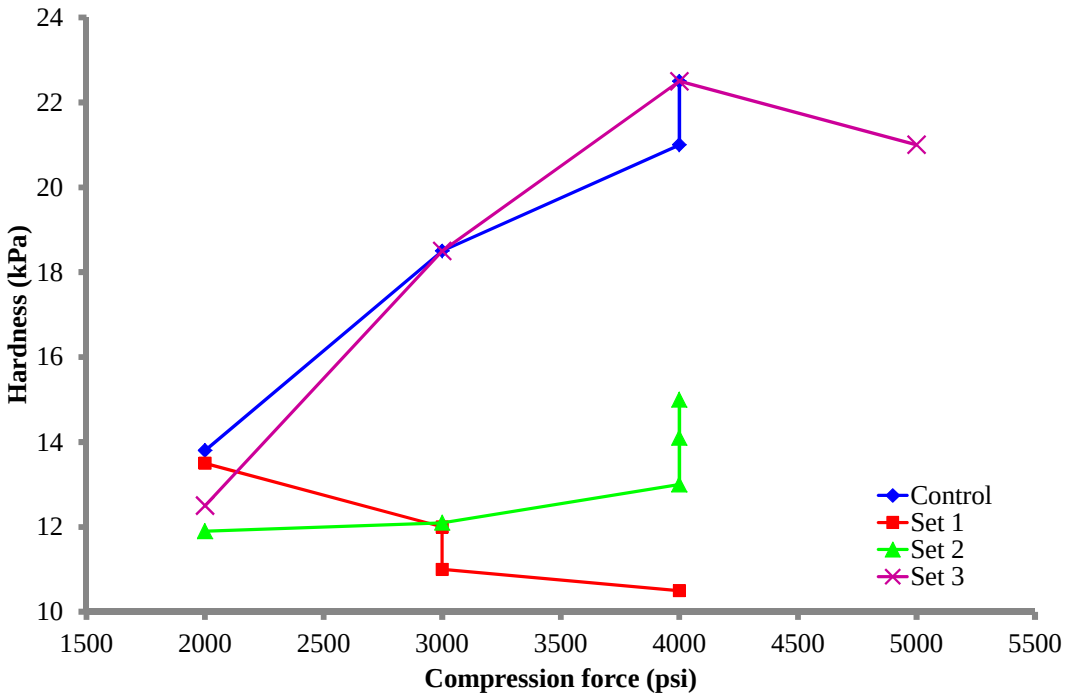

Figure 7-15: Compression profiles for tablets prepared using granules manufactured using the proposed process train and control granules prepared using the current process train (described in Figure 7-1 a) and b)).

Considering both Table 7-1 and Figure 7-15, the granules produced when the API and both excipients were wet milled did not have similar tablet characteristics to those production from the original manufacturing train (control). Set 3, however, which wet-milled only the API, before adding the intra-granular excipients during drying showed a similar compression profile to the control set, and furthermore, the dissolution characteristics were also similar. This demonstrated that wet-milling the excipients used in the intra-granular blend had a negative effects on the properties of the oral dose formulation of the drug product.

7.4 Summary and conclusions

The potential to create API granules during primary rather than secondary manufacturing was investigated in order to enable only the direct compression of the drug substance during secondary manufacturing. If successful, the number of processing steps would be reduced to 4 instead of 7. *In situ* spectroscopic

measurements alongside FBRM were also carried out to assess the suitability of each of the techniques to monitor the unit processes performed. The conclusions from a corporate perspective were that the reduction of the number of processing steps would complicate the API supply chain, which although suitable for the oral solid dosage formulation, would not be applicable to the intravenous formulation. It was recommended, however, if the compound were to make it to market as a high volume product, that the approach should be revisited as a second generation process for the oral dose formulation only. From a research perspective, it can be concluded that FBRM is more suitable to monitor physical changes to particles while in slurry for this particular API, where control of the desired polymorph is well understood. Although Raman measurements were able to monitor the crystallisation processes, and both NIR and Raman spectrometries successfully tracked the wet-milling process, the information contained in the *in situ* spectroscopic data did not offer significantly more information than did use of the FBRM probe. Where *in situ* spectrometries showed most potential was in environments where FBRM measurements were not suitable, such as granulation or drying. It is recommended that the proof of concept experiments carried out in the short time available to do this research should be expanded to assess more fully the capabilities of the spectroscopic measurements for the manufacturing processes.

7.6 References

1. M. C. Enright, D. A. Robinson, G. Randle, E. J. Feil, H. Grundmann and B. G. Spratt, *Proc. Nat. Acad. Sci.*, 2002, **99**, 7687-7692.

2. J. Cornel, C. Lindenberg and M. Mazzotti, *Ind. Eng. Chem. Res.*, 2008, **47**, 4870-4882.

3. E. Da Silva, S. Bresson and D. Rousseau, *Chem. Phys. Lipids*, 2009, **157**, 113-119.

4. Y. R. Hu, J. K. Liang, A. S. Myerson and L. S. Taylor, *Ind. Eng. Chem. Res.*, 2005, **44**, 1233-1240.

5. Z. Német, G. C. Kis, G. Pokol and Á. Demeter, *J. Pharm. Biomed. Anal.*, 2009, **49**, 338-346.

6. M. Tkacz, T. Palasyuk, J. Graetz and S. Saxena, *J. Raman Spectrosc.*, 2008, **39**, 922-927.

7. G. M. Walker, S. E. J. Bell, K. Greene, D. S. Jones and G. P. Andrews, *Chem. Eng. Sci.*, 2009, **64**, 91-98.

8. J. W. Mullin, *Crystallization*, Reed Elsevier plc, Oxford, 2001.

9. K. Sepek, *Investigation of the effects of flow on crystallisation process*, PhD, University of Strathclyde, 2011.

10. S. G. S. Cesur, *Cryst. Res. Technol.*, 2008, **43**, 720-728.

11. X. S. Liu, D. Sun, F. Wang, Y. J. Wu, Y. Chen and L. H. Wang, *J. Pharm. Sci.*, 2011, **100**, 2452-2459.

12. D. O'Grady, B. O'Sullivan, J. Schoell, T. Redman and M. Barrett, *Chim. Oggi-Chem. Today*, 2008, **26**, 22-24.

13. E. Kougoulos, A. G. Jones, K. H. Jennings and M. W. Wood-Kaczmar, *J. Cryst. Growth*, 2005, **273**, 529-534.

14. Z. Q. Yu, J. W. Chew, P. S. Chow and R. B. H. Tan, *Chem. Eng. Res. Des.*, 2007, **85**, 893-905.

15. C. R. Bull, *J. Mod. Opt.*, 1990, **37**, 1955-1964.

16. C. R. Bull, *Analyst*, 1991, **116**, 781-786.

17. L. J. Bellamy, A. Nordon and D. Littlejohn, *Analyst*, 2008, **133**, 58-64.

18. A. Nordon, D. Littlejohn, A. S. Dann, P. A. Jeffkins, M. D. Richardson and S. L. Stimpson, *Analyst*, 2008, **133**, 660-666.

8 Conclusions and suggestions for future work

8.1 Conclusions

The aims set out at the beginning of this work were:

- To evaluate the suitability of particle size analysis techniques as a reference method to determine the extent of attrition that occurs during a drying process for needle-shaped particles.
- To determine the relationship between drying parameters on the length of drying time required and the extent of attrition that occurs during drying.
- To assess non-invasive instrumentation to monitor *in situ* the physical and chemical processes that take place during drying.
- To apply *in situ* instrumentation to an industrially relevant drying process.

8.1.1 Evaluation of particle size analysis techniques to measure the extent of attrition that occurs during pharmaceutical powder drying.

The measured distributions and calculated statistic from five particle size analysis techniques (based on either laser scattering or dynamic image analysis) were evaluated with respect to particle shape by measuring increasing size ranges of needle-shaped COA particles and granular Avicel particles. The key points from the evaluation were as follows:

- Laser diffraction (LD) and FBRM measurements gave qualitative information about changes in particle size that occurred during drying. LD measurements are only truly quantitative for spherical particles due to the complexity of the mathematics required to develop Mie and Fraunhoffer theories for non-spherical particles. FBRM analyses particles irrespective of shape, however, the average orientation of the particles in a slurry means that the FBRM laser cuts needle-shaped particles predominantly along their width axis.

- It was found that the Feret Min diameter from dynamic image analysis (shortest diameter between two parallel tangents) correlated well with the chord length distribution data obtained with FBRM. In this example, the average needle width increased with average needle length which meant that the average needle length could be inferred from the FBRM measurements.
- The Feret Max dimension obtained from dynamic image analysis provided the best quantitative method to determine the change in needle particle size due to breakage occurring predominantly along the length axis. Feret Max is a measure of the longest dimension between two parallel tangents of a particle, i.e. the needle length.

8.1.2 Determine the effect of varying drying parameters on the drying time and extent of attrition that occurred – a DoE approach.

A full factorial (2 level, 3 factor (2^3)) design of experiments with two centre points was carried out to determine the effects of the agitation strategy and jacket temperature and starting solvent content (defined as the percent solvent loss on drying – SLOD), on the drying time observed and the extent of attrition that occurred during drying. The two centre point experiments were on either side of the design cube due to the categorical nature of the agitation strategy parameter. Analysis of both the solvent and particle drying curves were performed *in situ* using non-invasive Raman spectrometry and off-line particle size measurements (based on laser diffraction and dynamic image analysis) were performed to determine the extent of attrition that occurred. The key points from the study were:

- It was found that agitation strategy had the greatest effect on both the overall drying time and the extent of attrition observed. Whereas, all three variables had a significant effect on the drying end point (determined using non-invasive Raman spectrometry), it was found that continuously agitated particles resulted in the greatest needle breakage owing to the extent of shear caused by the agitator.
- From off-line Raman experiments, it was found that the 1st derivativeRaman signal arising from the particles increased as particle size decreased until a

threshold particle size was reached where there was no further increase in Raman signal observed. The effect of particle size on the Raman signal was attributed to changes in the bulk density of the particles rather than the change in average particle size, owing to packing effects.

- Non-invasive Raman measurements were suitable to monitor the removal of methanol from COA particles during drying in real-time, either by plotting the intensity ratio of a methanol peak: COA peak (both two point baseline corrected) in the Raman spectra versus time, or by plotting the univariate decay of a methanol peak from the 1st derivative Raman spectra versus time at a wavenumber where there was little or no contribution from COA.
- The narrow bands observed by Raman spectrometry meant that the combined methanol and COA spectrum could be divided into regions where only the particles contributed to the Raman data. This allowed for real-time detection of the formation and break up of aggregates that occurred during powder drying in real-time due to changes in the average bulk density of the particles (owing to the effect on the Raman intensity). The position of the probe (through a window in the lid), however, meant that fluctuations in the bed height appeared to have a greater effect on the Raman signal than the effects of particle size or bulk density, and therefore, for future experiments, a second probe position from the side at the bottom of the drier was used.

8.1.3 Application of the knowledge gained from the DoE study to an industrially relevant drying process.

Slurries of COA and methanol were prepared and dried using a pressure filtration stage followed by a vacuum agitated drying stage, in order to simulate an industrial drying process. By varying the length of the pressure filtration stage, a range of starting percent loss on drying (LOD) was achieved. Agitated vacuum drying was performed either with continuous or intermittent agitation meaning that the relationship between agitation time, particle wetness and extent of attrition could be investigated (as all other parameters were constant during this stage). The drying end point was determined in real-time using non-invasive Raman spectrometry, and

particle size analysis (based on laser diffraction and dynamic image analysis) was performed at the end of each stage to determine the extent of attrition. The key points from the study were:

- The pressure filtration did not cause significant needle-breakage using 0.5 bar of N_2, therefore, the pressure filtration step was deemed suitable for the process.
- The Raman probe was able to monitor both the removal of methanol, and the increase in bulk density caused by the positive pressure of N_2 univariately by tracking the intensity of either a 1st derivative methanol or COA band versus time.
- The extent of attrition was independent of the starting LOD for continuously agitated drying experiments, however, was related to the starting LOD for intermittently agitated drying experiments. This was due to the rate of attrition (needle breakage) being greatest during the initial 30 min of agitation, regardless of starting LOD (the rate slowed significantly after 30 min). As all continuously agitated experiments were agitated for more than 30 min, the majority of needle particles had already undergone the needle breakage process. For the intermittent drying experiments, the total agitation times were 4 and 6 min, respectively, meaning the attrition rate was on the steep side of the attrition versus agitation time curve, and therefore, each additional minute of agitation caused a significant amount of needle breakage.
- The detection of the formation and break-up of aggregates in real-time using non-invasive Raman spectrometry was confirmed. This is relevant to industry as these aggregates can cause severe detrimental effects to the inside of a drier, and therefore, real-time detection means that agitation can be stopped until a threshold LOD has been reached where the aggregates break up.
- Non-invasive Raman spectrometry can be used to monitor the average bulk density of the particles as the drying process occurs, however, the effect of average bulk density caused by the solvent removal process (the formation and destruction of liquid bridges at decreasing LODs etc.) was found to be greater than the effect of change in bulk density cause by a reduction in particle size.

- The use of the non-invasive P^{h}AT probe meant that the drying process could be monitored without disruption to the mixing process (like would be the case with in-line probes) owing to the "point-and-shoot" nature of the probe. Furthermore, the 6 mm spot size with around 3 mm penetration depth into the sample resulted in a greater amount of powder analysed per measurement than compared with traditional probes with con-focal optics. This meant that the use of the P^{h}AT probe gave more representative measurements than would be expected from con-focal in-line probes.

8.1.4 Application of *in situ* process measurements in the development of an active pharmaceutical ingredient.

The use of PAT instrumentation was evaluated for its role in supporting API development and formulation for a phase II antibiotic at GSK. FBRM, Raman and NIR measurements were applied to crystallisation, drying, wet-willing and granulation experiments to determine if the number of processing steps required for the production of the oral dose formulation could be reduced from 7 to 4. The key points from a research perspective were:

- FBRM measurements were more suitable for unit operations where particles are in slurry and control of polymorph is well understood. Although Raman (and NIR for wet-milling) were able to monitor these processes, the information contained in the spectroscopic data was not significantly greater than that gained from FBRM.
- In situ spectroscopic measurements were most suited to measurements where the solvent content is low such as granulation or drying. Scoping studies were performed where a combination of Raman and NIR were utilised to monitor a novel granulation process for the API, where the API was wet-milled with the intra-granular components and then granulated during the vacuum agitated drying process. Although more work was required, similar features to those observed

during the laboratory scale drying experiments were observed in the Raman data for the API.

8.2 Suggestions for future work

The studies carried out for this work revealed a great deal about the drying and attrition processes for needle-shaped COA particles, and furthermore, demonstrated that non-invasive Raman spectrometry allowed for real-time monitoring of the solvent removal and detection of the physical phenomena that occurred during drying. However, there is scope for further research into this area, and some possible suggestions are given below:

- Improved particle size analysis technology should be evaluated for monitoring of particle size in real-time during drying. For example, the FBRM C35 probe has a window wiper designed to eliminate probe fouling that occurs with wet sticky particles.
- Further study into the use of other spectroscopy techniques that can be used *in situ* could be carried out. Although some in-line NIRS work using a dispersive spectrometer was carried out in the bespoke drier used during this project (significant probe fouling and a baffle effect was observed), the application of diode array and fourier transform NIRS measurements to other processes has shown that particle size measurements can be inferred from the NIR data. Furthermore, the use of passive acoustic emission spectroscopy has shown potential for monitoring drying processes and could be studied in more depth.
- The work carried out here focused on the attrition and agglomeration processes that occurred during agitated powder drying, however, several other phenomena are known to occur such as solvate or hydrate changes. Raman spectroscopy is known to be sensitive to changes in polymorph, and therefore, polymorphic systems could be studied in future using this technique. NIRS is known to be sensitive to hydration state changes and therefore may be a suitable technique to monitor such changes during drying.

- The drying processes of other compounds with varying crystal shape and densities could be performed, in doing so, guidelines could be produced on how materials with similar physical properties may perform when dried.
- In this work, all the experiments have been carried out at a laboratory scale. Future studies could involve transfer of the Raman practices devised for monitoring of drying processes for assessment at a much larger scale, i.e. in pilot plant or full industrial driers.